POTENTIAL FOR NON-CONVENTIONAL USE OF SPLIT-BEAM PHASE DATA IN BOTTOM DETECTION

By

Leonardo Gomes de Araujo

B.Sc. Naval Sciences, Brazilian Naval Academy, Brazil, 2008
Extension Course in Hydrography (IHO category "A"), Brazilian Navy
Directorate of Hydrography and Navigation, Brazil, 2011

THESIS

Submitted to the University of New Hampshire
in partial fulfillment of
the requirements for the degree of

Master of Science

in

Earth Sciences

December, 2020

This thesis has been examined and approved in partial fulfillment of the requirements for the degree of Master of Science in Earth Sciences by:

Thesis Director, John E. Hughes Clarke, Professor,
University of New Hampshire.

Brian Calder, Research Professor,
University of New Hampshire.

Thomas C. Weber, Associate Professor,
University of New Hampshire.

On December 14th, 2020

Original approval signatures are on file with the University of New Hampshire Graduate School.

DEDICATION

To the love of my life, my wife Elaine, whose presence, endless support, and incentive were essential to my success.

ACKNOWLEDGEMENTS

Without a doubt, nothing that has been achieved would exist without the help of some institutions and people. For all that has been done, it is up to me to thank:

- Brazilian Navy, for trusting me, assigning me to this mission, and for supporting me financially. My knowledge in the area of hydrography has significantly been expanded, and this will be reflected in my future works in the Navy.

- John Hughes Clarke, my main advisor, for making it all possible, from data collection, through the processing and development of scripts, to the review of each line of this thesis. There are no words I can use to describe my gratitude. It was a great pleasure to have been your student and to meet the kind person you are. Even when no answer was found, you knew how to ask the right questions to get me to develop this research. The joy of having you on my committee is immeasurable.

- Brian Calder, for receiving me at CCOM/UNH, for guiding me in choosing some courses, for your classes, and for helping me change my initial thesis. Your guidance and sincerity were essential for me to get on the current path. I am very grateful to have you as a member of my committee.

- Thomas Weber, for the knowledge transmitted in the classroom, for the questions asked, and for helping to improve the path followed by this thesis. It is an honor to have you as member of my committee.

- Department of Education of the Directorate of Hydrography and Navigation (DHN), current Admiral Radler de Aquino Instruction and Training Center (CIAARA), and their teachers and instructors, for my training as a Hydrographer.

- CMG (Ref) Alenquer and Lieutenant Alana, for their help and guidance during the selection process.

- Dr. Geraldo, for his friendship, availability and recommendation letter.

- CF Rodrigo Carvalho, for his guidance at different times in my career, his recommendation letter, and for our conversation on the eve of my move to the United States.

- CC Douglas Luiz, for exchanging experience, his recommendation letter, and for the contribution to my research.

- CC (T) Freire, for the advice and guidance on my arrival.

- CC (T) Borba, for his recommendation letter, and for his tips on the city of Portsmouth and life at UNH.

- CC Peçanha, for his recommendation letter, and his safe guidance throughout the selection process, and for all the stages experienced between moving abroad and returning to Brazil. I am very grateful for your availability, attention and cordiality. I hope I can soon reciprocate with my work.

- CC Pimentel, for the conversations, support, ideas and suggestions.

- CC Ivan, my class friend, for experiencing a similar situation simultaneously, sharing with me his successes and mistakes, and helping me to lighten this challenge experienced.

- My executive officer, CT Barja, my officers, and the AvHoFlu Caravelas crew, for their professional competence and tranquility transmitted to me, during the brief period of my preparation for the selection process exams.

- All my friends from CAHO and Dodsworth class, for your valued help.

- Semme Dijkstra, for the classes, for the availability and attention, and for the challenging labs, which contributed a lot to develop my programming skills, without which I would not have completed this research.

- Andrew Armstrong, Firat Eren, James Irish, James Pringle, Joel Johnson, Jo Laird, John Kelley, Larry Mayer, Paul Johnson, Rochelle Wigley, Rosemarie Came and Steve Wineberg for your memorable teachings.

- GEBCO 2018-2019 Scholars, Victoria Obura, Mekayla Dale, Victor Chilamba, Kemron Beache, Rafeq Paimin and Keshav Sauba, for their support and help in our studies and group work.

- CCOM grad students, Jaya Roperez, Tamer Nada, Jordan Pierce, Jeffrey Douglas, Katie Kirk, Dylan Wilford, Casey O'Heran, Jonathan Hamel, Brandon Maingot, Hilary Kates Varghese, Coral Moreno, Alexandra Padilla and Indra Prasetyawan. Especially Jennifer Johnson, Aditi Tripathy and Anne Marie Hartwell, for their support in some difficult moments.

- R/V Gulf Surveyor team, Emily Terry, Matthew Rowell and Daniel Tauriello, for their support when using the vessel.

- Wendy Monroe, Renee Blinn and Kris Tonkin for all support, warmth and help with some documents.

- Will Fessenden and his IT team, for all their support in software, printers and licenses.

- Other faculty and staff members of the Center for Coastal and Ocean Mapping / Joint Hydrographic Center (CCOM / JHC), for your valuable support.

- Brazilian community in New Hampshire, especially those who became great friends, Lívia, Jack, Luiz, Márcia, Gabriel, Lara, Gustavo, Giovanna, Dante, Anna Laura, Julia,

Cristiano, Rita, João, Miriam, Suzana, Ana Carolina and Márcio, for their attention and friendship.

- Carlo Lanzoni and his wife Neide, for your attention, availability and care for me and my family on our arrival.

- God, for blessing my life and providing me with challenges so that I can increasingly become a better person.

- My family, father, mother, father-in-law, mother-in-law, sister, brother, sisters-in-law, brothers-in-law, nephews, and niece, for the support, visit, prayers, and for all the help they have offered me throughout my life.

- My son, for bringing me new meaning in my life and forcing me to be someone better to set the right example for you to follow. Despite the short time you are in our arms, I am already very proud of you and your achievements.

- Finally, my wife, for everything you've done for me. For helping me to make my star shine brighter and for making my dreams part of yours. Without you I never would have made it this far. All my love for you can only be expressed in the language of my heart:

"*Te amo muito, minha vida, minha amiga, minha esposa*".

TABLE OF CONTENTS

LIST OF TABLES

LIST OF FIGURES

LIST OF SYMBOLS, NOMENCLATURE OR ABBREVIATIONS

BDI - Beam Deviation Indicator (or Bearing Direction Indicator)

CSL - Canadian Survey Launch

DHN - Directorate of Hydrography and Navigation (subordinate to the Brazilian Navy)

DOA - Direction of arrival

HDBF - High Density Beam Forming

IHO - International Hydrographic Organization

KM - Kongsberg® Maritime

KMALL and KMWCD - KM file formats

MBES - Multibeam echo sounder(s)

MRA - Maximum Response Axis

MSR - Minimum Slant Range

NORMAM - Maritime Authority Norms (portuguese: Normas da Autoridade Maritíma)

OHS - Official Hydrographical Service

PDI - Phase Deviation Indicator

S-44 - Special Publication N° 44, IHO Standards for Hydrographic Surveys

SNR - Signal-to-noise ratio

TOA - Time of arrival

TVG - Time varying gain

TWTT - Two-way travel time

UNB - University of New Brunswick

WC - Water column

WMT - Weighted Mean Time

ABSTRACT

Because the safety of the navigation depends on accurate knowledge of the submerged features, any improvements in the ability to resolve those features are of major interest. Ultimately this reflects the bottom detection performance of the bathymetric measuring system (most commonly multibeam sonar) utilized. To this end, different algorithms for the detection of the seafloor or other targets have previously been developed, all presenting advantages and disadvantages. The two most common techniques are designed around time-series or angle-series analysis, although by far the most focus has been on time-series. The option of recording both amplitude and phase data of the water column permit the development and testing of new algorithms to be carried out in post-processing.

This research evaluates the use of water column data to perform bottom detection in a non-conventional way, that is, analyzing angle-series instead of time-series. The proposed algorithm is based on the Beam Deviation Indicator (BDI) method with the inclusion of phase information. It sequentially evaluates each time-slice (angle-series), applying absolute and relative threshold filters to select echo envelopes based on intensity data. Then, the phase data of each echo envelope is analyzed for zero-crossings (across beams), which are then converted into angles. Thus, time-angle pairs are obtained, defining depth measurements. Such a method, herein termed Phase Deviation Indicator (PDI), can be applied in an alternative and mainly complementary way to the currently existing methods.

Four different shallow waters seafloor relief types were investigated using an EM 2040P MkII multibeam echosounder, and collected datasets were evaluated with a focus on target or seafloor detection in many different geometries. The results obtained indicate that there are cases in which the analysis made only within a time-series, even using multi-detection features, can be

incomplete and could be complemented by the analysis made within a beam-series (PDI). Particularly notable geometries included mast-like-objects, discontinuous surfaces or features whose lateral extent is confined mostly within a short range of incidence angles, thereby requiring multiple detections within the same beam. Such results emphasize the idea that the best detection method results from the integrated use of all available techniques.

CHAPTER 1 – INTRODUCTION

1.1 – Problem Statement

For a navigator to be able to steer his vessel over safe waters, accurate and precise knowledge of the guaranteed clearance depth is necessary. To ensure that the measured depth accurately reflects all scales of relief, the minimum size of the features that were detected as well as the size of those that may have been missed must be known (IHO, 2008). As such, improvements in the ability to resolve those features are of major interest. Ultimately this reflects the bottom detection performance of the bathymetric measuring system (most commonly multibeam sonar) utilized. This thesis is focused on that aspect.

1.1.1 – Bottom detection requirements of Official Hydrographical Service and hydrographic surveys

In each country, the Official Hydrographical Service (OHS) is the organization responsible for the safety of navigation in the areas within its jurisdiction. The Directorate of Hydrography and Navigation (DHN), subordinate to the Brazilian Navy, responds as the OHS of Brazil (DHN, 2017). Among the products that the OHS needs to generate, one of the most important for navigators are nautical charts, both paper and electronic (IHO, 2005). Although a chart may be a reliable representation of the seafloor at the time it is produced, its usefulness is hindered over time because submerged features are subject to various forces that can alter the shape of the seabed. In addition, ships may sink or lose part of their cargo when involved in accidents, becoming part of the seabed. In this way, in order to keep the mapped information coherent and to guarantee the safety of navigation, it is mandatory to constantly update the nautical chart, demanding the

performance of periodic hydrographic surveys (IHO, 2005). Those surveys must thus utilize mapping tools that are capable of resolving features of designated interest.

Hydrographic surveys are, according to DHN (2017), a series of activities for acquisition of bathymetric, geomorphological, geophysical, tidal, topographic, oceanographic or geodetic data that can be carried out in maritime or fluvial areas, also encompassing environments like lakes, natural or artificial channels. As such each activity may have specific bathymetric resolution requirements that the bottom detection approach must meet. For example, all hydrographic surveys must meet specific accuracy and resolution requirements when dealing with safety of navigation (IHO, 2008).

Of specific relevance for this thesis is the resolution requirements of the International Hydrographic Organization (IHO) S-44 publication, which defines hydrographic surveys in four different orders, Special Order, Order 1a, Order 1b and Order 2, listed from the most rigorous to the most moderate criteria. The specific resolution characteristics of those orders (that have feature detection requirements) are:

- Special Order - 1m cube to an unspecified depth (but herein conservatively extended to 40m and thus 2.5% of depth).
- Order 1a - 2m cube up to 40m. Thus 5% of depth.

In addition to these “cubes” (realistically boulder-sized objects), the most commonly investigated feature is wrecks and other man-made structures (e.g., oil field infrastructure). The most concerning feature of these man-made structures is narrow protuberances, such as masts, davits and other pole-like features. These do not fit the simple aspect ratio description of cubes or boulders. Rather they appear discontinuous, far above the natural sediment-water interface and thus pose a particular challenge for conventional multibeam bottom detection. Previous works

have identified the problem of tracking masts (Hughes Clarke, 2006, Hughes Clarke et al, 2006a, Hughes Clarke et al 2006b, Van Der Werf, 2010) and boulders (Pereira and Hughes Clarke, 2015).

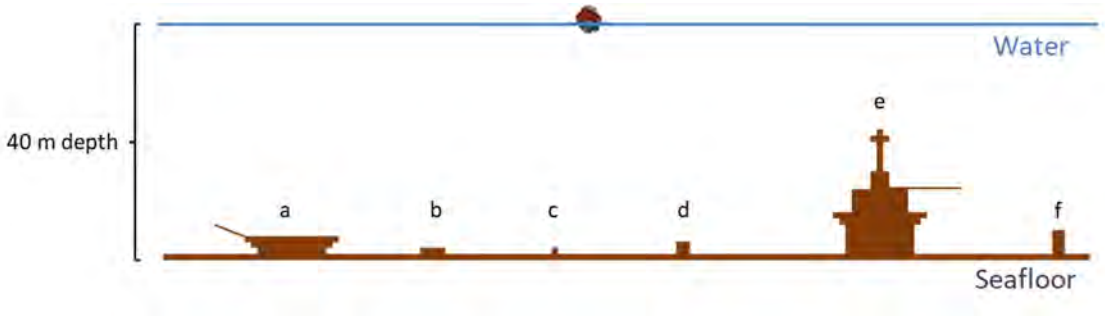

Figure 1 - Features of different characteristics. a - wreckage with an oblique mast. b - object with an aspect ratio smaller than 1. c - 1-meter cubic boulder. d - 2-meter cubic boulder. e - shipwreck, with a mast (vertical) and a loading spar (horizontal). f - object with an aspect ratio greater than 1.

In Figure 1, six different objects are represented in a flat seafloor, whose local depth is 40 meters. The object "a" represents the wreckage of a vessel whose forward mast was damaged and tipped over, stabilizing obliquely to the bottom. Although it is easy to detect the main bulk of the ship due to its dimensions, its pole, being suspended above the seabed, is much more difficult to detect and can easily be confused with spikes. Object "b" has an aspect ratio smaller than 1, which means wider than high. The objects "c" and "d" represent, respectively, 1-meter cubic and 2-meter cubic boulders. The "e" object represents a shipwreck, with a mast in a vertical position and a loading spar in a horizontal position. Finally, the object "f" has an aspect ratio greater than 1, which means higher than wide. An ideal bottom detection should be able to differentiate these situations and detect seabed attached objects showing different aspect ratios or detect objects suspended above the seabed, whether they are in a vertical, horizontal, or oblique position.

1.1.2 - Multibeam Echosounder detection

To carry out a hydrographic survey, focusing on the need to determine depths and detect submerged objects, several equipment exist, among which are bathymetric echosounders. The

main task of a bathymetric echosounder is to determine the depth, through the conversion of two-way-travel-time in distance, knowing the speed of sound in the water column. However, when analyzing the received signal, determining the exact moment when the transmitted pulse touched the bottom or a target can be challenging.

In the case of multibeam echosounders (MBES), in which hundreds of beams are received simultaneously in a single swath, in addition to determining the aforementioned time, it also is necessary to determine the angle at which the signal was received. Each time-angle pair defines a depth measurement (Lurton, 2010). In order to obtain a time-angle pair, several techniques can be applied. Among this variety of techniques, some of them are better for tracking a continuous surface and some are better for discontinuous surfaces.

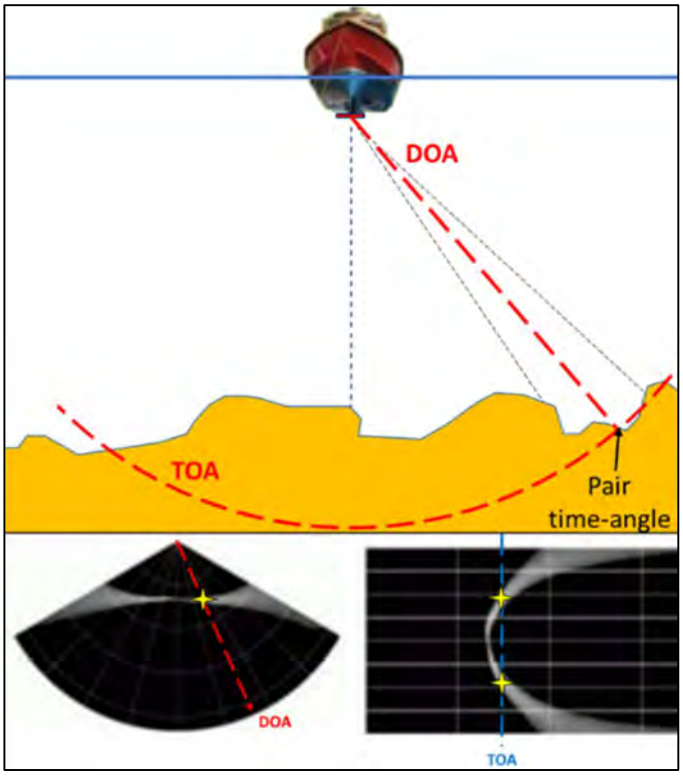

Figure 2 – Time-angle pair. Top: illustrates how a time-angle pair represents depth information. Bottom: Left: Direction-based method, given a DOA, one time is sought. Right: Time-based method, given a TOA, one (or more) direction(s) is sought.

Using the amplitude and phase difference information collected for each beam, different detection methods and algorithms have previously been developed (Morgera, 1976, Farr, 1980, Morgera and Sankar, 1984, Satriano et al, 1991, Hammerstad et al, 1991, de Moustier, 1993), each one presenting certain advantages and disadvantages. The two most common, illustrated in Figure 2, are:

- For a given direction of arrival (DOA), the instant (time of arrival) in which the detection occurred is sought. In the present research, this method will henceforth be referred to as the "Direction-based method"; or
- For a given time of arrival (TOA), the direction (direction of arrival) in which the detection occurred is sought. In the present research, this method will henceforth be referred to as the "Time-based method".

Direction-based methods can be divided into detection by amplitude and detection by phase and are widely used nowadays. On the other hand, time-based methods (Satriano et al, 1991, de Moustier, 1993, SeaBeam, 2000, Pereira and Hughes Clarke, 2015) have been used a minority of times and appear to have been abandoned (Lurton, 2010).

In spite of the proven quality obtained by direction-based methods, it is to be expected that some limitations exist. The ability to discriminate targets from an MBES varies according to the angle of elevation and the type of object. Continuous surfaces, such as the seabed, favor detection by direction-based methods. However, objects limited to one cubic meter or man-made objects are not always detected by this method. Van der Werf (2010) showed how these algorithms could be improved for a particular case of mast tracking capability. In some cases, short wavelength targets sitting on a continuous surface are not detected and the shadow in the backscatter image, combined

with the data gap within the bathymetric surface, may be the only indication of its presence (Hughes Clarke et al., 2013, Pereira and Hughes Clarke, 2015).

A few years ago, a study showed that the Beam Deviation Indicator (BDI) algorithm can improve low-grazing-angle target detection/definition (Pereira and Hughes Clarke, 2015). Such results call into question the reason why BDI is in disuse and emphasize the importance of the combined use of direction-based and time-based methods. In addition, it should be noted that the studies that applied the time-based method had their main focus on the amplitude data for determining the maximal amplitude direction. Since the phase detection (determination of the instant when the null phase difference occurs) is widely used in direction-based methods, the question arises of what would be its impact on time-based methods.

In this context, some models of multibeam echosounders, while they already use the phase in real-time, have added the option of recording phase information. Further, this phase information is not just retained for the duration of the real-time chosen bottom detection window, rather it is available for the full ping duration along with the water column data. This situation combined with the scarcity of studies of time-based method extended with the use of phase data became an opportunity to explore new capabilities and to seek a complementary detection method.

Based on the idea that the best detection method results from the integrated use of all available techniques (de Moustier, 2009; Hughes Clarke et al, 2013, Hughes Clarke, 2018), this thesis intends to build upon preexisting works taking the advantage of the water column phase data.

1.2 – Research Questions

Focused on the problem previously described, the following questions summarize the present study:

a) Is the phase difference information logged in the water column data able to perform seafloor or target detection using time-based methods (analogous to, and in concert with, BDI approach)?
b) How do the results obtained by this method behave when compared to the solutions obtained by conventional along-beam methods?

1.3 – Research Objectives

To answer the research questions, three objectives were defined in this study:

a) Develop a seafloor/target detection algorithm built on time-based method, including phase difference information from the water column.
b) Test the elaborated algorithm in different areas, including regions with targets of known characteristics, to evaluate its detection capacity.
c) Compare the results achieved by the present algorithm with the results obtained by using the conventional detection methods.

1.4 – Thesis Structure

This thesis is structured in five chapters. The current chapter (chapter 1) presents the problem statement and discusses the research questions and research objectives. Chapter 2 contains the background of the concepts considered essential for the development of this research and includes a discussion of previous works. Chapter 3 presents the methodology used for the

development of the algorithm, the approximations and assumptions, and also describes the steps involved in the filters used. Chapter 4 contains information about the areas where hydrographic surveys were carried out, the specifications and characteristics of the echosounder and its selected configuration. It also presents the tests performed and the results found (which are further elaborated in the appendix). The conclusions, discussions and suggestions for future work are present in chapter 5.

CHAPTER 2 - BACKGROUND

Both the process for determining the depth and for detecting features are based on the displacement of an acoustic wave transmitted by the transducer through the water column and the return of this signal after interaction with the seabed or a target (IHO,2005). For the case of a multibeam, in general, a pulse with a wide across-track beamwidth and a small along-track beamwidth is transmitted. Then, several receiving beams with small across-track beamwidth are electronically generated in defined directions (Tucker, 1961, Glenn, 1970). Through electronic signal processing techniques, amplitude data and phase difference data are recorded in a defined sample-rate, forming a "time-series" for each receiving beam (Figure 3). The set of data received in all the receiving beams forms a "ping".

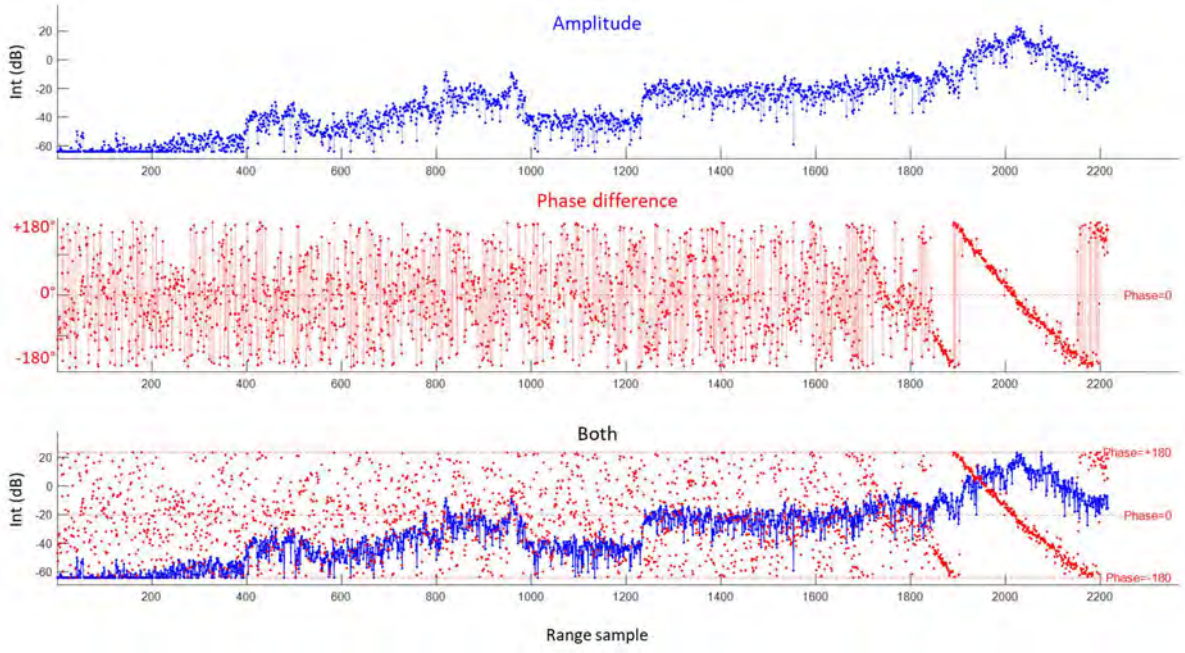

Figure 3 - Time-series. Top: Amplitude data. Center: Phase difference data. Bottom: Both data combined. Note that in the region next to the range sample number 2000 the highest amplitude values are found. In this same region, phase difference data, which previously appeared to behave in a random manner, forms a well-defined phase ramp.

Note that the dB values used throughout this study are offset by a fixed amount of 30 dB recorded in datagrams. Thus, for Figure 3, the scale should really be -90 and -10 dB. More details on the intensity levels and their corrections can be found in section 2.6.

2.1 – The visualization of a "ping"

Once having data from all time-series, they can be combined into a single matrix, representative of everything that was captured during a transmission and reception cycle. There are several ways to visualize a ping and the main forms presented in this research are:

- Matrix form: numerical values are inserted in matrix form, maintaining the consistency of the information of each beam and each time sample (Figure 4-a).

- Time-series set: Each column of the matrix form is presented in two dimensions in this view. It facilitates the visual identification of peaks when compared to matrix form (Figure 4-b. In this example, for easy viewing, there is a jump of about 30 beams between images).

- Time-Angle diagram: Displays the previous data by replacing the amplitude dimension with a color code. This visualization allows a great understanding of the submerged structures. However, by disregarding the angles involved, it presents distortions of shapes (Figure 4-c).

- Pie diagram: Corrects previous distortions by adjusting the image with the angles associated with each receiving beam. This visualization is the one that best allows the identification of the bottom and submerged features (Figure 4-d).

- 3D pie diagram: Similar in value to the previous one, this visualization facilitates the distinction of signals received by secondary lobes and allows the insertion of a light effect (sun-illumination), to highlight different parts of ping, according to the study to be carried out (Figure 4-e).

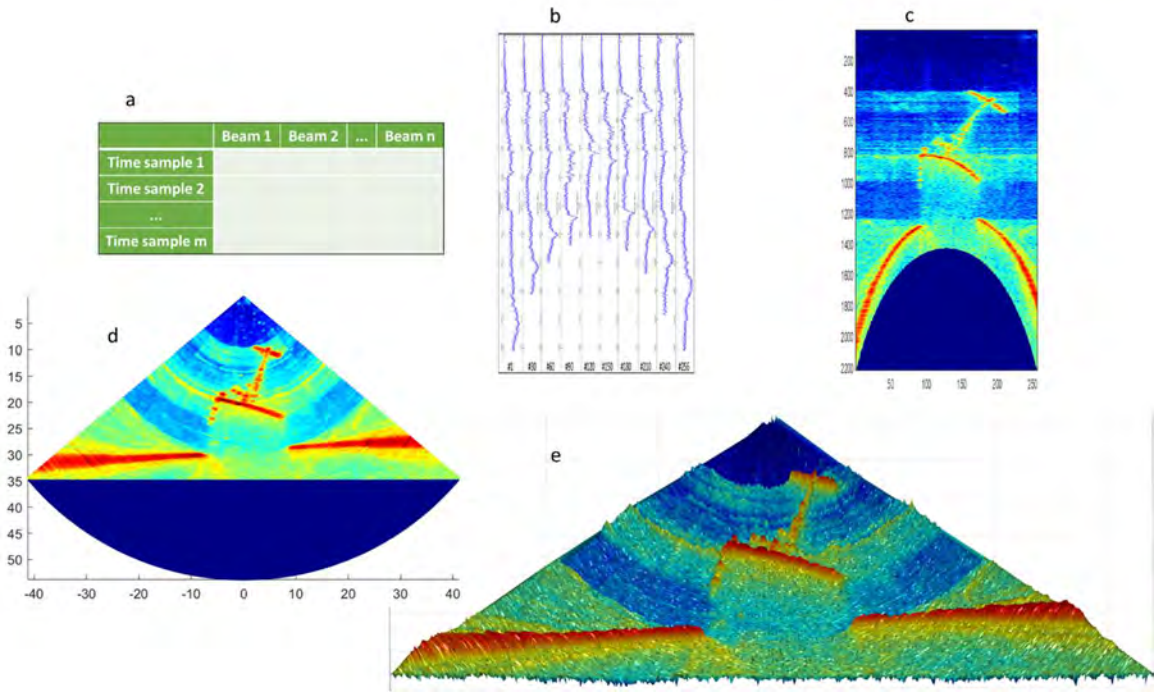

Figure 4 – Different ways to view the amplitude component of a ping. a) Matrix form. b) Time-series set. c) Time-Angle diagram. d) Pie diagram. e) 3D pie diagram.

When observing the time-series of a given beam (direction-slice), it will be represented by a straight line along the time-sample axis in the time-angle diagram. In a pie diagram, it will also be represented by a straight line, but with an inclination corresponding to the angle of incidence associated with the selected beam (Figure 5).

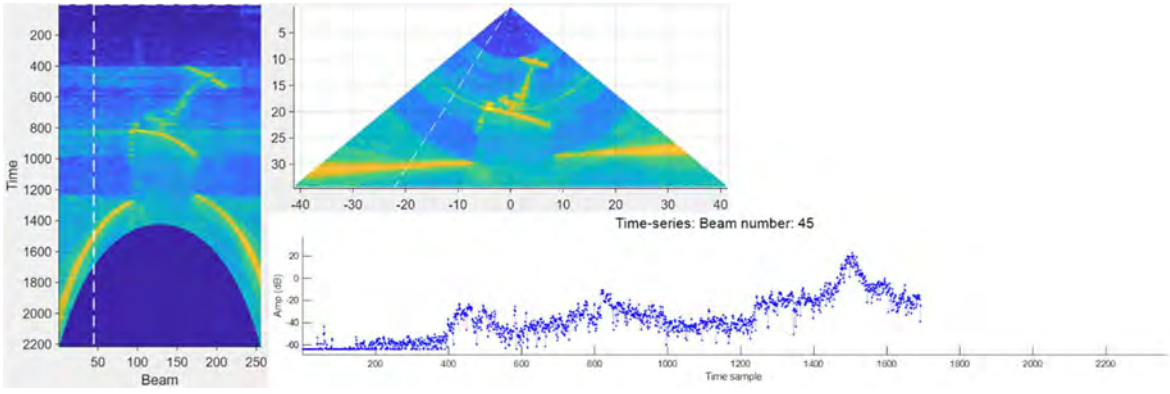

Figure 5 – Representation of an angle-slice (bottom) in time-angle diagram (left) and in pie diagram (top). The beam number 45 corresponds to an angle of about 33 degrees with the vertical.

On the other hand, a time-slice (angle-series) is represented by a straight line across the time-sample axis in the time-angle diagram. In a pie diagram, it is represented by a curved line, whose radius is proportional to the selected time-sample (Figure 6).

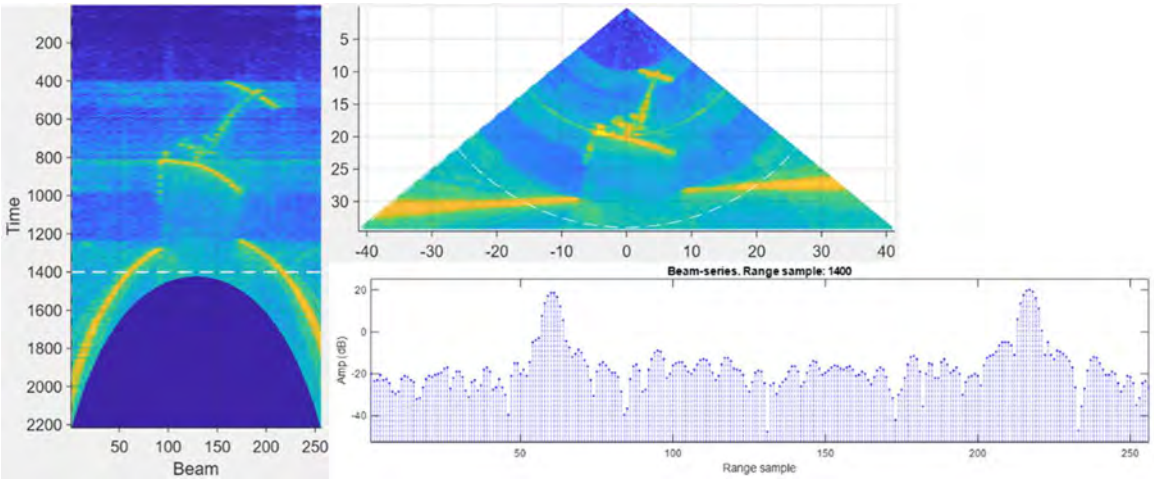

Figure 6 – Representation of a time-slice (bottom) in time-angle diagram (left) and in pie diagram (top).

2.2 – Beam footprint

As will be presented in the next sections, the choice between amplitude or phase detection is related to the beam geometry and its footprint, implying advantages or disadvantages in the use of each one. Thus, its main characteristics need to be reviewed.

Initially, a wide across-track and short along-track pulse is transmitted (Figure 7-a). Several reception beams are generated, this time being short in across-track dimension (Figure 7-b). The result of the transmission and reception beam patterns product, when intercepting a typical low relief surface such as the seabed, is referred to as its beam footprint (Figure 7-c). Given the characteristics of this described geometry, the dimensions of the footprints of the different beams are not the same (Figure 7-d) and vary with the angle of incidence.

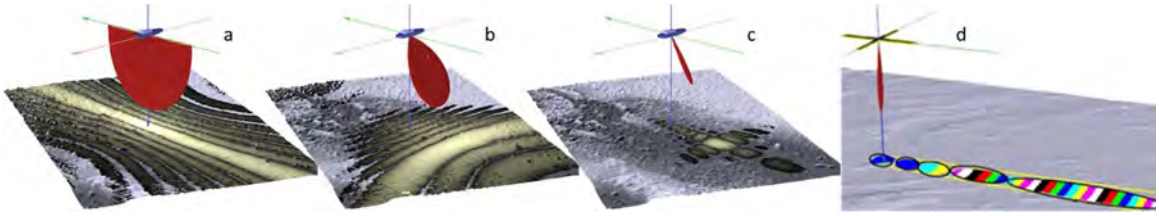

Figure 7 – Beam footprint geometry. a: transmission beam. b: reception beam. c: beam pattern product and its footprint. d: footprints variations.

The dimension of the instantaneously ensonified area also varies with the angle of incidence, due to the variation of the radial dimension of the projected pulse length. Under angles of incidence close to normal, the radial dimension of the projected pulse length is greater than the across track projected beam footprint. In this case we say that the ensonified area is beam-width limited. On the other hand, in oblique incidences, the projected pulse length is smaller than the across track beam footprint, and, consequently, the ensonified area is pulse-length limited (Figure 8). Note that the pulse-length and beam-width limited conditions depend on the local grazing angle, not just the beam angle.

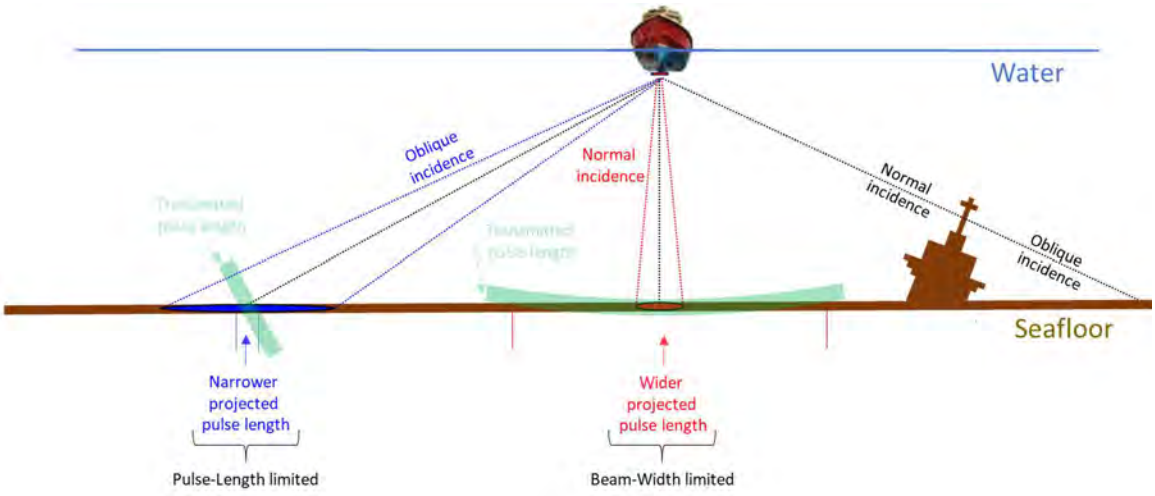

Figure 8 - Instantaneously ensonified area and angle of incidence (adapted from Pereira, 2015).

Due to this difference in types of ensonification, the beams whose incidence angle are close to normal have few time-samples and short echo envelope lengths, making it easier to estimate the

center of the echo (Figure 9, top). In turn, the oblique incidence angle beams are composed by several time-samples, with a long echo envelope length. Estimating the center of the echo requires a more elaborate process (Figure 9, bottom).

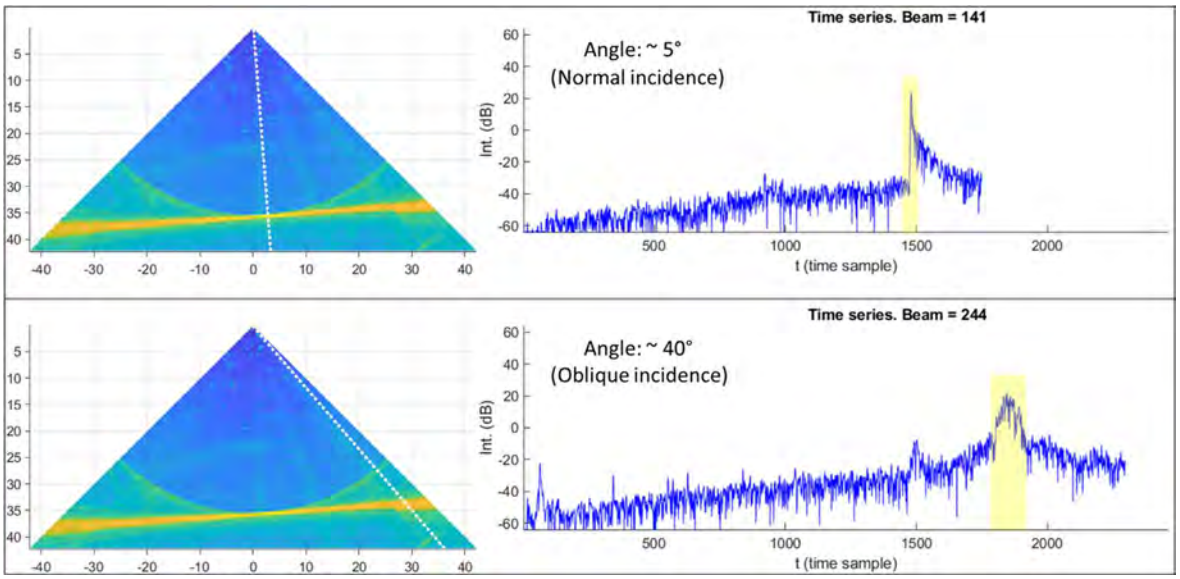

Figure 9 - Echo envelope length at normal (top) and oblique (bottom) incidence cases.

2.3 – Bottom detection algorithms

As mentioned in the introduction (chapter 1), to measure the depth of each receiving beam, it is necessary to find time-angle pairs. These pairs are obtained using bottom detection algorithms. Regardless of the choice of a method, each of them has strengths and limitations and the combined use of more than one method makes the detection process more robust.

2.3.1 – Direction-based techniques

Direction-based methods consist of for a given angular direction (Figure 10), finding a maximal amplitude instant, henceforth Amplitude Detection, or finding a null phase-difference instant, henceforth Phase Detection.

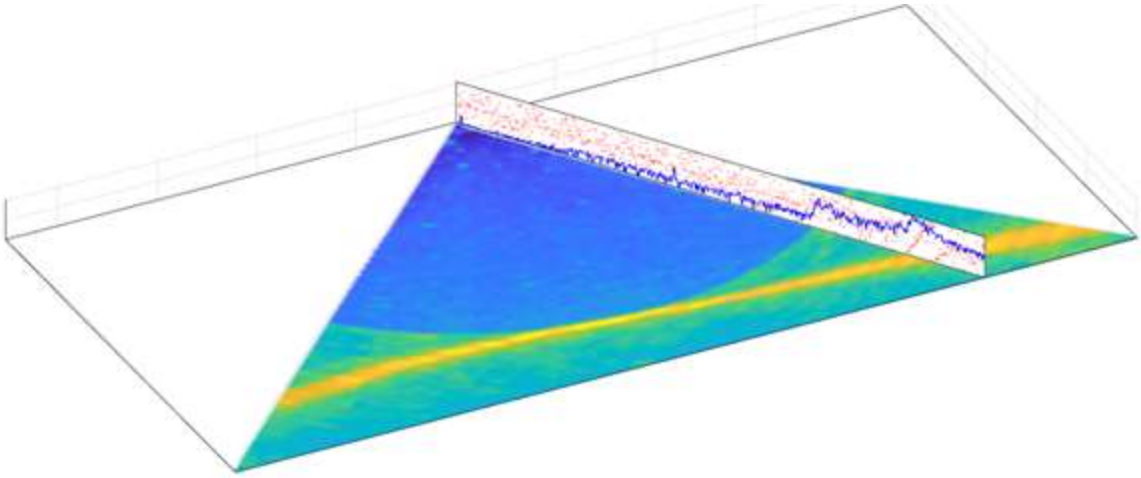

Figure 10 – Fixed angular direction and its time-series (angle-slice).

2.3.1.1 – Amplitude detection

The detection by amplitude consists of the analysis of the amplitude data of a time-series, whose angle has already been defined, considering that the highest values correspond to the instant of detection of the bottom or of a target.

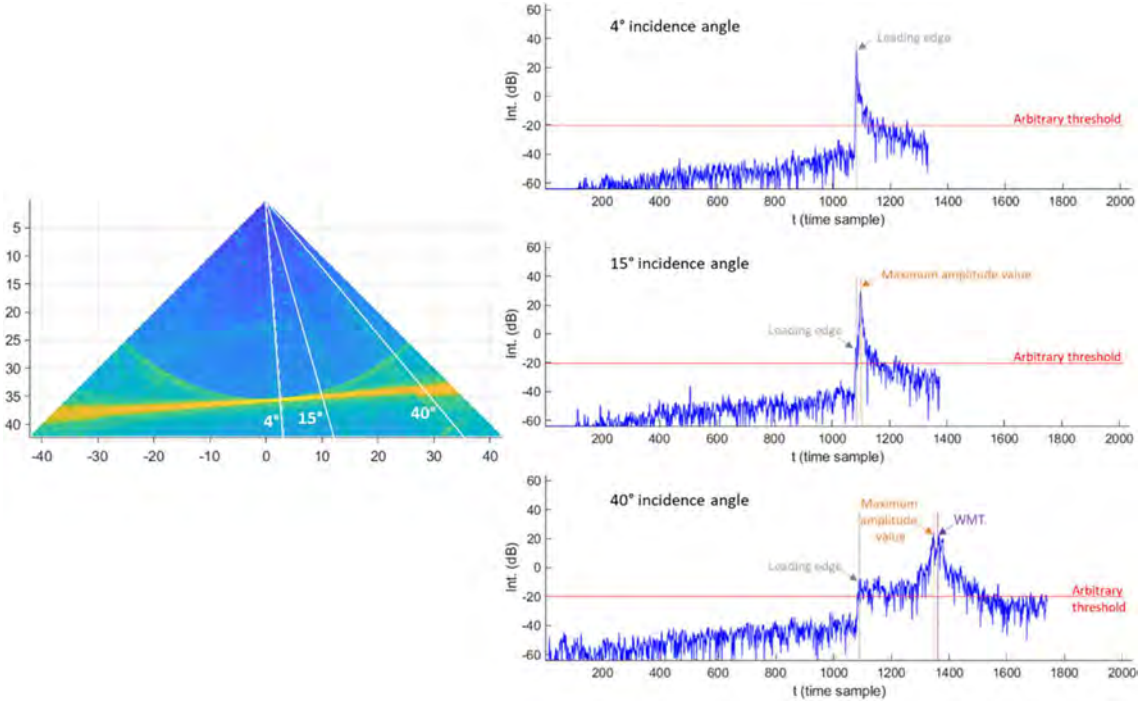

Figure 11 – Amplitude detection techniques. Top: Leading edge. Middle: Maximum amplitude value. Bottom: Weighted Mean Time (WMT).

Usually, the process starts with the choice of a section of the time-series that contains the highest values, defining an envelope to be analyzed and a threshold level. Then, different techniques can be used to define the instant of detection within the created envelope. The main techniques are:

- Leading edge: It adopts as a solution the instant when the value defined as threshold is exceeded for the first time (Figure 11, top).

- Maximum amplitude value: It considers the maximum value of the signal (peak value) to be the detection instant (Figure 11, middle).

- Weighted Mean Time (WMT): It uses the concept of center of mass to define the instant of detection (Figure 11, bottom).

Comparing the three previously mentioned, the leading edge is usually used for incidence angles close to zero degrees, since the received signal has an accentuated shape. For having as a solution the first result in which the threshold is exceeded, it tends to register the smallest depths within the receiving beam, presenting a conservative characteristic and increasing the safety of navigation. However, as the analyzed beam moves away from the normal incidence, the leading edge loses meaning. Although it continues to indicate the first moment when the transmitted beam interacts with the seafloor, it is necessary to identify the moment when the receiving beam maximum response axis (MRA) intersects the seafloor. Then, an alternative is to use the maximum amplitude value and register the instant when the peak occurs. As long as there is clearly a peak that stands out before the other data from the time-series this technique can be used. Even for short echo envelopes, however, given the random noise, an instantaneous peak may not reflect the center of the envelope. Thus, slight time averaging is usually used to smooth out the noise.

A further complication that starts to occurs, as the echo envelope lengthens with the increase in the angle of incidence, is that the interaction of the transmitted beam with the seafloor starts with sidelobes and there is a gradual transition up into the main lobe which is diluted over time. As a result, several peaks within the elongate mainlobe, which have similar characteristics are recorded, potentially leaving the maximum value meaningless. This situation leads to the last case, in which a weighted mean time is used to define the instant of detection. Its calculation involves weighted average using amplitude and times, according to the expression: $t_{WMT} = \frac{\sum_i^n t_i.a_i^2}{\sum_i^n a_i^2}$, where t_{WMT} is the detection instant, n is the number of samples within the selected envelope, t_i and a_i are time-sample and its amplitude value, respectively. The result obtained by this method is more accurate than that obtained by the maximum value, since it integrates more solutions and is less subject to both the speckle and seabed patchiness noise present in the received signal.

Some problems are linked to the use of WMT. The backscatter for the same type of seabed varies with the angle of incidence, presenting higher values with normal incidence and decreasing values as the grazing angle decreases. This means that within the same beam, the inboard part may have higher values than the outboard part, causing a bias towards the nadir. Another factor is linked to the fact that a single footprint can represent a portion of the seafloor composed of more than one type of material. Since the value of the backscatter depends on the material, the WMT would cause a bias towards the material with the highest target strength. Thus, in a heterogeneous seabed, assuming the main rather than sidelobe peak is chosen, this variation in backscatter strength across the seafloor as the pulse propagates through the beam footprint complicates finding the center of the echo envelope. These angular and spatial variations ("patchiness problem") promote a bias

towards the highest seafloor backscatter strength, indicating that the detection instants are not necessarily related to the direction of the receiving beam point angle, as shown in Figure 12.

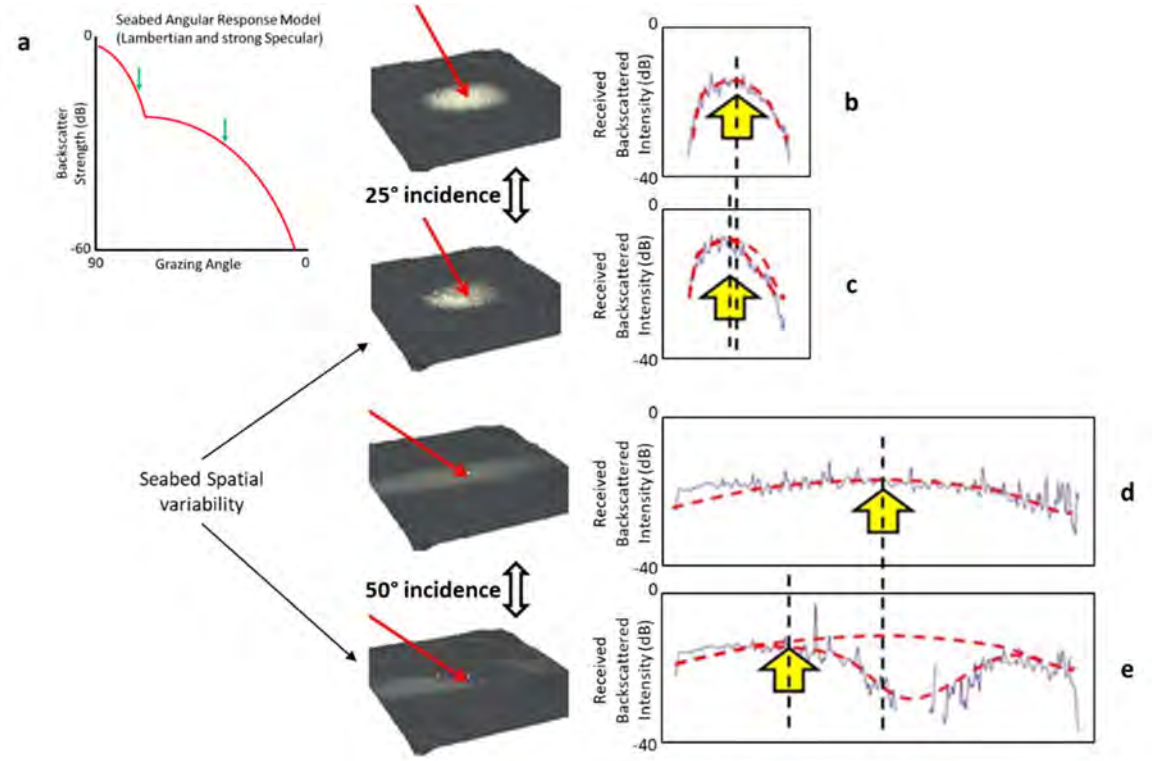

Figure 12 - Angular and spatial variations of backscatter strength. a: Angular backscatter strength response curve. The green arrows indicate the angles of incidence represented in cases b to e. b: beam close to nadir and a flat seabed. c: beam close to nadir and a seabed with a steep-sloped. d: oblique beam, without spatial variability. e: oblique beam, with patchiness. (Adapted from Hughes Clarke, 2018).

The net result of the issues previously addressed is that the amplitude detection performs best when used in normal incidence (flat seabed close to the nadir or in the presence of a slope). In this region, due to the angle of incidence, the highest backscatter values are expected to be received with a small number of samples, facilitating the use of the techniques listed and avoiding their weaknesses. On the other hand, as the angle of incidence increases, the number of samples increases, diluting the amplitude values of the signal received over time, increasing the uncertainty of the amplitude detection (OHI, 2005) and potentially adding a bias (often a shoal bias) at that. In

these cases, it is convenient to use other detection methods that have better performance in oblique beams.

2.3.1.2 – Phase detection

Phase detection, which, like the previous one, is also based on the principle that the MRA has already been defined, seeks to find the instant of detection by analyzing the moment when the phase difference crosses the null value. To understand the physical meaning of the phase difference null value, it is necessary to clarify how these values are calculated.

2.3.1.2.1 – Phase difference measurement

Consider a discrete linear receive array of length L, composed of n elements equally spaced at a distance d, where, $L = (n-1).d$. Electronically, this array can be divided into two sub-apertures (here called *split port* and *split starboard*) and each of these parts has an acoustic center. Consider the distance between these acoustic centers to be s (Figure 13, left). Each of these sub-apertures can generate a receiving beam steered (by time delay) to the same point on the seafloor, with an overlapping between their footprints (Figure 13, center). The receiving signal, by going through different paths until reaching each sub-aperture, would be received at different instance times, resulting in different phase values in each sub-aperture. With this information, it is possible to calculate the phase difference, given by $\Delta\varphi = Phase_{port} - Phase_{starboard} = \varphi_{port} - \varphi_{starboard}$ (Figure 13, right).

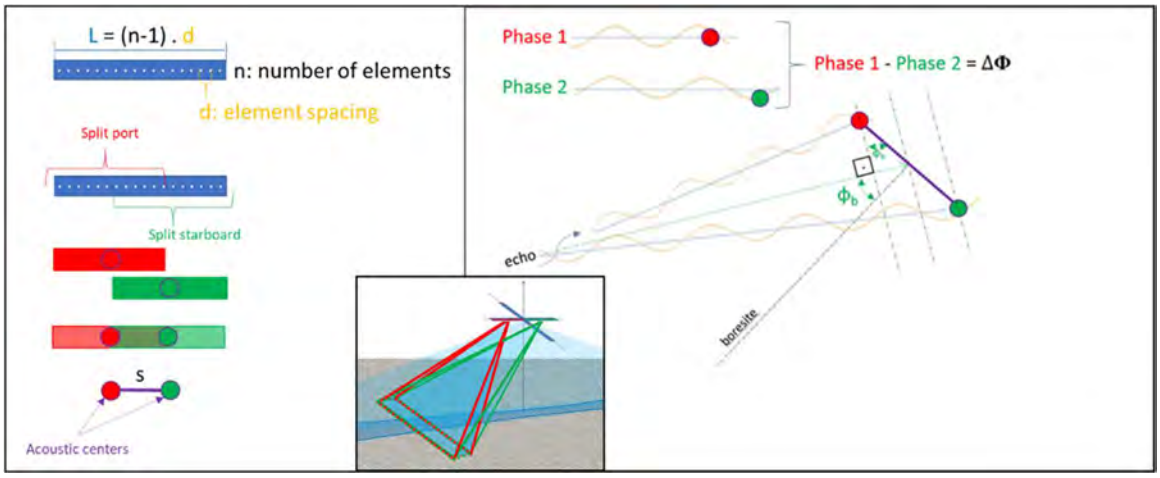

Figure 13 – Phase measurements. Left: Sub-apertures formation. Center: Footprint overlapping. Right: Phase difference measurement.

The decision on how to divide the array into two parts (defining s) is up to the manufacturer, who will find a balance between sub-apertures size and acoustic centers distance to avoid wraps causing ambiguity.

2.3.1.2.2 – Phase ramp and "Zero-cross"

Once the way of obtaining the phase difference values is defined, it is necessary to understand the physical meaning associated with it. When generating a receiving beam, a MRA associated with this beam is created. Every signal registered in this beam is, in the first analysis, considered to come from this direction. However, return signals from other directions can be received at any time. Such signals will travel to the acoustic centers of each sub-aperture through paths of different length, depending on the distance they are at, and will reach each part at different times, promoting the recording of different differential-phase values in each one of them.

Three situations can occur: the return signal may be received from a location closer to the split starboard (first case) or split port (second case), or the signal may be equidistant to both (third case). In the first case, since the phase difference was defined as $\Delta\varphi = \varphi_{port} - \varphi_{starboard}$, signals

coming from locations closer to the split starboard will first have a $\varphi_{starboard}$ phase value. Then, these same signals will have phase value in the split port given by $\varphi_{port} = \varphi_{starboard} + \delta\varphi$, where $\delta\varphi > 0$ and represents an increase in the phase value due to the distances associated with each sub-aperture. Rearranging the equations, $\Delta\varphi = (\varphi_{starboard} + \delta\varphi) - \varphi_{starboard} = \delta\varphi > 0$, which means that the recorded phase difference value will be a positive value (Figure 14, left).

Similarly, in the second case, signals coming from locations closer to the split port will first have a φ_{port} phase value. Then, these same signals will have phase value in the split starboard given by $\varphi_{starboard} = \varphi_{port} + \delta\varphi$ (where again $\delta\varphi > 0$). Thus, $\Delta\varphi = \varphi_{port} - (\varphi_{port} + \delta\varphi) = -\delta\varphi$, which means that the recorded phase difference value will be a negative value (Figure 14, center).

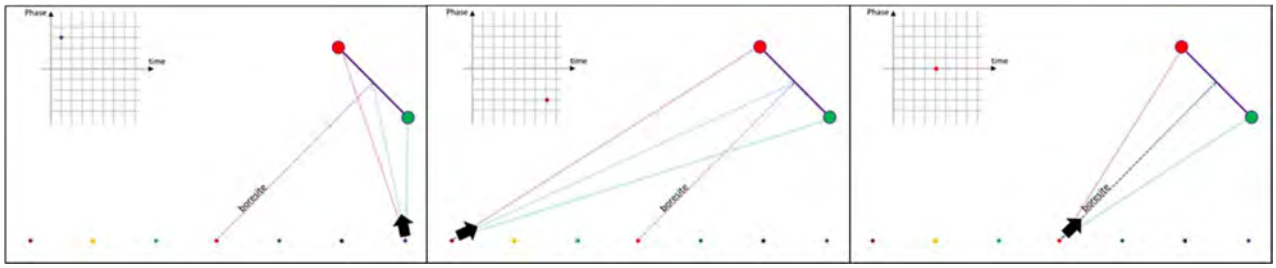

Figure 14 – Split beam concept, with positive (left), negative (center) and null (right) phase difference value.

Finally, in the third case, the signal comes from a location equidistant to both sub-apertures (Figure 14, right). In this case, the signal is received simultaneously on both parts, registering the same phase value on each part ($\varphi_{port} = \varphi_{starboard}$). This implies $\Delta\varphi = \varphi_{port} - \varphi_{starboard} = 0$, that is, the phase difference is null. Note that this case only occurs when the signal is being received by the direction of the MRA. Another important observation is that this is only true when the sub-apertures have been beamformed using a time-delay beamformer.

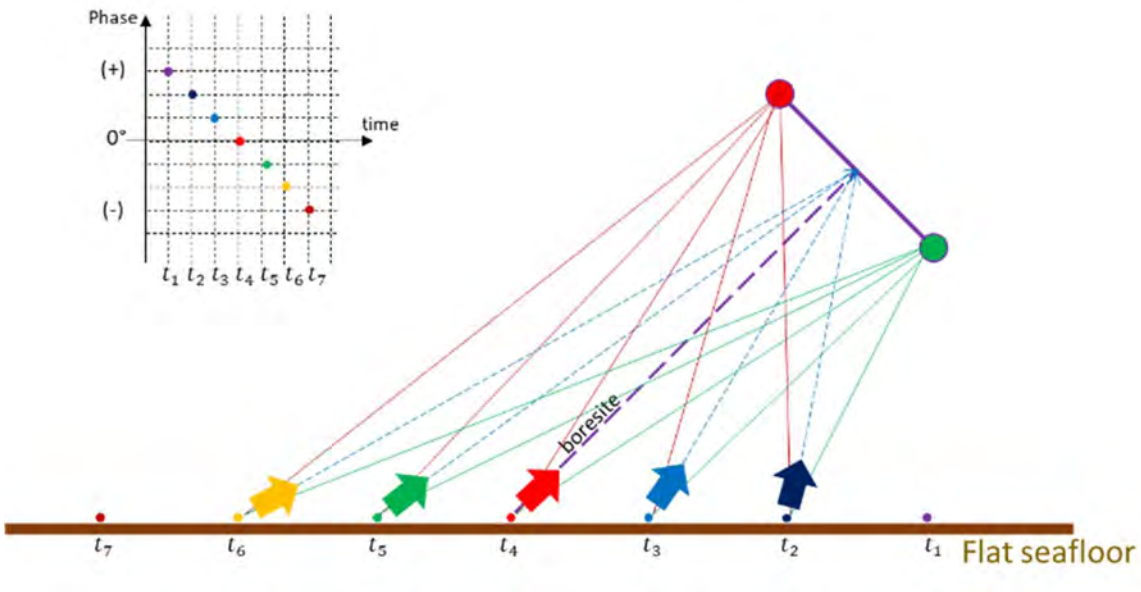

Figure 15 – Phase ramp. When the phase values form a phase ramp, the zero-crossing instant indicates the moment when the return signal is being received by the MRA of the receiving beam.

Therefore, the phase difference values can provide estimates about the direction from which the signal is being received, be it in MRA (zero phase difference) or under other angles (positive or negative phase difference). As the transmitted sound pulse propagates, moving away from the transducer, these three cases start to occur sequentially, with the phase difference values varying from negative to positive (or vice versa). The recording of phase values over time then takes the form of a ramp (phase ramp) and the instant when the phase is null indicates the moment when the signal was received from the axis of maximum response. In other words, the zero-crossing instant indicates the moment when the return signal is being received by the direction of the MRA of the receiving beam (Figure 15).

It should be noted, however, that up to this moment, the three cases presented consider the existence of a bottom or target as the origin of the return signals. In their absence, the returns occur by random processes (noise) along the water column and the phase difference values, whether

positive, null or negative, no longer occur in the form of a ramp. On these occasions, the phase difference information is ignored (Figure 16).

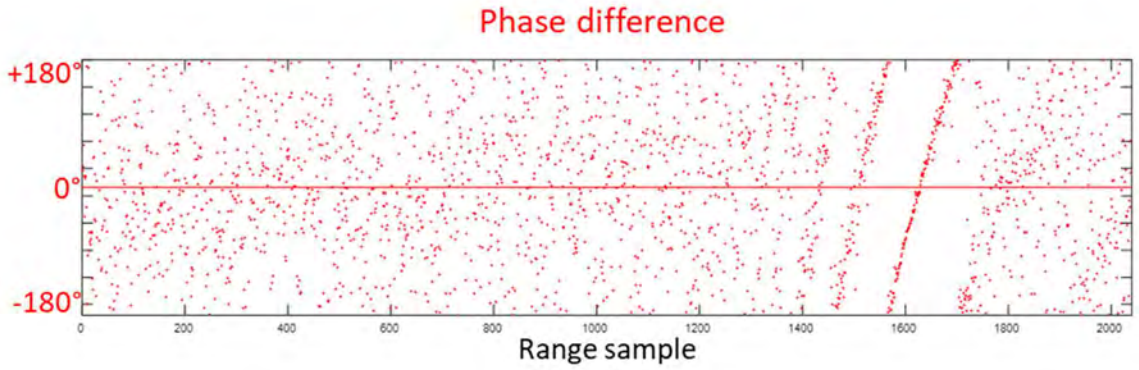

Figure 16 – Real phase data corresponding to a flat seafloor. Observe the random behavior of the phase difference data outside the range between range sample 1400 and 1800. In the vicinity of the range sample 1600, the generated phase ramp can be clearly observed and the instant corresponding to zero-crossing can be obtained.

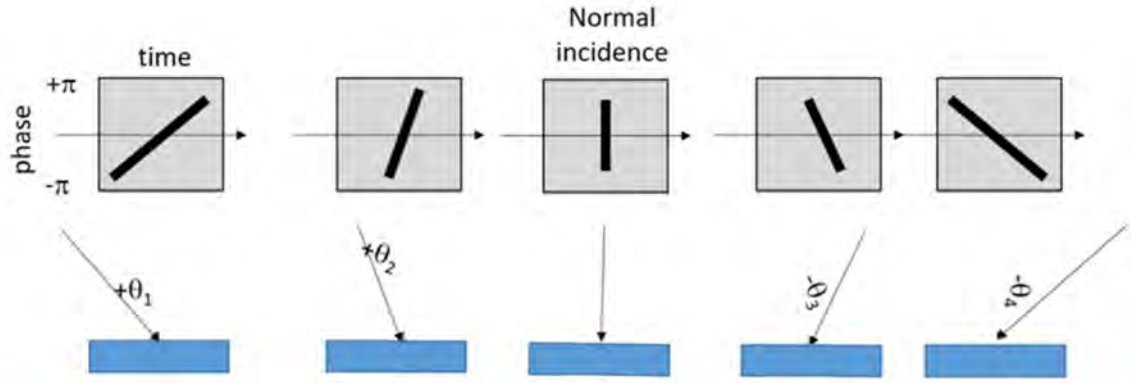

Figure 17 - Beam vector relative to seabed surface and its corresponding sign and slope of phase time-series.

As a logical continuation, the trend of the phase-ramp (positive or negative) indicates the orientation of the surface within the main lobe relative to the beam. And the slope of the trend can be used to obtain the slope of that surface relative to the beam axis (Figure 17). This relationship between the phase-ramp and the surface will be discussed in the high-density beam forming section.

2.3.1.2.3 – Phase detection process

As seen previously in the amplitude detection process, using the maximum amplitude data, a threshold and an envelope are defined before determining the detection instant. In the case of phase difference data, again looking at Figure 16, it can be seen that the data cross the null value several times throughout the time-series (as if the phase difference is more than π it wraps). Using only these data, it is not possible to define an envelope to be able to evaluate within it the instant of detection to be considered. Thus, this method uses the envelope defined in the amplitude detection process. As a result, the phase detection process is always preceded by an amplitude detection.

Once the envelope has been defined, one only need to look for the instant when zero phase crossing occurs as the sub-aperture spacing is designed so that only a single wrap occurs within the width of the main lobe. In the absence of noise, an instantaneous $\Delta\varphi$ value might be used to indicate the local MRA relative angle. In reality, however, since there is noise present in all data, determining zero phase crossing sometimes can be difficult. In practice, a linear or quadratic regression is performed on the phase ramp (Pohner and Lunde, 1990) to estimate the instant of the intersection (Figure 18). Another important step is to check the residuals from the linear (or quadratic) regression. Phase detection should only be used when residuals are low, indicating that the phase sweep is coherent as expected from a seafloor within the beam footprint that has a low grazing angle. The regression residuals reflect the angular uncertainty in the MRA arrival time and thus can be used as a measure of uncertainty for example in the quality factor defined by Lurton and Augustin (2010).

Note that the number of phase samples used in this regression is a choice of the algorithm and is dictated by the length of the echo envelope which reflects the beam width and incidence angle. For near normal incidence, the phase slope is steep and thus there may not be enough samples to do the regression.

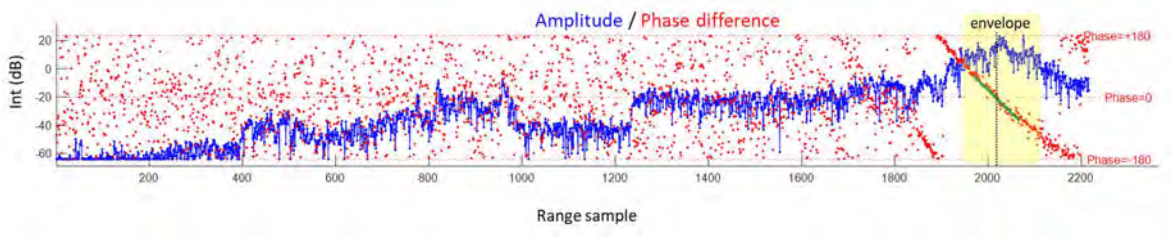

Figure 18 - Phase detection. In this figure, the amplitude (blue) and phase (red) values are displayed overlapping. The envelope (yellow) defined by the amplitude detection process is used. A linear regression (green) is performed to estimate the instant of the intersection (black dotted line).

Note the phase trend in Figure 18 is not exactly linear. In this circumstance, either only a short subset of the phase sweep is regressed linearly, or a non-linear regression is used. And if the seafloor is not planar within the beam footprint, changes on the across track seafloor slope will introduce corresponding changes in the slope of the phase curve.

2.3.1.2.4 – Normal and oblique incidence cases

As discussed previously, the differential phase value reflects only the elevation angle of the seafloor relative to the MRA, and should be independent of the local seabed backscatter strength, being free from spatial variations in the backscatter characteristics of the seafloor. Thus, the patchiness problem described for low grazing angle amplitude detects should not apply (Hughes Clarke, 1998).

Comparing the two forms of detection presented so far, by the characteristics discussed in the previous sections, it was possible to conclude that under normal incidence, the amplitude

detection offers advantages. On the other hand, under oblique incidence, phase detection becomes the preferred choice.

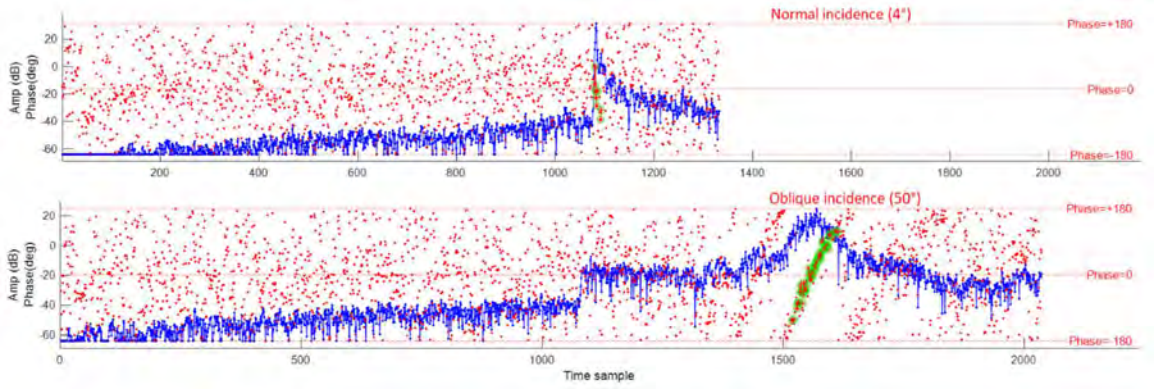

Figure 19 - Normal and oblique incidence time-series. Top: normal incidence, preferred amplitude detection. Bottom: oblique incidence, preferred phase detection.

Figure 19 exemplifies this comparison. In the top image (4° incidence), the amplitude characteristics highlight a peak with short echo envelope, favoring amplitude detection. In it, the phase data varies quickly in a short range of time, making it difficult to analyze a phase-ramp. In the bottom image (50° incidence), the situation is reversed. The highest amplitude data have a long echo envelope and are more subject to angular and spatial variations of the backscatter. The phase data, in the region highlighted in green, forms a phase-ramp, and a curve-fitting allows the determination of the zero-crossing instant, favoring phase detection.

There is a practical limit to this however, in that if the seabed backscatter strength is locally low within the beam footprint, the influence of the noise (due to low SNR) is higher leading to noisier phase (Burdic, 1984) and thus less confidence in the angle. Thus, local shadows within an echo envelope can corrupt any regressions done on the whole echo envelope time series. This is particularly problematic for the case of shadow-casting seabed targets within a single beam footprint.

2.3.1.3 – High Density Beam Forming (HDBF)

The two methods previously presented address solely a single fixed direction to estimate the instant when the MRA touches the seafloor. Thus, only one time-angle pair is obtained for each physical beam. Since the beams away from the nadir region have an increased cross-track dimension of the projected beam footprint, as long as there is no layover geometry within the beam footprint (see section 2.7), it would be beneficial to have more than one independent solution within a beam. This approach is termed high-density beam forming (HDBF) by one manufacturer. To understand its principle, it is necessary to expand the idea presented when the phase difference calculation was defined, including the notions of virtual array, beam steering and angle with respect to MRA.

2.3.1.3.1 – Conversion between phase difference and angle with respect to MRA

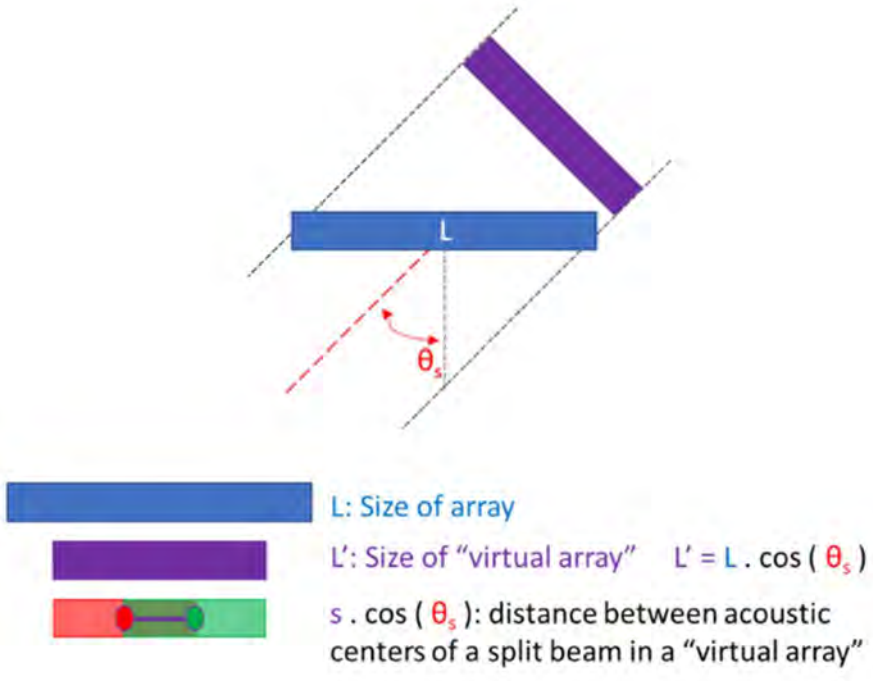

Figure 20 – Virtual array.

Recalling the linear discrete receive array of length L defined in 2.3.1.2.1, a receiving beam steered in the θ_s direction can be represented by a "virtual array" of length $L' = L.\cos(\theta_s)$. In this case, the distance between the split beam acoustic centers is reduced (Figure 20) and becomes $s.\cos(\theta_s)$.

It is known that a signal received by MRA would have zero phase difference. Any direction other than MRA would generate a phase difference value (positive or negative) proportional to the different distances traveled (δr) until reaching each part of the split beam. The expression that relates $\Delta\varphi$ to δr is given by: $\Delta\varphi = \frac{2\pi}{\lambda}.\delta r = k.\delta r$, where k is the acoustic wave-number, the spatial rate of change of phase.

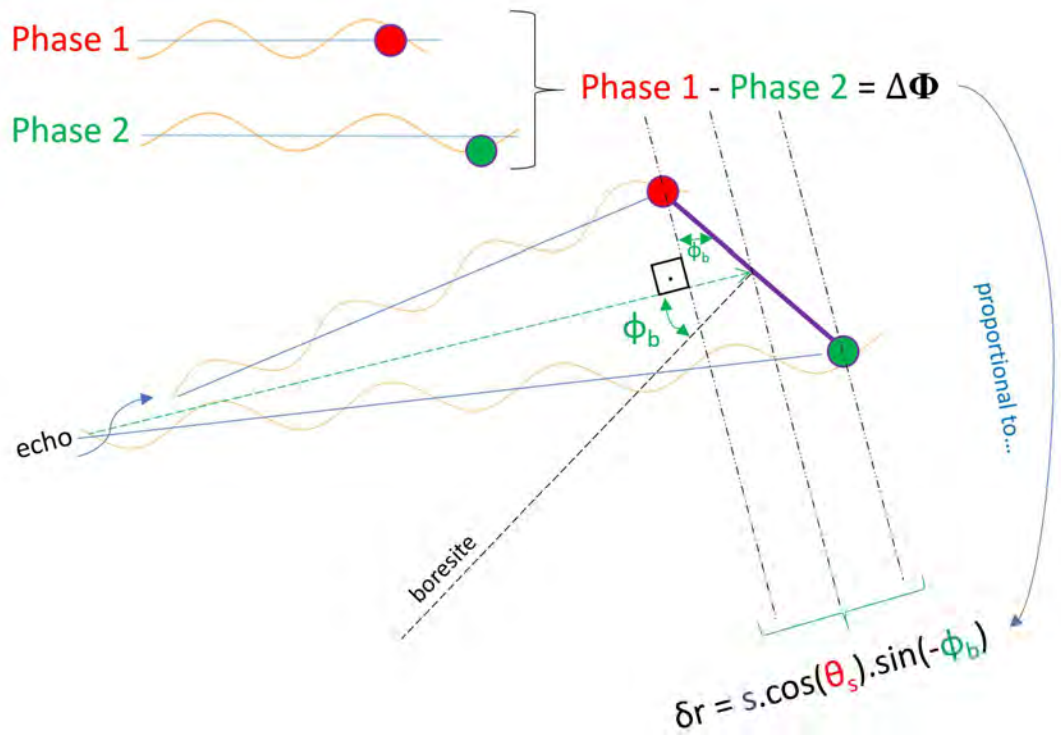

Figure 21 - Relation between phase difference and angle with respect to MRA.

On the other hand, the angle ($\emptyset_b$) between the signal source and the MRA is also related to the distance between the split beam acoustic centers and the δr distance. Before continuing, it is

important to note that each multibeam echosounder system follows an arbitrary convention to define the positive and negative directions of distances and angles. In this thesis, for angles, positive values are those that increase towards the port side (as reported in the logged data). Analyzing the geometry of this situation represented by Figure 21, the following expression is obtained: $\sin(-\emptyset_b) = \frac{\delta r}{s.\cos(\theta_s)}$. The reader is referred to Burdic (1984) for further details.

By joining the last two expressions, it is possible to associate the angle measurement with respect to MRA ($\emptyset_b$) with $\Delta\varphi$ through the following expression:

$$\begin{cases} \delta r = \sin(-\emptyset_b) \,.\, s.\cos(\theta_s) \\ \delta r = \dfrac{\Delta\varphi}{k} \end{cases} \rightarrow \quad \sin(-\emptyset_b) \,.\, s.\cos(\theta_s) = \frac{\Delta\varphi}{k} \quad \rightarrow \quad \sin(-\emptyset_b) = \frac{\Delta\varphi}{k.s.\cos(\theta_s)}$$

$$\emptyset_b = \sin^{-1}\left(\frac{-\Delta\varphi}{k.s.\cos(\theta_s)}\right)$$

The previous equation tells us that the angle between the return signal and the reception beam MRA ($\emptyset_b$) can be obtained by using the phase difference value ($\Delta\varphi$), the acoustic wave number (k), the distance between the acoustic centers of the split beam (s) and the cosine of the steering angle of this beam (θ_s), considering the positive port angle conventions. These values are known to the manufacturer and are used to obtain solutions in HDBF.

2.3.1.3.2 The values other than zero phase crossing of the phase ramp

As seen in the phase detection method, as the transmitted pulse travels along the footprint of a receiving beam, several returning signals are generated. Each of them represents a moment when the wave interacted with the seafloor. Although the classical technique focuses on zero-crossing, all other moments also represent a potential time-angle pair solution and this is explored in HDBF. Because of its ability to convert phase difference information to angles in relation to

MRA, and therefore to angles to the vertical, in principle, in the absence of noise, any point on the phase ramp can be used to define a time-angle pair.

The caveat that is made is the same applied to the previous case. It is necessary to have a high signal-to-noise-ratio (SNR) so that the phase ramp is well defined. In practice, just as was done with the zero-crossing estimate, several time samples around a time of interest have to be used and regressed to get a robust estimate. An indicator of the quality of that estimate can be obtained from the residuals in the linear or quadratic regressions used. A second caveat to do this is that there must be no layover geometry at the time of differential phase measurement (see section 2.7 and its Figure 30). This implies that the across-track slope is not as steep as the wave front.

The process of choosing pairs in HDBF occurs as follows:

- For each beam (fixed direction), amplitude detection is performed and the envelope to be analyzed is defined.
- In the defined envelope, a linear or quadratic regression is performed in the phase ramp (Hughes Clarke, 2018).
- If the residuals are low, the zero-crossing point is defined as a solution based on a shorter subset of the phase ramp close to the zero crossing.
- The number of solutions along the phase ramp will be dictated by the minimum number of phase samples needed to get a stable average and the total length of the usable phase ramp. Thus, there will typically be only one solution anyway at high grazing angles, increasing to 5-7 at low grazing angles (see Figure 22). Note that these numbers should not be considered as absolute truth. The values are highly dependent on both the receive beamwidth and the pulse length.

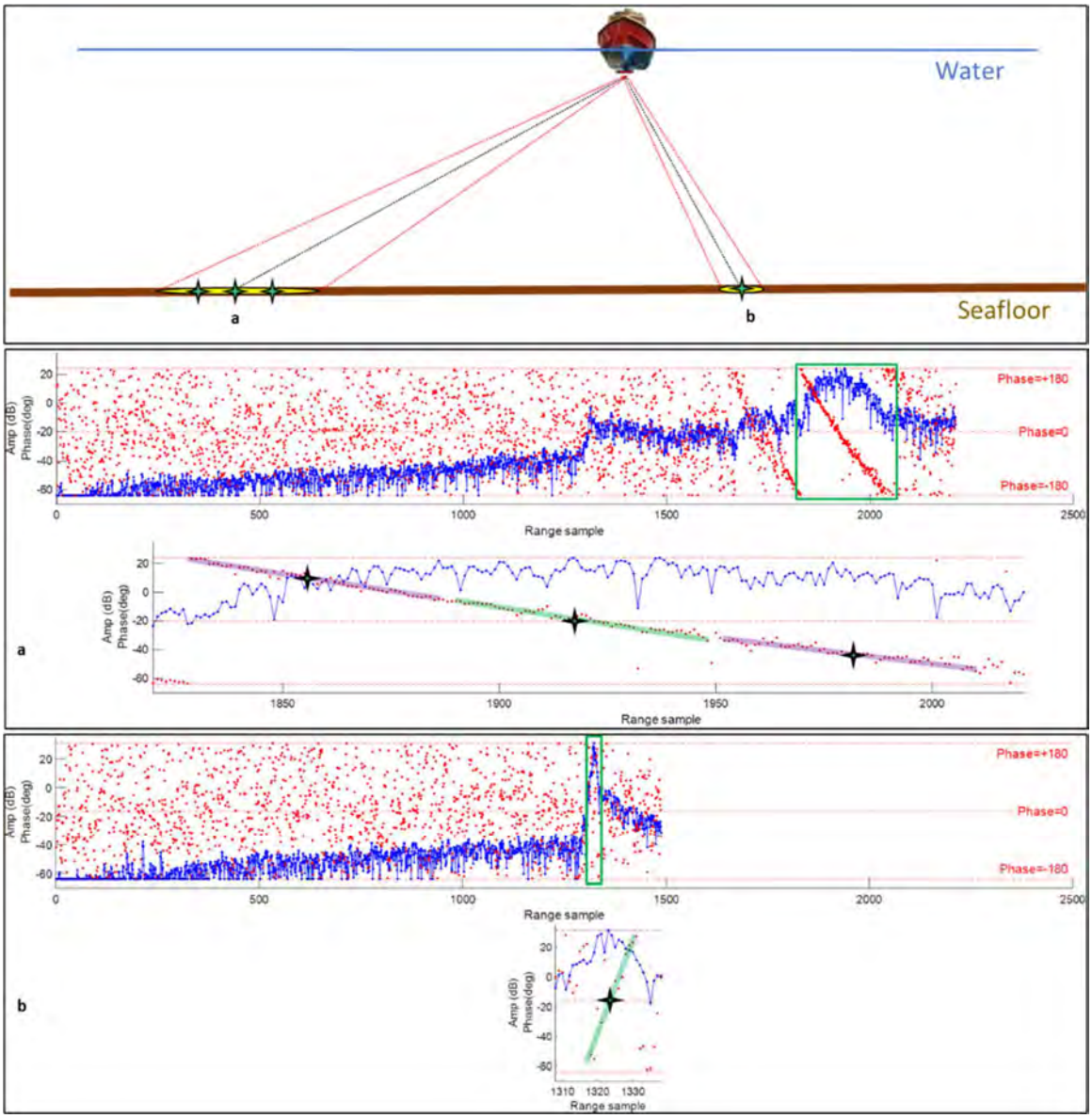

Figure 22 - High-density beamforming and its additional time-angle pairs. Top: scheme with two beams, one with low grazing angle (case a) and one with high grazing angle (case b). Middle: case a time-series and a zoom of the echo envelope and its main phase wrap (green rectangule). Note that under a low grazing angle, it is possible to perform multiple local regressions through some samples to pick additional time-angle pairs. Bottom: case b time-series and a zoom of the echo envelope and its main phase wrap. Under a high grazing angle, given its smaller number of samples, fewer local regressions are performed.

- If the phase ramp is long enough, a few points before and after the zero crossing are picked. These can either be A: time locations (e.g., zero crossing time $\pm \frac{n}{3}$ of the phase ramp length) or B:

approximate phase angle locations (e.g., phase differences of $-\pi/4$, $+\pi/4$, $-\pi/2$, $+\pi/2$, $-3\pi/4$, and $+3\pi/4$).

- Looking at a short time-series of differential phase samples around the time of interest, a local regression is done to find either A: the phase angle at that time or B: the time that the π/n crossing occurs (either way, in this manner the phase noise is reduced).
- With the phase difference angle defined, the instant is obtained and the angle with respect to MRA and its value corresponding to the vertical is calculated. Thus, a new time-angle pair is found, representing more than one solution within a single beam.

This method is often considered to be an expansion of phase detection. However, note that this method is a special hybrid case. Since it starts from a fixed direction (the beam MRA) to obtain an instant of detection and then obtains one or more new direction values, it cannot be defined exactly as a direction-based method.

2.3.1.4 - Limitations of phase data

In the absence of any noise, a single differential phase sample should be an adequate indicator of the angle with respect to beam MRA. As the SNR decreases (increasing noise), however, each independent sample has a noise vector superimposed on both subarrays, resulting in a noisy differential phase sample, stating that a phase difference measurement is sensitive to the SNR (Burdic, 1984). That SNR varies naturally throughout the received echo envelope, peaking at the MRA, where that SNR defines how good the zero crossing is. Assuming that samples before and after this point have random phase-noise vectors added, by averaging multiple phasors one can decrease the noise bias.

Thus, in directional-based methods, several neighboring time-samples are averaged. However, the counterpart is that the averaging causes a loss of resolution (Lurton, 2008). In other words, good accuracy is achieved, but with a poorer resolution. A real object can be considered noise and removed by the averaging process (Figure 23). When aiming to define objects or confirm the presence of a mast, this becomes a challenge. A balance between resolution and accuracy is necessary, and a way to evaluate this choice is made with the use of quality estimators applicable to sounding measurements (see section 3.6).

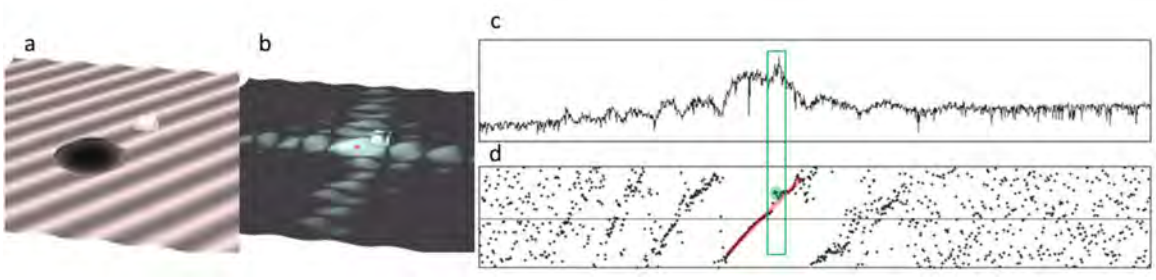

Figure 23 - Curve fitting within a phase-ramp. a: Oblique view of model terrain (depth 50m) with both topographic and textural variability, showing sinusoidal "bedforms", high backscatter block target and low backscatter circular depression. b: backscattered energy from a beam (incidence angle of 45 degrees), with 0.066 ms pulse. Greyscale ranges from white indicating peak backscattered intensity to 50 dB below that level. For both c and d, a 67 ms time-series is shown. c: backscattered intensity. The vertical axis ranges over 60 dB. d: differential phase time series. The vertical axis is from -180° to +180°. The red line represents the curve-fitting process. The green rectangle indicates the portion of data referring to the block and the green ellipse shows that the phase data of the block is out of the curve fitting. Note that the block is treated as noise, being rejected by the averaging process. (Adapted from Hughes Clarke, 1998).

In addition to being associated with signal-to-noise-ratio, the bottom detection process using phase difference data is also subject to errors associated with other factors. For more information, the reader is referred to Jin and Tang (1996) and Lurton (2000), which deal with the baseline decorrelation and the shifting footprint effect, respectively.

2.3.2 – Time based- techniques

Time-based methods consist of at a given instant, finding one or more directions from which echoes are coming from (Figure 24). This can involve finding the maximal amplitude direction (Satriano et al., 1991) or, as is examined for the first time in this thesis, finding a direction by measuring the phase difference on two split receivers. The first case is known as Bearing (or Beam) Deviation Indicator (BDI) and has previously been implemented in some models of multibeam echosounders (notably the early SASS systems, which are now historic). The second case is rarely found in textbooks or in practical applications and is the subject of this research.

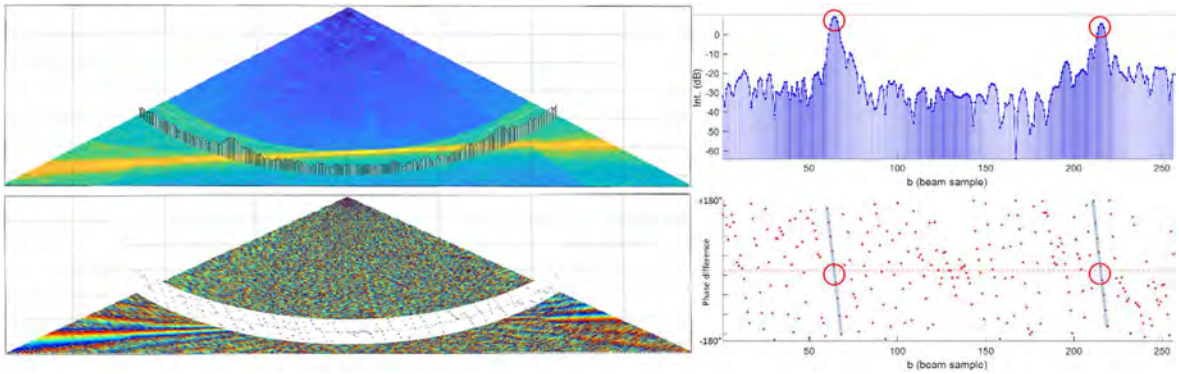

Figure 24 – Fixed instant and its beam-series. Top-left: swath amplitude data superimposed by a time-slice. Bottom-left: swath phase data superimposed by a time-slice. Top-right: Amplitude data of a beam-series. Note that the two peaks (red circles) correspond to the directions where contact with the seabed occurs for this considered moment. Bottom-right: Phase data of a beam series. Note that in the directions where the maximum amplitude values occur, a phase-ramp (blue lines) is clearly defined.

An important observation about the application of time-based methods is that it is necessary that beam spacing be significantly tighter than that part of the receiver main-lobe beam that can contribute (that part above the background noise, so if 20 dB of SNR, 20 dB down). This condition ensures that the same point scatterer on the seabed is registered by many neighboring beams (Figure 25). It is worth highlighting that, according to Marques (2012), the dimension of the beamwidth that might contribute significant echoes is typically three times larger than the nominal beamwidth (-3dB limit).

For example, a swath with 175° of aperture obtained by an echosounder model with 256 physical beams presents, in the equiangular configuration, a beam spacing of 0.68°. This same model, which has an unsteered nominal beamwidth of 1.3° and an array shading which allows the mainlobe and the maximum sidelobe level to be separated by about -20dB, can have an effective beamwidth of 3.9° (3x1.3°). This combination ensures that each scatterer point is registered in at least 5 beams (3.9°/0.68°), allowing the use of time-based methods. Note that this number can be increased according to the beam-steering applied or with the reduction of the swath aperture.

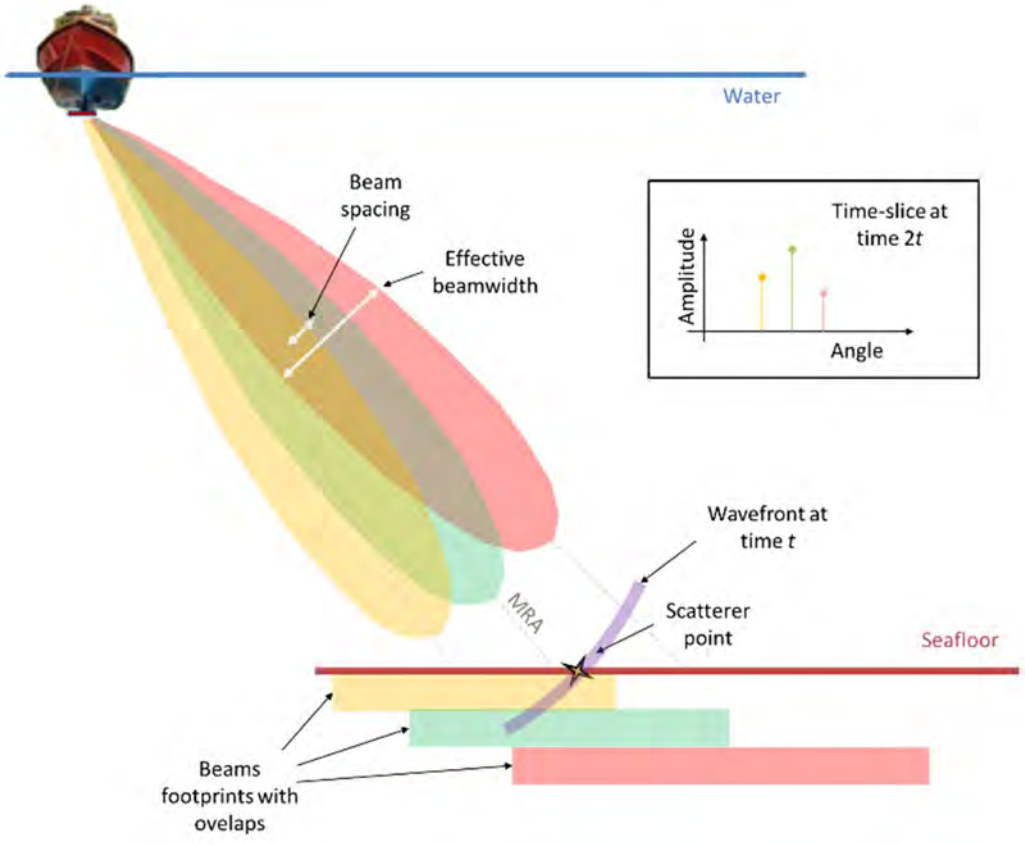

Figure 25 - Footprint overlapping. Note that the beam spacing is tighter than the effective beamwidth. Thus, the same scatterer point can be present in several adjacent beams. (after Pereira, 2015).

2.3.2.1 – BDI

Bearing Direction Indicator, also described as Beam Deviation Indicator, or simply BDI, is a method that evaluates the amplitude information recorded in all beams at a fixed time (angle

or beam-series), to obtain the angle(s) that indicates the origin of the strongest signal and thus form one (or more) time-angle pair(s). In this method, just as it is done with amplitude detection (from direction-based method), it is assumed that the maximum acoustic intensity value represents the location of the ensonified object (feature or seabed). Since each physical beam provides only one amplitude datum, the accuracy of this method depends on the number of reception beams and the angular spacing between them.

Note that, by picking a single time, all beams are actually listening to any scatterer at a fixed radial distance from the receiver. Correspondingly, all beams receive the same instantaneous noise. As, at a fixed radial distance there is normally only one point (per side), all the beams are effectively hearing exactly the same echo but with different elevation sensitivity. Thus, the across angle pattern should represent solely a map of the receiver beam pattern in elevation without any signature of the spatially variable seabed backscatter strength.

Returning to Figure 25, it can be seen that the scatterer point on the seafloor at time t is received in the main lobes of beams yellow, green and red. Considering a common beam pattern (they all use exactly the same shaded receiver and only differ in a slightly different steering angle), it is expected that the intensity of the received signal decreases as it moves away from the maximum response axis, mimicking the receiver beam pattern of any one of the beams, including all the sidelobes. With these concepts, it can be concluded that at time t, the green beam would have the highest recorded value (closest main lobe) and the beams yellow and red would have high values, but with reduction according to the distance between the scattered point and their axes of maximum response. Note, however, that none of the beam-pointing angles in these beams necessarily represent the exact direction of the scattered point. It is easy to predict that the point is somewhere between beams yellow and red, closer to green beam. To get as close as possible to

the correct value, one can perform a curve fitting, usually using parabolas (as it reasonably mimics the main lobe of a typical beam), and select the maximum point of the curve, as done by SeaBeam Instruments (2000) or Pereira and Hughes Clarke (2015).

2.3.2.1.1 – The use of parabolas

Similar to amplitude detection, the BDI process starts with the choice of one (or more) section(s) of the time-slice that contains the highest values, defining echo envelope(s) to be analyzed and a threshold level. As seen before, the simple use of the beam direction that has the highest amplitude value within the time-series does not exactly represent the direction of origin of the received signal, only indicating the nearest beam. It is necessary to apply some technique and the use of parabolas has showed to be a good approximation for the compensation of the beam pattern (Satriano et al., 1991), leaving the question about how many points to use in the curve fitting.

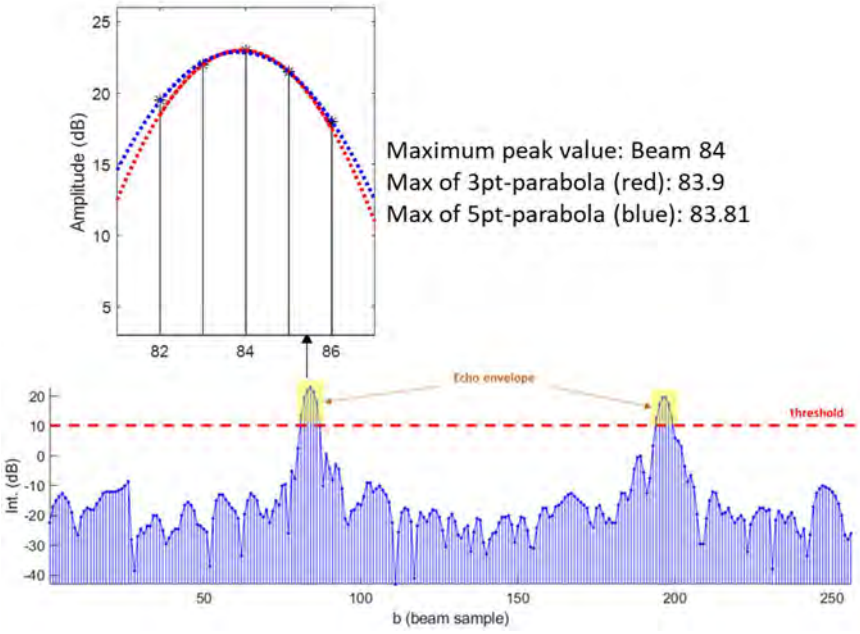

Figure 26 - Parabola fitting in BDI approach. Bottom - selected echo envelopes. Top - inflection location changed depending on the curve fitting process.

Figure 26 exemplifies the BDI detection process. At its bottom, the amplitude data of a time-slice, whose wavefront is in contact with a flat seafloor at two points (one on each side of the swath, similar to the situation in Figure 24), are displayed. A threshold (dashed red line) was defined and two echo envelopes were obtained (highlighted in yellow). One of these echo envelopes is detailed at the top-left of the figure, and a parabola fitting with three points (red) and five points (blue) was made. The maximum values obtained (in terms of beam number, not converted to angles) are written next to it. Note that the peak values (maximum recorded at the inflection points of the parabolas) are very similar, but the inflection location is slightly different, indicating that the exact angle estimate can be changed depending on the number of points used in the curve fitting.

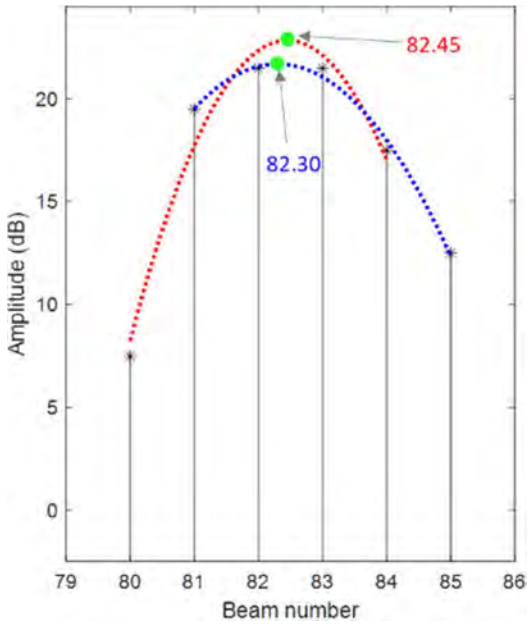

Figure 27 – Directions according to parabola fitting. The green circles indicate the point of inflection (maximum value) of each parabola.

The smallest possible number is 3 points, and represents a perfect parabola fitting. The more the number of samples above noise the better the representation of the effective receiver main-lobe beamwidth in the parabola fitting process. Using more than 3 points can result in an

imperfect fit, and thus the least mean square method is used. The maximum usable number of points for the fit depends on the beamwidth, beam steering, beam spacing, swath aperture and beam pattern.

A special case occurs when the echo envelope has two beams of equal amplitude value as the maximum value. If an odd number of beams is used in the fit, the choice of which beam to use as a center of the parabola fitting points can generate a bias in the result. This case is exemplified in Figure 27. It contains the amplitude values of an envelope echo composed of six beams (numbered from 80 to 85). Beams numbers 82 and 83 have the same amplitude value, which is the maximum value of this envelope echo. To make a 5-point parabola fitting, one must use the maximum value beam and include two beams before and after it. Centering the choice of points on beam 82 (consequently generating a parabola with points 80 to 84), the curve in red is obtained. Repeating the process centered on beam 83 (using points 81 to 85), the blue curve is obtained. The point of inflection of the curves (maximum value) is represented by the circles in green. The abscissas of these points are 82.45 (red parabola) and 82.30 (blue parabola), emphasizing that the choice of the central point (beam) influences the direction of the result. In this way, the quality of the direction obtained by BDI is dependent on a good choice of the number of points considered in the parabola fitting and the way in which these selected points are distributed.

2.3.2.1.2 – Normal and oblique incidences

Analyzing the performance of BDI in situations where the wavefront touches the seafloor under normal and oblique incidence, it is observed that echo envelopes are more poorly defined when the signal comes from a near-normal incidence. This is due to the wider projected pulse length that it has, allowing several adjoining beams to receive the return signal simultaneously,

with very similar and high intensities, making the parabola fit process difficult. Figure 28 (top) represents this case. Note that the peaks of higher amplitudes (above the defined threshold) have similar values, making it difficult to define a single direction of signal reception.

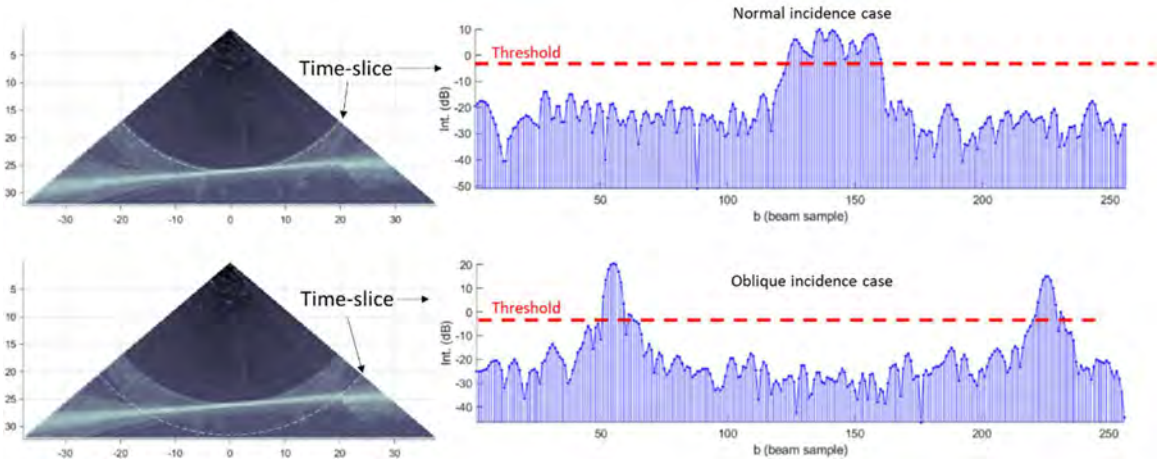

Figure 28 - BDI at normal (top) and oblique incidences (bottom).

On the other hand, in oblique incidence cases, due to its narrower projected pulse length, a small portion of the seafloor is analyzed in each time-slice, allowing the amplitude values to be highlighted in the directions of signal reception. Figure 28 (bottom) represents this case, showing two prominent peaks regarding the contact between the wavefront and the seafloor. For this reason, the use of BDI is recommended in oblique cases.

2.3.2.1.3 – Why was BDI left aside?

A clear and documented reason that has led BDI to disuse has not been found, however, it is believed that it was gradually discontinued for some of the reasons listed in this section. Before phase data was used, when only amplitude data was made available, amplitude detection (using time-series) and BDI (using time-slices) were complementary solutions. The first was used for near-normal incidence and the second was used for oblique incidence.

Once phase data were available, some factors contributed to its use and consequent disuse of BDI, such as:

- Phase detection works better (more accurate) in oblique incidence than at normal incidence (same situation than BDI), meaning a detection status complementary to the amplitude detection method.
- Phase detection uses the same echo envelope generated for amplitude detection, which can save processing time.
- Time-series analysis is done individually for each beam, representing a task in a universe of hundreds of beams. The beam-series analysis is done individually for each time-sample, being able to easily reach thousands of time-slices. In times of limited data processing resources, the apparent reduction in iterations favors direction-based methods.
- The number of solutions obtained by the time-series can be fixed at one per beam. On the other hand, the number of solutions obtained by BDI is random, impacting the management of data storage capacity or demanding more processing (filter).
- Studies on the measurement of uncertainties have shown that higher accuracy can be obtained by means of a time-sample average, reducing the noise.

A combination of these factors with probable others led to the replacement of BDI by phase detection. However, the use of time-series and time-slices should not be thought of as competing alternatives. Both are complementary and can perform better according to the combination of the angle of incidence and geometry of the object.

2.3.2.2 – Phase difference direction (“PDI”)

Now that the phase difference data can be retained through logging and includes the entire water column, it is also possible to analyze its behavior in time-slices. In it, since only one datum

is recorded per beam, the visual arrangement of the values is not as diverse as in the time-series. Phase-ramps can be also observed and its zero-crossing directions visually appears to be associated with the amplitude peaks (Figure 29). In this way, the question of what would happen if the phase data were used in addition to the BDI approach can be addressed.

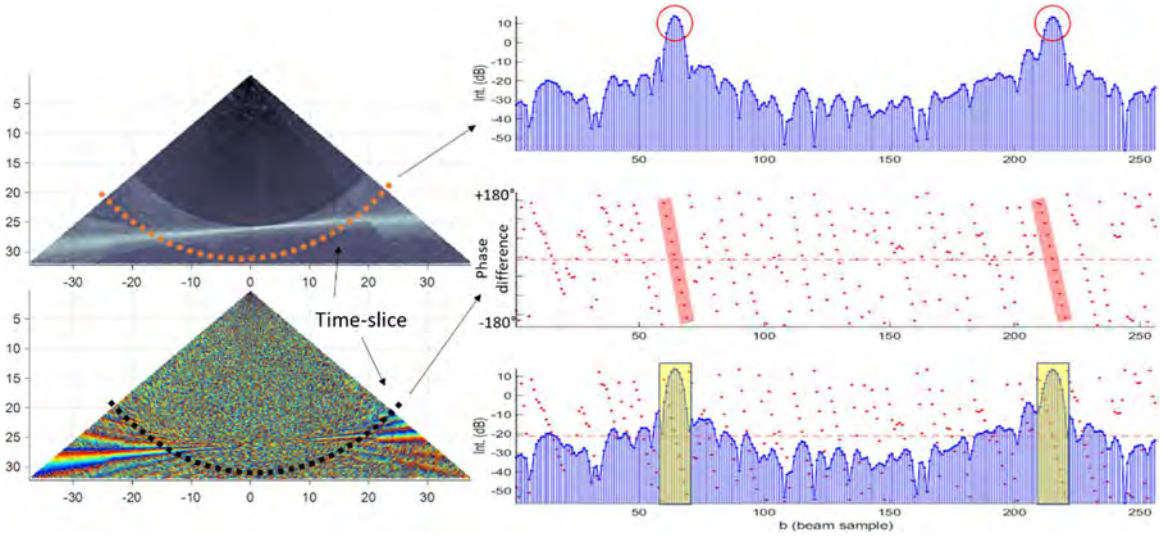

Figure 29 - Phase difference direction. Left: Amplitude (top) and Phase (bottom) data, with a time-slice. Right: Amplitude data (top), as presented in BDI. The red circles indicate the main peaks. The phase data (middle) displays several phase ramps. Superimposing both data (bottom), it can be observed that there is some relationship between the amplitude peak and the null phase value.

This thesis, for the first time adds a fourth method (or fifth, if HDBF is considered a separate method), herein termed Phase Deviation Indicator (PDI) which uses the angle-series of differential phase. This method, complementary to BDI, chooses instead of doing curve fitting of parabolas in the amplitude data, to use the phase difference information between adjacent beams to equivalently estimate the angle that represents the location of the ensonified object.

The next chapter assesses how a zero-crossing at a time-slice can be used to indicate an angle, irrespective of knowledge of wavelength separation, explaining the methodology used. Subsequent chapters show the tests, results and conclusions, emphasizing that this is another option to be considered in the search for more robust bottom detection algorithm.

2.4 – Raytracing process

Once the solutions of the bottom detection algorithm are defined, a series of integrations is performed, taking into account the lever arms (GNSS antenna position, motion sensor, transmission and reception transducers), the speed of sound in the water column and on the face of the transducer, the observed attitudes (roll, pitch, yaw, heave) at both transmission and reception times, the tide and the uncertainties associated with all these measurements. With all this data it is possible to perform raytracing and geographically locate each sounding obtained.

It is noteworthy, however, that the objective of the present study aims to evaluate the use of phase difference data in a time-based method of bottom detection. The angle estimated is strictly the instantaneous steering angle with respect to the long-axis of the receiver. That same value is recorded for every detection for the other methods, and thus the comparison can take place completely within a receiver-relative reference frame, without the need for the full georeferencing. Thus, the complete realization of the data integration process and the geographic location of the obtained soundings is not required to do this analysis and will not be presented. To give the reader an approximate across-along track referenced view, a simplified 2D positioning is performed just using local-level relative beam elevation angle and travel time.

2.5 – Previous works

Multibeam echo-sounders systems are one of the great advances in bathymetric survey methods (de Moustier, 1988). The basis of its theory of operation is well known (de Moustier, 1988, SeaBeam Instruments, 2000), and previously-established bottom detection methods have been described and analyzed (Satriano et al, 1991, Hammerstad et al, 1991, de Moustier, 1993).

With the growing ability to retain the full beam-time-series of acoustic returns allowed the emergence of studies on water column applications of multibeam systems. The first applications, which only examined the amplitude part of the return, involved fisheries acoustics (Mayer et al, 1997, Gerlotto et al, 1999, Mayer et al., 2002) and later expanded to other areas, such as geophysical and oceanographic applications, as reviewed by Colbo et al. (2014).

In the ocean mapping area, Hughes Clarke (2006) showed that the water column imaging can provide several significant advantages to the hydrographer in quality control, such as calculating a new bottom pick or identifying bottom mistracking or a wreck delineation. In Hughes Clarke et al (2006b) it is demonstrated that protruding mast and spars from shipwrecks, important in hydrography due to the minimum clearance required to be represented on the chart, are among the most extreme target detection problem because they are discontinuous targets and small cross-section. In it, it is demonstrated that reliable detection of the Wreck Least-Depth may be achieved.

Following this line of research, Van der Werf (2010) proposed a method for wreck least depth determination using water column imaging, in which a selected pixel is transformed to depths in the geographic frame. His study focused on in-between surface and bottom high-aspect-ratio target identification. Subsequently, Marques and Hughes Clarke (2012) proposed an automatic mid-water target tracking method, in which specific objects can be detected and positioned in a 3D reference frame by analyzing the survey in its along-track direction.

In contrast to in-water targets, in order to improve seabed object identification, Pereira and Hughes Clarke (2015) proposed the application of BDI in shallow water at low grazing angles. They were based on the fact that in the very outermost beams, beyond 60° incidence angle, where the current Kongsberg Maritime (KM) bottom detection algorithm might not identify a target, the logged water column imagery can be used to recognize its presence. It was shown that the BDI

method could provide such an alternate approaching in the presence of high-aspect-ratio targets, due to the fact that it is less affected by layover and poor signal-to-noise conditions than direction-based phase detection is.

All of these previous works used only the water column amplitude data, due to the unavailability of phase data. However, some manufacturers (e.g., Reson and Kongsberg) recently allowed the user to record the water column phase difference data as well, opening up new research opportunities, such as the present study.

2.6 – Intensity levels used in this study

It is important to highlight that the amplitude data recorded in the water column and used throughout this study are those coming from the datagrams of the multibeam system used. Such data is already saved with some corrections applied. In general, according to Kongsberg Maritime (2018), its final value is obtained by:

$BS = EL - SL - M + TVG + BScorr$, where:

- BS: Beam intensity, in dB. It is the value used in this thesis.

- EL: Detected Echo Level. Not recorded on datagrams.

- SL: Source level applied, in dB. It is corrected for transmission beampattern (along and across) at the transmit frequency and vessel attitude. It is composed of SL = SLnom + SLcorr, where: SLnom = Nominal maximum SL, recorded per TX sector and SLcorr = SL correction relative to nominal TX power based on measured high voltage power level and any use of digital power control.

- M: Receiver sensitivity, compensated for RX beampattern at transmitting frequency and vessel attitude.

- TVG: Time Varying Gain function applied. It is given by: TVG = X.log (R) + 2.Alpha.R + OFS. Where: X = Operator selected and common to all beams in datagram. R = range. Alpha = Mean absorption coefficient, in dB / km, and is given for each beam. OFS = Time Varying Gain offset used, in dB, to compensate for TX source level, receiver sensitivity, etc.
- BScorr: Backscatter calibration offset applied (the default value is 0 dB).

As can be seen in Table 3, section 4.3, the value "30" was used for X and for OFS. Thus, the TVG applied was TVG = 30.log (R) + 2.Alpha.R + 30. As a result, in the present thesis it is common to find BS values above 0 dB.

Most significantly for the algorithm development in this thesis (see chapter 3), for the optimal identification of the peak echo and any range-independent thresholding, the 30.log (R) + 2.Alpha.R term adequately removes the gross range-scaling effects. This is because, for the pulse length limited case, the ensonified area varies with range (hence 10.log (R)) so that when combined the spherical spreading component (40.log (R)), 30.log (R) is the net result.

2.7 – The layover effect

Within a beam, all echoes at a common slant-range are combined. If the along-track slope, due to the seabed or a combination between seabed and an object, is steeper than the expanding wave-front, echoes from two or more points will be received at the same time and will be smeared. This is a common problem in side-scan sonar, in which all elevation angles (each side) are listened to together (a single receiving beam per side), mixing multiple echoes without being able to separate them by elevation angle.

In multi-beam systems, if the distance between the points received simultaneously is greater than a beamwidth, the points will be detected separately within the corresponding receiver

beams that have a MRA in that direction. However, if they are within the same beam, their separation might only be possible through the analysis of time-slices, again, considering beam spacing significantly tighter than the effective receiver main-lobe beamwidth.

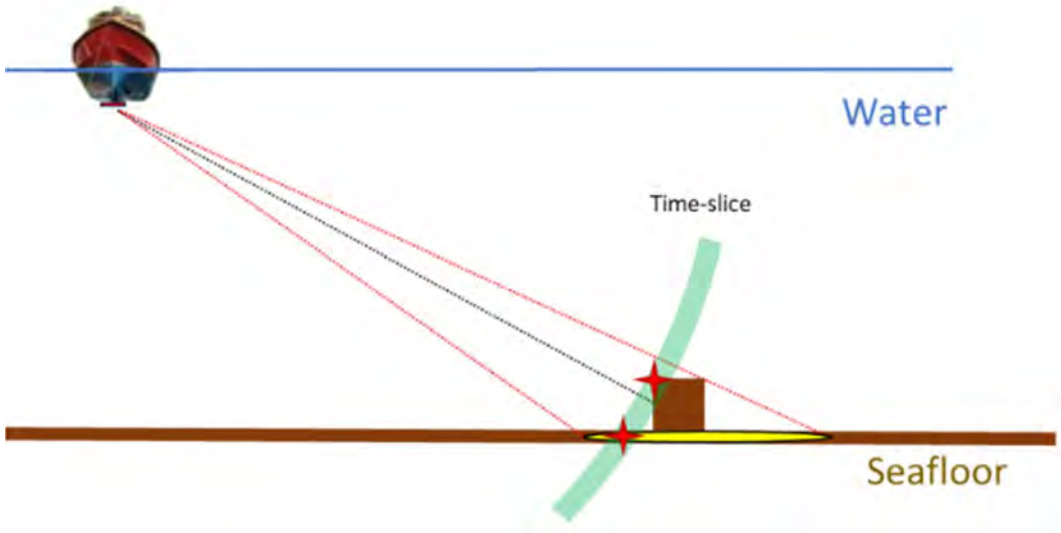

Figure 30 - Layover geometry. Within a single beam, the wave-front is touching the inward face of a 1-m cube and the seafloor in front of the cube at the same time. These two points (red stars) will be mixed together, and direction-based methods cannot separate them in different elevation angles.

Note that all the preceding discussion of regressing phase time-series, assumes that within a single time sample, only seafloor from a single elevation angle is contributing to the echo. This assumption is violated if there is layover within the beam footprint. A common example of this, as indicated in Figure 30, is a short wavelength target such as a cube or boulder in which a single time-slice intersects both the inward facing side of the target and the seafloor in front of it. In this case, as with bathymetric sidescan, the phase elevation estimate is corrupted. As will be seen in the result section, direction-based methods do not generally do a good job of defining low grazing angle target dimensions.

2.8 - Multiple targets within a beam (extra-detections)

An existing feature in some echo sounder models allows for more than one detection per beam, analyzing other echo candidate envelopes in all beams (Kongsberg Maritime, 2018). This approach is termed extra-detections by one manufacturer. Its principle is based on the fact that, under the same beam, if targets exist that incompletely occlude the beam, subsequent additional targets can also be detected.

While conventional detection focuses on the echo envelope with the highest amplitude values, the extra-detection feature looks for possible solutions in other lesser amplitude candidate echo envelopes. It is also important to differentiate this concept from HDBF. Extra-detections refer to the search for new detections outside the same echo envelope, analyzing completely separate echo envelopes. Once a new echo envelope is selected, conventional direction-based amplitude or phase detection is performed. While HDBF also seeks for more soundings, the distinction is that it is using only one echo envelope, that is, within a single phase-ramp.

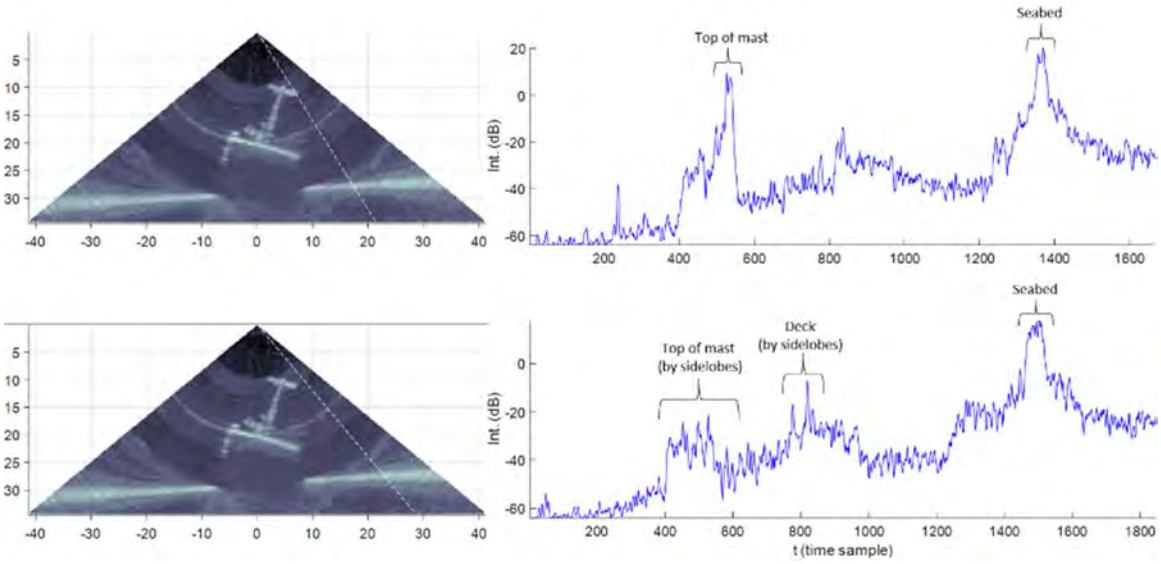

Figure 31 - Extra-detection feature. Top - extra-detection within the same beam. Bottom - Sidelobe detections.

The great challenge of this extra-detection feature is to differentiate the returns coming from the main lobe from those coming from sidelobes, within a single beam. In this way, although this feature allows more detections and, consequently, might allow a better definition of the target's geometry, its setback is the possibility of increasing the number of spikes (detection of sidelobes).

Figure 31 exemplifies this issue with two examples. Both images on the left represent the same swath. Its dotted white line indicates the beam under analysis, whose time-series is displayed on the right plots. In the first case (top-right), if only one echo envelope per beam were used, only the seabed would be detected (higher amplitude values). The extra-detection feature allows the analysis of a second echo envelope and the consequent detection of the top of the mast. In the second case, note (bottom-left) that the main lobe of this beam does not intercept the shipwreck. It is expected only the detection of the seabed. If the extra-detections feature were applied to the data of this beam (bottom-right), there would be a great chance that the envelopes referring to the top of mast or deck sidelobes would be selected, introducing spikes. This problem can be avoided if the user defines parameters (e.g., quality factor, reflectivity, or SNR) that limit the choice of extra envelopes.

CHAPTER 3 – METHODOLOGY

3.1 – The “other” zero-crossing

As presented in the previous chapter (section 2.3.2), when beam spacing is significantly tighter than the effective receiver main-lobe beamwidth, time-based methods can be employed, as the instantaneous scattered contribution within the ensonified area on the seabed is registered by many neighboring beams. In this situation, the BDI can be used to evaluate the directions where the amplitude data forms the highest peaks within a time-slice. However, due to existing limitations, the accuracy depends on the number of samples used in this evaluation process. On the other hand, phase data, previously not considered, can also be used in a complementary way. In this case, after using the amplitude data to define the peak where the direction is to be sought, the phase data, after being combined in a certain way, could equivalently estimate such direction.

Consider a hypothetical case of two independent beams (with exaggerated dimensions for illustrative purposes), represented by the colors yellow and orange (Figure 32-a). The maximum response axes are represented by dashed lines in red and blue colors respectively. And the detection instants of each beam are represented by dashed curves with the same colors. In this way, the crossing point between the lines of the same color form a sounding (time-angle pair), represented by stars. However, it is known that the interaction of the beam with the seabed happens over a time range before and after the MRA (the echo envelope). Thus, other instants can also provide soundings, for example being analyzed through its time evolution of the phase ramp (HDBF principle). In this way, another fixed instant (green dashed curve), between the detections of each beam, also has a sounding (green star), being only necessary to find the direction (green dashed line) that forms its time-angle pair.

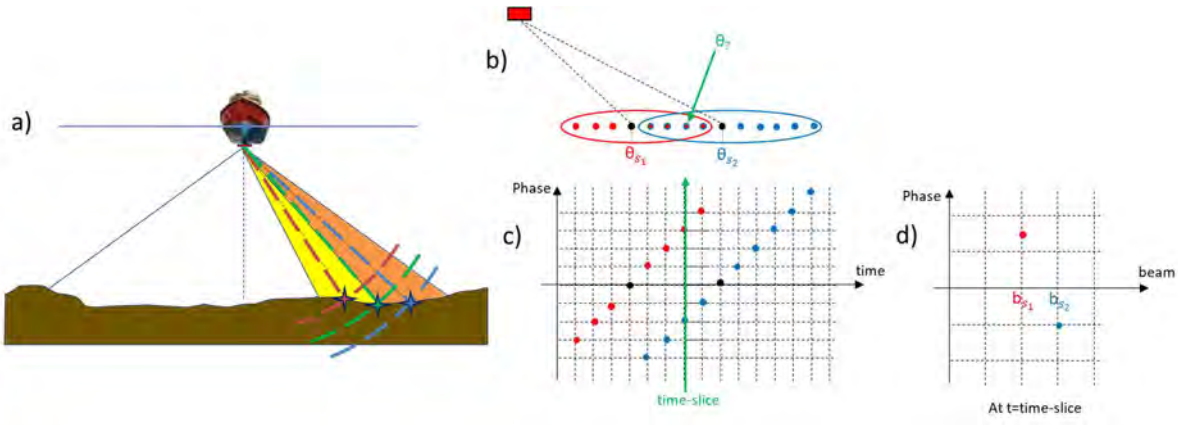

Figure 32 – Two adjacent beams in time-series and time-slice. a) two independent beams (yellow and orange) with its MRA (dashed lines) and detection instants (red and blue stars). An extra-sounding (green star) can be determined, being only necessary to find the direction. b) the extra-sounding (green arrow) is present in both beams' footprints, indicated in red and blue. c) whereas an extra-sounding will always be between the MRA of two adjacent beams, a time-slice (green arrow) made on the phase difference time-series of each beam shows a negative and a positive value. d) time-slice data.

From a quick analysis, it is possible to conclude that this extra-sounding (green star) could near equivalently be obtained with only one beam, using HDBF (section 2.3.1.3). However, due to the limitations of phase data (section 2.3.1.4), this is not always possible, and thus the use of an alternative method would be beneficial.

Assuming a beam spacing smaller than the effective main-lobe receiver beamwidth, the same point on the seabed is registered by more than one beam and information about its amplitude and phase data can be read in the time-series of these beams (angle-series). While the time-series phase-ramp may be too short, the angle-series phase-ramp will always be of the same width, designed by the choice of subarray separation, as discussed in section 2.3.1.2.1. A time-slice always has an amount of data equal to the number of existing physical beams (one data per beam). And the data related to phase-ramp are linked to the number of adjacent beams that record information from the same point on the seabed/target.

In the current hypothetical case, the Figure 32-b shows the extra-sounding under analysis (green arrow) in both footprints, indicated in red and blue. Observing the phase difference time-

series of each beam on the same axis (Figure 32-c), and their respective phase-ramps, it is apparent that a time-slice (green arrow), when positioned between the moments corresponding to the maximum response axes detection (black dots), presents phase data from both beams, one being with a negative value and the other with a positive value. This difference in signs is due to the behavior of the phase ramp already presented, since the data of phase difference changes sign when crossing the MRA (null phase difference). Whereas an extra-sounding will always be between two adjacent beams (obviously disregarding this occurrence before the first beam or after the last beam, when no data is available), and that the sound pulse moves in a direction that increases the radial distance from the source (i.e., not a surface normal to the average beam orientation), with respect to one of the beams the extra-sounding will be located after the MRA (positive red value on Figure 32-c) and with respect to the other beam it will be located before the MRA (negative blue value on Figure 32-c).

Figure 32-d provides the data for the two beams for the same time-slice. Note the characteristic highlighted earlier, of a positive and a negative phase value. As seen in section 2.3.1.3.1, it would be equivalently possible to perform conversion between phase difference value and angle with respect to each MRA, knowing the values of the acoustic wave number (k), the distance between the acoustic centers of the split beam (s) and the steering angle of this beam (θ_s). The combined use of these conversions between phase angle to angle with respect to MRA and the knowledge of the beam's steering angle allows one to obtain the estimated direction of the intermediate point scatterer.

To explain this process, consider an instant (t') when the only interaction of the pulse with the seabed occurs at the point represented by the yellow star (Figure 33-bottom). At the time equal to 2.t', the data for this interaction is recorded in the adjacent red and blue beams. The red beam,

whose MRA angle is given by θ_{s_1}, presents, in this time-slice, a positive phase value which, after being converted to an angle with respect to MRA, is given by $\emptyset_{b1}$. The blue beam, whose angle of the MRA is given by θ_{s_2}, presents, in the same time-slice, a negative phase value that is converted to the angle $\emptyset_{b2}$. Taking into account the convention that positive angle values are those that increase towards the port side, it is observed that θ_{s_1}, θ_{s_2} and $\emptyset_{b1}$ are negative. Likewise, $\emptyset_{b2}$ is positive.

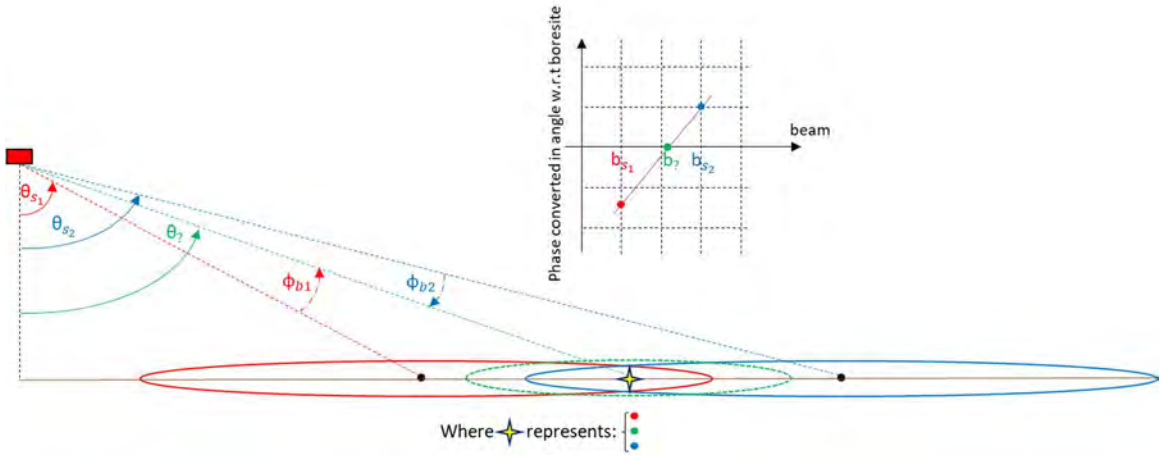

Figure 33 – Zero-crossing at a time-slice.

The estimate of the direction corresponding to the yellow star ($\theta_?$) can be obtained either by $\bar{\theta}_? = \bar{\theta}_{s_1} + \overline{\emptyset}_{b1}$ or by $\bar{\theta}_? = \bar{\theta}_{s_2} + \overline{\emptyset}_{b2}$. Now imagine that it was possible to create a third (virtual) beam (green) whose axis of maximum response was exactly in the $\theta_?$ direction. Since it is under MRA, its phase difference angle would be zero. Note that the yellow star now contains three pieces of information: before the red beam, it has a negative angle value in relation to that MRA; before the green beam, it has a zero angle in relation to its MRA; and before the blue beam, it has a positive angle value with respect to MRA. These three pieces of information are displayed in the beam-series of this time slice (Figure 33, top). Note that, similar to that existing in a time-series,

the beam-series (time-slice) also displays a phase-ramp-like in the vicinity of a point scatterer (yellow star), with the null value corresponding to its direction.

To summarize more generally, in a beam-series, whose time is defined, a zero-crossing within a “angle w.r.t. MRA” ramp (obtained in an across-beam slice by converting the phase data in angles) indicates the direction sought, forming a time-angle pair (sounding). In addition, due to the convention, it was seen that the conversion from phase to angle modifies its sign. Thus, when it is desired to find an estimated direction of the instantaneous scattered contribution, it is necessary to observe between which beams the phase sign change occurs (a zero-crossing), either in a phase-ramp or converted-angle-ramp.

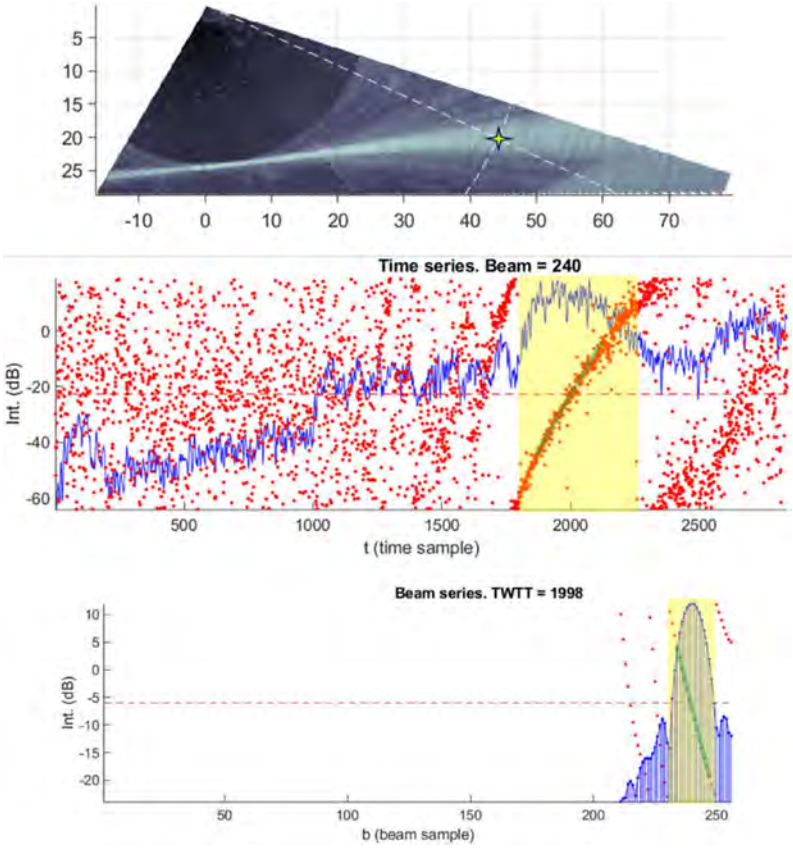

Figure 34 – Time-angle pair and their respective time-series and beam-series. Top) a ping amplitude data, with a highlighted time-angle pair (yellow star). Middle) time-series that contains the yellow star. Bottom) beam-series that contains the yellow star. The blue data represents the amplitude information and the red data represents the phase difference information. Highlighted in a yellow box is the echo envelope and the peak analyzed.

An example with real data can be seen in Figure 34. In the top, there is an image of the ping amplitude data. In it, a time-angle pair is highlighted (yellow star), being composed by beam number 240 (white dashed line) and time-sample number 1998 (white dashed curve). In the middle, there is the time-series of beam #240. And in the bottom, there is the beam-series of time-sample 1998. In these two last images, the blue data represents the amplitude information. The red data represents the phase difference information. The horizontal dashed line in red indicates the null phase. Highlighted in a yellow box is the echo envelope and the peak analyzed. The green line indicates the phase-ramps.

In Figure 34-bottom, the peak of higher amplitudes has a clear across-beam phase-ramp. Note that this peak also shows the change in the phase sign, from positive to negative. In this way, it is clear that there is a connection between zero-crossing phase and the direction of the scatterer point (note that how to get this direction has not yet been addressed and will be the subject of the next section). It is important to note that the null phase value across beam is not always associated with a detection. There are three phase-ramps that cross the null value in this example. The first two are related to phase wraps (i.e., angles larger or smaller that the designed $\pm\pi$ around the MRA) and should not be considered. Only the third (within the yellow box) can be associate to detection by the main-lobes. Making an analogy to the conventional method (direction-based method), over a time-series the phase value crosses zero several times (Figure 34-middle). However, the detection is considered as the zero-crossing that occurs in the envelope defined by the detection amplitude (within the yellow box). A similar concept is used in the case of beam-series, and the analysis of the phase-ramp must be performed only on the selected echo envelopes (peaks).

Recapitulating the main concepts, the phase information indicates the angle between the scatterer point and the MRA of each beam. Within a time-series, whose beam is already defined,

the instant when the null value occurs, the conventional zero-crossing (when the scatterer point is exactly in the MRA), is sought to obtain the time-angle pair of the detection. On the other hand, within a beam-series, whose time is defined, the direction containing the scatterer point is searched among the various MRAs of the receiving beams, specifically between those neighboring beams whose phase information crosses the zero value, the other zero-crossing. As proposed in the next section, the estimated direction is then calculated using those neighboring beams around the zero-crossing phase data.

Note that, for the same reason that the angle-series of intensities is so smooth, reflecting only the receiver beam pattern, the angle-series of phase is also smooth. This is in contrast to the time-series of phase which is examining multiple time periods when the SNR is fluctuating (due to changes in both the noise and the local seafloor scattering). For the angle-series, whatever the noise phasor contribution, is common to all the receiver beams and thus the phase sweep is smooth. Note that this implies that, although the zero-crossing is readily estimated, it actually will have a fixed mechanical angle error due to the instantaneous noise. If we move one time-step in or out, the zero-crossing estimate will jump in the same manner that an HDBF solution would register if it used just a single, rather than an average differential phase sample. Only by averaging a few adjacent time samples zero-crossings it is possible to manage the noise (equivalent to regressing the time-series of phase).

3.2 – Obtaining directions with zero-crossing across-beams

Once clarified that the phase information in a time-slice can indicate the direction of a scatterer point when there is zero-crossing within a peak with high amplitudes, it remains to be defined how to obtain its value. The essence of this concept is linked to the possibility of converting

the phase information into angles with respect to MRA. The expression presented in section 2.3.1.3.1, $\emptyset_b = \sin^{-1}\left(\frac{-\Delta\varphi}{k.s.\cos(\theta_s)}\right)$, highlights the need to know the value of the distance between the acoustic centers of the split beam (s). Thus, two cases exist: whether the distance between the acoustic centers of the split beam (s) is known or not.

3.2.1 - "s" is known

In the first case, the solution is simple and, once the envelope (amplitude) to be analyzed is defined, the zero-crossing direction (on a time-slice) can be obtained by following four steps:

i) inside the envelope, the phase-ramp is checked and the beam before or after the zero-crossing is searched. Note that either the beam inboard or outboard could be used. If "s" is known for both beams, the final answer should be the same.

ii) the phase information of the beam found (either one) is converted into an angle in relation to the MRA.

iii) the angle obtained is then added to the steering angle value.

iv) the result is corrected for the desired coordinate system, including, if necessary, the information of mount angles and motion sensors (mainly roll).

Note that these steps are similar to the final HDBF steps, with the exception that the time-angle pair selected in that method depends on the amount of phase averaging along that part of the phase-ramp. Thus, it is presumed that manufacturers that already have an algorithm for calculating HDBF and that have phase data along the water column have the necessary knowledge of sub-aperture spacing to include time-based phase detection.

3.2.2 - “s” is unknown

Unfortunately, knowledge about how the split beam is divided or how its value varies with the different steering angles is not always available. An estimate of ‘s’ from the data itself was tried. However, the existence of multiple sectors, multiple soundings within the same beam (HDBF), the noise in the instantaneous phase values, the estimates of the involved angles to MRA, and the use of some unknown tapering function in the received signal made the results of this attempt questionable. Thus, it is necessary to find an expression that allows the conversion from $\Delta\Phi_1$ and $\Delta\Phi_2$ to $\emptyset_{b1}$and $\emptyset_{b2}$ without any need for knowledge of “s”. Some assumptions and approaches were made, reaching an expression to circumvent this need, as explained below.

The starting point is the same as before, however, it is necessary to use both beams (before and after zero-crossing). Each beam has its own steering angle and phase information. In other words, the initial data is: θ_{s_1}, θ_{s_2}, $\Delta\Phi_1$ and $\Delta\Phi_2$.

The first step was the attempt to simplify the expression of conversion between phase and angle, since it has the arcsine function in its content. This was achieved through the Taylor series, in which the arcsine function can be written as follows:

$$\sin^{-1}(z) = \arcsin(z) = z + \left(\frac{1}{2}\right)\frac{z^3}{3} + \left(\frac{1\,.\,3}{2\,.\,4}\right)\frac{z^5}{5} + \left(\frac{1\,.\,3\,.\,5}{2\,.\,4\,.\,6}\right)\frac{z^7}{7} + \cdots$$

$$= \sum_{n=0}^{\infty} \frac{(2n-1)!!}{(2n)!!}\,\frac{z^{2n+1}}{2n+1}$$

$$= \sum_{n=0}^{\infty} \frac{(2n)!}{(2^n n!)^2}\,\frac{z^{2n+1}}{2n+1};\ |z| \le 1$$

The number of terms defines the accuracy of this series. In the case under analysis, the angle considered is that between the scatterer point and the MRA of the nearest beams. In other words, it is always smaller than beam spacing. Since the swath width is always less than 180

degrees and it is common for current multibeam systems to have more than 90 physical beams, it is reasonable to believe that beam spacing is rarely more than 2 degrees (in an equiangular configuration).

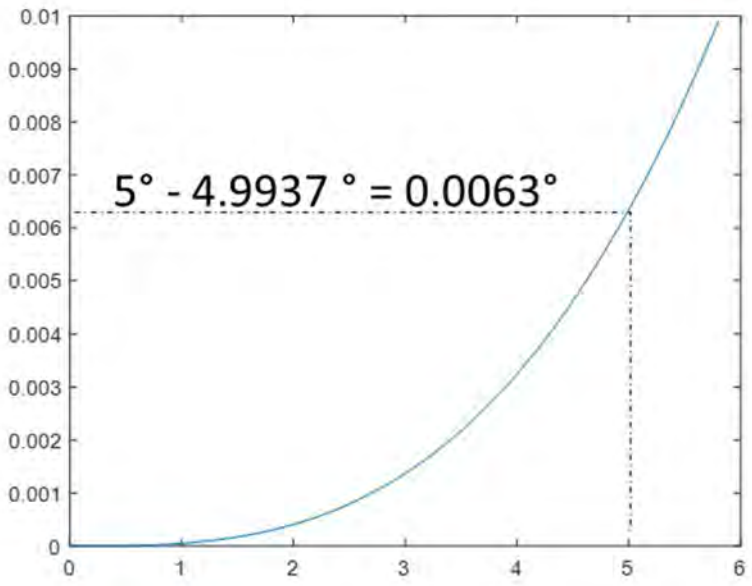

Figure 35 – Taylor series evaluation.

Checking the accuracy of the Taylor series with only one term ($\sin^{-1}(z) \cong z$), a graph (Figure 35) was generated whose abscissa axis indicates the angle with respect to MRA and the ordinate axis indicates the absolute value, in degrees, of the difference between $\sin^{-1}(z) - z$, limited to a tolerable maximum of 0.01 degrees (defined due to the accuracy of the motion sensor). In this graph it can be seen that the approximation generated by the use of a single term in the Taylor series presents an error lower than the accuracy of the motion sensor up to about six degrees. The error of its use with an angle of 5 degrees is 0.0063 degrees. Thus, the approximation was considered acceptable. In this way, the expression becomes:

$$\emptyset_b = \sin^{-1}\left(\frac{-\Delta\varphi}{k.s.\cos(\theta_s)}\right) \rightarrow \emptyset_b \cong \frac{-\Delta\varphi}{k.s.\cos(\theta_s)}.$$

The second step consists of trying to relate the previous expression to the two adjacent beams. For each beam, it is possible to write: $\emptyset_{b_1} \cong \frac{-\Delta\Phi_1}{k_1.s_1.\cos(\theta_{s_1})}$ and $\emptyset_{b_2} \cong \frac{-\Delta\Phi_2}{k_2.s_2.\cos(\theta_{s_2})}$. Before proceeding, a reservation must be made. To provide yaw stabilization, the swath is divided into sectors. Each sector uses a different frequency to avoid cross-detection. Thus, considerations involving adjacent beam analyzes cannot occur between different sectors. This subject is further detailed in section 3.3.1.2.1. Considering that the neighboring beams are within the same sector, they have the same frequency and, consequently, the same acoustic wave number ($k_1 = k_2$). At this point an assumption is made. Although the value of "s" is not known, it is expected that its value for two neighboring beams is very close. Thus, $s_1 \approx s_2$. Rewriting the equations, and isolating the value of $s_1$and s_2:

$$s_1 \cong \frac{-\Delta\Phi_1}{k_1.\emptyset_{b_1}.\cos(\theta_{s_1})} \approx s_2 \cong \frac{-\Delta\Phi_2}{k_2.\emptyset_{b_2}.\cos(\theta_{s_2})} \therefore$$

$$\frac{\Delta\Phi_1}{\emptyset_{b_1}.\cos(\theta_{s_1})} \approx \frac{\Delta\Phi_2}{\emptyset_{b_2}.\cos(\theta_{s_2})}$$

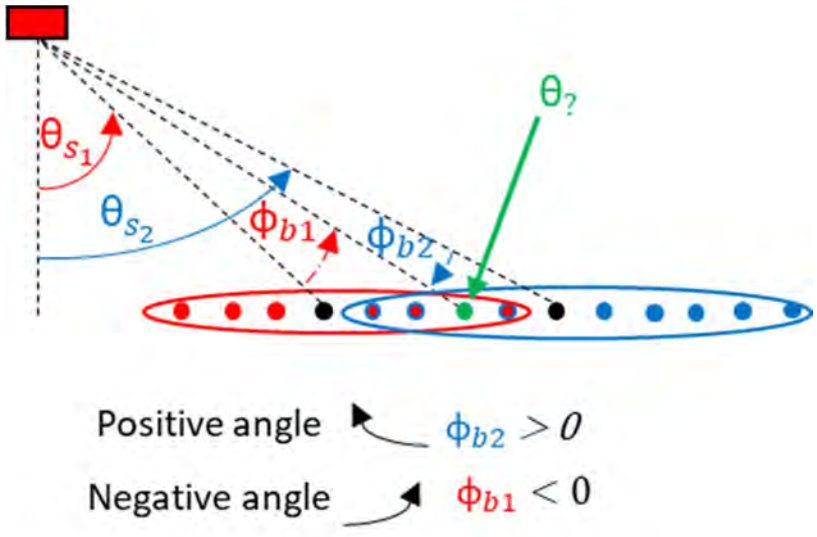

Figure 36 – Angles between two neighboring beams.

In the previous equation, the unknowns are $\emptyset_{b_1}$ and $\emptyset_{b_2}$. That is, there is an equation for two unknowns. Another relationship must be found so that the system can be resolved. Evaluating the angles involved (Figure 36), the following expressions are obtained: $\bar{\theta}_? = \bar{\theta}_{s_1} + \bar{\emptyset}_{b1}$ and $\bar{\theta}_? = \bar{\theta}_{s_2} + \bar{\emptyset}_{b2}$. In this way, a system with three equations and three unknowns was formed.

Solving the system:

$$\begin{cases} \theta_{s1} + \emptyset_{b1} = \theta_? \\ \theta_{s2} + \emptyset_{b2} = \theta_? \\ \dfrac{\Delta\Phi_1}{\emptyset_{b_1}.cos(\theta_{s_1})} = \dfrac{\Delta\Phi_2}{\emptyset_{b_2}.cos(\theta_{s_2})} \end{cases}$$

$$\theta_{s1} + \emptyset_{b1} = \theta_{s2} + \emptyset_{b2} \rightarrow \theta_{s1} - \theta_{s2} = \emptyset_{b2} - \emptyset_{b1}$$

$$\frac{\Delta\Phi_1.\sec\theta_{s_1}}{\emptyset_{b1}} = \frac{\Delta\Phi_2.\sec\theta_{s_2}}{\emptyset_{b2}} \rightarrow \frac{\Delta\Phi_2.\sec\theta_{s_2} - \Delta\Phi_1.\sec\theta_{s_1}}{\Delta\Phi_1.\sec\theta_{s_1}} = \frac{\emptyset_{b2} - \emptyset_{b1}}{\emptyset_{b1}}$$

$$\frac{\Delta\Phi_2.\sec\theta_{s_2} - \Delta\Phi_1.\sec\theta_{s_1}}{\Delta\Phi_1.\sec\theta_{s_1}} = \frac{\theta_{s1} - \theta_{s2}}{\emptyset_{b1}}$$

$$\emptyset_{b1} = (\theta_{s1} - \theta_{s2}).\left(\frac{\Delta\Phi_1.\sec\theta_{s_1}}{\Delta\Phi_2.\sec\theta_{s_2} - \Delta\Phi_1.\sec\theta_{s_1}}\right)$$

$$\theta_? = \theta_{s1} + \emptyset_{b1}$$

$$\theta_? = \theta_{s1} + (\theta_{s1} - \theta_{s2}).\left(\frac{\Delta\Phi_1.\sec\theta_{s_1}}{\Delta\Phi_2.\sec\theta_{s_2} - \Delta\Phi_1.\sec\theta_{s_1}}\right)$$

$$\theta_? = \theta_{s1}.\left(1 + \frac{\Delta\Phi_1.\sec\theta_{s_1}}{\Delta\Phi_2.\sec\theta_{s_2} - \Delta\Phi_1.\sec\theta_{s_1}}\right) - \theta_{s2}.\left(\frac{\Delta\Phi_1.\sec\theta_{s_1}}{\Delta\Phi_2.\sec\theta_{s_2} - \Delta\Phi_1.\sec\theta_{s_1}}\right)$$

And finally:

$$\theta_? = \theta_{s1}.\left(\frac{\Delta\Phi_2.\sec\theta_{s_2}}{\Delta\Phi_2.\sec\theta_{s_2} - \Delta\Phi_1.\sec\theta_{s_1}}\right) - \theta_{s2}.\left(\frac{\Delta\Phi_1.\sec\theta_{s_1}}{\Delta\Phi_2.\sec\theta_{s_2} - \Delta\Phi_1.\sec\theta_{s_1}}\right)$$

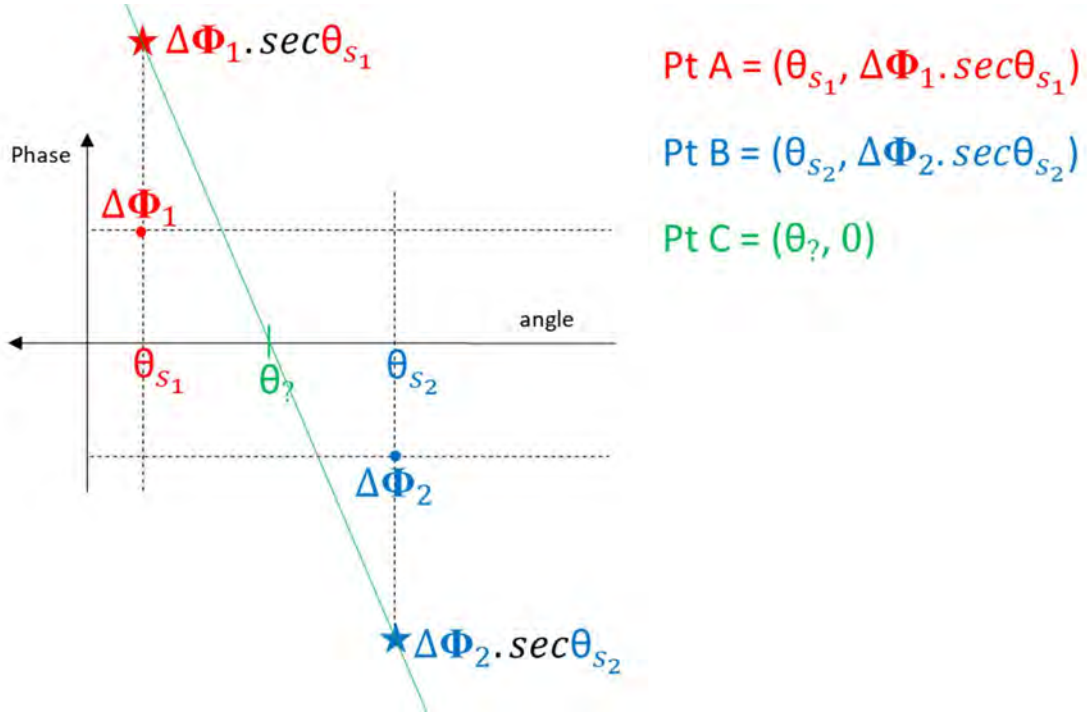

Figure 37 – Graphical representation of the system solution.

Figure 37 shows that the former expression graphically represents a line between points "A" and "B", at the point that it crosses the axis of the abscissa ("zero-cross"). Such proof can be carried out using the properties of the determinants.

Pt A = $(\theta_{s_1}, \Delta\Phi_1.\sec\theta_{s_1})$

Pt B = $(\theta_{s_2}, \Delta\Phi_2.\sec\theta_{s_2})$

Pt C = $(\theta_?, 0)$

$$\begin{vmatrix} \theta_{s_1} & \Delta\Phi_1.\sec\theta_{s_1} & 1 \\ \theta_{s_2} & \Delta\Phi_2.\sec\theta_{s_2} & 1 \\ \theta_? & 0 & 1 \end{vmatrix} = 0$$

$$\theta_{s_1}.\Delta\Phi_2.\sec\theta_{s_2} + \theta_?.\Delta\Phi_1.\sec\theta_{s_1} - \theta_?.\Delta\Phi_2.\sec\theta_{s_2} - \theta_{s_2}.\Delta\Phi_1.\sec\theta_{s_1} = 0$$

$$\theta_?.\left(\Delta\Phi_1.\sec\theta_{s_1} - \Delta\Phi_2.\sec\theta_{s_2}\right) = -\theta_{s_1}.\Delta\Phi_2.\sec\theta_{s_2} + \theta_{s_2}.\Delta\Phi_1.\sec\theta_{s_1}$$

$$\theta_? = -\frac{\theta_{s_1}.\Delta\Phi_2.\sec\theta_{s_2}}{\Delta\Phi_1.\sec\theta_{s_1} - \Delta\Phi_2.\sec\theta_{s_2}} + \frac{\theta_{s_2}.\Delta\Phi_1.\sec\theta_{s_1}}{\Delta\Phi_1.\sec\theta_{s_1} - \Delta\Phi_2.\sec\theta_{s_2}}$$

$$\theta_? = -\theta_{s1}.\left(\frac{\Delta\Phi_2.\sec\theta_{s_2}}{\Delta\Phi_1.\sec\theta_{s_1} - \Delta\Phi_2.\sec\theta_{s_2}}\right) + \theta_{s2}.\left(\frac{\Delta\Phi_1.\sec\theta_{s_1}}{\Delta\Phi_1.\sec\theta_{s_1} - \Delta\Phi_2.\sec\theta_{s_2}}\right)$$

Which leads to exactly the same expression as the previous one:

$$\theta_? = \theta_{s1}.\left(\frac{\Delta\Phi_2.\sec\theta_{s_2}}{\Delta\Phi_2.\sec\theta_{s_2} - \Delta\Phi_1.\sec\theta_{s_1}}\right) - \theta_{s2}.\left(\frac{\Delta\Phi_1.\sec\theta_{s_1}}{\Delta\Phi_2.\sec\theta_{s_2} - \Delta\Phi_1.\sec\theta_{s_1}}\right)$$

This expression shows that, using only the initial data available, it is possible to obtain an estimated value of the direction of the desired scatterer point by interpolating a line between the points neighboring zero-crossing.

3.3 – Algorithm

An algorithm was created in the MATLAB environment to determine the time-angle pairs for each swath using the PDI method (Figure 38). For this, the following steps are necessary:

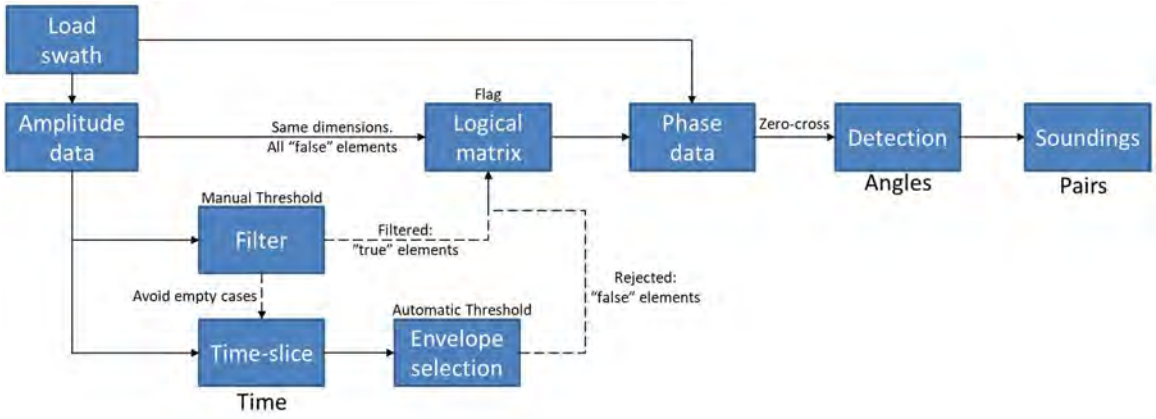

Figure 38 – PDI algorithm overview.

- Load the amplitude and phase data from the water column of the selected swath.

- Create a logical matrix (“true” or “false” elements) with the same dimensions as the amplitude data matrix (whose dimensions are identical to the phase data matrix) and all values set to “false”. This matrix will be used as a flag to indicate the phase elements to be considered.

- Set an initial threshold (“manual threshold”) for the entire swath and use it as a filter in the amplitude data. The logical matrix will become "true" in the elements corresponding to the amplitude values greater than or equal to this threshold. Smaller values will remain "false".
- Sweep all time-slices and for each one of them:
- Define a dynamic threshold (“automatic threshold”) that allows selecting the envelopes that have the highest amplitudes compared to their neighbors. The elements rejected in this process will have a false value in the logical matrix.
- Apply the logical matrix to the phase data, to keep only the information for the selected envelopes.
- Obtain, in each selected envelope, the beam before and after zero-crossing (across-beams).
- Use the expression presented in the previous section to calculate the angle of the scatterer point.
- Save the time-angles pairs obtained.

It is important to note that the initial threshold filter and the subsequent automatic envelope selection are two independent processes and both exist to update the logical matrix. As will be seen in the automatic threshold section, it is necessary to use all the data available in the time-slice to calculate averages and determine maximum or minimum values. Thus, the initial data for performing the envelope selection are those coming from the amplitude data and not those resulting from the initial threshold filter. The only interaction between these two processes occurs when it is found that a time-slice has had all its data rejected by the initial threshold. In this case, for this time-slice, the selection envelope is not performed to save processing time. Another important point to note is that this algorithm does not limit the number of solutions per time-slice. Assuming a flat seabed it would be reasonable to conclude that only two solutions (one for port and one for starboard) are necessary. However, the present study, in which high-aspect geometries

were deliberately investigated, chose not to make any assumptions about the seabed, allowing any number of envelopes selected by the process to be considered.

3.3.1 - The need for thresholds

The use of thresholds is necessary in both direction and time-based methods, as ultimately one wishes to isolate echoes levels that are likely to come from main-lobe seabed interactions, rather than sidelobe seabed interactions or noise in the water column or after the seabed echo. Those thresholded data ultimately define the envelopes that contain, in a time-series, the time-range used for the amplitude or phase detections or, in a beam-series, the angle-range for application of BDI or PDI. However, time-based methods, when compared to direction-based methods, are more dependent on this choice of a threshold as, for a given direction, the seabed is always expected to arrive, whereas, for a given time, there may be no seabed in view.

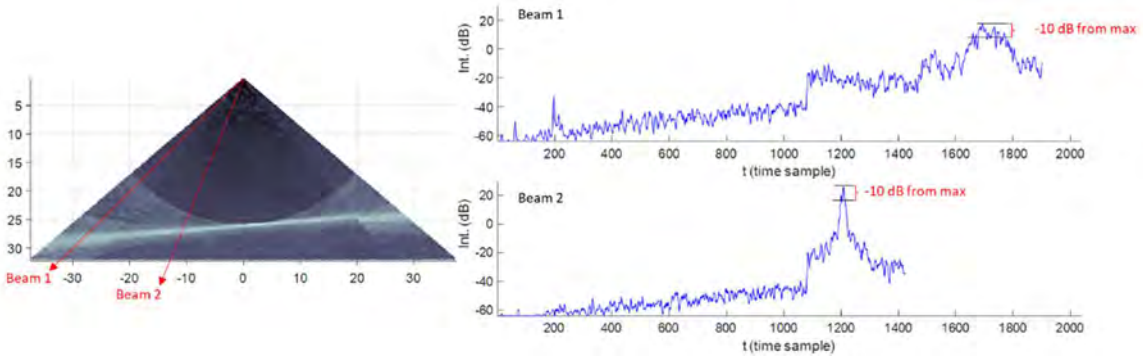

Figure 39 - Threshold of -10dB from maximum value applied in two beams.

In the case of direction-based methods, as long as reasonable TVG is applied (section 2.6), it is possible to define one threshold for each physical beam (typically, hundreds of beam) as a fixed value offset to be applied at the maximum amplitude value (usually after using a moving time-average). The same single fixed offset value (for example -3dB or -10dB from maximum value) can be used for all beams (Figure 39), so that a reasonable estimate of the beam footprint

trace is preserved. This simple step guarantees that the data analyzed to generate an envelope are among those of the highest amplitudes and, consequently, it might contain the desired time-angle pair (sounding).

Considering Figure 39, under the eyes of physical beams, each one of the hundreds of directions (represented by beams 1 and 2) will interact with the seabed at some point. In this way, their respective time-series will present amplitude data with low values while moving purely through the water column and will present high values when they start to interact with the seabed. In other words, within a time-series it is always possible to define an envelope that corresponds to this interaction. Due to this characteristic, the use of a threshold based on a fixed offset value (-10dB in this case) below the maximum value would limit a time-range corresponding to the interaction with the seabed, creating a valid envelope to be analyzed.

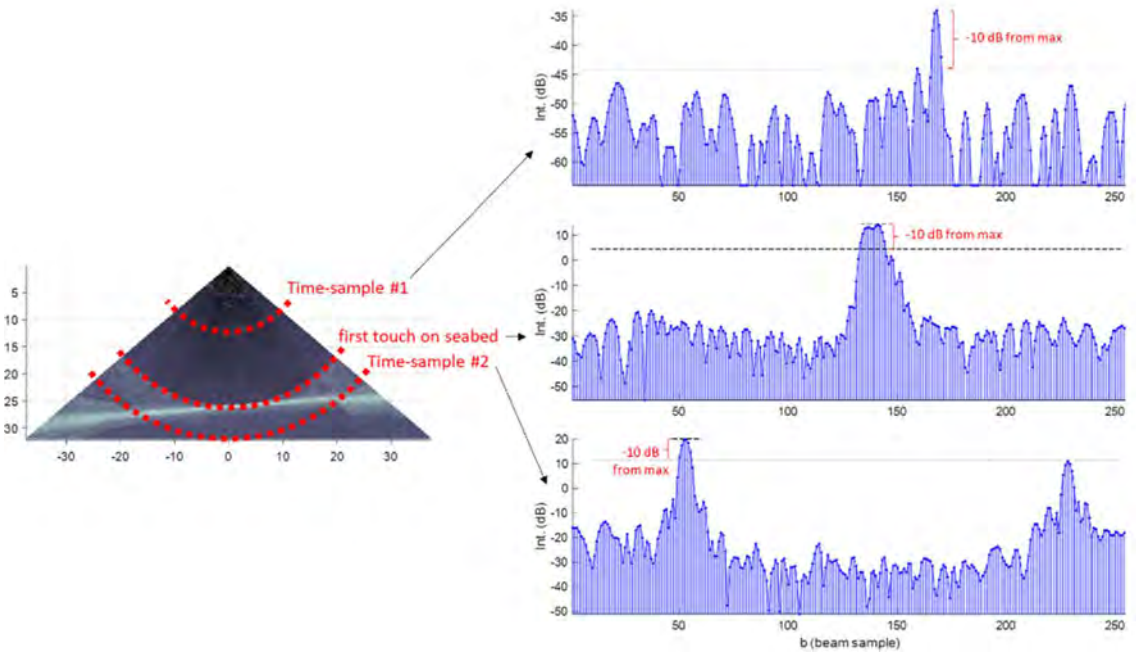

Figure 40 – Three time-slices using a fixed threshold offset from maximum amplitude value. Note that all cases generated an echo envelope (above the threshold line). However, each case should receive different treatment. Time-sample 1 should be rejected, due to the absence of a target. The echo envelope of the first touch was correctly identified. And time-sample 2 should use a higher offset value to include the second maximum peak, as this case finds the seabed in two directions.

For the case of time-based methods, it is also necessary to define one threshold for each time-sample, which now represents an order of magnitude of thousands of samples (compared to a few hundred for direction-based methods). However, the use of just a fixed offset relative to the maximum amplitude value (as done in the previous case) does not ensure that the selected data actually forms a reliable envelope for obtaining a time-angle pair, as exemplified in Figure 40.

From the point of view of time-slices, where a seafloor or target echo is not guaranteed to be contained within every time-slice, there is not always a direct relationship between the variation in amplitude across-beams and the detection of seabed or a target. It is only after the first touch that the time-slice begins to interact with the seabed. In this way, all previous time-slices will not bring any valid sounding information, and these entire time-slices should be disregarded. From the first-touch each time-slice starts to contain data about the interaction with the seabed, which can occur in one or more directions. Note, however, that the envelopes to be analyzed are those whose peaks stand out from the rest of the time-slice peaks. Again, the definition of a single fixed offset value from the maximum to be applied to all time slices does not bring the best result, as it is necessary to take into account relationships between the different peaks of each time-slice. The definition of this threshold needs to take into account the unique variation that each time-slice presents, that is, it is necessary to create a dynamic threshold.

Pereira and Hughes Clarke (2015) solved this dynamic threshold problem by creating an "automatic threshold" (see section 3.3.1.2). One of the imperfections resulting from its application is the existence of several spikes from time-slices prior to the first-touch. However, the objective of that study was to use the BDI to assess target detection only at low grazing angles and, due to this, the region close to the first touch (minimum slant range) was out of their scope. Thus, before using their automatic threshold, they applied a filter that considered only time-slices after the first

touch, even in the presence of strong echoes. Using these criteria, they managed to remove many spikes, however, mast-like objects could also be disregarded. Depending on the application and purpose of the research, this possibility may be acceptable.

As the present study does not aim to be limited to low grazing angles and aims to see the performance of the PDI method even on suspended objects, a different filter must be applied to avoid the exclusion of real soundings that may occur before the first-touch on the seafloor. Thus, the problem of choosing thresholds in time-slices was approached in two ways: a dynamic threshold, adapted from the automatic threshold of Pereira and Hughes Clarke (2015), was used to deal with the selection of envelopes where the PDI will be applied and to reject data when necessary. Prior to it, in order to reduce the spikes that result from that filter, an initial threshold, referred to as the "Manual Threshold", was used to remove part of the data before the first touch, while maintaining strong echoes. Each one of these two distinct thresholds is detailed in the next sections.

3.3.1.1 – Manual Threshold (initial threshold filter)

There are at least two ways to reject data from time-slices prior to the first interaction with the seabed: consider only time-slices after the first touch or set a threshold value in such a way that all data (or most of them) representing only the time period passing through the water column are ignored.

The first case is the most logical and is probably used as the first option in developing algorithms. However, a very sensitive detail is hidden in this logic: the criteria used to find the first touch are based on the first interaction with the seabed. This is very useful, as it ignores any gas

bubbles or fish that are in the water column (see Figure 41). For disregarding all data prior to the first-touch any possible object such as the top of a mast can be filtered out.

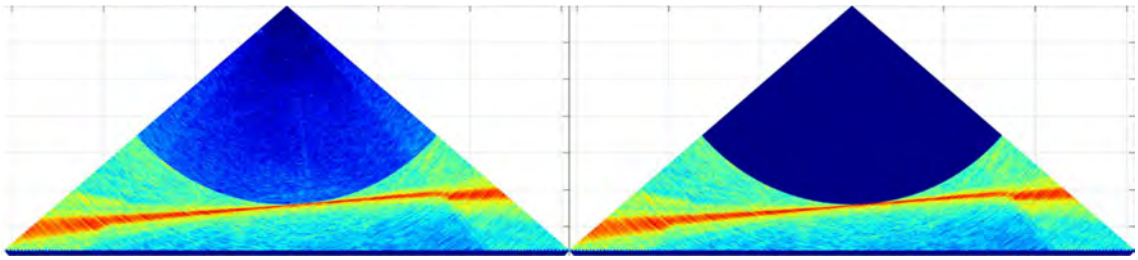

Figure 41 – The use of the minimum slant-range as a cutoff. On the left, the complete swath (amplitude). On the right, all time slices prior to the first touch were rejected.

The second case, which may be more permissive or restrictive than the first, aims to define a minimum threshold value. All values below it is ignored (in the entire swath, not just before the first touch) and only values equal to or greater are analyzed. The challenge then becomes finding an appropriate value to use. Very low values would keep much of the noise and spurious data, and the use of the filter is of little benefit. Very high values would maintain only the highest contrast returns from acoustic impedances and could remove real soundings.

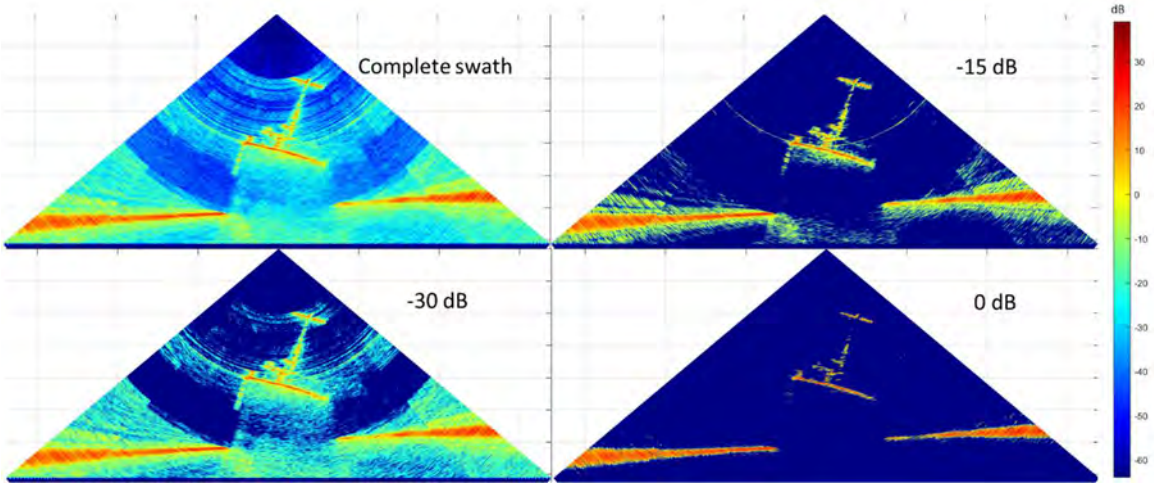

Figure 42 – The use of a threshold to filter the amplitude data.

Considering Figure 42, on left-top the complete swath (amplitude data), which has an offset of -30dB, is presented. On left-bottom it shows a threshold of -30dB. Note that much of the noise and spurious data remains. On the right-top image, all values below -15dB have been rejected. In this situation, the most important features of this swath are already more clearly defined, although spurious data still exists. On right-bottom, a high threshold is applied. The regions that correspond to the seabed and shipwreck are well defined, but part of the mast is already starting to be lost. This gradual sequence exemplifies the difficulty in choosing this threshold, which must be neither too low nor too high. In this context, it is clear that the ideal value of this threshold ends up demanding user experience, which is very undesirable, since an ideal algorithm is one that depends less on user interference to generate the best result.

Note that whatever the level chosen, as it is applied independent of range (whole swath), it is presupposed that the manufacturer has applied a reasonably appropriate TVG so that equivalent bottom backscatter strength echoes are about the same irrespective of range. For the case of the system used (EM2040P) a TVG is already built in (as discussed in section 2.6).

Since the current objective is to show the detection potential with the use of PDI, the use of high thresholds will be avoided, trying not to exclude real soundings. On the other hand, by using more permissive values, the appearance of several undesirable spikes in the solutions of each evaluated swath is expected. Because, however, following the initial manual thresholding, there is also a subsequent automatic threshold for each time-slice, it is expected that such occurrence of spikes will be reduced. Thus, although the user can override defaults and indicate the value of the manual threshold if they wish, two alternatives are presented, aiming to reduce the need for an experienced user:

- Use of the 90th percentile of the swath amplitude data.

- Use of the lowest amplitude value associated with a detection performed by direction-based methods, considering all beams.

The choice of using the 90th percentile occurred after evaluating some data and started with the search for a value that could decrease the chances of excluding real soundings and that could be obtained independently of other detection methods, even if this represented an increase in spikes. Current multibeam models have hundreds of beams and have a sample rate so high that thousands of time samples are common. By forming a matrix whose columns have the data for each beam and the rows contain each time-sample, the number of elements would be over one hundred thousand. Among all these elements, probably less than a thousand would be needed to represent the detections in this swath (1% of all data). However, due to the possibility of the highest values being concentrated in the nadir region or the existence of multiple echoes, the number of elements to be analyzed was increased by an order of magnitude (from 1% to 10%), considering those of greater intensity (10% top). Thus, the 90th percentile was reached on the amplitude data.

The second way to obtain a manual threshold is based on the concept of complementary use between the various methods. Since, by using conventional direction-based amplitude or phase detection, soundings can be obtained for each beam and it is possible to verify the intensity value, in dB, recorded for each one, it is reasonable to use the minimum amplitude value among all the beam detections as a manual threshold, as this would ensure in advance that pairs accepted by direction-based methods would not be excluded by the misuse of a high manual threshold value.

Once the value to be used is defined, all the amplitude data are compared with it. When an element is greater than or equal to it, a positive flag is registered in the logical matrix, in order to be applied in the phase data, after the automatic threshold step (next section).

3.3.1.2 – Automatic Threshold (envelope selection)

As seen as part of the previous initial filter step, those elements whose amplitudes are less than the value established for the manual threshold receive a rejection flag registered in the logical matrix. Such a comparison is made across the entire swath, independently of the beam or time-slice to which the element belongs. When observing a single time-slice, however, it is noted that this criterion presented is not sufficient to restrict the data in envelopes to be analyzed, within which the angles that would form the time-angle pair would be sought. Each time-slice presents a different combination of amplitude data recorded in each beam and the directions sought in them must be those with the highest amplitudes when compared to the amplitudes of the other beams. In other words, it is necessary to relativize the amplitudes and adopt cut-off values based on each time-slice data. Consequently, a dynamic and automatic threshold change is required.

To illustrate the problem, consider the two example cases presented in Figure 43. Each plot represents a different time-slice from the same swath. In both, the amplitude data recorded in each beam is represented by the color blue. The horizontal black dashed line indicates the manual threshold utilized in the first filter. The same fixed value (in this case, -10dB) is applied throughout the swath. Values above this threshold are highlighted by red circles. Considering these data in red, note that the use of this manual threshold is not sufficient to adequately limit those envelope(s) that are suitable to have their phase data analyzed. In both images, more than ten peaks are highlighted. Considering all of them would result in erroneous soundings. In order to identify whether is a useful subset within this time-slice where valid phase will be analyzed, another filter step is required, which utilizes a variable value based on instantaneous amplitude distribution.

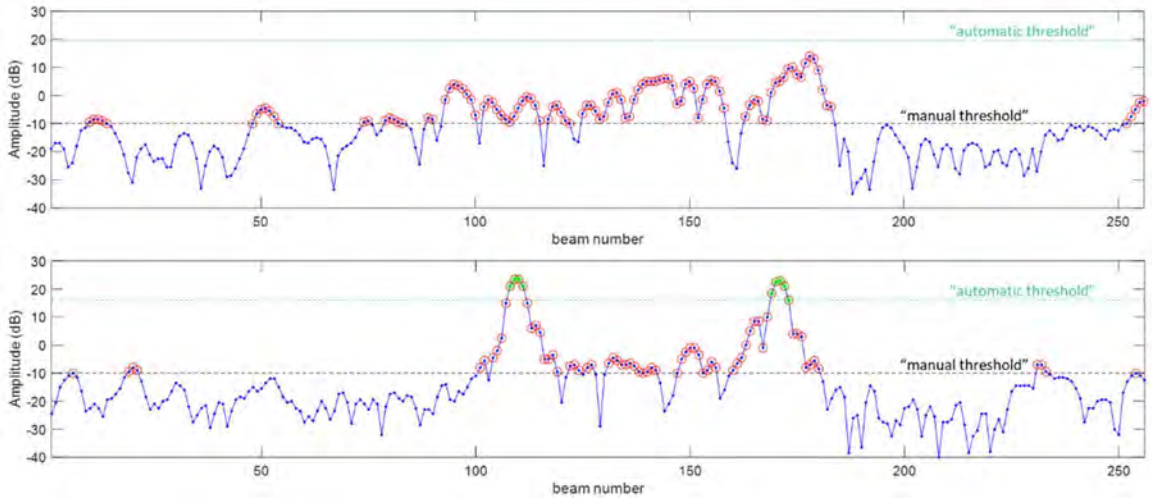

Figure 43 – Threshold in time-slices. Top) all data rejected. Bottom) two echo envelopes accepted by the automatic threshold.

A very insightful solution was proposed by Pereira (2015) which has been adopted in this study. Continuing with the example of Figure 43-top, note that the time-slice has peaks whose amplitudes have very similar values. As a result, it is not possible to emphasize any of them in specific to estimate an angle to form a sounding. For this time-slice, the ideal would be to disregard all peaks. This could be achieved with a threshold value (horizontal green dashed line) higher than all data for this time. Figure 43-bottom, in contrast, presents a completely different situation. In it, clearly two peaks stand out before all the others. To separate these two cases, an algorithm is needed that examines the distribution of candidate peaks, and identify whether one or more stand out from the average. Such an algorithm would be capable of setting a threshold capable of limiting the envelopes to only these two peaks, as shown in the figure by data above green dashed line (green asterisks). The retained envelopes would then be generated for the region(s) containing the data that remained after both filters, manual and automatic threshold.

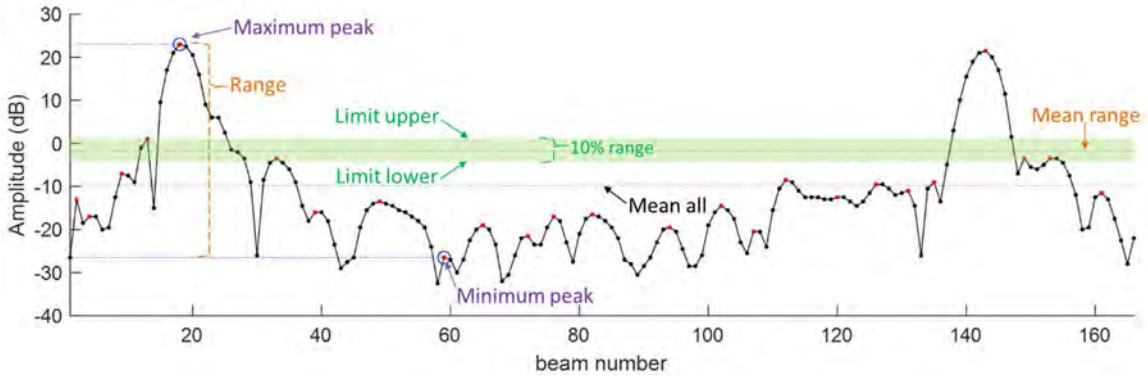

Figure 44 – Automatic threshold main variables (after Pereira, 2015).

In order to distinguish the two cases, Pereira (2015) proposed the creation of the following aid variables, highlighted in Figure 44, having each sector evaluated independently, for each time-slice:

- Maximum peak: Highest peak found in the sector under analysis.

- Minimum peak: Lowest peak found in the sector. Note that this is not the lowest value, but the lowest peak.

- Mean all: Average of all peaks in the sector. Again, note that this is not the average of all data, but of all peaks.

- Range: range between the maximum and minimum peak.

- Mean range: Midpoint between the maximum peak and the minimum peak. It represents how much the data in this sector varies.

- Limit lower and Limit upper - Centered on the "mean range", a window of 10% of the "range" is generated. 5% below the mean range defines the lower limit and 5% above the mean range defines the upper limit.

Note that all these statistics are performed in logarithmic (dB) space.

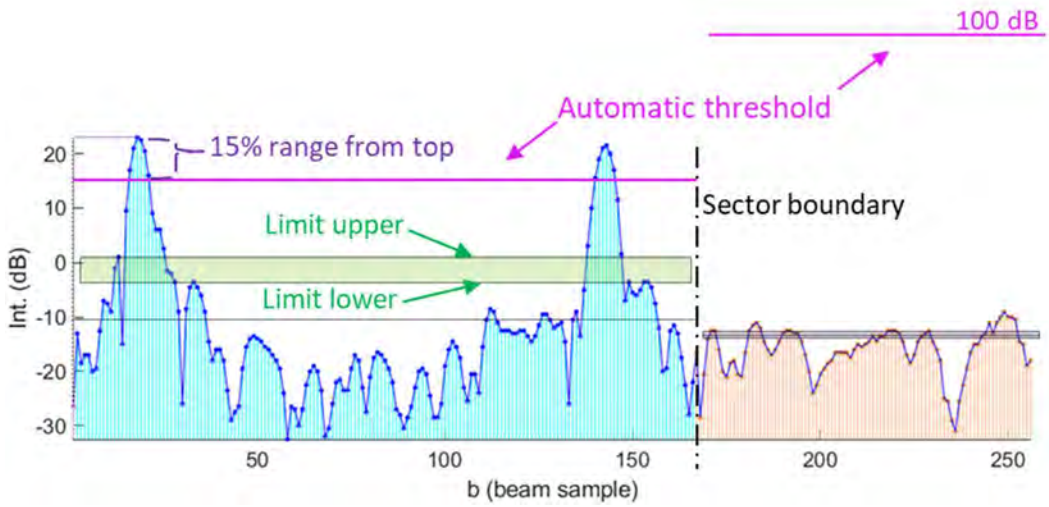

Figure 45 – Automatic threshold cases.

Once these variables are defined, the mean all value is compared to the demarcated limits and can be outside or within the limits. When it is within the limits, the mean all has a value close to the mean range. Thus, it is assumed that all the peaks are similar, with no peak that stands out. In this case, the automatic threshold is set to a very high value (100 dB) and the entire time-slice is rejected. This was found to be a useful solution for ignoring some random data from the water column. This procedure, however, also limits the detection in the nadir region, when several central beams are received at almost the same time (similar peaks). On the other hand, when it is outside the limits, the distance between mean all and mean range must occur due to the existence of some peaks that stand out from the others. A cutoff value of 15% range below the maximum peak is defined and all solutions above this cutoff are accepted for use in BDI or PDI. The others are rejected. Figure 45 exemplifies these two cases. The blue sector has mean all outside the defined limits and, therefore, has its threshold set to 15% of the range below the maximum peak. With that, two envelopes are generated for analysis of the phase data. The red sector shows the mean all within the limits and therefore must be rejected. Its threshold is then set to 100 dB and no envelope is analyzed.

Note that the values of 10% of the range for the limit window and 15% of the range for the cutoff from top are arbitrary. The change in their values causes changes in results. In the case of the limit window, a percentage greater than 10% would increase the number of rejected cases, losing real soundings. A smaller one would increase tolerance and could include more false detections. The opposite situation would occur with the cutoff from top percentage. Values greater than 15% would increase the amount of data accepted, including false detections. Lower percentages would limit the solutions to just the highest peak, rejecting others possible soundings. The values of 10% and 15% remained in use because they were those that allowed good results in the tests conducted by Pereira (2015) and for presenting similar results in the tests conducted in the present study. However, without a doubt, it is a section that deserves attention to be improved in future works.

3.3.1.2.1 – Dealing with different sectors

As stated before, each sector has so far been treated independently, having its own variables, averages and limits. Within a single sector all the beam footprints are adjacent and slightly overlapping. A multi-sector system (with specific system considered, EM2040P) has each sector steered independently fore-aft and thus, at the sector boundary, the adjacent edge beams are not normally examining the same point on the seafloor and thus cannot be used to corroborate each other.

As a result, the PDI method cannot be applied between sector boundaries because each sector has its own frequency (thereby potentially wavelength spacing between subarrays) and its own transmit steering angle. As pointed out by Pereira (2015), adjacent beams belonging to two different sectors can refer to two completely different locations on the seabed. Figure 46, in which

a swath composed of three sectors is represented by the red line (right), exemplifies this situation. Zoom (left) is done on both sectors' boundaries. In each case, the beam footprints on either side of the boundary sector are shown in yellow. Note their abrupt offset.

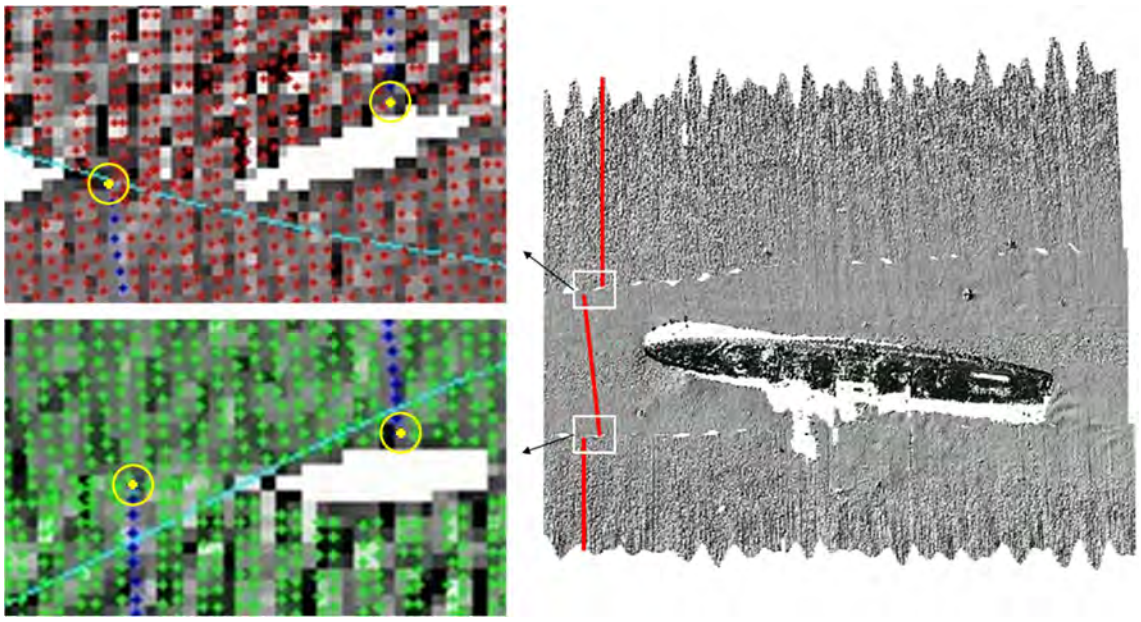

Figure 46 – Sectors with non-adjacent seabed locations.

An additional complication, however, results from limiting the second step threshold filter to a single sector During tests of this algorithm, some solutions clearly identifiable as spikes were being found. See Figure 47-a, which represents the amplitude data of a swath divided into two sectors, whose contrast has been highlighted. A time-slice (white dotted line) is performed and the procedure for calculating the automatic threshold in each sector is performed. Note that in the nadir sector at least one detection must occur. In the same way, in the external sector, as no main lobe interaction with the seabed has yet occurred, no detection is expected. Its occurrence would be indicative of spike.

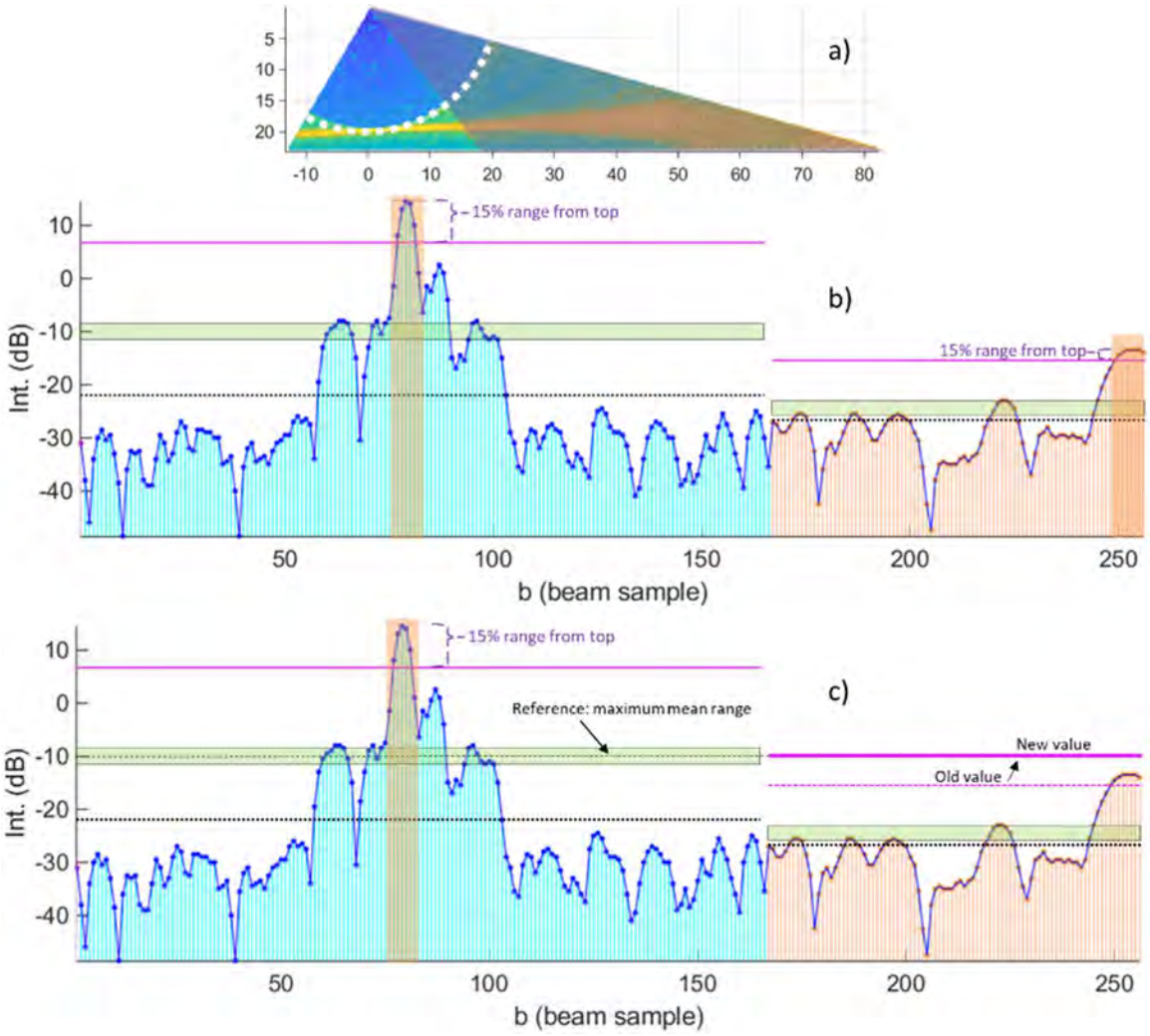

Figure 47 – Additional step in automatic threshold calculation.

The beam-series of the time-slice under analysis is shown in Figure 47-b. The automatic threshold result for the nadir sector (blue) is, as expected, generating a single envelope (highlighted in orange) where a sounding will be obtained. However, the external sector (red) has a problem. The configuration of its data causes the mean all (black dotted line) to be outside the limits (green box) and, consequently, an envelope is erroneously generated. Although no detection was expected, a spike will be registered, due to the automatic threshold not recognizing that all these amplitude data must come from side-lobes of this sector interacting in the nadir region. The false detection occurred because the amplitude data in that sector had a slightly higher peak than the

others and the comparisons between mean all and the window of limits did not allow it to be ignored.

In order to avoid the occurrence of these false detections, even though final detections can only be based on phase within a single sector, to derive valid statistics it is necessary to observe the entire time-slice, including all sectors, to conclude which sector is dealing with main lobes and which contains only sidelobes. Consequently, sectors had to stop being considered as a completely independent dataset. Thus, an additional step was included in the automatic threshold developed by Pereira (2015). After defining all the variables for each sector and calculating each automatic threshold, a final check is made. The mean range values for all sectors are compared and the largest of them is used as a reference for the minimum tolerable automatic threshold value. Thus, if any sector has an automatic threshold lower than the reference mean range, it is replaced by this value. Note that to be justified in comparing different sectors to obtain a common reference, it is assumed that the data from each sector are reasonably balanced. Complications could occur where inter-sector source level and beam pattern differences are not adequately accounted for.

Figure 47-c indicates this modification. No changes occur in the blue sector, as its automatic threshold is greater than the reference. In the red sector, the automatic threshold ("old value") is smaller than the reference. As a result, the automatic threshold is changed to the reference value ("new value") and, as a consequence, all values are rejected preventing the appearance of a spike. If the maximum peak of the red sector was greater than the reference, it would have amplitude values comparable to the main lobes of the blue sector and its envelope would continue to be considered, as it is now assumed to be an acceptable solution.

3.4 – The data gaps problem

It is important to note that the current approach to recording water column data (both amplitude and phase) presents a special problem. The amplitude data already has the characteristic of being very large. When comparing files containing water column data with files without this data, the former takes up almost 10 times more disk space than all the rest of the datagrams combined. This situation becomes more sensitive when the phase recording is enabled. Based on the Kmall format (rev F), depending on the selected resolution, the phase data can occupy either the same disk size as the amplitude data (low-resolution case) or can occupy twice that size (high-resolution case). Thus, such data can potentially take up to 30 times more disk space.

In order to keep the files from getting even bigger, manufacturers usually save data only up to a few samples after the time-sample identified as the trailing edge of the bottom detection envelope. All subsequent data are not recorded. The wider the swath, the more data is erased. Figure 48 shows a swath whose angular opening is 30 degrees for port and 75 degrees for starboard. In this case, it is estimated that about 65% of the data has been deleted.

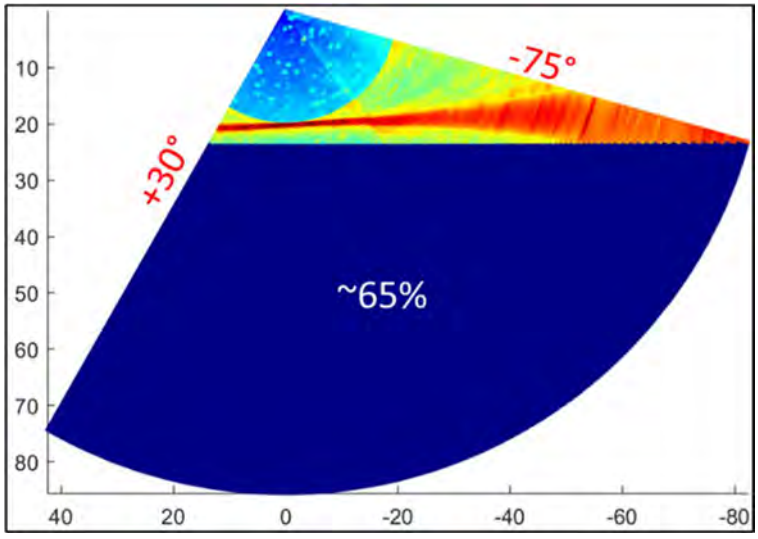

Figure 48 – Gaps (dark blue) after detection of the seabed.

In general, for the conventional within-beam methods, this exclusion is not a problem. Considering that the focus is on bathymetry, in which the information below the seabed is not relevant, or that the frequencies used do not penetrate it, this is a wise decision. For direction-based methods, time-series analysis remains possible and does not change with this exclusion: the envelope for seabed detection is included; the previous data exists and can be used to obtain extra-detections or to generate water-column imagery; and subsequent data is unnecessary (bathymetric point of view) and ignored.

The problem arises, however, when time-based methods are used. The region corresponding to the shortest distance between the seabed and the transducer (usually in the vicinity of the nadir) will find the bottom first and, after a few samples, it will stop recording data. Subsequent time-slices will now contain gaps that will gradually increase. In other words, after the first detection, the existence of gaps starts to affect the derived statistics utilized in the performance of time-based methods.

It is known that the data corresponding to the interaction with the seabed at that moment will still be present in the time-slice. Therefore, the envelope to be analyzed to define the direction of the scatterer point remains available. The problem lies in the identification of the envelopes to be analyzed (envelope selection), due to the characteristics of the automatic threshold (previous section). The current algorithm uses the information of maximum peak, minimum peak, average of peaks and peak-range to establish the criteria for selection or rejection of envelopes within a time-slice. Although there is no doubt that the maximum peaks will continue to be present, the existing gap will obviously be excluding some peaks from the process. This, in itself, affects the average peak. There is also a chance that the minimum peak would be present in the gap region. Therefore, the minimum peak information would be affected (the next data with the lowest

available peak value would be used) and, consequently, the peak-range would also be affected (as it needs the maximum and minimum peak values to be defined). As a conclusion, the presence of gaps affects the automatic threshold.

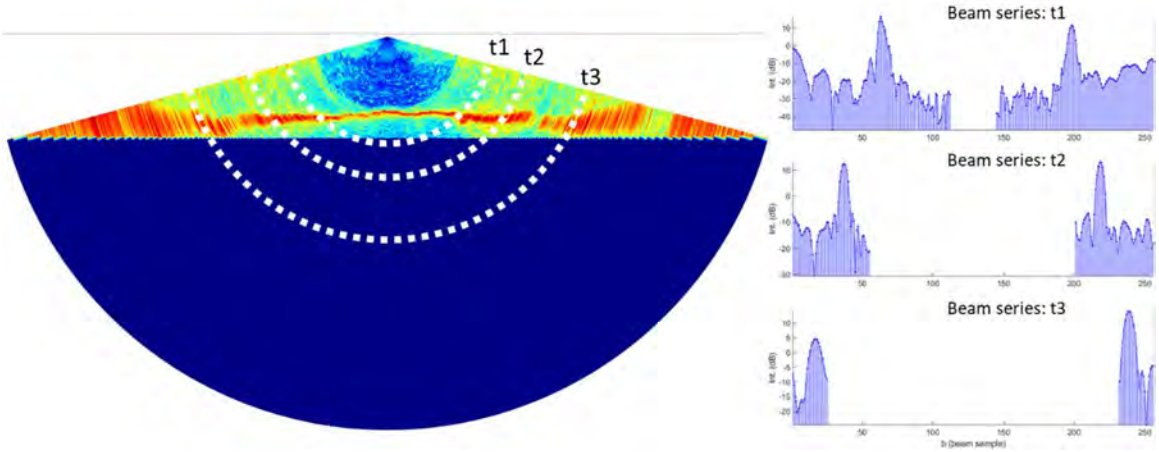

Figure 49 – The impact of gaps on time-slices.

The issue is illustrated in Figure 49. On the left, three time-slices (t1, t2 and t3) are represented in a white dotted line. On the right are their respective beam-series. Observe the gradual increase in gaps as time increases (from time t1 to t3). Although the maximum peaks continue to indicate the main directions (envelopes to be analyzed), the reduction in the amount of available data makes it increasingly difficult to have sufficient statistics to properly define the automatic threshold for selecting envelopes.

Note that this automatic threshold limitation is not associated with a problem with the present algorithm. It is related to the decision of the manufacturers to exclude data hitherto considered unnecessary. In the presence of complete data, nothing would change and it would not be necessary to create special cases. In addition, it would be interesting for manufacturers to allow operators to choose whether they would like to keep or delete these data.

In order not to abort the automatic threshold calculation in the presence of gaps, two special cases have been created. One deals with gaps in the middle of a sector and the other deals with the case where the gap is so big that there are not enough peaks to assess whether the remaining peaks should be considered or rejected. This second case was also a problem found and circumvented in Pereira (2015).

3.4.1 – A gap in the middle of one sector

Observe the case presented in Figure 50. On the top (a), a swath with an angular aperture of +30 degrees (port) and +75 degrees (starboard) is displayed. A time-slice represented by the white dashed line contains information about interaction with the seabed in two directions, whose angles are +27 degrees and -33 degrees (respectively in the vicinity of beams number 7 and 155). Figure 50-b shows the beam-series for this time-slice. The data, without distinction of sectors at this moment, are presented in hatched dark blue, emphasizing the gap that exists between beams 57 and 91 (from -7 to +7 degrees). Figure 50-c shows the same information as before, but differentiates the two existing sectors by colors (light blue and light red). For each sector, the automatic threshold will be calculated. The sector in red does not have a peak that stands out before the others, having only peaks of similar amplitudes. Thus, it will be rejected and no pair will be obtained in this time-slice for this sector. In turn, the sector in blue clearly has two peaks that stand out and a gap. When calculating the automatic threshold for this data set, the value obtained is that one indicated by the horizontal line in red. Due to the gap, this value may be biased upwards. As a result, although it was expected that two envelopes would be selected, only one of them was selected (only one peak above the red line). The second envelope was below the automatic threshold and has been rejected.

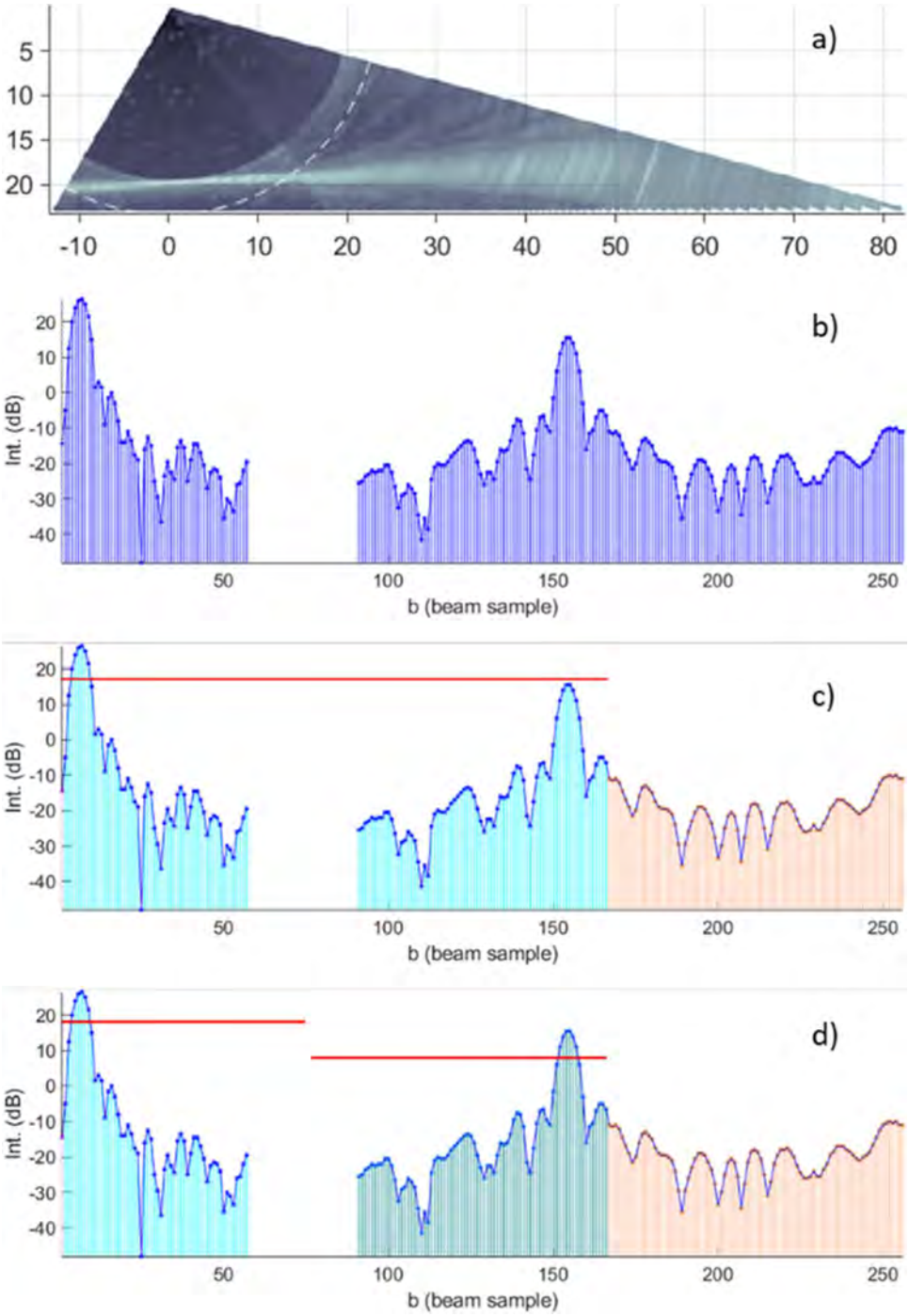

Figure 50 – A gap in the middle of one sector.

To reduce the impact (non-detection) of the gap in this situation, the algorithm was set to automatically divide the sector into two when it find gaps in its middle (the user can modify it if required). Figure 50-d shows this division. The section before the gap remains as before,

maintaining the light blue hatch color. The data after the gap are considered to belong to a new (virtual) sector and are presented in green. When considered as from different sectors, the algorithm stops using a single automatic threshold for them and starts calculating a value for each one (two red horizontal lines). Once inside the blue and green sectors, peaks that stand out above the others are found, two envelopes are selected and two time-angle pairs (as initially expected) are obtained in this time-slice.

Note that the solution presented is not the only possible one. Another possibility would be to limit it to a single envelope whenever a gap is found in the sector, ensuring that the most intense interaction is captured. Although registering a single pair is still better than aborting the process, this limitation runs counter to one of the objectives of this study. As seen in the section that details the manual threshold, it is intended that each time-slice has as many pairs as possible, being preferable to obtain spikes rather than excluding real soundings.

3.4.2 – A gap that leaves fewer than 3 peaks in one sector

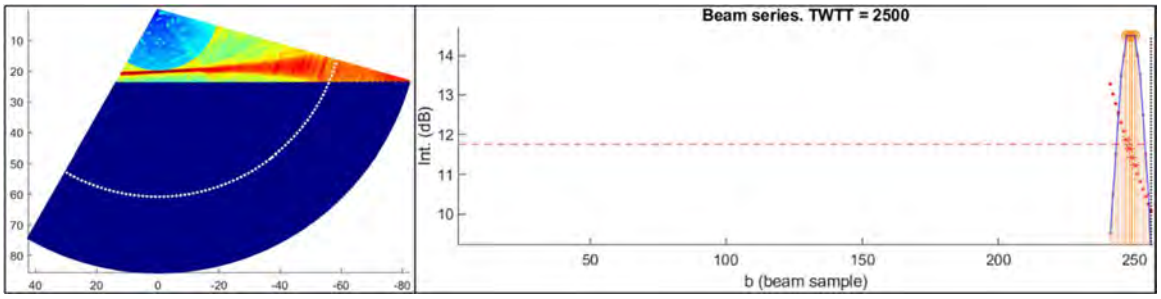

Figure 51 – A gap that leaves fewer than 3 peaks in one sector.

This second special case seeks to reduce the problem that arises when the gap is so large that there are fewer than three peaks left for analysis of envelopes to be selected or rejected (Figure 51). Recalling that the automatic threshold, in superficial analysis, results from comparisons between the mean of all peaks and the mean range, and that the latter is given by the average

between the maximum and minimum peak values, when there are only two or one peaks, mean all and mean range are always the same. According to current criteria, this would always result in rejection of the envelopes. In other words, the outermost angles of the swath would be rejected and no solution would be presented due to gaps.

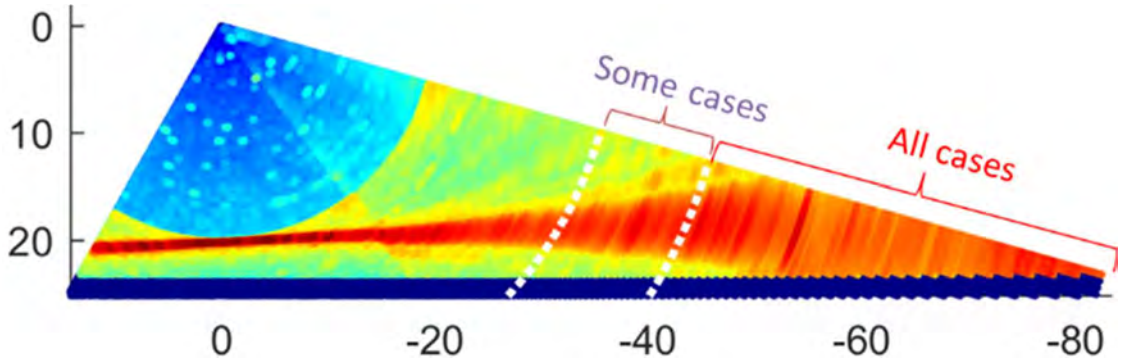

Figure 52 - Existence of fewer than 3 peaks.

To have a rough idea of how this can affect solutions in time-based methods, see Figure 52. In it, two time-slices are represented by white dotted lines. The first defines the first occurrence of fewer than 3 peaks. From this moment on, such gaps start to affect the solutions. The second indicates the instant after which there will always be fewer than 3 peaks. From it, the gaps compromise all subsequent solutions. Pereira (2015) worked around this problem using the last valid threshold as a reference for time-slices in which it would not be possible to calculate the automatic threshold. A similar solution, with modifications, was implemented in this study to try to get as close as possible to the end of the swath. The steps implemented were as follows:

- Select a time-slice, separating the data by sectors.

- In each sector, check the number of existing peaks.

- If there are 3 or more peaks, apply the automatic threshold as previously defined and record its value in the variable (vector) "last threshold".

- If there are fewer than 3 peaks, select the highest peak value and compare it with the average of the last 20 available last threshold values, accepting it if it is higher.

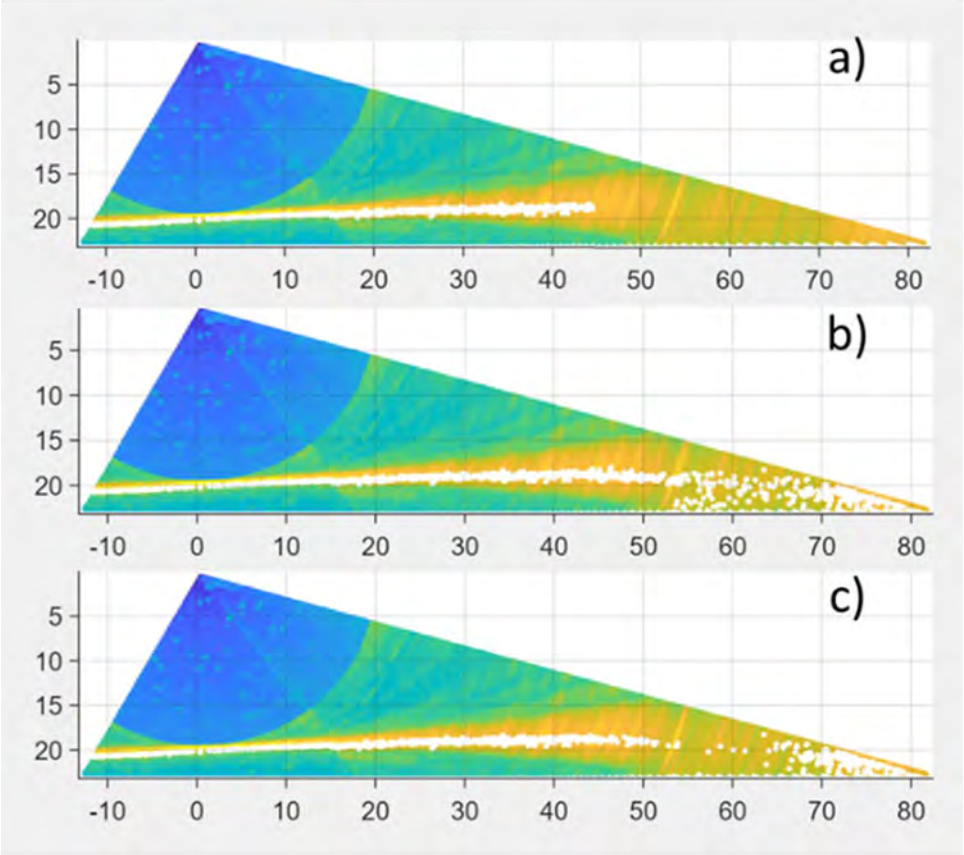

Figure 53 – Use of last threshold to get around the swath gap problem.

Figure 53 shows the impact of the gap and the attempt to circumvent it. Figure 53-a represents the solutions that would be obtained if the algorithm only aborted when it found fewer than 3 peaks. Note the drastic swath reduction. Figure 53-b shows the solutions if the highest peaks were always accepted, without comparisons with last threshold. Note the huge amount of spikes. Figure 53-c shows solutions considering the use of the average of the 20 last valid automatic thresholds. Although it is not yet an ideal situation, it presents the best result compared to the previous options.

3.5 – Summary of Algorithmic Flow and practical MATLAB implementation

After detailing the specifics of the manual threshold, automatic threshold and the problem with the gaps, the final algorithm can be further detailed by Figure 54, in addition to the overview transmitted by Figure 38.

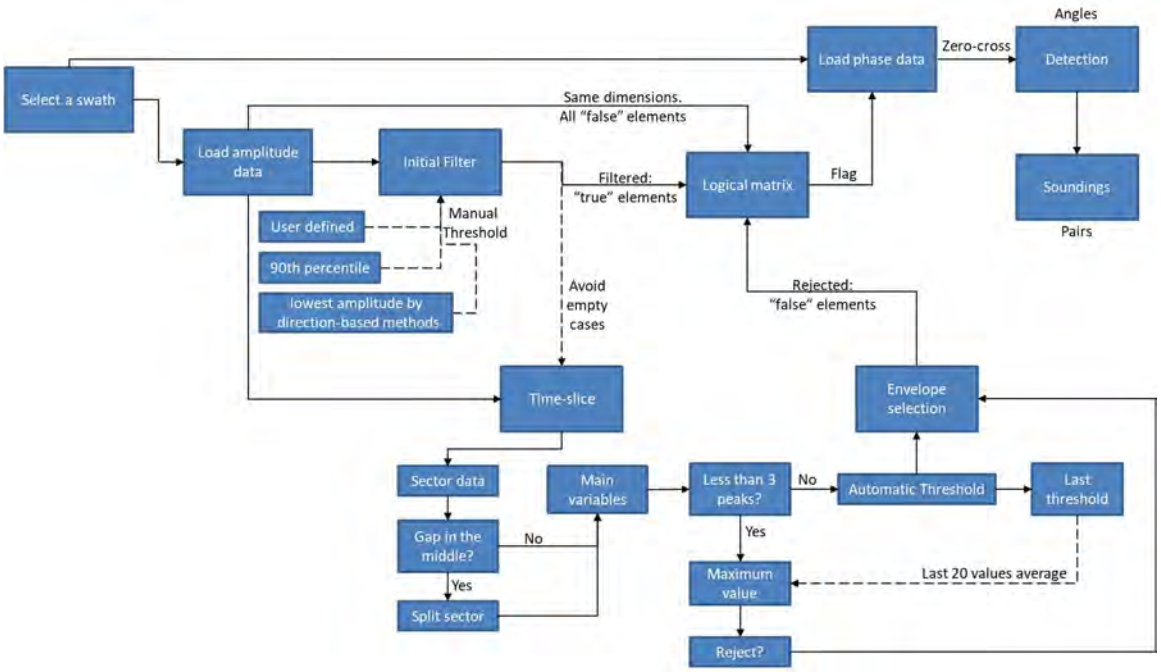

Figure 54 – Expanded PDI algorithm.

Once the algorithmic flow was developed, in order to allow the user to interact effectively with the parameters and assess the resulting bottom detection relative to the manufacturer solutions, a custom graphical user interface (GUI) application was developed in MATLAB, build using App Designer (Figure 55).

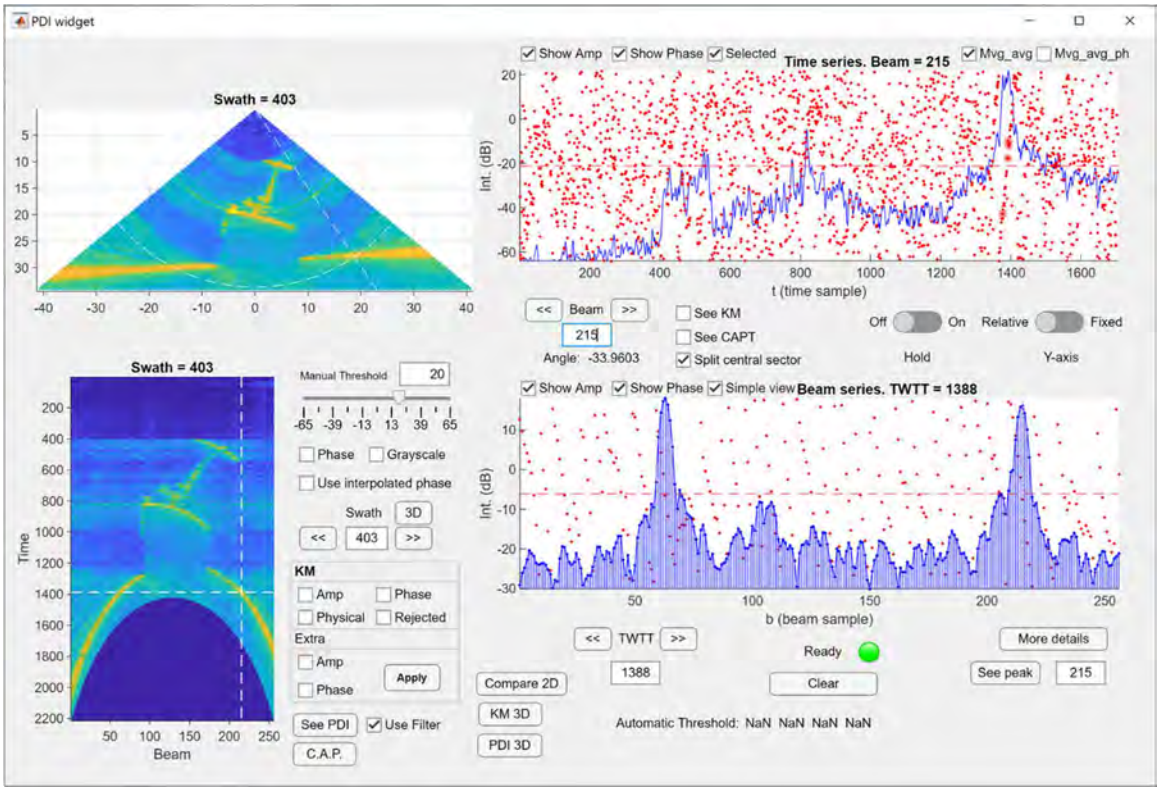

Figure 55 - Overview of the PDI widget developed in MatLab.

The simultaneous visualization of the swath in the forms of pie diagram and time-angle diagram, including the time-series and beam-series of the selected time-angle pair, showing both the amplitude data and the phase data, allowed a wide understanding of each ping. The soundings obtained by conventional detection could also be displayed and allowed a comparison with the results of the method under development.

3.6 – Uncertainties discussion

Just as important as making a measurement is knowing how wrong it can be. The impacts that the specifications of a multibeam system, its auxiliary sensors, and its configuration on the vessel used in the survey, can have on the accuracy of each individual sounding were shown in Hare et al (1995), and highlighted the importance of investigating all associated sources of errors.

A relative error in depth ($\frac{\delta z}{z}$), related to the errors of measurement of time (t) and angle (θ), is defined as $\frac{\delta z}{z} = \frac{\delta t}{t} + tan\theta . \delta\theta$ (Lurton, 2001), and, to deal exclusively with the assessment of soundings, a bathymetry quality estimator (IFREMER Quality Factor, IQF), with the intention of being independent of the sonar type or model, was defined by Lurton (2010) as the logarithmic value of the inverse relative error in depth.

$$IQF = \log_{10}\left(\frac{z}{\delta z}\right)$$

This expression is usually divided into two cases. The first deals with direction-based methods, where the direction is considered to be fixed ($\delta\theta \approx 0$), and is expressed by $IQF = \log_{10}\left(\frac{z}{\delta z}\right) = \log_{10}\left(\frac{t}{\delta t}\right)$, being relevant for MBES processing (either for amplitude or phase detection). The second case seeks an angle estimation at a given instant, considered fixed ($\delta t \approx 0$), resulting in $IQF = \log_{10}\left(\frac{z}{\delta z}\right) = \log_{10}\left(\frac{1}{tan\theta . \delta\theta}\right)$, used in interferometric side scan sonars (ISSS) processing.

Since the PDI analyzes the data by time-sample, it is expected that the measurement of its uncertainties will be done by a similar procedure adopted for ISSS, based on phase difference measurement. For this, it is necessary to calculate an estimate for $\delta\theta$.

As seen in section 3.1.4, the phase measurements are sensitive to the SNR and its conversion to angles may be inaccurate. A differentiation of the expression that relates phase difference ($\Delta\varphi$) and angle w.r.t. MRA ($\emptyset_b$), leads to:

$$\sin(-\emptyset_b) = \frac{\Delta\varphi}{k.s.\cos(\theta_s)} \therefore \Delta\varphi = \sin(-\emptyset_b).k.s.\cos(\theta_s)$$

$$\frac{\delta\Delta\varphi}{\delta\emptyset_b} = \frac{\delta(\sin(-\emptyset_b).k.s.\cos(\theta_s))}{\delta\emptyset_b} \therefore \frac{\delta\Delta\varphi}{\delta\emptyset_b} = k.s.\cos(\theta_s).\frac{\delta\sin(-\emptyset_b)}{\delta\emptyset_b} \therefore$$

$$\delta\Delta\varphi = -k.s.\cos(\theta_s).\cos(\emptyset_b).\delta\emptyset_b$$

As seen on section 2.3.3, $\theta = \theta_s + \emptyset_b$. Therefore:

$$\frac{\delta\theta}{\delta\emptyset_b} = \frac{\delta(\theta_s + \emptyset_b)}{\delta\emptyset_b} = \frac{\delta\theta_s}{\delta\emptyset_b} + \frac{\delta\emptyset_b}{\delta\emptyset_b} = \frac{\delta\theta_s}{\delta\emptyset_b} + 1$$

And $\frac{\delta\theta_s}{\delta\emptyset_b} \approx 0$, since the angle is fixed by the beam steering. Accordingly:

$$\frac{\delta\theta}{\delta\emptyset_b} = 1 \therefore \delta\theta = \delta\emptyset_b$$

Applying $\delta\emptyset_b$ in the former expression for $\delta\Delta\varphi$:

$$\delta\Delta\varphi = -k.s.\cos(\theta_s).\cos(\emptyset_b).\delta\theta \therefore$$

$$\delta\theta = \frac{-\delta\Delta\varphi}{k.s.\cos(\theta_s).\cos(\emptyset_b)}$$

(as seen in Lurton, 2000, with different symbols and angle orientation). This last expression indicates that the angular error ($\delta\theta$) is proportional to the phase difference error ($\delta\Delta\varphi$), beam steering direction (θ_s) and angle w.r.t. MRA ($\emptyset_b$). Note that the negative sign only indicates the convention of the direction adopted for positive angles and can be omitted for the purpose of logarithmic calculations.

Substituting $\delta\theta$ (without sign) in the IQF expression:

$$IQF = \log_{10}\left(\frac{z}{\delta z}\right) = \log_{10}\left(\frac{1}{tan\theta.\delta\theta}\right) = \log_{10}\left(\frac{1}{tan\theta.\frac{\delta\Delta\varphi}{k.s.\cos(\theta_s).\cos(\emptyset_b)}}\right) \therefore$$

$$IQF = \log_{10}\left(\frac{k.s.\cos(\theta_s).\cos(\emptyset_b)}{tan\theta.\delta\Delta\varphi}\right)$$

In conclusion, IQF values for PDI can be obtained as long as the acoustic wavenumber ($k = \frac{2\pi}{\lambda}$), the beam steering direction (θ_s), the angle in w.r.t. beam MRA ($\emptyset_b$), the final PDI solution direction (θ), the distance between the acoustic centers of the split beam (s), and the

uncertainties in the phase difference value ($\delta\Delta\varphi$) are available. From this list, due to the data available in the recorded datagrams, the last two items are the most problematic, and limit the calculation of the IQF in this study.

The first problem, exposed in section 3.2.2, occurs due to the lack of knowledge of the value of "s". This need was circumvented in PDI by the use of some assumptions and approaches, and its value was not calculated. It would also be possible to obtain an approximate value of s, through statistical analysis of the data, in order to constrain their uncertainties to the extent that the error in s have little influence on the IQF value, although this case has not been tested in this research.

The second problem, phase difference value ($\delta\Delta\varphi$), as seen in Lurton (2010), is dependent on the knowledge of the SNR. In the system used, among the recorded datagrams there is an IQF value for each sounding. Thus, it is expected that the manufacturer has a real-time estimate of SNR values or has models that can estimate these values. Such values, however, do not appear in any datagram. Note that both of these data are available to the manufacturer, and therefore the IQF can be calculated by them without any major problems.

Two other alternatives to obtain a value similar to the IQF were considered, without using data that is not registered in the datagrams. The first one considered using the IQF expression most used in MBES ($IQF = \log_{10}\left(\frac{t}{\delta t}\right)$). This method, detailed in Lurton (2010) for both amplitude and phase detections, needs time averaging to be done on "N" samples, which means that it is only possible if adjacent time-samples are used. This would partly defeat the PDI advantage, as it assumes that prior and post-time-slices are looking at the same surface. As no time-average was done in the PDI method, the result obtained with this form of IQF calculation would not reflect the method's uncertainties, and, therefore, the idea was discarded.

The second idea planned to use the manufacturer's solutions, assuming they are right. Then a comparison between the PDI solutions and the reference solutions would be made, to indicate how much the PDI differs from the first. However, away from continuous seafloors, one cannot really compare KM with PDI solutions because they differ in the total amount of solutions and the targets detected, making the process of choosing pairs to be compared difficult. Even for continuous seafloors, the comparison is not adequate, as the PDI has chosen to do no time-averaging, its noise relative to the KM should reflect in the IQF obtained. For these reasons, this idea was also discarded.

Given the importance of the subject, it is expected that this issue will be addressed in future works, either by testing the expression presented here (based on the IQF) or by developing an expression that does not depend on data outside datagrams.

CHAPTER 4 - EQUIPMENT, SURVEY AREAS, TESTS AND RESULTS

The PDI algorithm explained in Chapter 3 was tested on real data acquired over a variety of specific seabed types. This chapter details the equipment, survey areas, the tests performed and illustrates significant results. Note that a full set of results are included in an appendix.

4.1 – Equipment

4.1.1 - Survey Vessel - CSL Heron

CSL Heron (Figure 56) is a 34 ft. hydrographic-geophysical-oceanographic survey launch, owned by the Canadian Hydrographic Service (CHS), on long term loan to the Ocean Mapping Group (OMG) at the University of New Brunswick (UNB). Nowadays, she is based at the Institute of Ocean Sciences (IOS) in Sidney, BC, Canada, convenient to the operating area for the experiments described in the section 4.2.

Figure 56 - The CSL Heron from the port side, bow and astern.

She has a permanently mounted 70-100 kHz multi-sector multibeam sonar (EM710). The EM710 is an older model of Kongsberg sonar and can only generate the previous *.ALL format which does not allow logging of the phase information. The newer EM712 (not installed) would

allow this. For the purpose of this thesis, the side pole was utilized to deploy the EM2040P to collect data for this experiment.

In her composition, CSL Heron has several notable pieces of survey equipment, of which the following are relevant for this research:

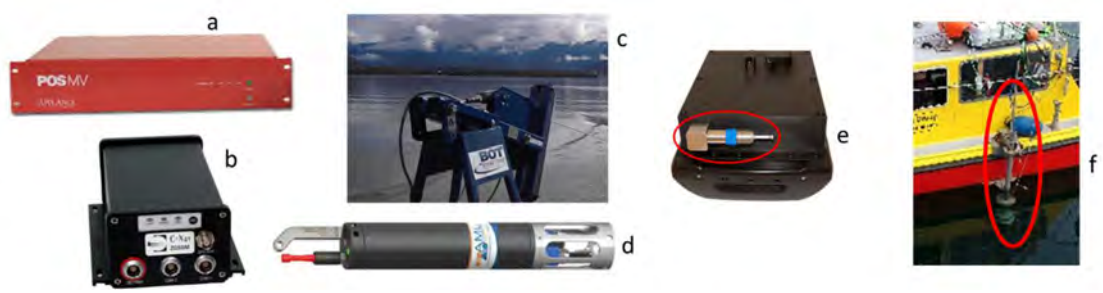

Figure 57 - CSL Heron's relevant equipment for this research.

- Applanix PosMV 320 V4 (Figure 57-a): Position and Orientation System for Marine Vessels (POS MV). The system provides accurate navigation and attitude data for use by equipment on board the vessel, such as a multi-beam sonar, to correct for the effects of vessel motion during survey operations. These data are used by the EM2040P for sonar beamsteering corrections and minimization of vessel motion artifacts. It was integrated with a C-Nav 2050M in order to using RTG corrections.

- C-Nav2050M (Figure 57-b): The C-Nav2050M is a GPS receiver system which delivers high accuracy to the positioning. It uses C-Nav Correction Service Network for decimeter-level position accuracy and provides RTG corrections to PosMV 320 v.5 system.

- MVP 30 (Figure 57-c): The Moving Vessel Profiler (MVP) collected sound speed profiles for the survey while the vessel was underway. This system is capable of underway profiles up to 30m and maximum stationary profiles to 125m. For each profile, conductivity, temperature and pressure was acquired with a CTD sensor.

- AML-SVP-16 (Figure 57-d): AML-SVP-16 was used to collect deeper profiles. It is manually lowered and can be used up to 300 meters.

- AML Smart SV&P (Figure 57-e): Surface sound velocity was collected using the Smart SV&P mounted on EM 2040P.

- A retractable port pole (Figure 57-f), where the EM2040P was installed.

4.1.2 - Echosounder

In order to test the algorithm developed in the detection of bottom and targets, a Kongsberg EM2040P MkII multibeam echosounder (Figure 58) was used, whose main technical characteristics and specifications are presented in Table 1.

Figure 58 - Kongsberg® EM2040P multibeam echosounder

According to Kongsberg Maritime (2017), the EM2040P Mk II is a wide band high resolution shallow water multibeam echo sounder, composed of a single "sonar head" (the transducers for transmitting and receiving sound pulses are integrated in a common housing). It features separate linear transducer arrays for transmit and receive, assembled with the Mills cross configuration. Three separate line arrays form the transmit transducer, pointing straight down and to 45 degrees to each side. This allows pinging up to three sectors simultaneously. It operates in the frequency range from 200 to 400 kHz, has roll, pitch and yaw stabilization, allows swath coverage of up to 160 degrees and an unsteered beamwidth of ~1.3x1.3 degree (at 300 kHz mode

used for these experiments). It is capable of electronically steering both its transmitting and receiving beams. It is also capable of using nearfield focusing on both transmit and receive. It features CW and FM chirp pulses (although only CW was used for this experiment). Optionally, it can offer Dual swath (increasing the sound density alongtrack) and Water column logging. Specifically, on this last resource, in addition to the already traditional possibility of recording the amplitude data, the recording of the phase difference data is also available.

Number of Swaths:	up to 2
Number of Sectors:	up to 3 (per swath)
Frequency range:	200 to 400 kHz
Selectable frequencies:	200, 300 and 400 kHz operating mode
Type of Stabilization:	Roll, Pitch, and Yaw
Receive beam spacing:	Equiangular Equidistant High density equidistant
Number of Physical Beams:	256 (per swath)
Number of soundings:	Up to 400 (per swath)
Bottom Detection Methods:	WMT Phase detection Extra-detections
Detected depth (Maximum):	Limited to 600 m relative to the surface
Detected depth (Minimum):	0.5 m relative to transducer face
Ping rate (Maximum):	50 Hz
Beamwidth (Tx x Rx):	200 kHz: 2 x 2 degrees 300 kHz: 1.3 x 1.3 degrees 400 kHz: 1 x 1 degree
TX Source level @ 300 kHz:	Up to 209 dB re 1 µPa at 1 m
Pulse shading:	Hanning

Table 1 – EM2040P main characteristics.

As it is a portable system, of reduced dimensions (length: 560 mm, width: 300 mm and height: 166 mm) and weight (19.5 kg, in air), it was easily installed on the lateral pole of CSL Heron, used in the hydrographic survey.

4.1.2.1 –SIS software and the new file format

The Seafloor Information System (SIS), version 5.2, was utilized for real-time acquisition of multibeam data during survey operations. This software can display simultaneously several windows defined by the user (Figure 59) and it is a useful tool for planning, monitoring, and performing data quality control of the survey (Kongsberg Maritime, 2019). Water line, lever-arms, sensors offsets, and sound speed values were processed and applied in real time to MBES data in SIS.

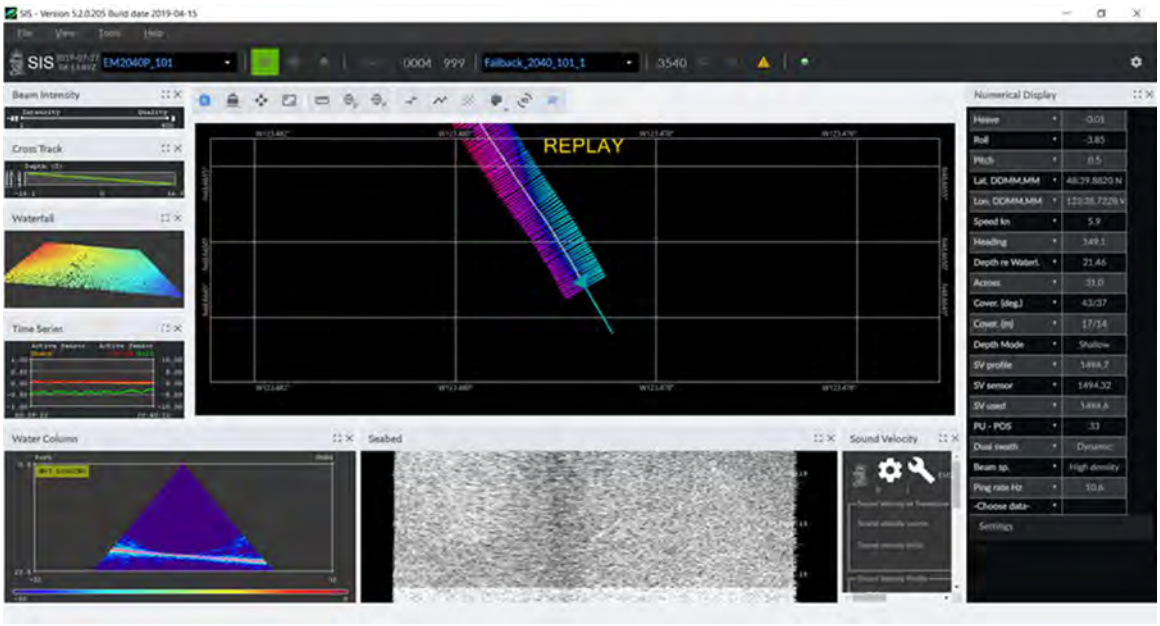

Figure 59 - Seafloor Information System (SIS) used for data acquisition.

One of the recently added features, which was essential for the development of this research, is the ability to record phase data from the water column. This resource can be accessed

(in SIS version 5.2) through the Water Column field of the Filter and Gains tab within the Runtime survey window, as shown in Figure 60. Among the available options, there is the recording of the phase data in low resolution, 8 bits, which provides a 180/128-degree resolution, or high resolution, 16 bits, which offers a 0.01-degree resolution. The decision on which resolution to adopt is up to the operator, which must take into account the objectives of its survey and the available disk space. For this research, the data was recorded in high resolution mode.

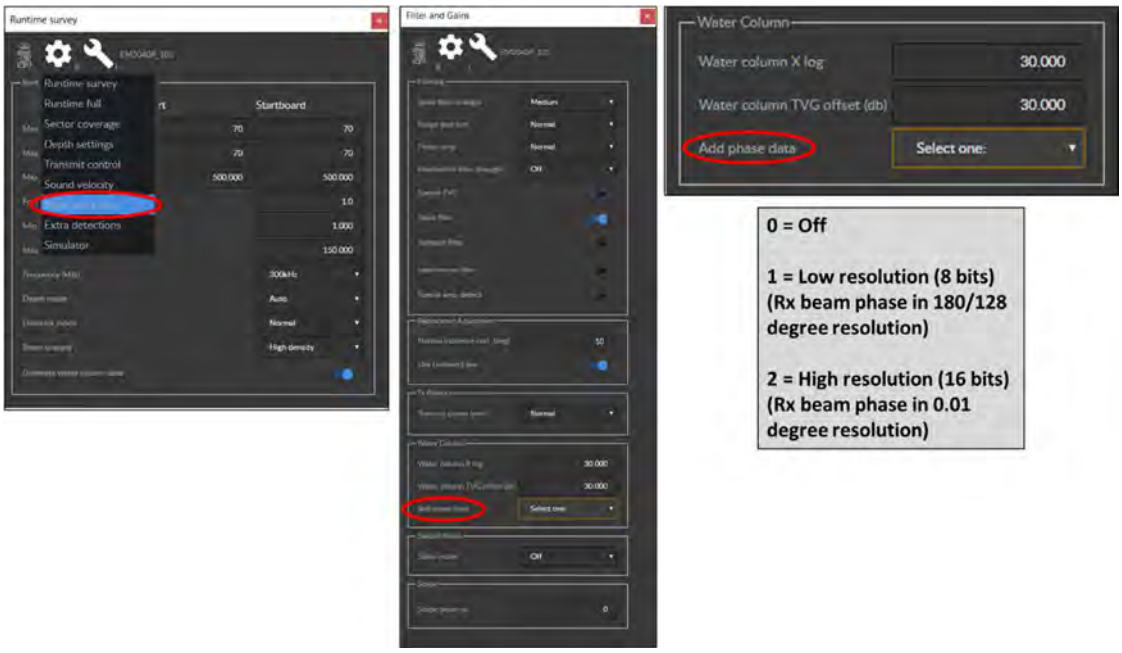

Figure 60 – Add phase data option available in SIS 5 water column.

As part of the new capability of delivering phase data, the KMALL format is required. This has significant additional features over the older *.ALL format. As the format was new, existing available KMALL reading scripts are limited. Although KM, in its description of datagrams (Kongsberg Maritime, 2018), provided a file (KMALL_reader.cpp) to demonstrate how to read the KMALL format, it was written in C ++ language, and no MATLAB script was available. Thus, a new MATLAB script, able to read all datagrams within any KMALL or KMWCD files, was developed and used in this thesis.

4.2 – Areas, targets, and objectives

As indicated in chapter 1, all OHS need to carry out hydrographic surveys to determine depths and detect submerged objects. This thesis aims to highlight the potential for non-conventional use of split-beam phase data in bottom detection, assessing the performance of this new algorithm in support of those objectives. Thus, to test the developed algorithm and check its performance, two regions were selected, nearby Squamish and Sidney (Figure 61, right), all in British Columbia, western Canada (Figure 61, left), due to the proximity of IOS (CSL Heron's base).

Figure 61 - Survey regions, in British Columbia, western Canada (left), nearby Squamish (right, top) and Sidney (right, center).

In the northernmost region, close to Squamish, an area was chosen due to the existence of steep-faced dunes in very shallow waters (Figure 62), ranging from 3 to 6 meters in depth, at the top of the delta of the Squamish river. These features are a challenge to do bottom detection when full or partial shadows are cast behind the bedforms, allowing the evaluation of the algorithm's

performance in these difficult situations. In addition, data had been collected in this area in July 2019.

Figure 62 - Steep-faced dunes at the delta of the Squamish river.

In the region near Sidney, three areas were chosen (Figure 63): two shipwrecks, MV GB Church and HMCS Mackenzie, and one area where there are a series of concrete cubes of different characteristics deposited on the seabed by the United States Navy's Naval Oceanographic Office (NavO) in 2011 to assess the target detection capability of its MBES installed in launches. In these three areas it is also possible to find sections of low relief seabed. Data had been collected in this area in October 2019.

Figure 63 - Areas near Sidney region, covering a series of concrete cubes, MV GB Church shipwreck, and HMCS Mackenzie shipwreck.

In addition, ten concrete cubes are present within this last area (Figure 64). Four of them are at 40-meters depth, all with 1-meter side, one without a pole. At a location of 20-meters depth, there are six of them, three with a 0.5-meter side and three with a 1-meter side, two of them having a pole. Only one cube of each characteristic (including depth) was selected for evaluation, in order to avoid needless redundancies. The selected ones are those that are highlighted in red circles in Figure 64. The evaluation of the performance of the algorithm in these cubes includes detection tests on different angles of incidence. Table 2 summarizes all the areas, targets, and objectives to be tested by the algorithm.

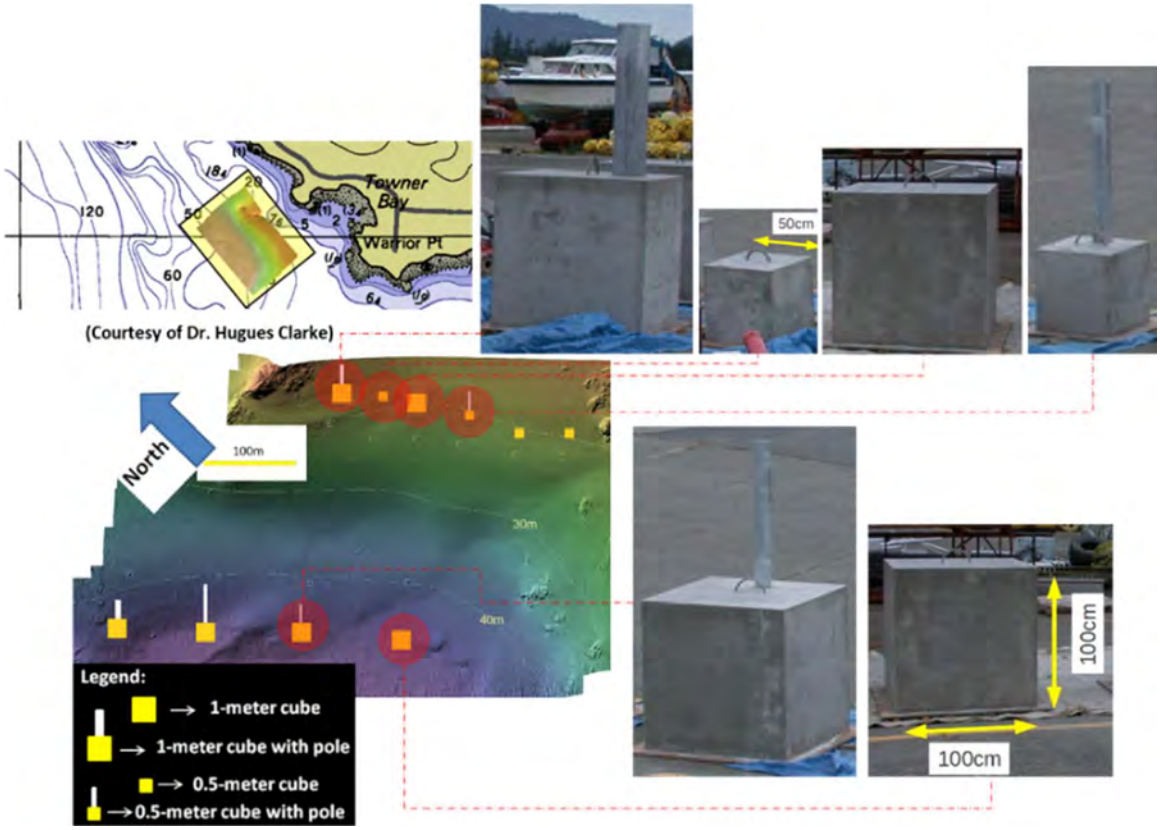

Figure 64 - Concrete cubes area and selected cubes (Adapted from Pereira, 2015).

Region:	Area:	Target:	Objective:
Squamish	Squamish River	Steep-faced dunes	very shallow waters with shadows
Sidney	MV GB Church shipwreck	MV GB Church shipwreck	features on the ship, particularly oblique and horizontal targets like davits and hold ribs.
	HMCS Mackenzie shipwreck	HMCS Mackenzie shipwreck	features on the ship, particularly the near-vertical rear mast.
	Concrete cubes	1-meter side cubes, with and without poles, at 20- and 40-meters depth 0.5-meter side cubes, with and without poles, at 20 meters depth	feature detection under different incidence angles
	MV GB Church shipwreck HMCS Mackenzie shipwreck Concrete cubes	Seabed	Low relief seabed

Table 2 - Areas and objectives

4.3 – Setting and surveyed lines

As seen in the previous section, data were collected in June (Squamish region) and October 2019 (Sidney region), in the four chosen areas. Several survey lines were acquired in each one of the testing areas, and Figure 65 indicates the direction in which they were run. Table 3 shows the main configurations adopted on all lines.

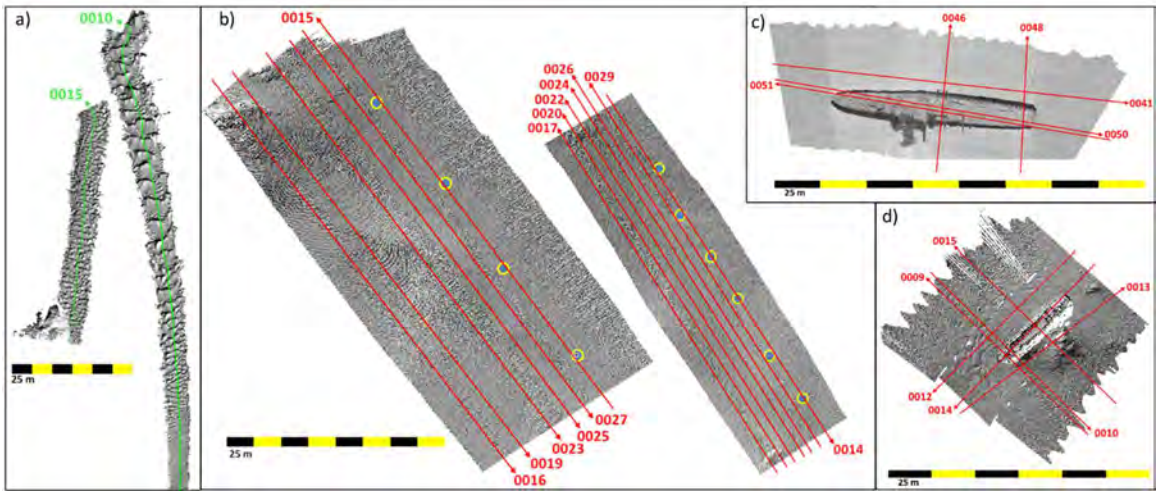

Figure 65 – Selected surveyed lines by areas. a) Squamish river. b) Cubes at 40m depth (left) and 20m depth (right). The positions of the cubes are indicated by the yellow circles. c) HMCS Mackenzie shipwreck and d) MV GB Church shipwreck.

Sector mode:	Normal
Beam spacing:	High density
Dual swath:	Dynamic
Frequency mode:	300 kHz
Detector mode:	Normal
Extra detection:	On
Water column data:	On
Water column TVG:	30 log R
Water column offset:	30 dB Offset
Water phase data:	High resolution
Survey speed:	~ 6 knots

Table 3 - Main configurations (common to all lines).

		Sector coverage		
Area:	**Line:**	**Max angle Port:**	**Max angle Starboard:**	**Others configuration changed:**
Cubes at 20m depth	0014_20191010_181817	45.0	45.0	---
	0017_20191010_183108	30.0	75.0	---
	0020_20191010_184042	30.0	72.0	---
	0022_20191010_185001	30.0	70.0	---
	0024_20191010_185857	30.0	65.0	---
	0026_20191010_190729	30.0	65.0	---
	0029_20191010_191602	30.0	65.0	---
Cubes at 40m depth	0015_20191010_182233	45.0	45.0	---
	0016_20191010_182619	75.0	30.0	---
	0019_20191010_183610	72.0	30.0	---
	0023_20191010_185445	65.0	30.0	---
	0025_20191010_190323	65.0	30.0	---
	0027_20191010_191150	65.0	30.0	---
Squamish river	0010_20190616_004957	75.0	75.0	Extra detection: Off
	0015_20190616_010445	75.0	75.0	Extra detection: Off
HMCS Mackenzie	0041_20191008_194038	65.0	65.0	Detector mode: Min. depth
	0046_20191008_194820	65.0	65.0	Detector mode: Min. depth
	0048_20191008_195040	65.0	65.0	Detector mode: Min. depth
	0050_20191008_195405	50.0	50.0	Detector mode: Min. Depth; Frequency mode: 400kHz
	0051_20191008_195549	50.0	50.0	Detector mode: Min. Depth; Frequency mode: 400kHz; Sector mode: Single sector center
MV GB Church	0009_20191007_173625	65.0	65.0	---
	0010_20191007_173733	65.0	65.0	---
	0012_20191007_174024	65.0	65.0	---
	0013_20191007_174133	65.0	65.0	---
	0014_20191007_174252	65.0	65.0	Frequency mode: 400kHz
	0015_20191007_174438	65.0	65.0	Frequency mode: 400kHz

Table 4 - Specific settings for each line.

Each area presented one or more different objectives in terms of evaluating the developed algorithm. In this way, different coverage angles were used to test the algorithm's behavior. In the area of the cubes, the swath varied from 90 to 105 degrees, depending on the relative position between the surveyed line and the expected location of the cubes. On the Squamish river, the swath was as wide as possible and the extra-detections feature was not activated. In the areas of

shipwrecks, for better registration of details, the swath was reduced to 130 degrees. In this same area some lines were collected in 400 kHz mode. Particularly in the case of the HMCS Mackenzie, the minimum depth detection feature was applied to its lines, and one of them was recorded using only the central sector. The coverage angles of each line, as well as possible changes in the settings, are compiled in Table 4.

4.4 –Tests

The algorithm was tested according to the targets and objectives previously presented in Table 2. Each of the survey lines has hundreds or thousands of pings, and choosing only a few dozen to represent the whole set is a difficult task, which could be done with subjective criteria. The following actions were taken to reduce this problem:

i) In the area of concrete cubes, targets that would allow the evaluation of all possible combinations between "size" (0.5 or 1m), "pole" (with or without), and "depth" (20 or 40m) were selected, discarding repeated features. Also, among the chosen cubes, all lines that had different angles of incidence on such targets were included.

ii) In both shipwrecks, easily identifiable characteristics were chosen, enabling the comparison between the expected shape of the target and the form obtained by the detection algorithms.

iii) In cases of low relief seafloor, a digital terrain model (DTM) generated in Swath-Ed was used to locate flat regions.

iv) In the steep-faced dunes, due to the similarity between the swaths, specific pings were selected, particularly focused on areas where conventional KM solutions indicated mistracking.

v) In the first two cases (cubes and shipwrecks), the choice of a ping took into account a series (from 3 to 13 pings) of consecutive swaths (waterfall view) in which the object was present. In this series, the swath close to the center that best represented the shape of the object considering solutions generated by the KM algorithm was selected. Figure 66 illustrates how this selection was made in three cases (numbered as they appear in the appendix). Note that the selected swaths (highlighted in yellow) are those close to the center of the series and have KM solutions with a better representation of the target.

Figure 66 - Waterfall view and swath selection (yellow).

In this way, all lines were evaluated and 57 cases were created. Among them, only some were included here, in order to avoid the unnecessary expansion of this thesis. The complete set can be accessed in the appendix section.

4.5 – Results

The selected cases were organized into four groups. The first deals with resolution requirements, displaying the results for a 1-meter cube sitting on the seabed at 20 m depth, under

seven different angles of incidence. The second case deals with a continuous target showing the results of low relief seafloor. The third case deals with undulating seabed, showing the results obtained in the dunes area. Finally, the fourth case deals with the detection of multiple orientations (vertical, horizontal, or oblique) suspended objects, displaying the results for the poles of the cubes, longitudinal profiles, davits, and mast of a shipwreck.

Before proceeding with these four cases, it is important to highlight an aspect observed on the along-track direction. All analyzes made in this study are applicable in the across-track direction within a single ping. Although the along-track direction is outside the scope of this thesis, when the selection of the swaths described in the previous section occurred, a sequence of swaths could be observed. In this situation, the object under analysis could be observed in the results of the PDI algorithm a few pings before and persisted for a few pings after when compared with KM solutions.

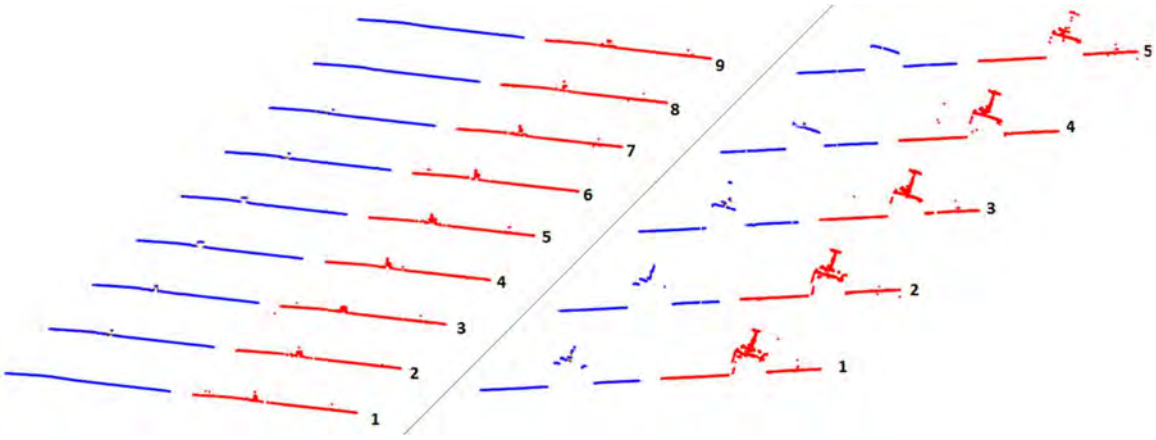

Figure 67 - Effects of transmission sidelobes on along-track PDI solutions

Figure 67 exemplifies this situation with two cases. On the left, a series of nine sequential pings on a 0.5 m cube with a pole. On the right, five pings on the rear mast of the HMCS Mackenzie shipwreck. In both cases, the same swath is presented in two ways: blue indicates KM solutions, and red indicates PDI solutions. On the left, notice that the cube is present in the KM solutions in

the pings from number 2 to 7. In the PDI solutions, it is seen in all swaths. On the right, the mast is partially observed in the pings from numbers 1 to 3. In the PDI solutions, it is again present in all swaths. These cases are believed to happen due to the detection on transmission beam sidelobes, which occur in the fore-aft direction and reach the target before and after the main lobe. Future studies that encompass the along-track direction could assess how to reduce the impact of these transmission sidelobes on PDI solutions, or use them in a beneficial way, such as confirming a target's presence through multiple hits on the same target, if correctly georeferenced.

4.5.1 - Resolution requirements

The results presented in this section involve appendix cases 01-3a to 01-3g, representing the detection of a 1-meter side cube without a pole, seated on the seabed in 20 m of depth, under seven different incidence angles. The images were rearranged to facilitate comparison, being compiled in Table 5. All images refer to the same target. Each row in this table represents a different angle of incidence. The left column shows KM solutions. The second column displays the results of the extra-detections. The third column displays the results of the PDI and the last column overlaps columns 1 and 3 with a cartoon of the expected shape of the cube (in black).

Regarding KM solutions, the cube is detected and well represented in the first two angles of incidence (~2º and ~26º). Under the angle of ~45º, the detection is still present, however, it is observed that the shape is softened as if there was a tendency of the algorithm to make the cube as a continuous part of the seabed. In the following four angles, there is no detection and just a gap in the swath becomes evident. Regarding the additional results promoted by Extra-detections, its presence is better noticed in the first two angles. Such solutions stretch the shape of the cube,

indicating that the detections are coming from adjacent beams sidelobes. In the following five incidence angles, their presence is modest, with no real gain in terms of cube detection.

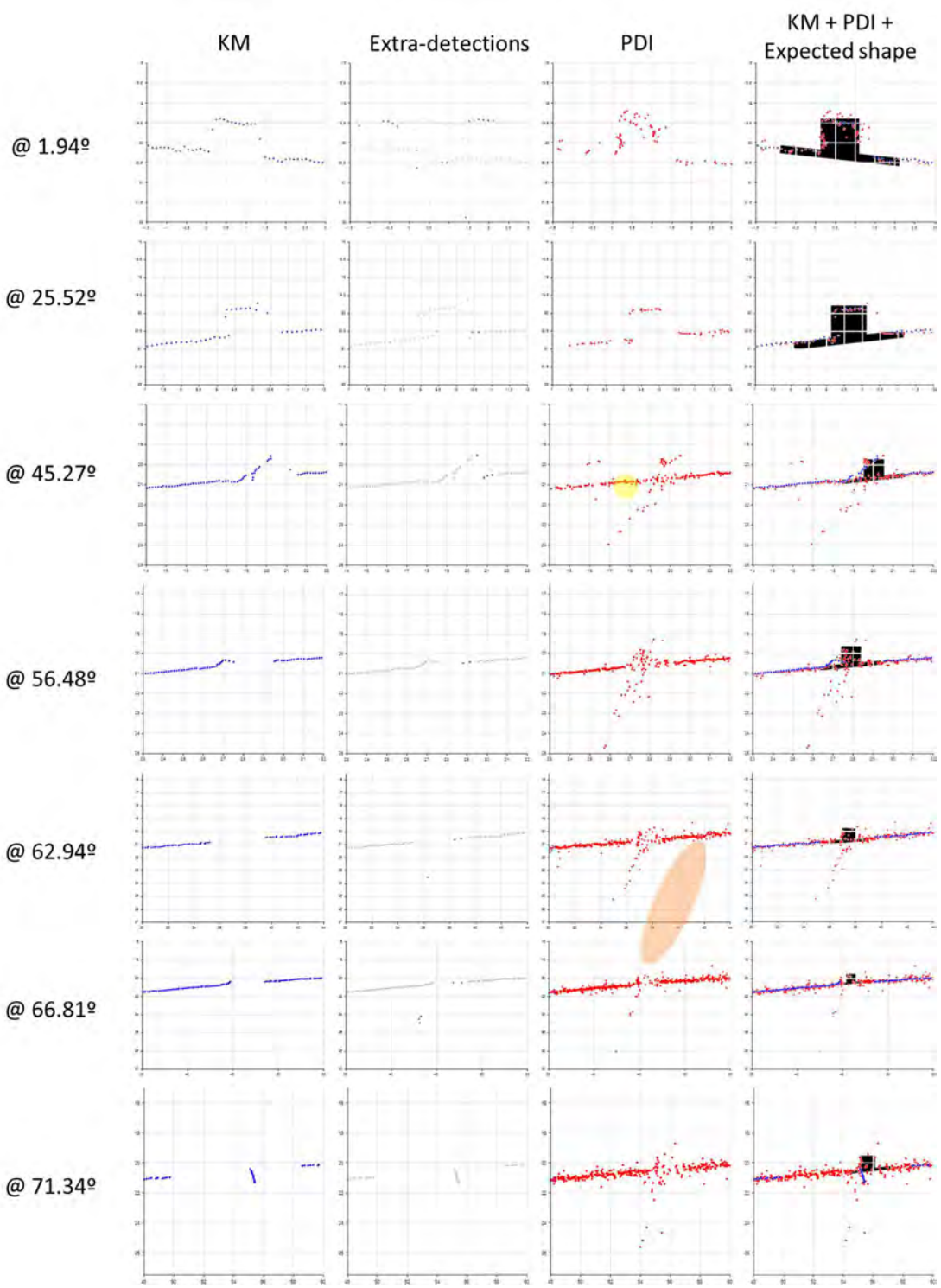

Table 5 - Solutions for a 1-meter cube at 20 m depth, at seven different angles of incidence.

Regarding the PDI solutions, the presence of the cube is well outlined at ~2º and ~26º, even though regions are close to the nadir, where inferior performance of the BDI is expected. For details on nadir PDI detection see section 4.5.2. In the image representing the ~45º incidence angle, a yellow circle highlights the presence of undesirable spikes. This problem is not exclusive to this angle of incidence and can be observed in several lines, on the boundaries between two sectors. Its presence is attributed to the imperfections of the automatic threshold used.

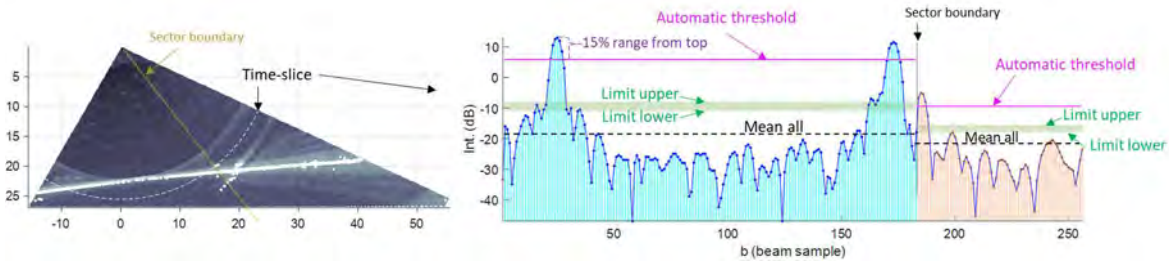

Figure 68 - Spike close to sector boundary.

During the elaboration of the algorithm, this problem was noticed and the attempt to eliminate it was presented in the section 3.3.1.2.1 of this thesis, with the inclusion of an additional step that used the highest mean range value as a reference for the minimum tolerable automatic threshold value, when dealing with different sectors. This solution appeared to be sufficient for the data set evaluated at that time. However, after generating the results present in the appendix, it was found that the problem persists. An even higher value should be used as a minimum automatic threshold reference in sectors that do not have the highest amplitudes considering the entire time-slice and a balance needs to be found to tolerate the difference in backscatter strength due to the presence of materials of different characteristics in different sectors. As a suggestion for future work, there is an improvement in the automatic threshold, with the addition of new steps or the joint use of filters that allow a better assessment of whether data from a sector that does not have the highest amplitude values should be rejected or considered.

Resuming the analysis of the PDI solutions from Table 5, with the exception of the first two angles of incidence, all the others present, in the expected location of the cube, solutions in the approximate shape of an arc, as highlighted by the orange ellipse. This characteristic has already been observed in Hughes Clarke (2013) and it is associated with the multipath phenomenon, in which the emitted pulse at elevations not corresponding to the receiver beam direction undergoes two specular reflection on two surfaces and returns to the receiver transducer along the beamformed path, with resulting false TWTT information, as shown in Figure 69.

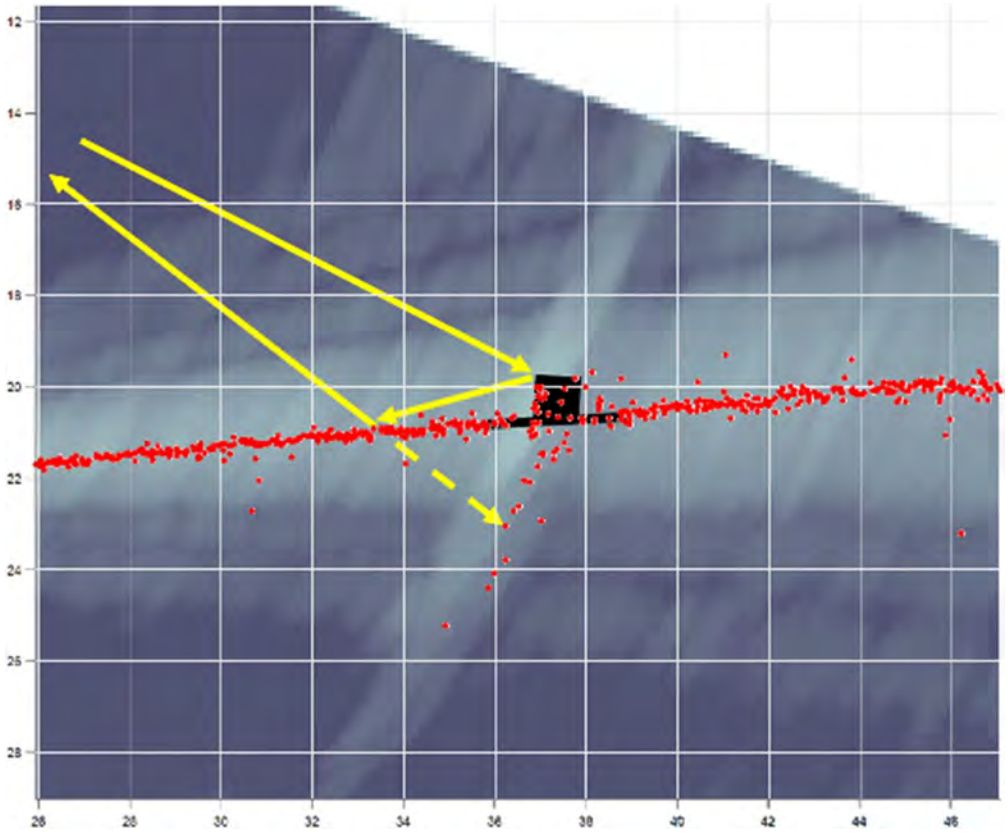

Figure 69 - Multipath and its relationship with an arc of solutions.

In a way, the existence of this arc of solutions can be used as an indicator of the presence of an object and a new survey line, under a more favorable angle of incidence, can be collected to better define the target.

4.5.2 - Continuous target (flat seafloor)

Considering the case of a continuous target (appendix case 03-1), a comparison was made between KM and PDI solutions on a flat seafloor (Figure 70). In this situation, the KM solution presents its best result, with no spikes or gaps. In relation to the PDI, the occurrence of the problem of boundary spikes (presented in the previous section) is noticed. At the outermost beams of the swath, notably on the left side, several gaps are observed, being associated with the problem of incomplete retention of the full angular series, described in section 3.4.2.

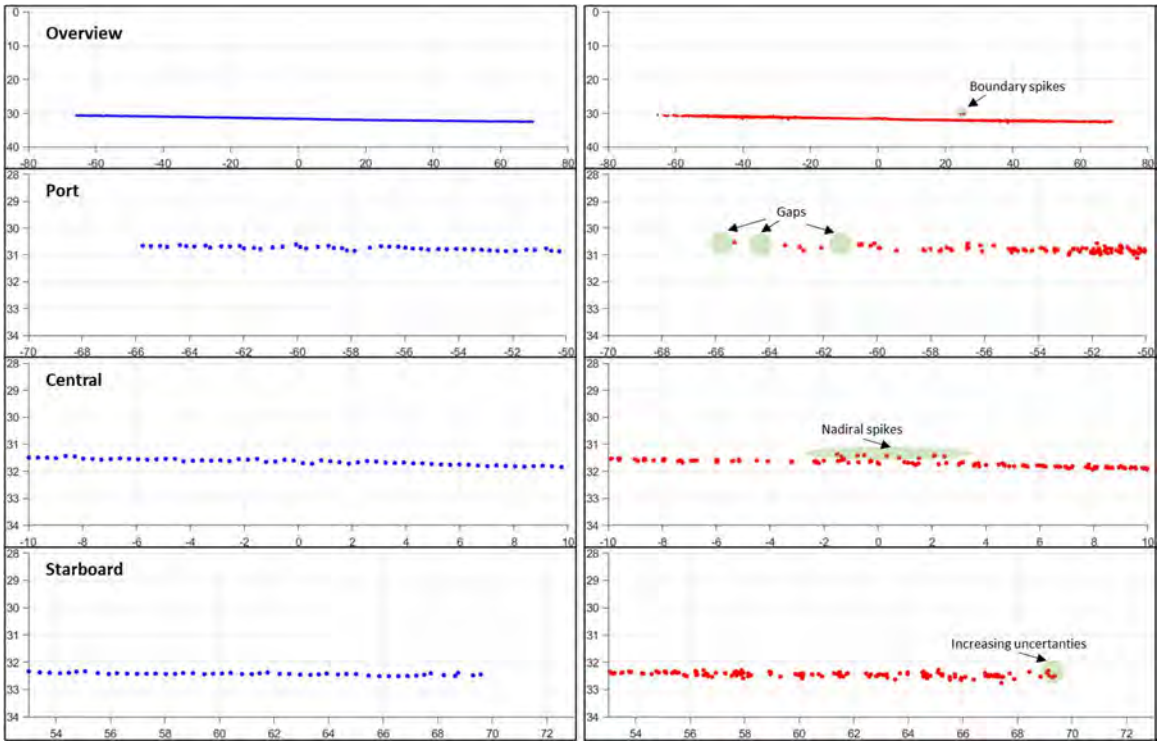

Figure 70 - Comparison between KM and PDI solutions for a flat seafloor.

Despite the difficulty inherent in the BDI approach in making detections in the vicinity of the nadir, it is observed that PDI detection in regions of normal incidence are possible, but may have some spikes. Another characteristic observed is the increase in uncertainties at the ends of

the swath. Whereas the HDBF is probably lengthening its regressed window, there is no time-averaging is being done in PDI, and the raw phase noise shows up as the SNR decreases. Thus, it is believed that this problem is associated with higher phase noise.

4.5.3 – Continuous target (undulating seafloor)

In contrast to the previous section, an undulating seafloor, due to steep-faced dunes, was analyzed in the present case (appendix case 04-3). Figure 71 shows a section at the Squamish river to exemplify this undulatory characteristic of the seabed in the region.

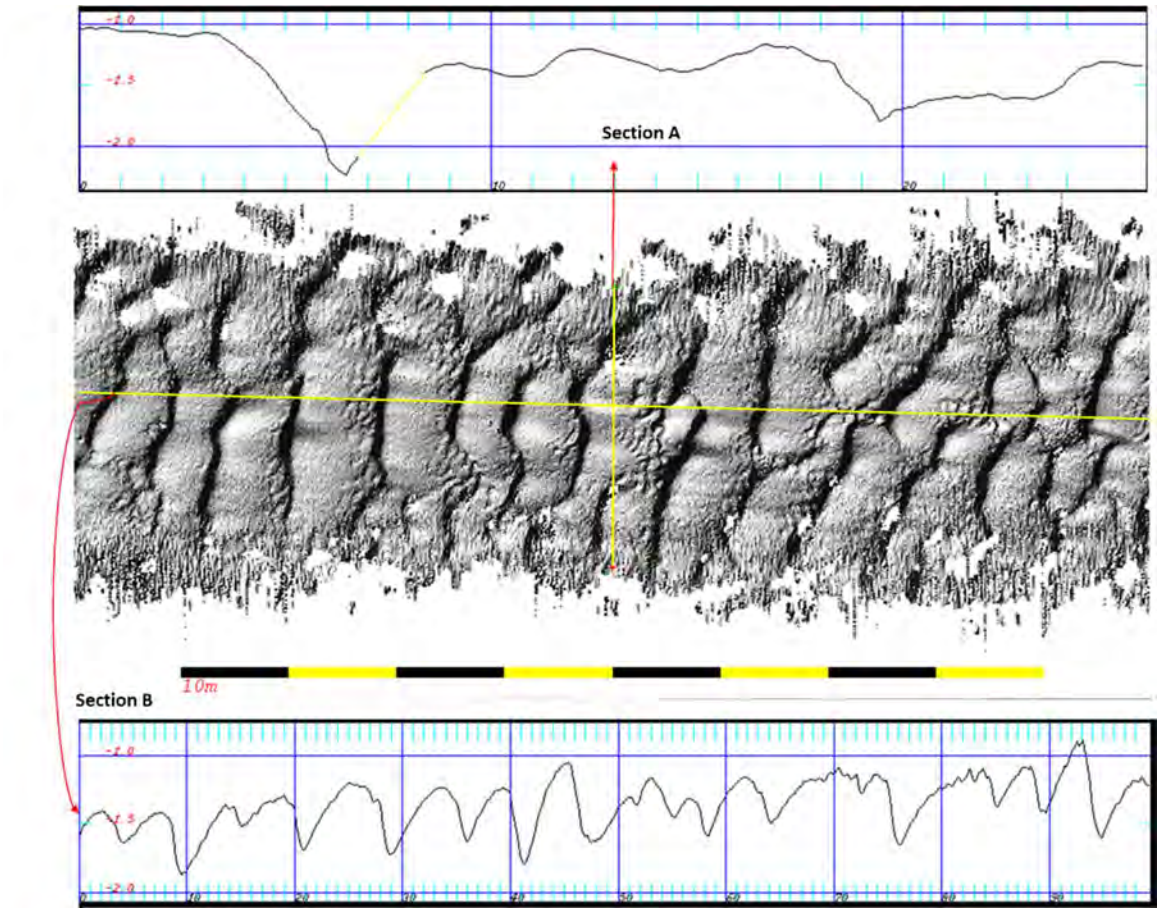

Figure 71 - Undulating seafloor at Squamish river. Middle: DTM displaying steep-faced dunes. The yellow lines indicate the position of the two sections analyzed. Top: Section A, showing a cross-track profile. Bottom: Section B and its along-track (nadir) profile.

The example chosen was a location where the KM solution shows abrupt mistracking. When looking at the associated backscatter one can clearly see when true shadows are cast. At the location indicated, however, while the BS is lower, a true shadow is not present. Nevertheless, the KM solution jumps abruptly to a longer range corresponding to the inward face of the next outboard bedform. This results in both a data gap and a set of false (deep) detections.

The comparison can be seen in Figure 72. Observing the KM solutions, two gaps (yellow circles) are noted. In contrast, PDI provides detections consistent with the adjacent bathymetric profile in these gaps. Again, evaluating the KM solution, two places where wrong tracking of the seafloor (green circles) exists. The same fact occurs with the PDI. However, due to its capacity of multiple detections within a same beam, it is noticeable that the solution of shoaler depth corresponds to the real seafloor and that the other solutions are associated with the phenomenon of multipath. In the same way as the previous case, at the outermost beams of the swath gaps are observed, due to incomplete retention of the water column data.

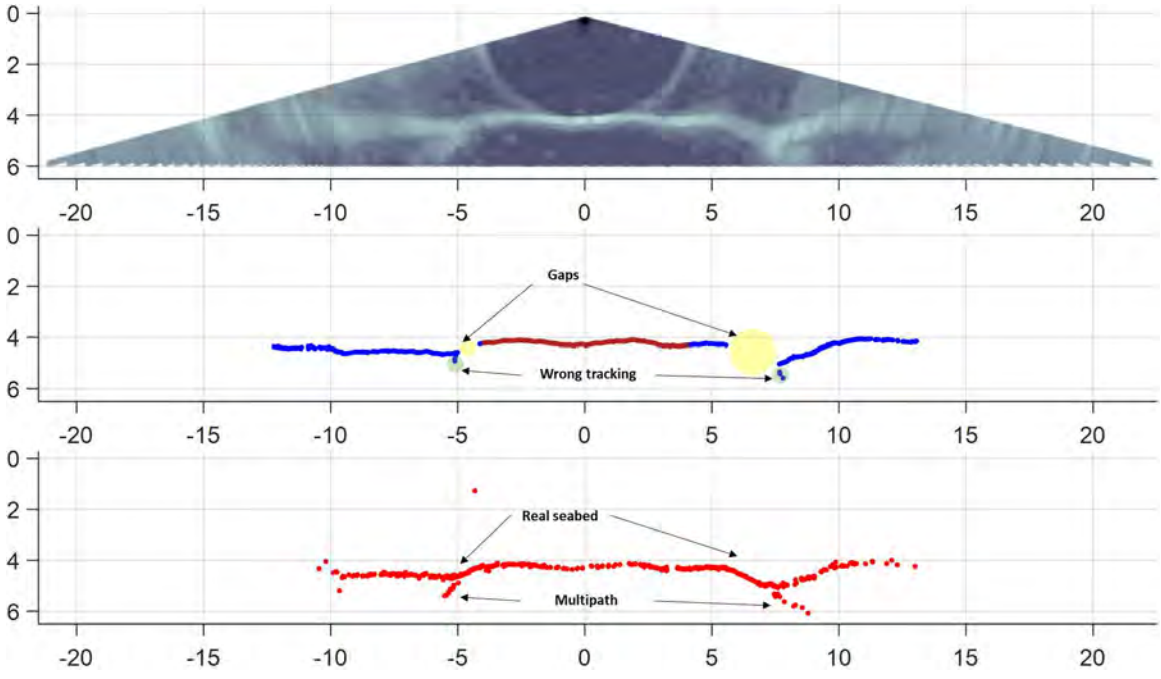

Figure 72 - Comparison between KM and PDI solutions in steep-faced dunes area.

To understand why there is gaps in the KM solution and why this does not occur in the PDI, it is necessary to compare time-series and time-slices and recognize how information is treated differently in each one. Figure 73 shows the swath in question and contains an example of time-slice and time-series.

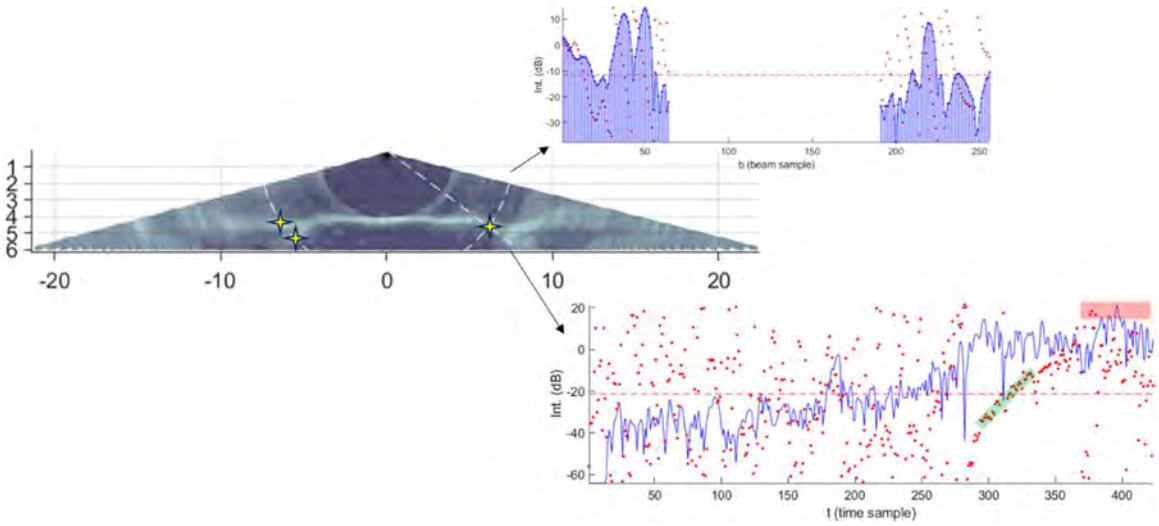

Figure 73 - Existence of gaps from the point of view of time-series and time-slice.

In this time-slice, three peaks stand out, two on the port side and one on the starboard. All of them are selected by the automatic threshold, and three solutions are generated (represented by the yellow stars). Considering the time-series, a phase-ramp (highlighted by the green rectangle) exists and has zero-crossing at the instant represented by the time-slice. In other words, the starboard solution could be obtained by direction-based methods. However, this phase-ramp is not associated with the highest amplitudes of this time-series. The highest values are found in the region represented by the red rectangle. These, in turn, present diffuse phase data. Thus, the solutions are rejected, and the gap is generated. Since the PDI evaluates time-slice by time-slice, it is not dependent on the highest amplitude value within a time-series to find solutions, which becomes an advantage in the presented situation.

4.5.4 - Suspended objects (multiple orientation)

This case was divided into vertical, oblique and horizontal targets (with respect to the "up" direction). It is important to note that this division is only intended to simplify the presentation of these results and comments, without strictly considering the meaning of these terms. As presented by Figure 74, it is noteworthy that the same oblique target for a nadir beam can be considered a vertical or even horizontal target for an oblique beam. In the same way, vertical or horizontal targets can be considered oblique depending on the reference beam.

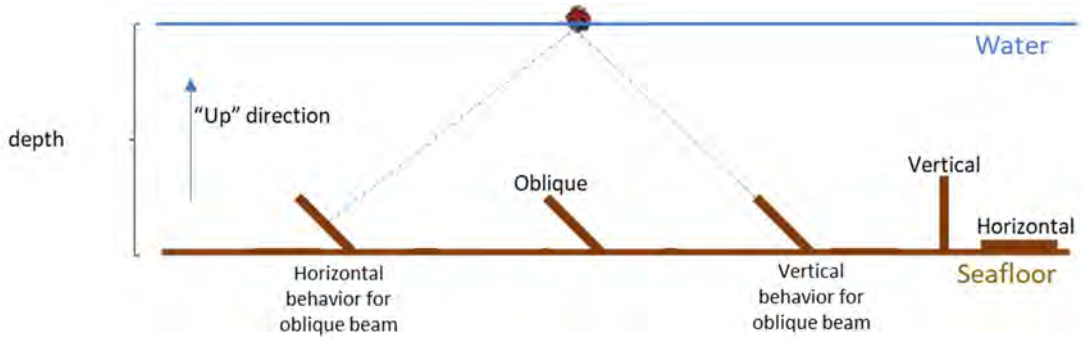

Figure 74 - Relative definition of horizontal, vertical and oblique targets.

4.5.4.1 – Vertical

The present case aims to expose the detection of a 0.5-meter cube at 20 meters deep, with a pole (case 01-4a of the appendix). Figure 75 show its results. Note that the WC amplitude data indicates the presence of the seabed, the cube and the pole. The phase data presents the colors in an orderly manner in the same region, indicating the presence of some object. Observe, in the region where the cube is expected to be found, how the phase has an almost constant value (keeps nearly the same color) in vertical (along beam) lines.

KM solutions, as already noted in section 4.5.1, have a tendency to make the shape of the cube more smoothed and appear as a continuous part of the seabed, completely ignoring the

existence of the pole. The extra-detections solutions are able to give evidence of the existence of only the top of the pole, but they are mostly amplitude detections and are actually detecting the sidelobes of the neighboring beams that reach the pole. This results in the observed arc shape of the solutions. PDI solutions are able to detect the seabed, the cube and, much better, both the top and the length of the pole, until then unnoticed.

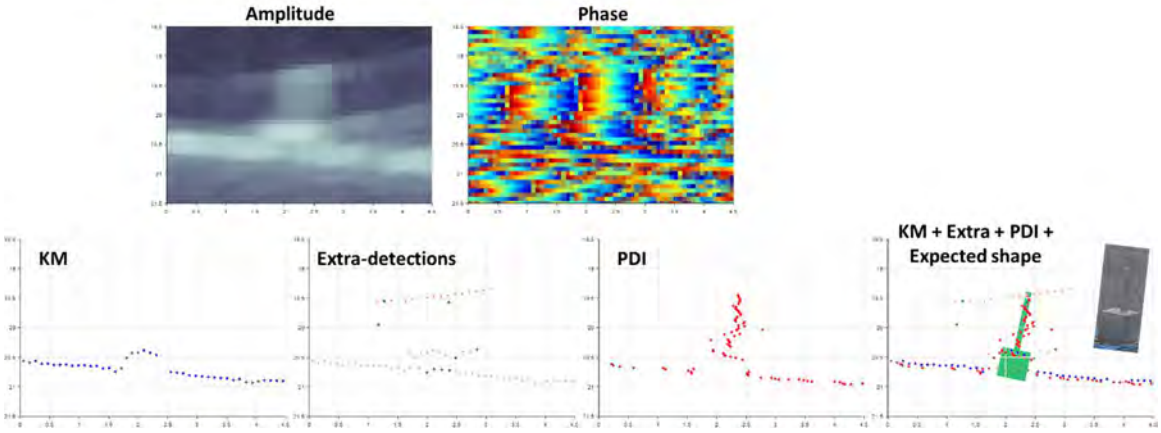

Figure 75 - Detection of a 0.5-meter cube and its pole.

The advantage of the PDI, in this case, lies in the fact that the pole, cube, and seabed detections occur at different times, allowing the clear identification of the peaks in each time-slice. Observe the time-slice present in Figure 76. In it, the pole is the only feature that stands out, allowing its inclusion as a solution. In the case of time-series, the selection of the envelope can be problematic due to the temporal proximity of the return signals and the possibility of including sidelobes. The time-series shown in the same Figure 76 uses the maximum amplitude value to detect the cube, rejecting the pole and the seabed. With the feature of extra-detections, the latter two are included, allowing the distinction between the three points but notably no points along the length of the pole. However, in the case of neighboring beams, it is common for sidelobes also to reach the same target and register their presence in the time-series. Figure 77 exemplifies this problem. It displays a beam whose main lobe does not reach the cube. The only detection of this

time-series is its encounter with the seabed. However, when the option of extra-detections is enabled, a new envelope is sought. This culminates with the use of data relating to sidelobes. Thus, the detections obtained by this method do not represent the shape of the object sought and the representation of the aspect-ratio of the target is better represented by PDI.

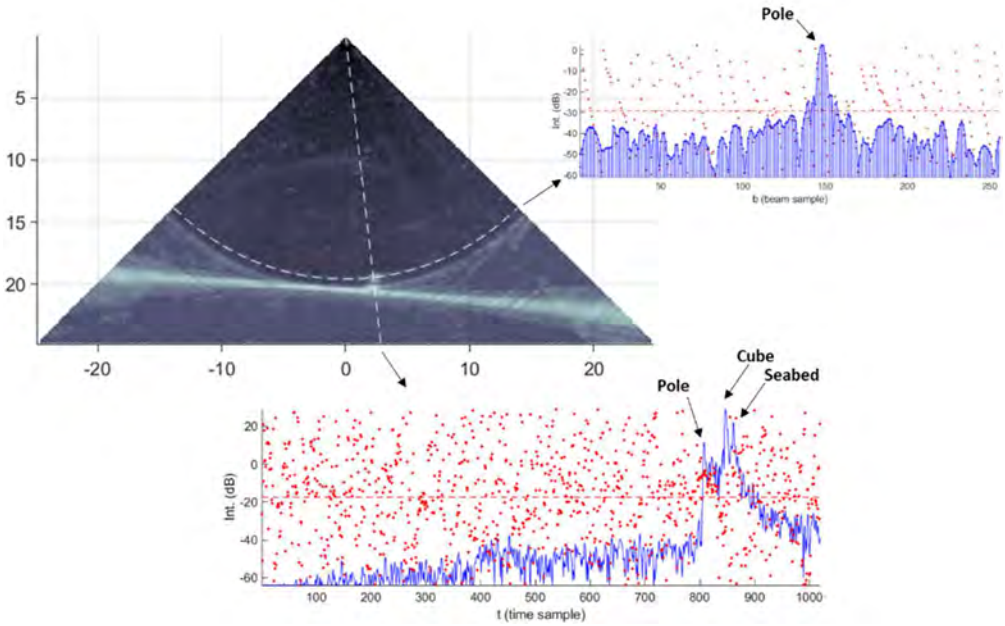

Figure 76 - Pole detection at a time-slice and time-series.

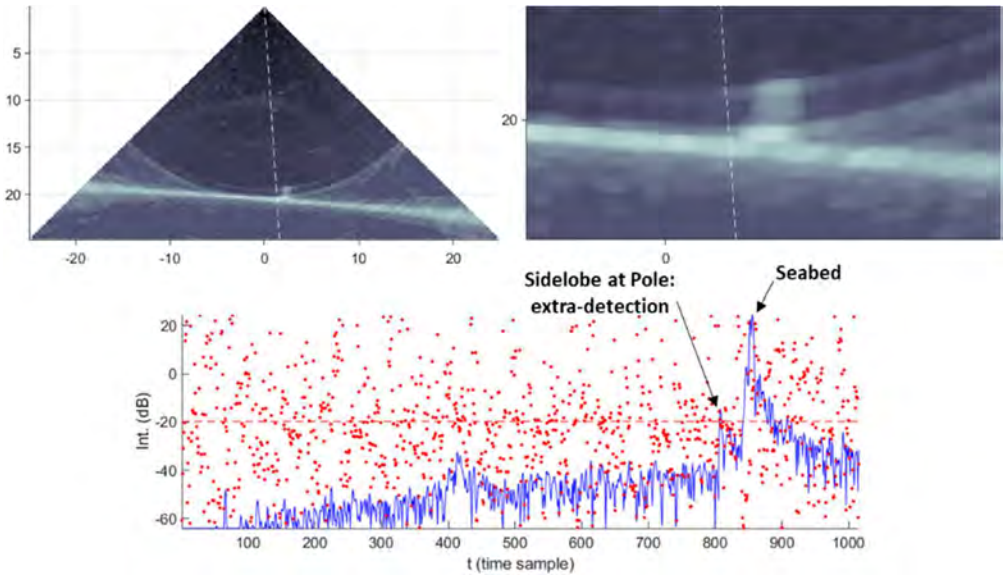

Figure 77 - Extra-detections and the sidelobe problem.

4.5.4.2 - Oblique

As oblique results, two cases are presented: the lifeboat davits of GB Church shipwreck and the rear mast of HMCS Mackenzie shipwreck, respectively cases 06-4 and 05-4 of the appendix.

In the first case, represented by Figure 78, the water column amplitude data clearly highlights the presence of davits. However, KM solutions do not include them and only horizontal profiles of this target are obtained. In a complementary way, the feature of extra-detections manages to outline the davits very well. The PDI also achieves this good definition, incorporating small additional details.

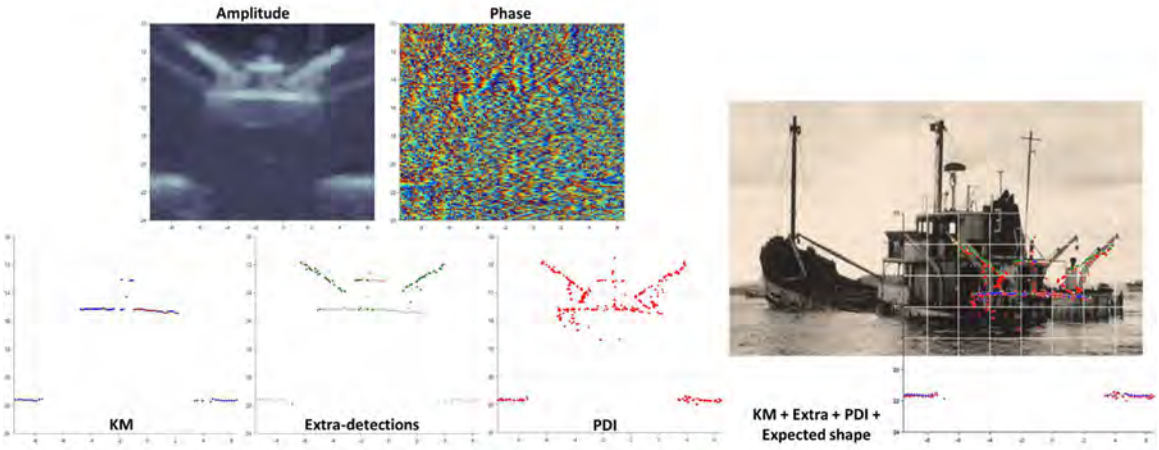

Figure 78 - Lifeboat davits detection.

To clarify why davits are not present in the KM solution, one example of lifeboat davits time-series is shown in Figure 79. It clearly identifies the peak amplitudes for davits and seabed. Note that the amplitude of the first is higher than that of the second. KM solutions seem to try to prioritize seabed detection. Unfortunately, this search for a better definition of the seabed impacts the rejection of suspended objects.

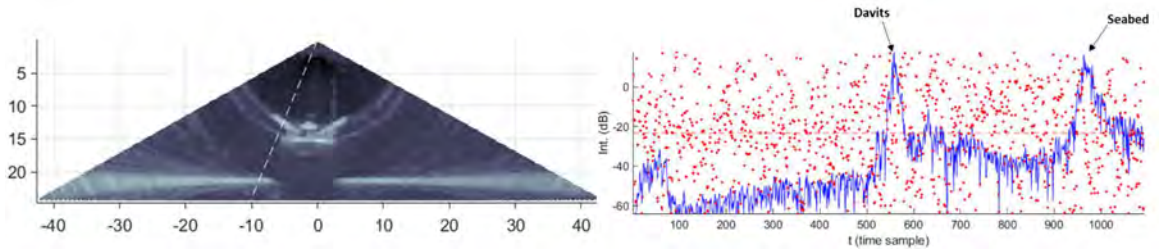

Figure 79 - One example of lifeboat davits time-series.

The second oblique case, in Figure 80, also presents water column data where the mast can be clearly identified. The phase data, in the midst of its common diffuse presentation, also exhibits orderly behavior in the presence of the mast, with the appearance of its colors under an almost constant value. Surprisingly, very little of the mast is detected. KM solutions are limited to partially displaying the top and bottom of the mast. The extra-detections feature brings an improvement, but still not enough to recognize the object only through its solutions.

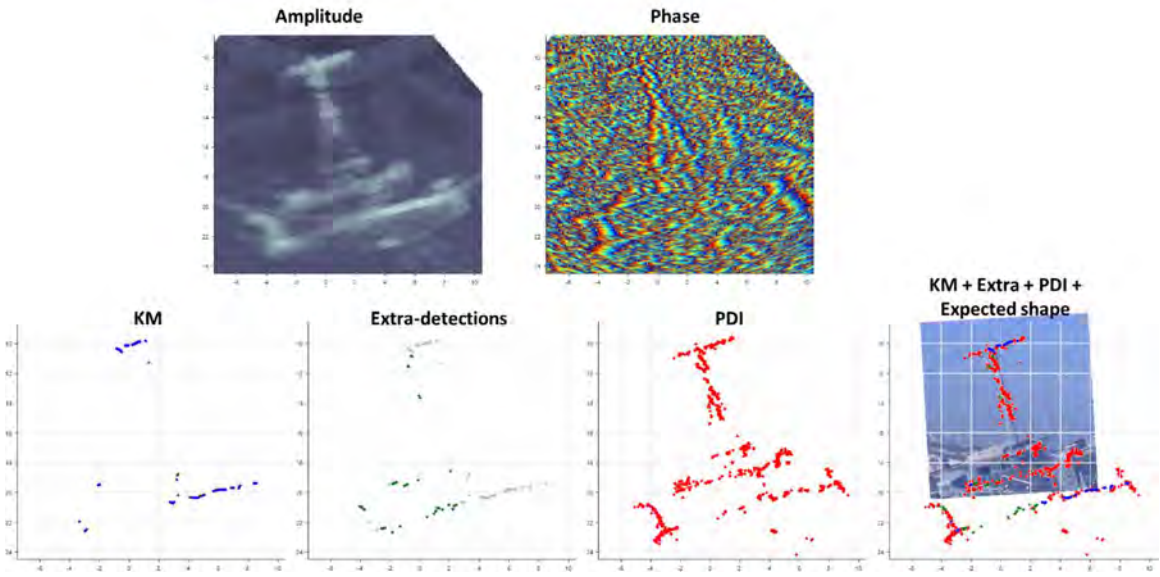

Figure 80 - Rear mast of HMCS Mackenzie shipwreck.

PDI solutions clearly define the mast, including its supporting parts. This is possible due to its characteristic of multiple detection in the same beam. In general, conventional methods are limited to a single or a few detections over a time series. This is highly harmful when the object is

in line with the beam vector. This problem is ignored by the PDI because it uses the orthogonal direction to the beams to detect the objects. As seen in the previous examples, this feature makes the PDI method an excellent option for detecting mast-like objects.

Taking advantage of the first example exposed in this section, it is worth emphasizing the importance of the manual threshold value in removing spikes from PDI solutions. Figure 81 shows the results for two different values. On the left, the 90th percentile was used. On the right, the lowest threshold value of KM solutions was used. A balance between solutions without spikes and with a minimum of details is necessary. In spite of the two manual threshold options proposed in this study indicating good results, the need for improvement and automation of this process is recognized, which is a goal to be included in future work.

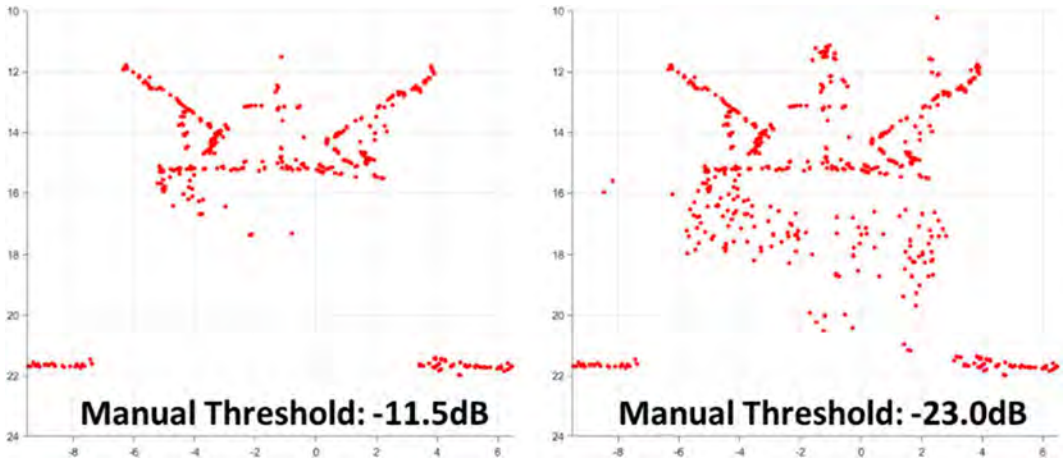

Figure 81 - PDI solutions at different manual threshold values.

4.5.4.3 - Horizontal

The last case considered in this chapter refers to the longitudinal profile of HMCS Mackenzie shipwreck (case 05-2 of the appendix). As can be seen in Figure 82, KM solutions are able to represent horizontal profiles very well, encompassing the main detections on shipwreck decks. Extra-detections add very little in the horizontal direction, being more active in the vertical

direction when partially delineating two masts. The PDI, which has been shown to be better in vertical objects, has the advantage of its facility in promoting multiple detection in the same beam. This allows different decks of horizontal profiles to be displayed, culminating in a better definition of the longitudinal profile.

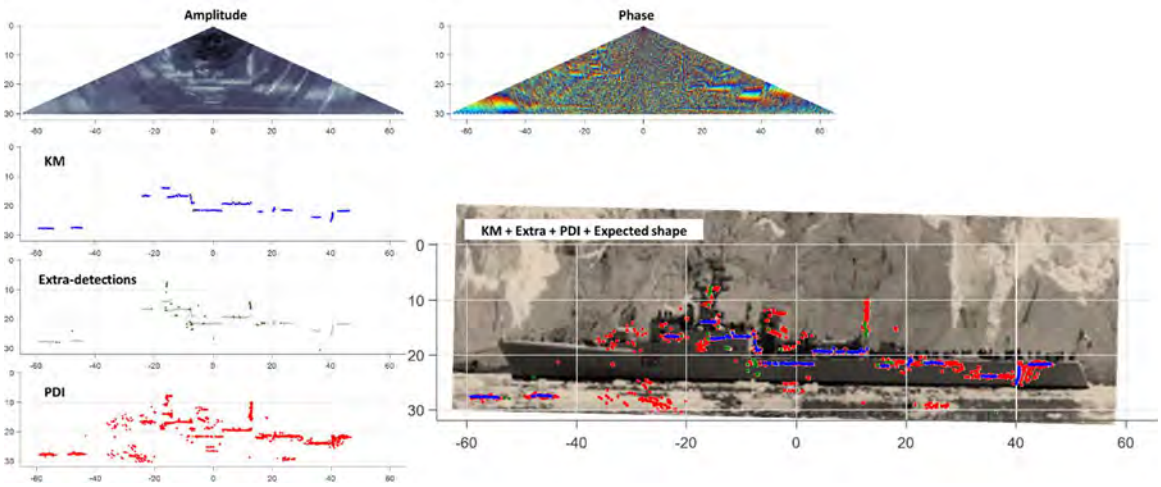

Figure 82 - Detections in a longitudinal profile of a shipwreck.

Considering all the cases presented here, it was seen that the PDI, like all other methods, has advantages and disadvantages. The presence of undesirable spikes (false detections) and gaps induces the need to improve the thresholds used. However, its ability to acquire multiple detections within a beam under suspended objects under various orientations (particularly features aligned with the beam) extends the detection of conventional direction-based methods.

CHAPTER 5 - CONCLUSIONS, DISCUSSIONS, AND SUGGESTIONS FOR FUTURE WORK

5.1 – Conclusions

As provided for in the stipulated research objectives, a seafloor/target detection algorithm was developed, built on a time-slice approach, and including phase difference information from the water column. This algorithm was tested in four different areas, all of them in shallow waters due to the characteristics of the echosounder used. These areas were used to verify the detection capacity in six study objects:

- Cubes sitting on the seabed of 1 or 0.5 meter-side, with or without a pole, at a depth of 20 meters, under different angles of incidence.

- Cubes of 1 meter-side, with or without a pole, at a depth of 40 meters, under different angles of incidence.

- Low relief planar or undulating seafloor.

- Extreme shallow waters where partial shadows are cast at the lowest grazing angles.

- HMCS Mackenzie shipwreck, with an emphasis on its longitudinal profile and the detection of suspended mast-like objects.

- MV GB Church shipwreck, with an emphasis on its longitudinal profile and the detection of multiple orientation suspended objects, including vertical (mast), horizontal (ribs in hold) or oblique (davits).

The study objects described above culminated in 57 different cases. A comparison of these results was made with the results obtained by using the conventional direction-based methods, as described as follows.

Recalling the research questions asked in chapter 1, we have:

A) Is the phase difference information logged in the water column data able to perform seafloor or target detection using time-based methods (analogous to, and in concert with, BDI approach)?

The results show that the use of phase data applied in time-based methods is capable of generating solutions for both extended seafloors and discontinuous target detection. As detection is acquired on a time-slice rather than a beam-slice approach, if there are valid echoes, commonly many multiple detections are obtained within the view of a single beam forming channel. This contrast with the standard singular (or very closely spaced if HDBF) solutions from direction-based methods. Even when the multi-detect option is enabled for beam-slice approaches, the number of solutions for a single beamforming channel remains very small.

B) How do the results obtained by this method behave when compared to the solutions obtained by conventional along-beam methods?

After comparing the methods (see the appendix to this study), it was observed that:

i - Notably, conventional along-beam results are "cleaner" and better represent continuous surfaces when there are no sudden variations in shape. The lower apparent sounding noise reflects the fact that whether amplitude or phase, the along-beam approach is implicitly doing time averaging (WMT, or phase slope fitting). In contrast, as implemented herein, across-beam solutions are estimated independently for a single time slice with no slice-to-slice time averaging, which results in an inclusion of noise and higher variance, particularly in the extremities of the swath.

ii - PDI has worse performance in low relief seafloor, presenting some gaps in the vicinity of the nadir region. This is still a marked improvement over the BDI method which has even less

capability at near normal incidence, but is still notably poorer and less dense than the direction-based amplitude detection solutions.

iii - In general, PDI solutions are limited to a smaller angular opening, due to the problem of incomplete retention of the full angular series that significantly affect the outermost beams.

iv - In low relief undulating seafloor, the PDI was able to maintain detections consistent with the adjacent bathymetric profile in situations where the conventional direction-based method often either did not produce a solution or tracked an erroneous one.

v - The PDI's ability to detect mast-like objects stands out, displaying a better definition of the objects even when it is ignored by the conventional method, as seen in the cases of longitudinal profiles of shipwrecks, poles, masts, lifeboat davits, or loading spar, using multiple detections within the same beam. This is interpreted to reflect two aspects. Firstly, the fact that such targets are discontinuous in that they do not completely occupy the full beam solid angle. As a result, with along-beam approach they are thus are obscured with time averaging including time sample that exclude the target of interest. Secondly, for targets that lie almost parallel to the beam, the intensity and/or phase do not notably change resulting in neither a clear echo peak or a coherent phase sweep. In contrast, time-slice approaches address the first problem by only examining that time subset (equivalent to the range resolution) when the target is within the beam solid angle, and, for the second problem, they take advantage of the fact that the intensity and phase both vary rapidly and coherently in the angle direction. It is important to note that these conclusions are restricted to the comparison made between PDI and the implementation of a manufacturer's direction-based method. Manufacturers of other equipment not analyzed may include different steps, generating different results and therefore different conclusions.

vi - Given the characteristic of the cubes, its correct angular definition and aspect ratio is best represented by the PDI solutions. Again, this is interpreted to be because the cube is small with respect to the projected beam footprint. PDI is able to return a unique time angle pair for the time subset when the cube is within the beam footprint.

vii - Some spikes were observed in the transition between sectors, indicating that an adjustment in the applied automatic threshold should be made or requiring that the initial manual threshold be more restrictive. Some possibilities are presented in the discussion section.

vii - The number of spikes obtained in the PDI is highly dependent on the selection of the initial manual threshold. This dependence exists due to imperfections observed in the automatic threshold. Improvements in the automatic threshold can reduce the occurrence of spikes and even make the use of this initial manual threshold unnecessary.

Such results, particularly the existence of discontinuous geometries when conventional direction-based methods do not track well, indicate the complementary nature of the direction and time-based methods. Their combined use should become frequent, bringing greater strength to the bathymetric solutions used by hydrographic services.

Current direction-based amplitude (WMT) and phase detections, when used in a complementary way, already present a robust and reliable performance for common geometries like continuous seabed surfaces. As a result, they have become the most established and widespread methods over the last decades. However, under certain circumstances, these methods have some imperfections. The arrangement of the object within a beam can make it difficult to detect. Objects of discontinuous nature, with a rapid variation in depth, especially those which do not completely occlude the full beam, such as mast-like objects or cubes in low grazing angle, can

be rejected because they do not appear consistent with the neighboring data. In these special cases, an alternative approach can offer tools that increase confidence in the solution found and avoid its rejection.

The objective of this research was to evaluate the potential of using phase data in an unconventional approach, aiming to find solutions unnoticed by current methods. Tests were carried out in areas with flat or undulating seafloor, shipwreck, and cubes. The results indicate that this method is capable of providing complementary solutions, mainly:

- in the presence of mast-like objects;

- in situations where multiple detections occur within the same beam (for example, several decks aligned in a shipwreck or the separation between an object and the seabed);

- in the presence of seabed targets that are smaller than the projected beam footprint (e.g cubes); and

- in situations where the shape of the object results in abrupt depth or across track distance variations between consecutive beams.

Although the test was performed only with the EM2040P, the algorithm can be used in post-processing in other models, as long as WC data for both amplitude and phase are available. In addition, with modifications, it could also be used in real time in order to, together with the current methods, increase confidence in the soundings obtained and expand the resolution of the current equipment. The net result of this would be gains for the safety of navigation and the scientific community, due better representation of the seabed.

5.2 – Discussions

In addition to the conclusions presented above, a number of findings are worthy of discussion.

5.2.1 – is PDI providing significant advantages over the classic BDI approach?

In relation to the previous BDI work (Pereira, 2015), that this study aims to complement, the following improvements were noticed:

- The characteristic of the phase difference between two neighboring beams eliminates the need to adjust parabolas to represent the beam of the main lobe of the receiver, avoiding the study of the best number of points (3, 5 or more) to be used in the adjustment.
- In the BDI approach, there are gaps close to the limits of each sector, due to the need to include 3 or 5 points in the parabola adjustment. Although these gaps between sectors also occur in the PDI, the fact of disregarding only the data between the two neighboring beams around the boundary sector promotes a gap reduction. In other words, in PDI the gaps caused by sectors are only one beamwidth wide. With care, even without a zero crossing, the phase trend could be extrapolated out by half a beam width and fill even those gaps.
- The present algorithm is not limited to a maximum of two solutions per time-slice. As many solutions as possible were considered per time-slice. Its limitation is now controlled by the use of the manual and automatic threshold used.
- In the case of several overlapping peaks, generally close to near normal incidence, in which the BDI method fails when trying to adjust parabolas, the phase data remains useful for identifying and individualizing them, allowing selection of soundings. Thus, although still limited, detections in regions of normal incidence are possible.

5.2.2 – how does PDI compare to the multiple phase solutions in HDBF?

In relation to HDBF, PDI has the following advantages:

- The HDBF, in the implementation presented in this study, relies on having a significant number of time samples to establish a phase trend. If within the window of those time-samples a situation occurs where a target is attached to the seabed and appears and disappears within just a few time slices (such as the inward face of a cube at low grazing angles), the HDBF angle estimation is compromised. PDI algorithm can handle it independent of the information before or after, by using time-slices.

- The HDBF, in the implementation presented in this study, is built on the concept of time-series, with analysis within a beam, and uses predetermined values of quantity of time-samples or fixed phase difference angles to establish a phase trend. In this way, it is more subject to the occurrence of the previous case. For PDI, the analysis of each time-slice determines which direction should be sought. The search is based on the characteristics presented by the data and not on predetermined values. Thus, the presence of objects is emphasized, and the possibility that the objects are softened through time averaging is minimized.

5.2.3 – how can manual and automatic threshold values be improved?

i) Manual threshold

As implemented herein, a fixed level was investigated. This appeared adequate, for the few cases considered, although in reality only a limited depth range was investigated. For that threshold to be universally appropriate for any depth investigated, the TVG applied would need to at least grossly compensate for all range dependent effect (spherical spreading, attenuation and ensonified

area). Similarly, unless the EM2040P inter-sector source level variations and sector-specific beam pattern are adequately compensated this could compromise the initial threshold. This is equivalent to an angle varying gain (AVG).

For both these cases, the KM data handling (Hammerstad, 2000) does a reasonable first order compensation. Even with those TVG and AVG, the choice of threshold would be dependent on the seabed target strength. Thus, variations in sediment type are important. It might be worth looking at the typical apparent backscatter strength estimates to allow automatic shifting of the initial threshold.

Lastly noise level is of concern. For most situations where the SNR is adequate, the threshold would not be sensitive. But to have a universally robust threshold estimator, situations where high vessel noise (e.g. higher prop speeds), or when operating the sonar close to is maximum range limit, could compromise this.

ii) Automatic threshold

The developed algorithm does not limit the number of solutions per time-slice, allowing all sectors to present several solutions. Given the unique characteristics of each time-slice, the automatic threshold generates different threshold values for each sector. The challenge is to find a balance between accepting an unlimited number of solutions or rejecting the entire sector when they do not exist. The current algorithm considered the highest mean-range value as a reference for the lowest acceptable automatic threshold value in other sectors. This choice, however, allows false detections.

Two future attempts at a solution are envisaged to minimize this problem. One of them would be to establish a lower cutoff from maximum value for automatic minimum threshold, for

example, 30% instead of 50%. The other would be to establish a fixed tolerable amount below the maximum amplitude, for example, a reduction of 15 dB.

5.3 – Suggestions for future works

The current algorithm developed is certainly not a finished product. Although significant effort has been expended, the following improvements are recognized that need to be addressed in future research, such as:

- Improvement in the calculation of the uncertainties of each sounding, taking into account the temporal and the angular uncertainties involved.

- Reduction of random noise in each time-slice by doing at least a few time-samples averaging in the phase data of each beam, removing the noisy characteristic of the phase.

- Improvement of the dynamic threshold parameters (as discussed above), with changes in the lowest acceptable automatic threshold value and limits created (upper and lower limit range), with an assessment of whether it is more permissive in the nadir region (higher cutoff and lower limit range) or the use of automatic values for each time-slice, to better obtain the relevant solutions and eliminate spurious data.

- Improve the comparison between the amplitudes of data from different sectors, to reduce the chance of spikes occurring due to the transition between sectors. Better sector source level and beam pattern compensation would help on this (as discussed above).

- Apply the correct (not an estimation) value of the split-beam acoustic center distance, "s", by asking the manufacturer or calculating it to have a statistically more representative value and results.

- In case the split-beam acoustic center distance ("s") is known, evaluate the individual use of more neighboring beams to determine the DOA, in order to promote the reduction of variance and reduce the uncertainties associated with this measurement.

- Establish criteria for rejection of soundings using along-track filtering, avoiding use of sidelobes of the transmitted beam in the solution, avoiding the stretching of the objects detected in the results.

- Improve the overall performance of the algorithm. While recognizing that MATLAB is ideal for algorithmic development and ease of data manipulation, the “all-in-memory” current implementation is not efficient for the rapid application of the final algorithm.

- Convince manufacturers of the importance of making complete water column data available, including those after the main detection, in the form of an optional record according to the operator's choice, so that the problems described with time-slice gaps are avoided, allowing studies that make the algorithm more robust.

- Convince operators that logging this information is beneficial.

- And finally, recognizing that TOA and DOA methods often excel in quite different but complementary geometries, future algorithms should consider applying both approaches and dynamically selecting solutions where the geometry is favored. For example, at low grazing angles, when no short wavelength targets are showing up in PDI or BDI, the smoother TOA HDBF solution should be selected. In contrast, when short duration discontinuous targets, such as cubes or masts, are identified, the BDI or PDI solution should be chosen. Such an approach would examine a moving local 2D time-angle array to monitor the amplitude and phase characteristics within. The preferred direction of analysis will depend on the variation of phase information along or across beams, avoiding the path that presents quasi-constant values.

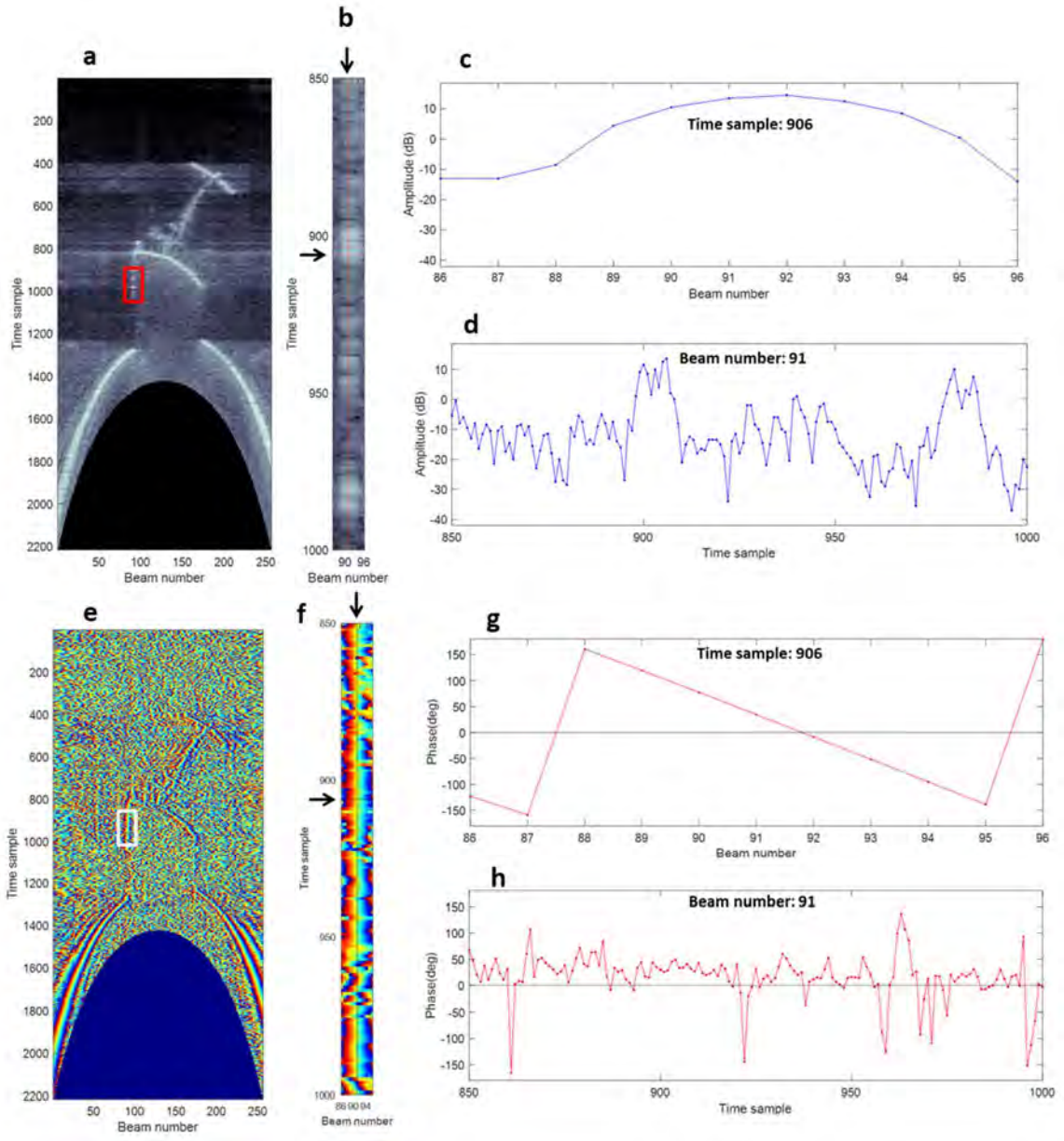

Figure 83 – Across and along beam data. The images from "a" to "d" refers to the amplitude data, and from "e" to "h" refers to the phase data. "a" and "e" show the complete water column data, with a rectangle emphasizing a small region. "b" and "f" display a zoom in the data related to the rectangle. "c" and "g" show part of the time-slice 906. "d" and "h" show part of the beam 91 time-series. Note that the amplitude peaks (in "c" and "d") are associated with the shipwreck's lateral extent. While "g" clearly shows a zero-crossing, this evaluation is not possible in "h", emphasizing that the geometry of this case favors detection by PDI.

The essence of this last idea is represented in Figure 83. In it, the phase data of a swath is shown on “e”. A white rectangle indicates the location under analysis, whose zoom in is shown in

the “f”. The black arrows indicate a time-slice (in time-sample 906) and a time-series (in beam number 91). The time-slice phase data is shown at “g” and the time-series phase data is displayed at “h”. Observe how it is clearly identified in the time-slice that the phase crosses zero between beams 91 and 92. On the other hand, the quasi-constant aspect of the phase data in this time-series does not allow identifying the instant that could be attributed to the detection. In this case, in the region defined by the white rectangle, the preferred direction of analysis is across beams using the PDI.

REFERENCES

- BURDIC, W.S. (1991). Underwater Acoustic System Analysis. 2nd Edition. Prentice-Hall.

- COLBO, K., ROSS, T., BROWN, C., and WEBER, T. (2014). A review of oceanographic applications of water column data from multibeam echosounders. Estuarine, Coastal and Shelf Science, vol 145, pp 41-56.

- DE MOUSTIER, C. (1988). State of the Art in Swath Bathymetry Survey Systems. International Hydrographic Review, Vol 65(2).

- DE MOUSTIER, C. (1993). Signal processing for swath bathymetry and concurrent seafloor acoustic imaging. In: MOURA J. M. F., Lourtie I. M. G. (eds). Acoustic Signal Processing for Ocean Exploration. NATO ASI Series (Series C: Mathematical and Physical Sciences), vol 388. Springer, Dordrecht.

- DE MOUSTIER, C. (2009). Bottom detection methods. Lecture Notes nº10. 51st Multibeam Sonar Training Course, Rio de Janeiro, Brazil.

- DIRETORIA DE HIDROGRAFIA E NAVEGAÇÃO (DHN, 2017). Normas da Autoridade Marítima Para Levantamentos Hidrográficos - NORMAM-25/DHN. 2ª Rev.

- FARR, H.K. (1980). Multibeam bathymetric sonar: Sea Beam and Hydrochart. Marine Geodesy, Vol.4(2).

- GERLOTTO, F., SORIA, M., and FRÉON, P. (1999). From two dimensions to three: the use of multibeam sonar for a new approach in fisheries acoustics. Canadian Journal of Fisheries and Aquatic Sciences. Vol 56. pp 6–12.

- GLENN, M.F. (1970). Introducing an operational multi-beam array sonar. International Hydrographic Review, Vol. 47(1), pp. 35-39.

- HAMMERSTAD, E. (2000). Backscattering and Seabed Image Reflectivity. EM technical note.

- HAMMERSTAD, E., POHNER, F., PARTHIOT, F., and BENNETT, J. (1991). Field testing of a new deep water multibeam echo sounder. Proceedings of the IEEE Oceans'91, Vol.2.

- HARE, R., GODIN, A., MAYER, L.A. (1995). Accuracy estimation of Canadian swath (multibeam) and sweep (multitransducer) sounding systems. Technical report. Canadian Hydrographic Service and University of New Brunswick, Fredericton.

- HUGHES CLARKE, J.E. (1998). The effect of fine scale seabed morphology and texture on the fidelity of swath bathymetric sounding data. Proceedings of the Canadian Hydrographic Conference, 168-181.

- HUGHES CLARKE, J.E. (2006). Applications of multibeam water column imaging for hydrographic survey. The Hydrographic Journal, April Issue. Vol. 120. pp 3-15.

- HUGHES CLARKE, J.E. (2018). Multibeam Bottom Detection (C-14). Lecture notes. ESCI 874 Integrated Seabed Mapping Systems, University of New Hampshire, Durham, N.H.

- HUGHES CLARKE, J.E., BRUCKER, S. and CZOTTER, K. (2006a). Improved Definition of Wreck Superstructure using Multibeam Water Column Imaging. Lighthouse, Journal of the Canadian Hydrographic Association, edition nº.68.

- HUGHES CLARKE, J.E., LAMPLUGH, M. and CZOTTER, K. (2006b). Multibeam Water Column Imaging: Improved Wreck Least-Depth Determination. Proceedings, Canadian Hydrographic Conference.

- HUGHES CLARKE, J.E., MARTINOLICH, R. and SMITH, G. (2013). EM 2040/EM 710 target detection trials: What qualifies as a successful detection? Forum for Exchange of Mutual Multibeam Experiences (FEMME), Boston, USA, April 18th (presentation only).

- INTERNATIONAL HYDROGRAPHIC ORGANIZATION (IHO, 2005). Manual on Hydrography - Publication C-13 (1st Edition). International Hydrographic Bureau, Monaco.

- INTERNATIONAL HYDROGRAPHIC ORGANIZATION (IHO, 2008). IHO Standards for Hydrographic Surveys - Special Publication No. 44 (5th Edition). International Hydrographic Bureau, Monaco.

- JIN, G., and TANG, D. (1996). Uncertainties of differential phase estimation with interferometric sonars, IEEE Journal of Oceanic Engineering, Vol 21, pp 53-63.

- KONGSBERG MARITIME (2017). EM 2040P Multibeam echo sounder - Installation manual (document number: 417418, Revision: B, December/2017). Horten, Norway.

- KONGSBERG MARITIME (2018). EM datagrams on *.kmall format (document number: 410224, Revision: F, November/2018). Horten, Norway.

- KONGSBERG MARITIME (2019). SIS - Seafloor Information System Reference Manual. Release 5.2 (document number: 429004, Revision: C, April/2019). Horten, Norway.

- LURTON, X. (2000). Swath bathymetry using phase difference: Theoretical analysis of acoustical measurement precision. IEEE Journal of Oceanic Engineering, vol 25(3), pp 351-363.

- LURTON, X. (2001). Précision de mesure des sonars bathymétriques en fonction du rapport signal/bruit. Traitement du Signal. Vol.18(3). pp 179-194.

- LURTON, X. (2008). Interferometry for Bathymetry Sonars: Accuracy, Resolution and Quality Factor. Shallow Survey 2008 Conference, Portsmouth, NH, October 21st (presentation only).

- LURTON, X. (2010). An Introduction to Underwater Acoustics - Principles and Applications (Second Edition). London: Springer / Praxis Publishing.

- LURTON, X., and AUGUSTIN, J.M. (2010). A Measurement Quality Factor for Swath Bathymetry Sounders. IEEE Journal of Oceanic Engineering. Vol 35(4), pp.852-862.

- MARQUES, C.R.V. (2012). Automatic mid-water target detection using multibeam water column. M.Sc.E. thesis, Department of Geodesy and Geomatics Engineering, University of New Brunswick, Fredericton, Canada.

- MARQUES, C.R.V., and HUGHES CLARKE, J.E. (2012). Automatic Mid-Water Target Tracking using Multibeam Water Column. Proceedings of the Canadian Hydrographic Conference, Niagara Falls.

- MAYER, L.A., HUGHES CLARKE, J.E. and DIJKSTRA, S. (1997). Multibeam Sonar: Applications in fisheries research. In: Changing Oceans and Changing Fisheries: Environmental Data for Fisheries Research and Management. Eds. G.W Boehlert and J.D. Schumacher. National Oceanographic and Atmospheric Administration. Vol. NOAA-TM-NMFS-SWFSC. pp. 79-92.

- MAYER, L.A., LI, Y., MELVIN, G. (2002). 3D visualization for pelagic fisheries research and assessment. ICES Journal of Marine Science. Vol. 59, pp.216-225.

- MORGERA, S.D. (1976). Signal processing for precise ocean mapping. IEEE Journal of Oceanic Engineering, vol OE-1, nº2.

- MORGERA, S.D., and SANKAR, R. (1984). Digital signal processing for precision wide-swath bathymetry. IEEE Journal of Oceanic Engineering, vol OE-9, nº2.

- PEREIRA, D.L.S. (2015). Improving Shallow-Water Multibeam Target Detection at Low Grazing Angles. M.Sc. thesis, Department of Geodesy and Geomatics Engineering, University of New Brunswick, Fredericton, Canada.

- PEREIRA, D.L.S. and HUGHES CLARKE, J.E. (2015). Improving shallow water multibeam target detection at low grazing angles. Proceedings of the US Hydrographic Conference, National Harbor, MD. 21pp.

- POHNER, F. and LUNDE, E.B. (1990). Hydrographic Applications of Interferometric Signal Processing. Proceedings of the FIG XIX Congress, Commission 4, Helsinki.

- SATRIANO, J.H., SMITH, L.C. and AMBROSE, J.T. (1991). Signal processing for wide swath bathymetric sonars. Proceedings of the IEEE Oceans'91, Vol.1.

- SEABEAM Instruments. (2000). Multibeam sonar theory of operation (Manual), East Walpole, USA.

- TUCKER, M.J. (1961). Beam identification in multi-beam echo-sounders. International Hydrographic Review, Vol. 38(2), pp. 25-32.

- VAN DER WERF, A. (2010). Mast tracking capability of EM 3002D using Water Column Imaging. M.Sc. thesis, Department of Geodesy and Geomatics Engineering, University of New Brunswick, Fredericton, Canada.

APPENDIX

For the present study, six objectives were defined: cubes at 20 m depth, cubes at 40 m depth, low relief seafloor, extremely shallow water with shadows, HMCS Mackenzie shipwreck, and MV GB Church shipwreck. Each objective presents several different situations, totaling 57 cases analyzed. Table 6 summarizes all cases, and the following pages of this appendix present a set of 16 images for each example, including the amplitude and phase data of the swath, the solutions by KM's bottom detection and by the extra-detections process, PDI (with two thresholds) and a combined image of all cases. In addition to the swath overview, a zoom in on the chosen feature is also available. For more details about the lines, see tables 3 and 4, and Figure 65.

Objective	Area	Target	Case	Line	Obs
01	Cubes at 20 m depth	Cube (1.0 meter side) with pole	01-1a	0014_20191010_181817	Incidence angle: 9.01º
			01-1b	0029_20191010_191602	Incidence angle: 41.52º
			01-1c	0026_20191010_190729	Incidence angle: 52.37º
			01-1d	0024_20191010_185857	Incidence angle: 62.07º
			01-1e	0022_20191010_185001	Incidence angle: 68.09º
			01-1f	0020_20191010_184042	Incidence angle: 70.85º
			01-1g	0017_20191010_183108	Incidence angle: 73.40º
		Cube (0.5 meter side), no pole	01-2a	0029_20191010_191602	Incidence angle: 12.46º
			01-2b	0014_20191010_181817	Incidence angle: 16.08º
			01-2c	0026_20191010_190729	Incidence angle: 36.71º
			01-2d	0024_20191010_185857	Incidence angle: 51.62º
			01-2e	0022_20191010_185001	Incidence angle: 67.70º
			01-2f	0020_20191010_184042	Incidence angle: 68.44º
			01-2g	0017_20191010_183108	Incidence angle: 72.16º
		Cube (1.0 meter side), no pole	01-3a	0014_20191010_181817	Incidence angle: 1.94º
			01-3b	0029_20191010_191602	Incidence angle: 25.52º
			01-3c	0026_20191010_190729	Incidence angle: 45.27º
			01-3d	0024_20191010_185857	Incidence angle: 56.48º
			01-3e	0022_20191010_185001	Incidence angle: 62.94º
			01-3f	0020_20191010_184042	Incidence angle: 66.81º
			01-3g	0017_20191010_183108	Incidence angle: 71.34º
		Cube (0.5 meter side) with pole	01-4a	0014_20191010_181817	Incidence angle: 6.89º
			01-4b	0029_20191010_191602	Incidence angle: 26.26º
			01-4c	0026_20191010_190729	Incidence angle: 42.66º
			01-4d	0024_20191010_185857	Incidence angle: 54.98º
			01-4e	0022_20191010_185001	Incidence angle: 62.98º
			01-4f	0020_20191010_184042	Incidence angle: 66.84º
			01-4g	0017_20191010_183108	Incidence angle: 70.01º

Objective	Area	Target	Case	Line	Obs
02	Cubes at 40 m depth	Cube (1.0 meter side) with pole	02-1a	0015_20191010_182233	Incidence angle: 0.88º
			02-1b	0027_20191010_191150	Incidence angle: 21.41º
			02-1c	0025_20191010_190323	Incidence angle: 40.35º
			02-1d	0023_20191010_185445	Incidence angle: 52.37º
			02-1e	0019_20191010_183610	Incidence angle: 66.23º
			02-1f	0016_20191010_182619	Incidence angle: 69.61º
		Cube (1.0 meter side), no pole	02-2a	0015_20191010_182233	Incidence angle: 8.30º
			02-2b	0027_20191010_191150	Incidence angle: 29.24º
			02-2c	0025_20191010_190323	Incidence angle: 45.26º
			02-2d	0023_20191010_185445	Incidence angle: 56.76º
			02-2e	0019_20191010_183610	Incidence angle: 66.97º
			02-2f	0016_20191010_182619	Incidence angle: 71.44º
03	HMCS Mackenzie shipwreck	Low relief seafloor	03-1	0048_20191008_195040	~ 30 m depth
	MV GB Church shipwreck		03-2	0013_20191007_174133	20 ~ 25 m depth
	Cubes at 20 m depth		03-3	0029_20191010_191602	15 ~ 20 m depth
04	Squamish Delta	Extreme shallow water with shadows	04-1	0010_20190616_004957	4 ~ 5 m depth
			04-2	0010_20190616_004957	~ 4 m depth
			04-3	0015_20190616_010445	4 ~ 6 m depth
05	HMCS Mackenzie shipwreck	Mooring line to stern	05-1	0041_20191008_194038	---
		Longitudinal profile	05-2	0046_20191008_194820	line at midship
		Rear Mast	05-3	0050_20191008_195405	line from bow to stern
			05-4	0051_20191008_195549	line from stern to bow
06	MV GB Church shipwreck	Longitudinal profile	06-1	0009_20191007_173625	line from port to starboard
			06-2	0010_20191007_173733	line from starboard to port
		Foremast	06-3	0012_20191007_174024	---
		Lifeboat Davits	06-4	0014_20191007_174252	---
		Mid section	06-5	0014_20191007_174252	---
		Mid section with loading spar	06-6	0014_20191007_174252	---
		Longitudinal profile	06-7	0015_20191007_174438	line at midship

Table 6 – Analyzed cases.

Case: 01-1a

Area: Cubes at 20 m depth. **Target:** Cube (1.0 meter side) with pole. **Line:** 0014_20191010_181817. **Ping number:** 526.

Manual Threshold: 90th percentile: -13.0 dB. **Min KM:** -15.5 dB. **Incidence angle:** 9.01º.

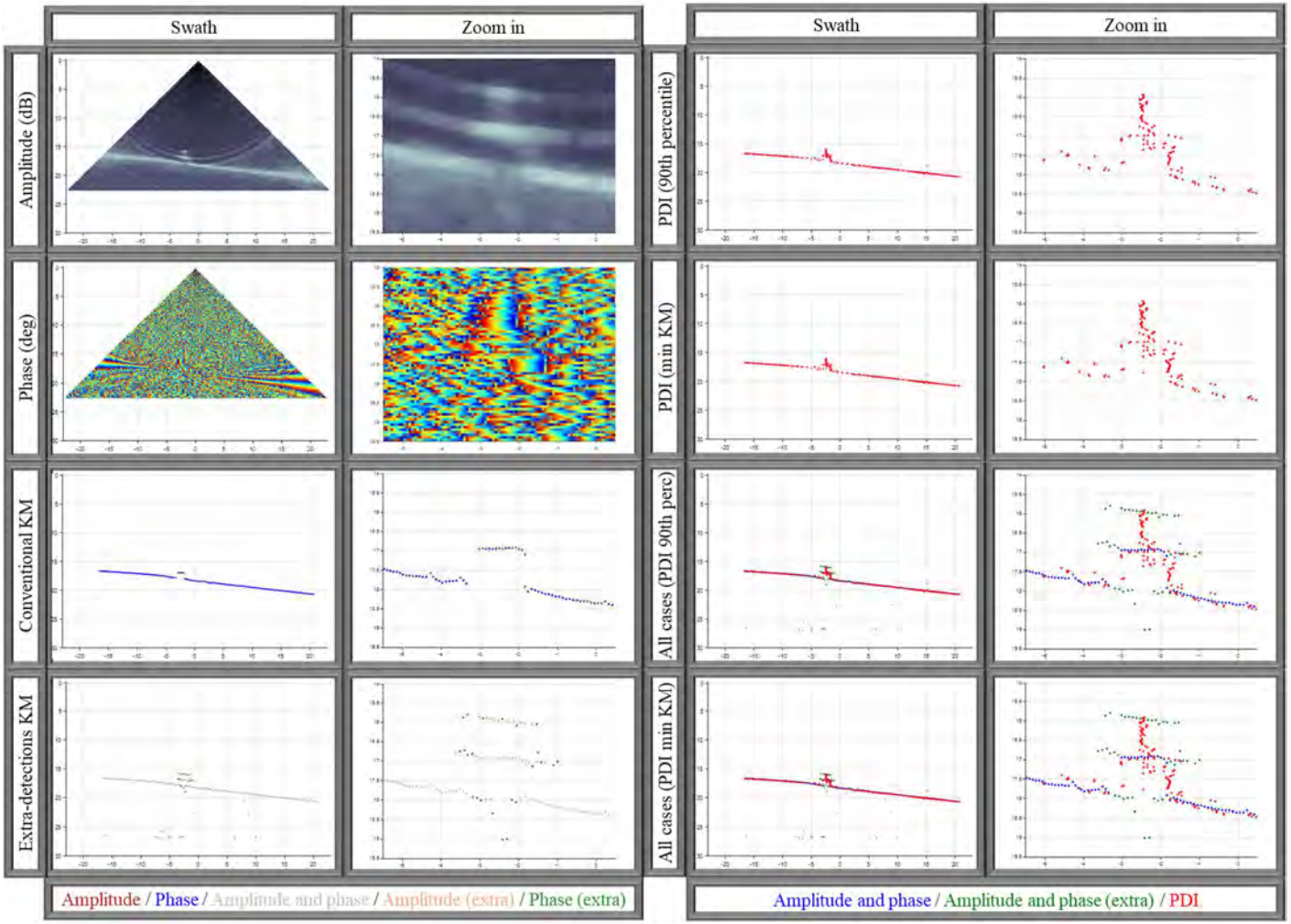

Case: 01-1b

Area: Cubes at 20 m depth. **Target:** Cube (1.0 meter side) with pole. **Line:** 0029_20191010_191602. **Ping number:** 1581.

Manual Threshold: 90th percentile: -7.5 dB. **Min KM:** -16.0 dB. **Incidence angle:** 41.52º.

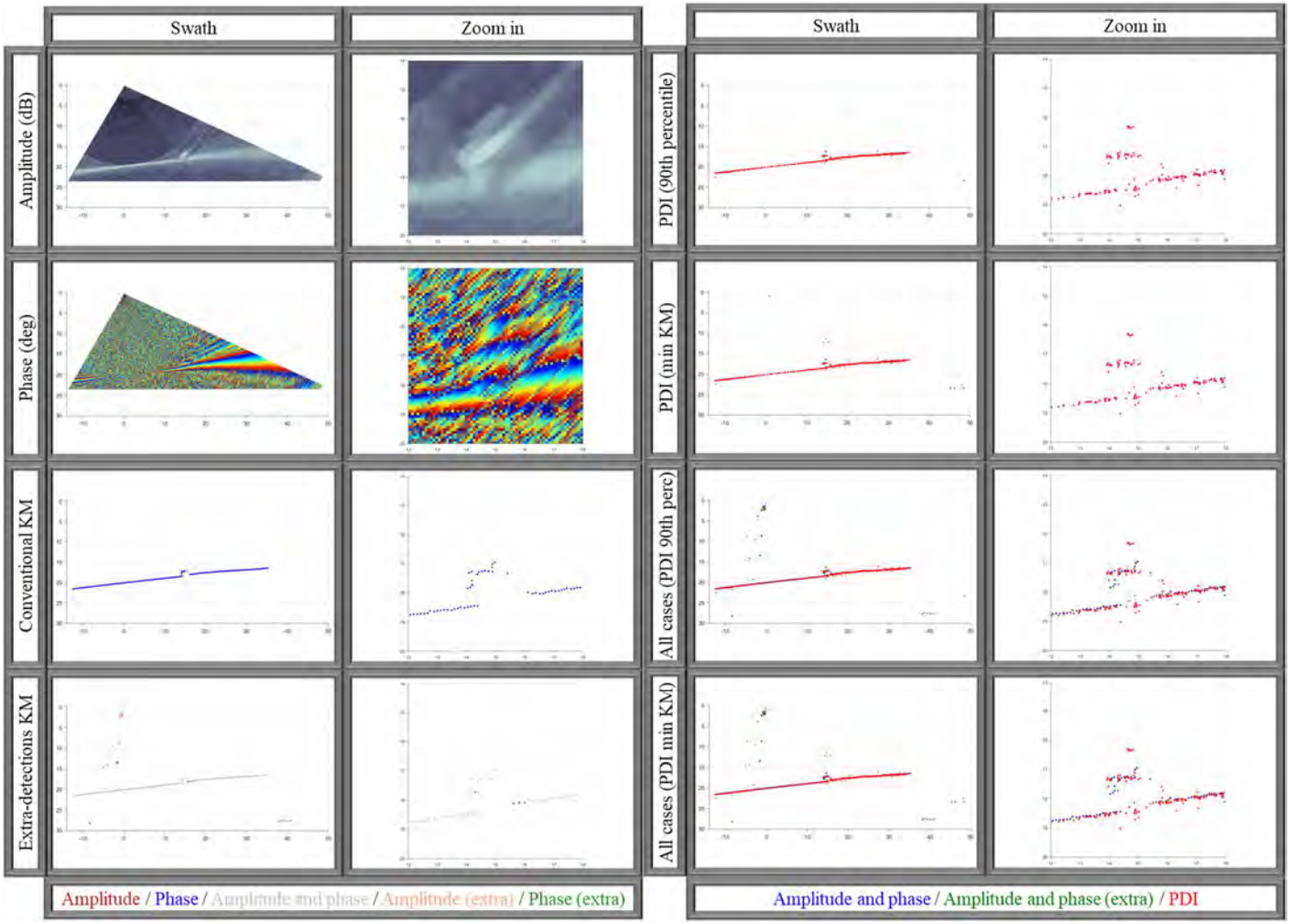

Case: 01-1c

Area: Cubes at 20 m depth. **Target:** Cube (1.0 meter side) with pole. **Line:** 0026_20191010_190729. **Ping number:** 1521.

Manual Threshold: 90th percentile: -7.5 dB. **Min KM:** -4.5 dB. **Incidence angle:** 52.37º.

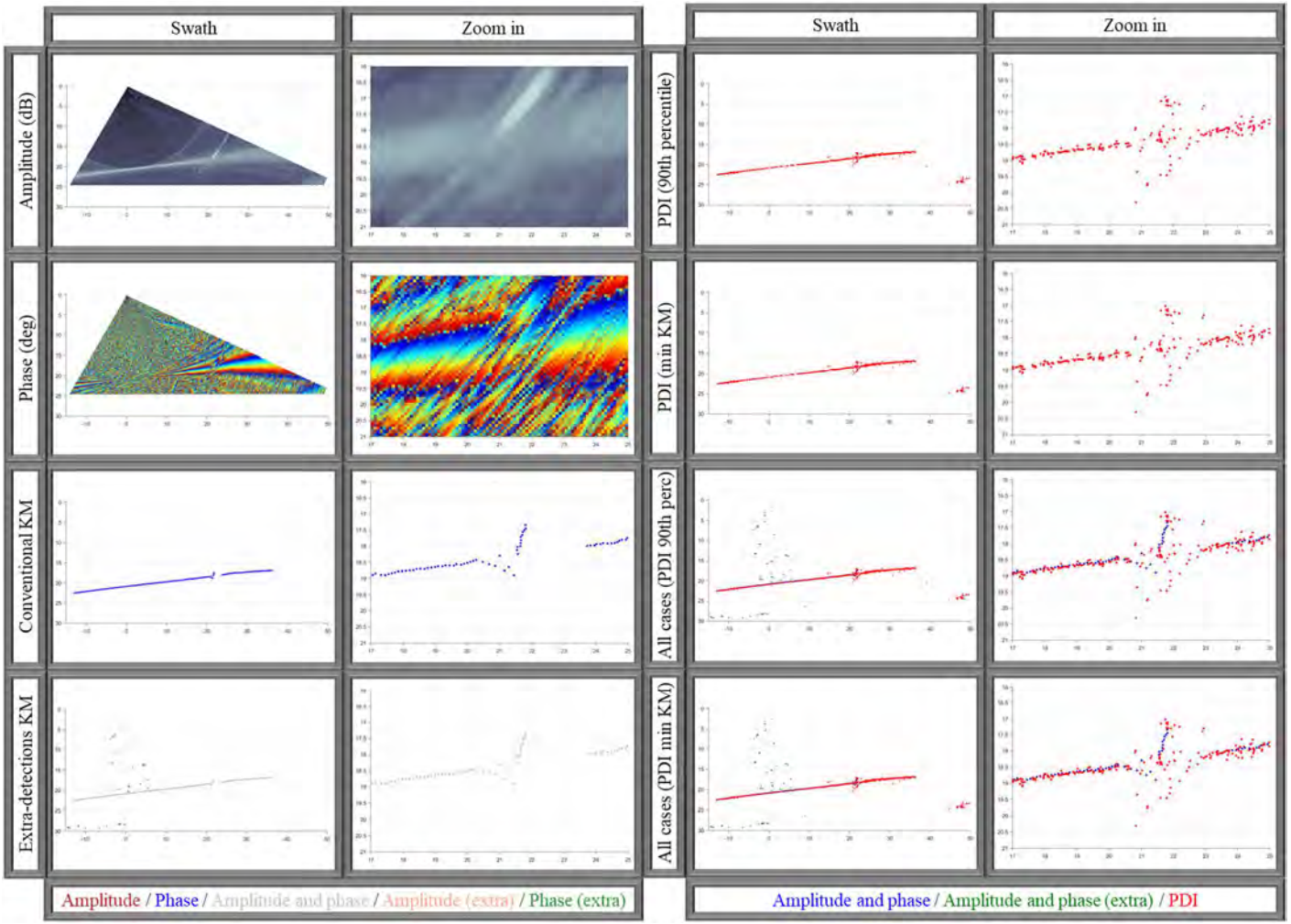

Case: 01-1d

Area: Cubes at 20 m depth. **Target:** Cube (1.0 meter side) with pole. **Line:** 0024_20191010_185857. **Ping number:** 1564.

Manual Threshold: 90th percentile: -10.0 dB. **Min KM:** -5.5 dB. **Incidence angle:** 62.07º.

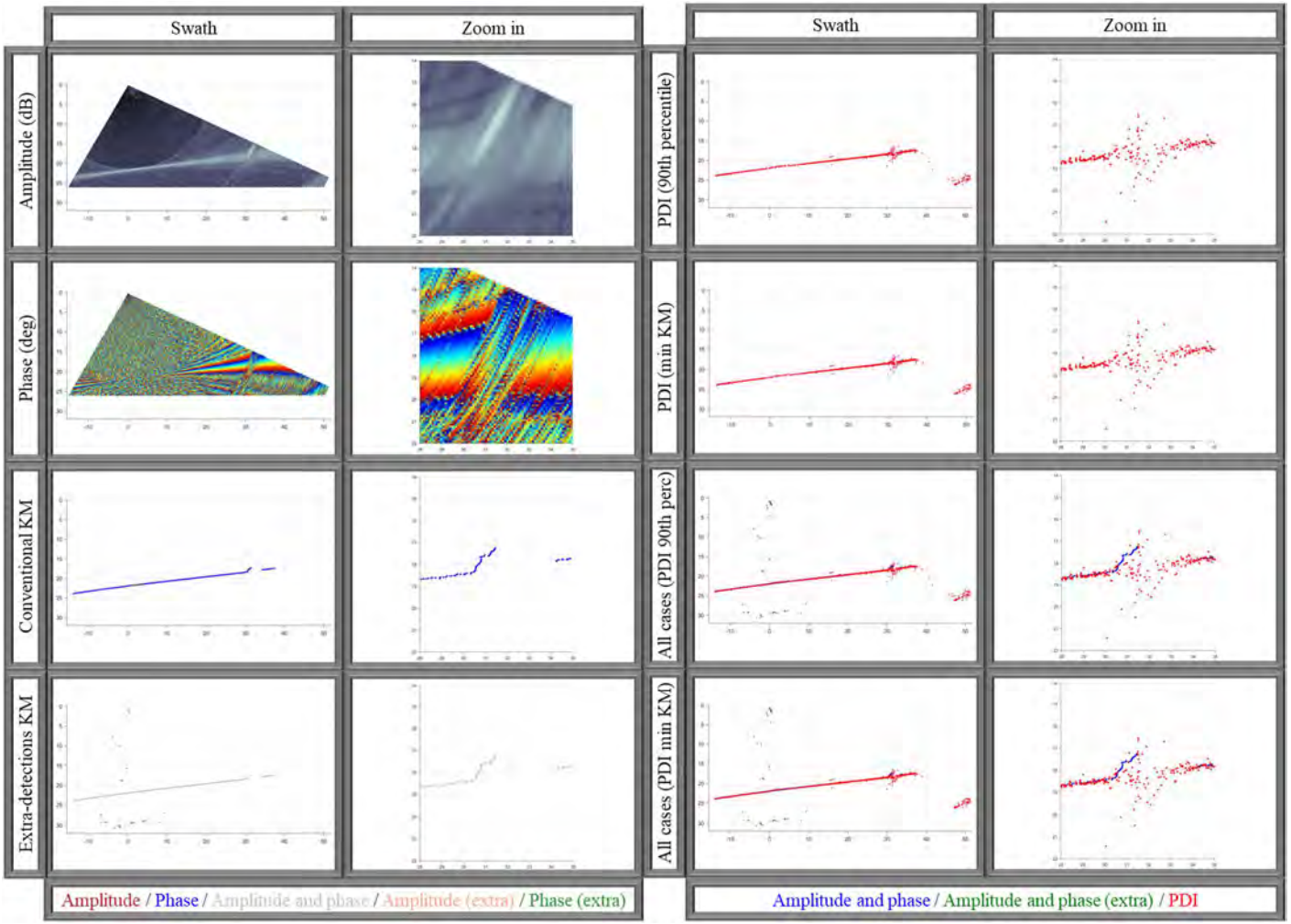

Case: 01-1e

Area: Cubes at 20 m depth. **Target:** Cube (1.0 meter side) with pole. **Line:** 0022_20191010_185001. **Ping number:** 1420.

Manual Threshold: 90th percentile: -6.5 dB. **Min KM:** -4.5 dB. **Incidence angle:** 68.09º.

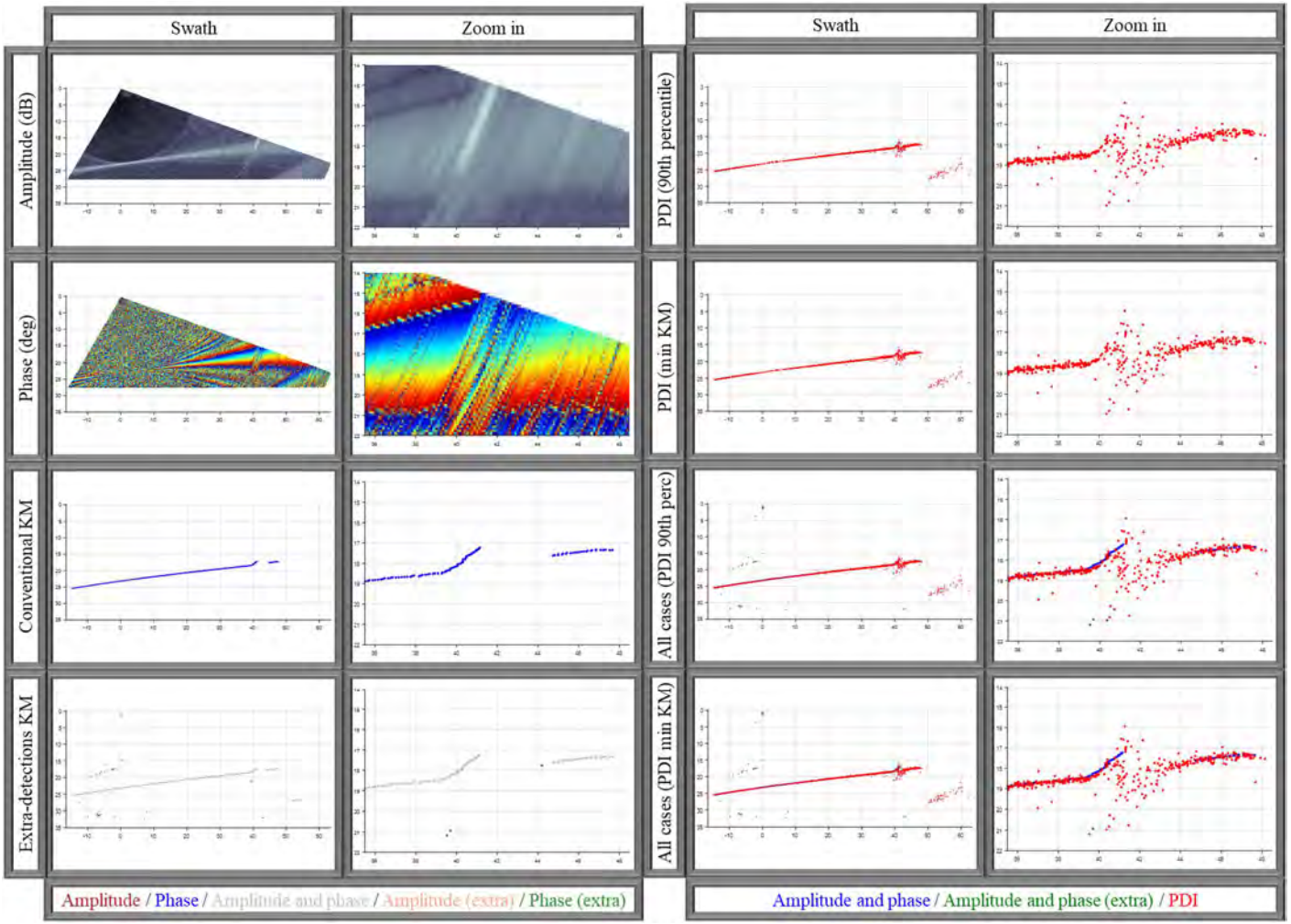

Case: 01-1f

Area: Cubes at 20 m depth. **Target:** Cube (1.0 meter side) with pole. **Line:** 0020_20191010_184042. **Ping number:** 1368.

Manual Threshold: 90th percentile: -4.5 dB. **Min KM:** -7.5 dB. **Incidence angle:** 70.85º.

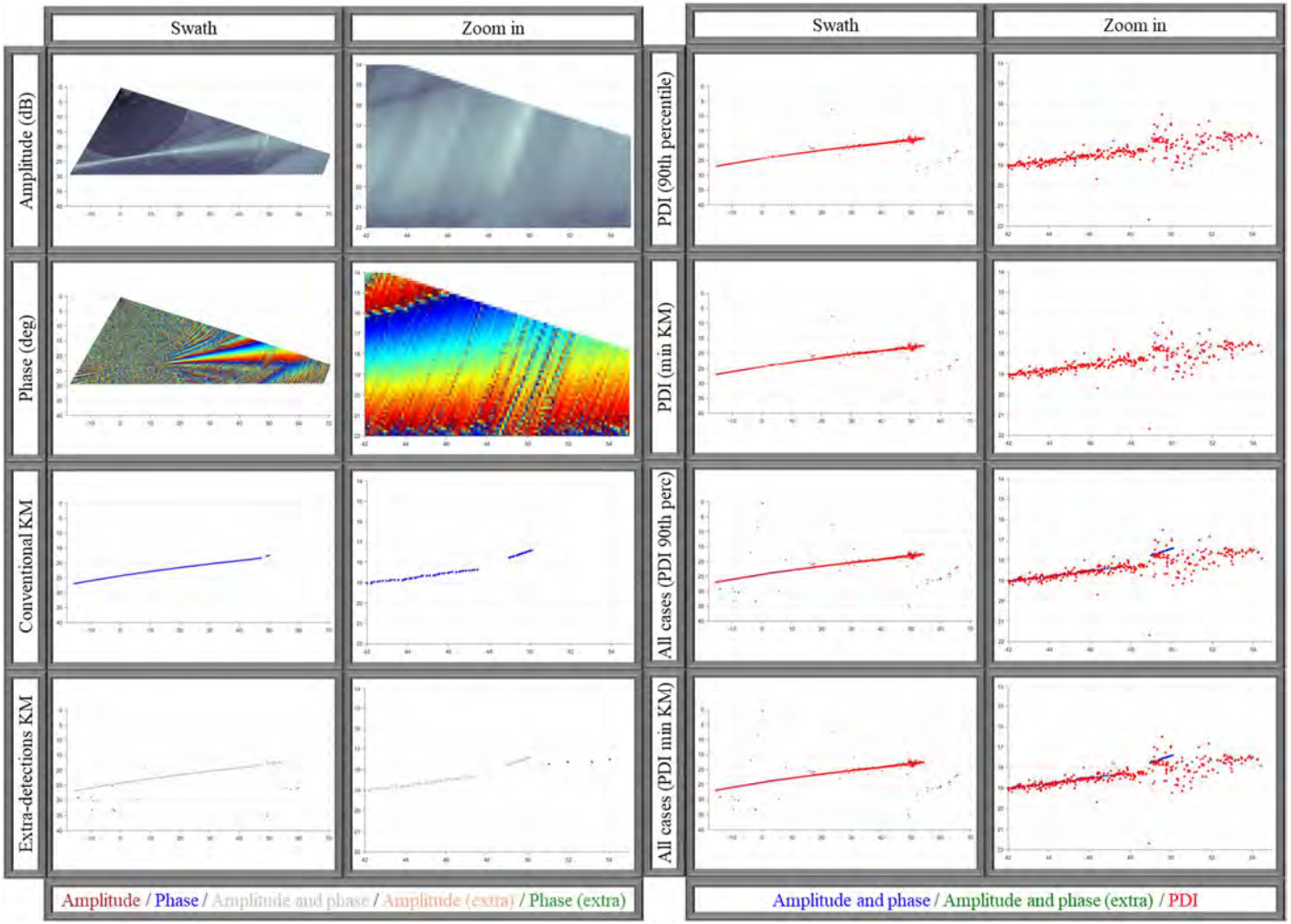

Case: 01-1g

Area: Cubes at 20 m depth. **Target:** Cube (1.0 meter side) with pole. **Line:** 0017_20191010_183108. **Ping number:** 1214.

Manual Threshold: 90th percentile: -1.0 dB. **Min KM:** -13.5 dB. **Incidence angle:** 73.40º.

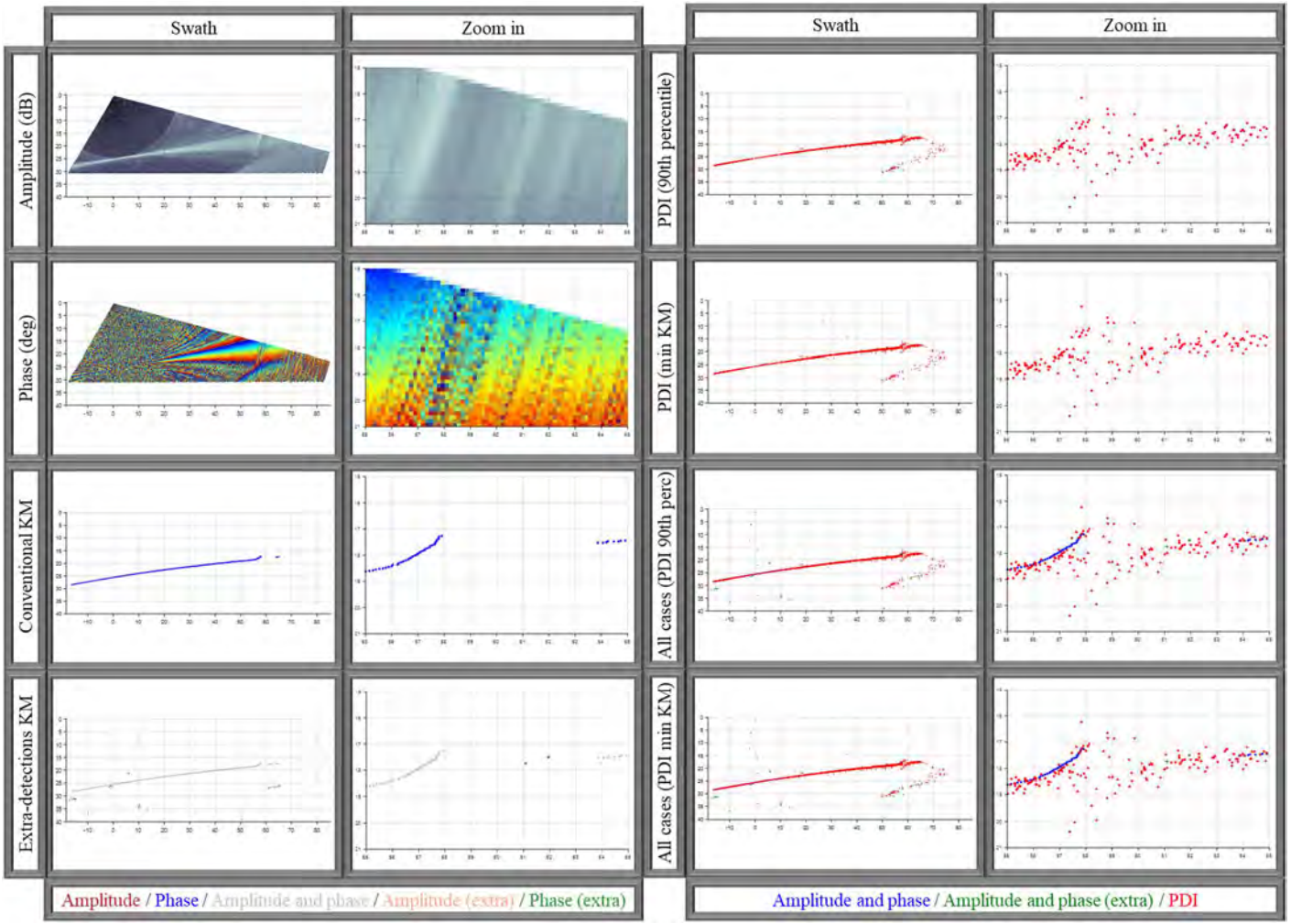

Case: 01-2a

Area: Cubes at 20 m depth. **Target:** Cube (0.5 meter side), no pole. **Line:** 0029_20191010_191602. **Ping number:** 1368.

Manual Threshold: 90th percentile: -10.0 dB. **Min KM:** -10.0 dB. **Incidence angle:** 12.46º.

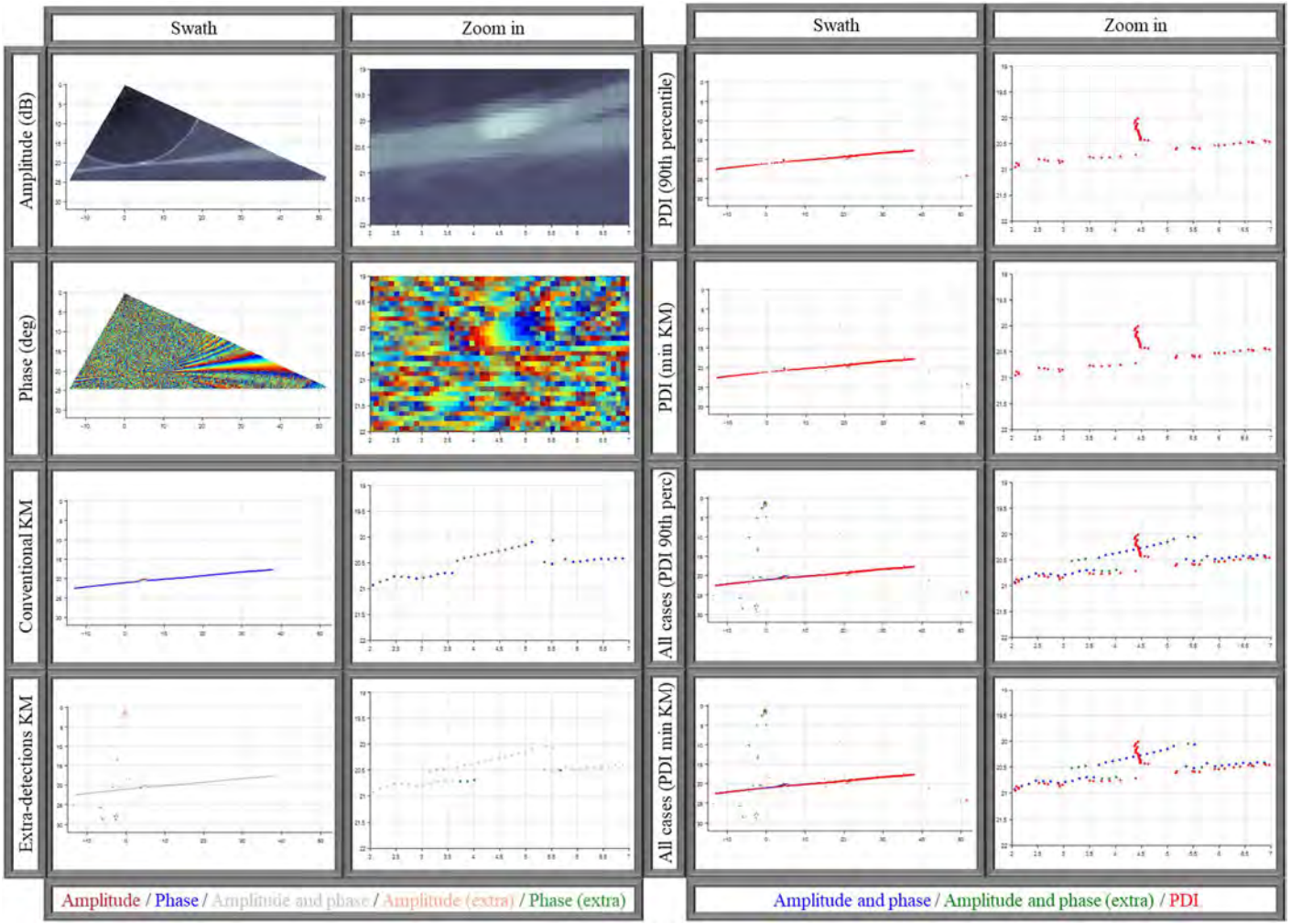

Case: 01-2b

Area: Cubes at 20 m depth. **Target:** Cube (0.5 meter side), no pole. **Line:** 0014_20191010_181817. **Ping number:** 757.

Manual Threshold: 90th percentile: -12.0 dB. **Min KM:** -14.0 dB. **Incidence angle:** 16.08º.

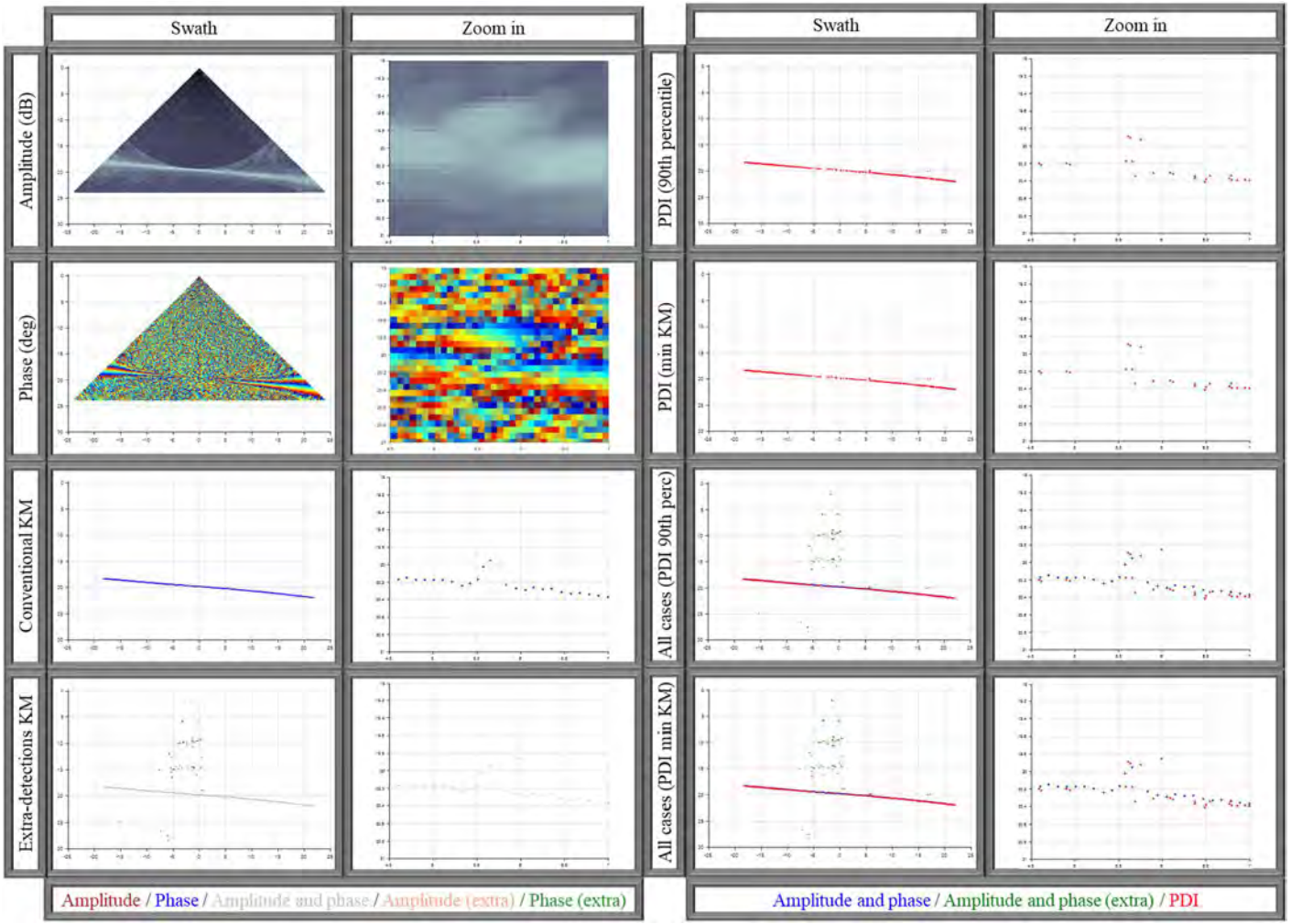

Case: 01-2c

Area: Cubes at 20 m depth. **Target:** Cube (0.5 meter side), no pole. **Line:** 0026_20191010_190729. **Ping number:** 1316.

Manual Threshold: 90th percentile: -11.5 dB. **Min KM:** -19.5 dB. **Incidence angle:** 36.71º.

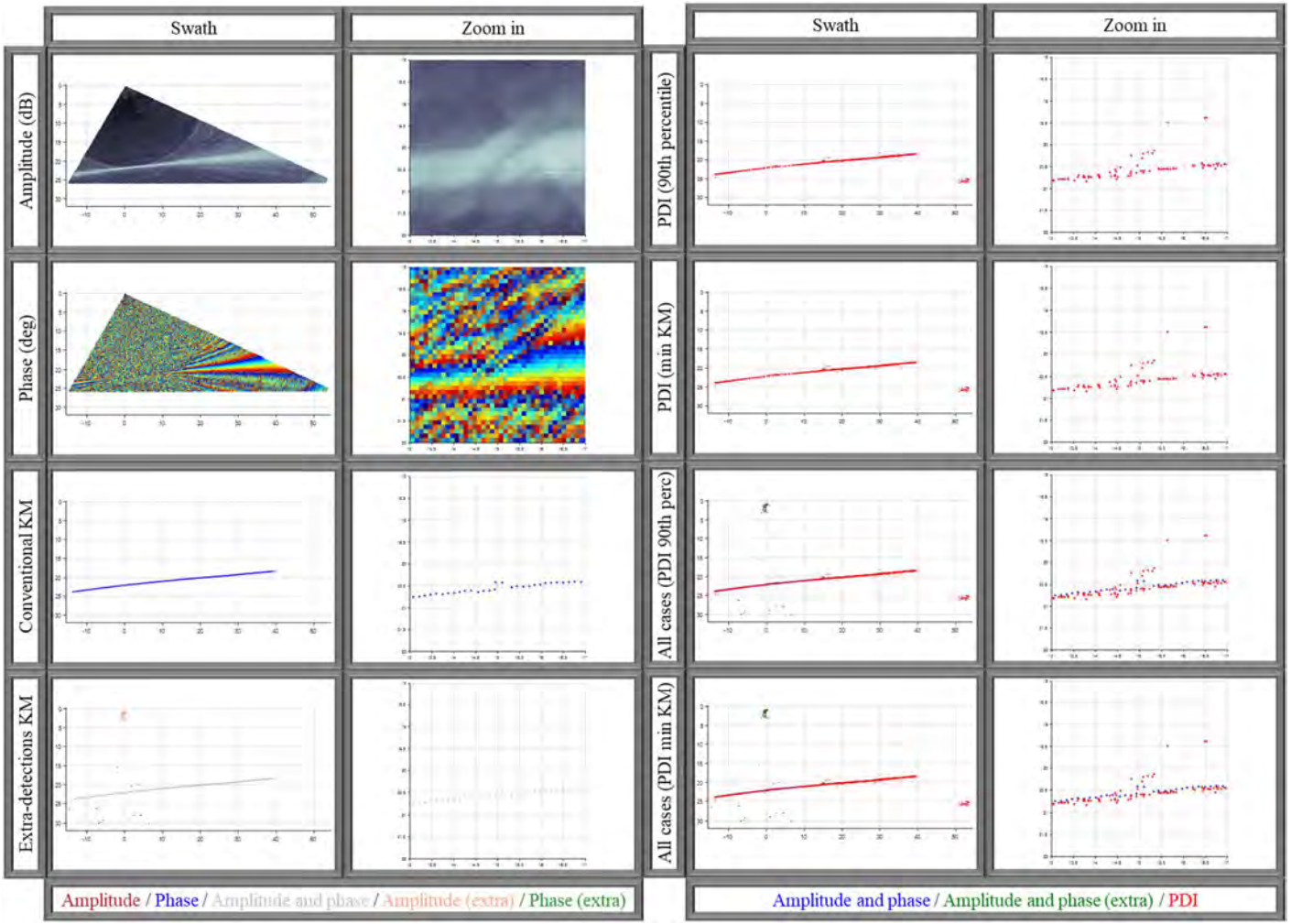

Case: 01-2d

Area: Cubes at 20 m depth. **Target:** Cube (0.5 meter side), no pole. **Line:** 0024_20191010_185857. **Ping number:** 1364.

Manual Threshold: 90th percentile: -12.0 dB. **Min KM:** -13.5 dB. **Incidence angle:** 51.62º.

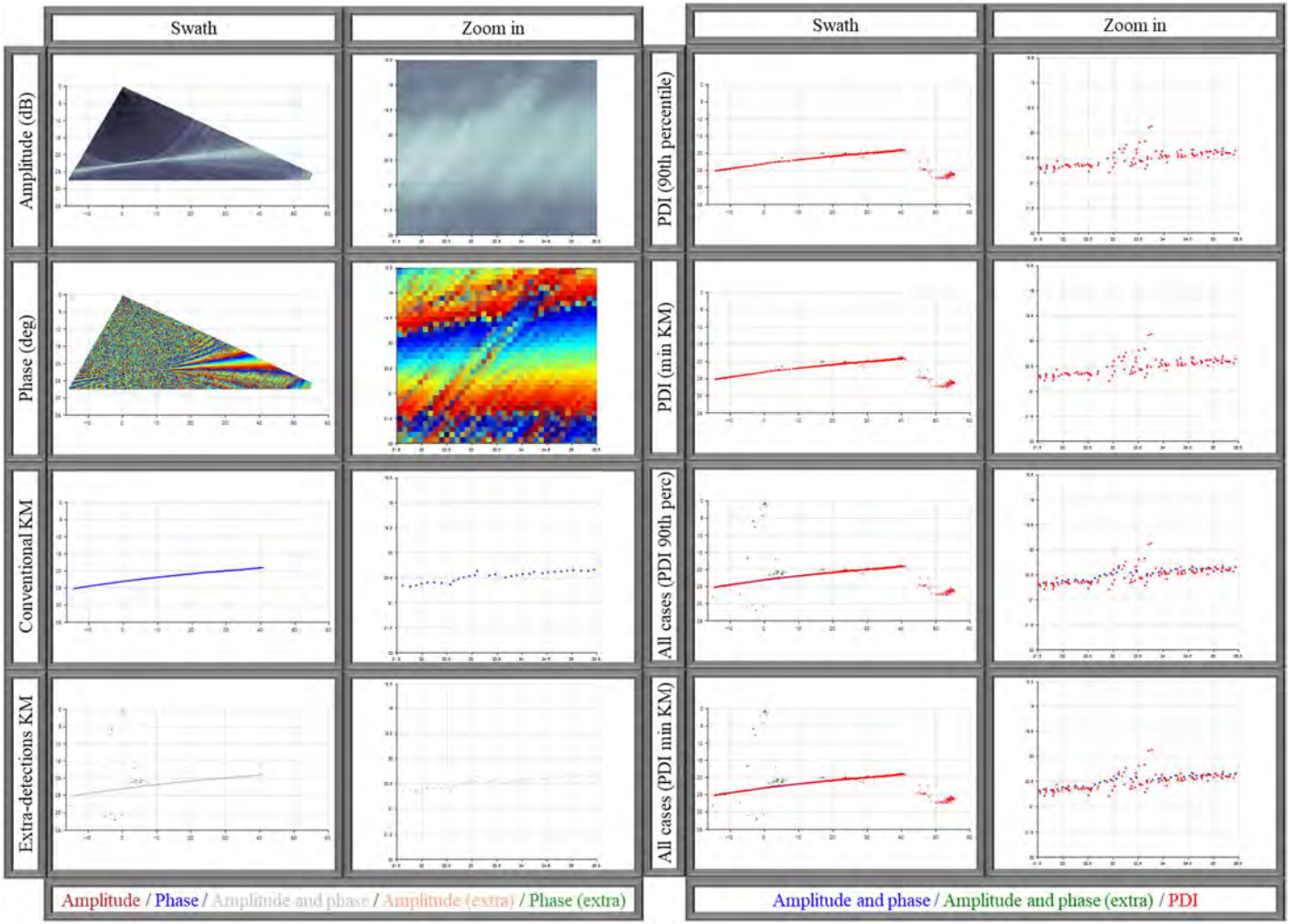

Case: 01-2e

Area: Cubes at 20 m depth. **Target:** Cube (0.5 meter side), no pole. **Line:** 0022_20191010_185001. **Ping number:** 1235.

Manual Threshold: 90th percentile: -6.5 dB. **Min KM:** -11.5 dB. **Incidence angle:** 67.70º.

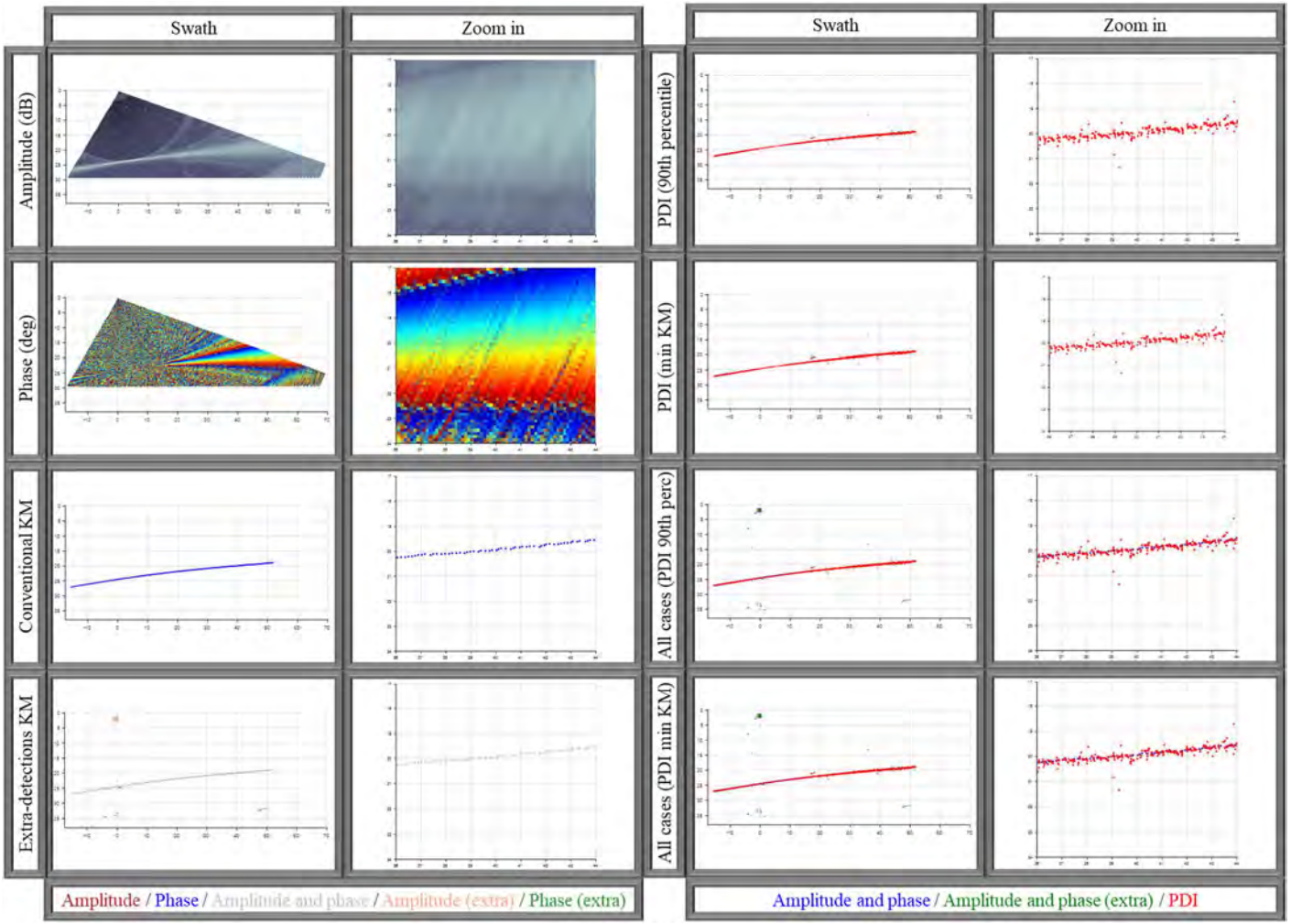

Case: 01-2f

Area: Cubes at 20 m depth. **Target:** Cube (0.5 meter side), no pole. **Line:** 0020_20191010_184042. **Ping number:** 1190.

Manual Threshold: 90th percentile: -7.0 dB. **Min KM:** -15.0 dB. **Incidence angle:** 68.44º.

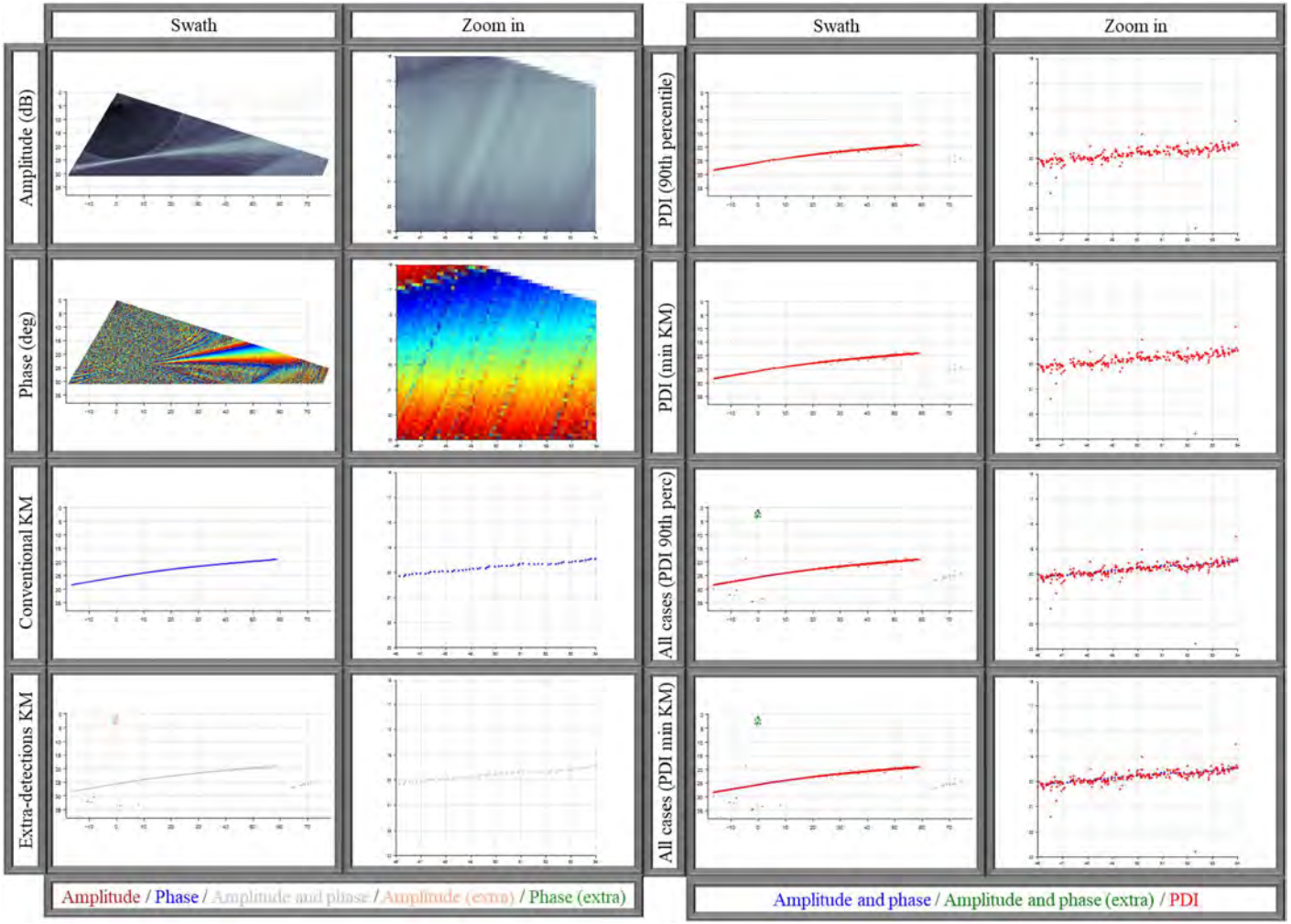

Case: 01-2g

Area: Cubes at 20 m depth. **Target:** Cube (0.5 meter side), no pole. **Line:** 0017_20191010_183108. **Ping number:** 1049.

Manual Threshold: 90th percentile: -1.5 dB. **Min KM:** -7.5 dB. **Incidence angle:** 72.16º.

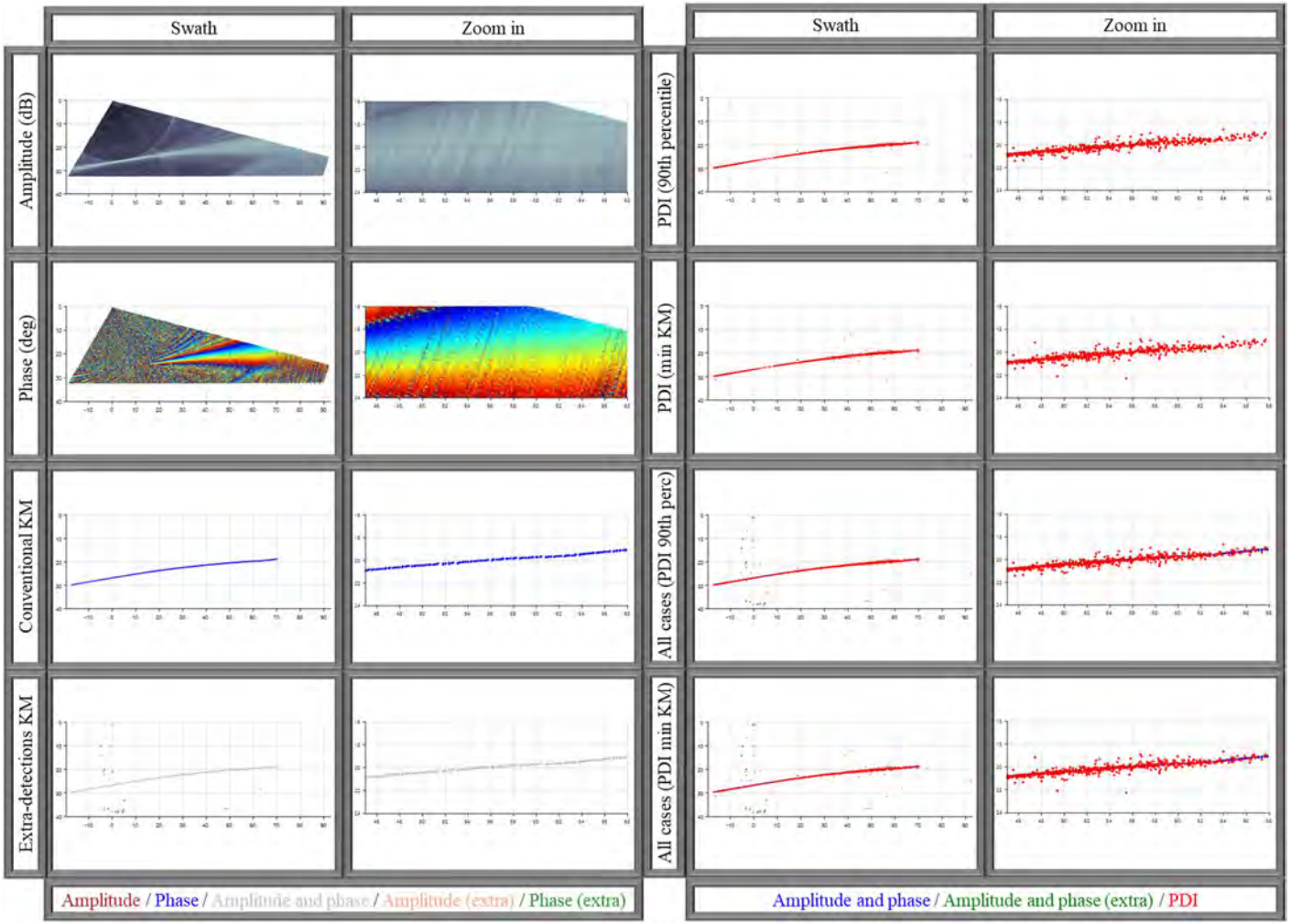

Case: 01-3a

Area: Cubes at 20 m depth. **Target:** Cube (1.0 meter side), no pole. **Line:** 0014_20191010_181817. **Ping number:** 984.

Manual Threshold: 90th percentile: -20.0 dB. **Min KM:** -27.0 dB. **Incidence angle:** 1.94º.

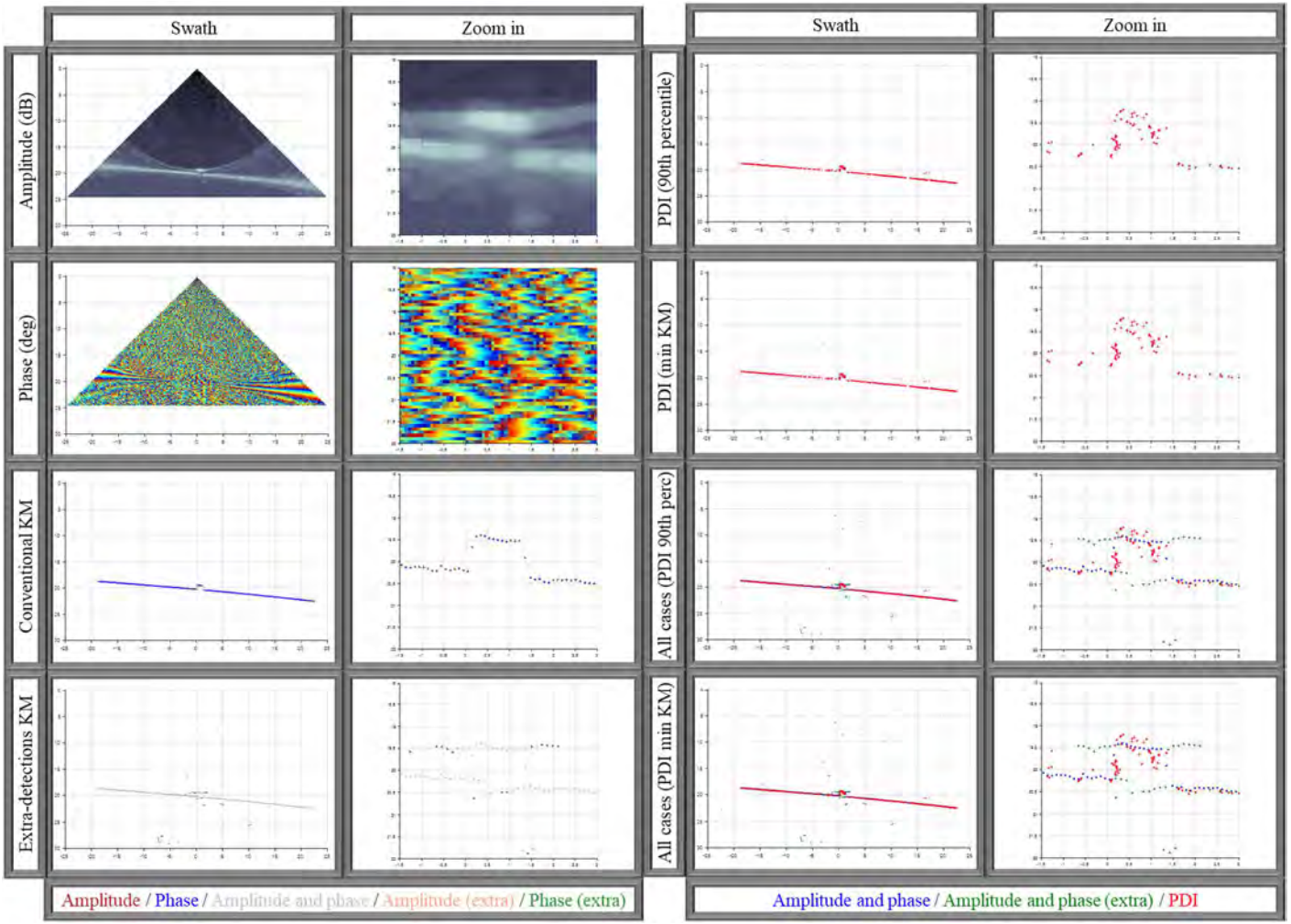

Case: 01-3b

Area: Cubes at 20 m depth. **Target:** Cube (1.0 meter side), no pole. **Line:** 0029_20191010_191602. **Ping number:** 1159.

Manual Threshold: 90th percentile: -13.5 dB. **Min KM:** -16.5 dB. **Incidence angle:** 25.52º.

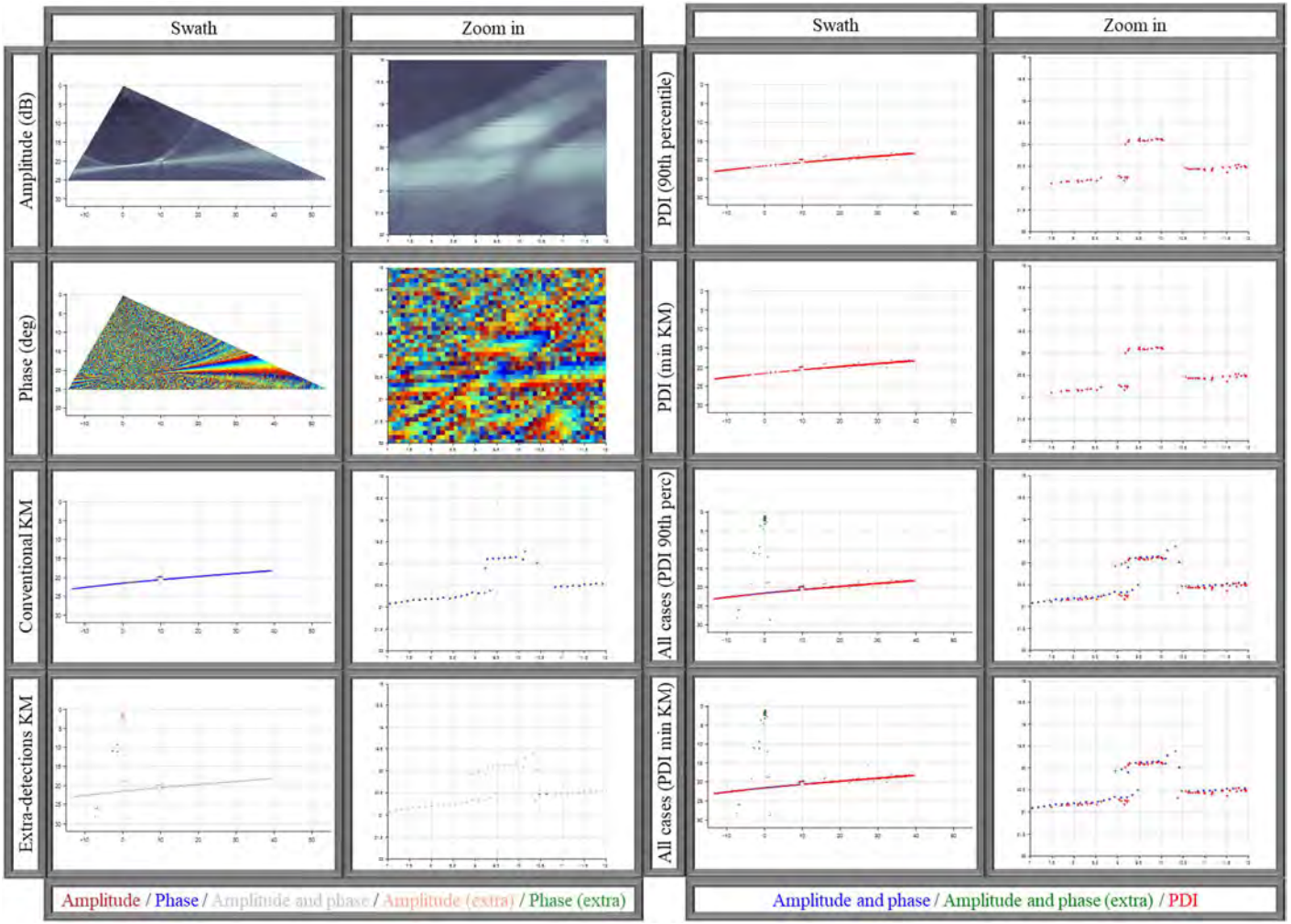

Case: 01-3c

Area: Cubes at 20 m depth. **Target:** Cube (1.0 meter side), no pole. **Line:** 0026_20191010_190729. **Ping number:** 1113.

Manual Threshold: 90th percentile: -13.5 dB. **Min KM:** -20.5 dB. **Incidence angle:** 45.27º.

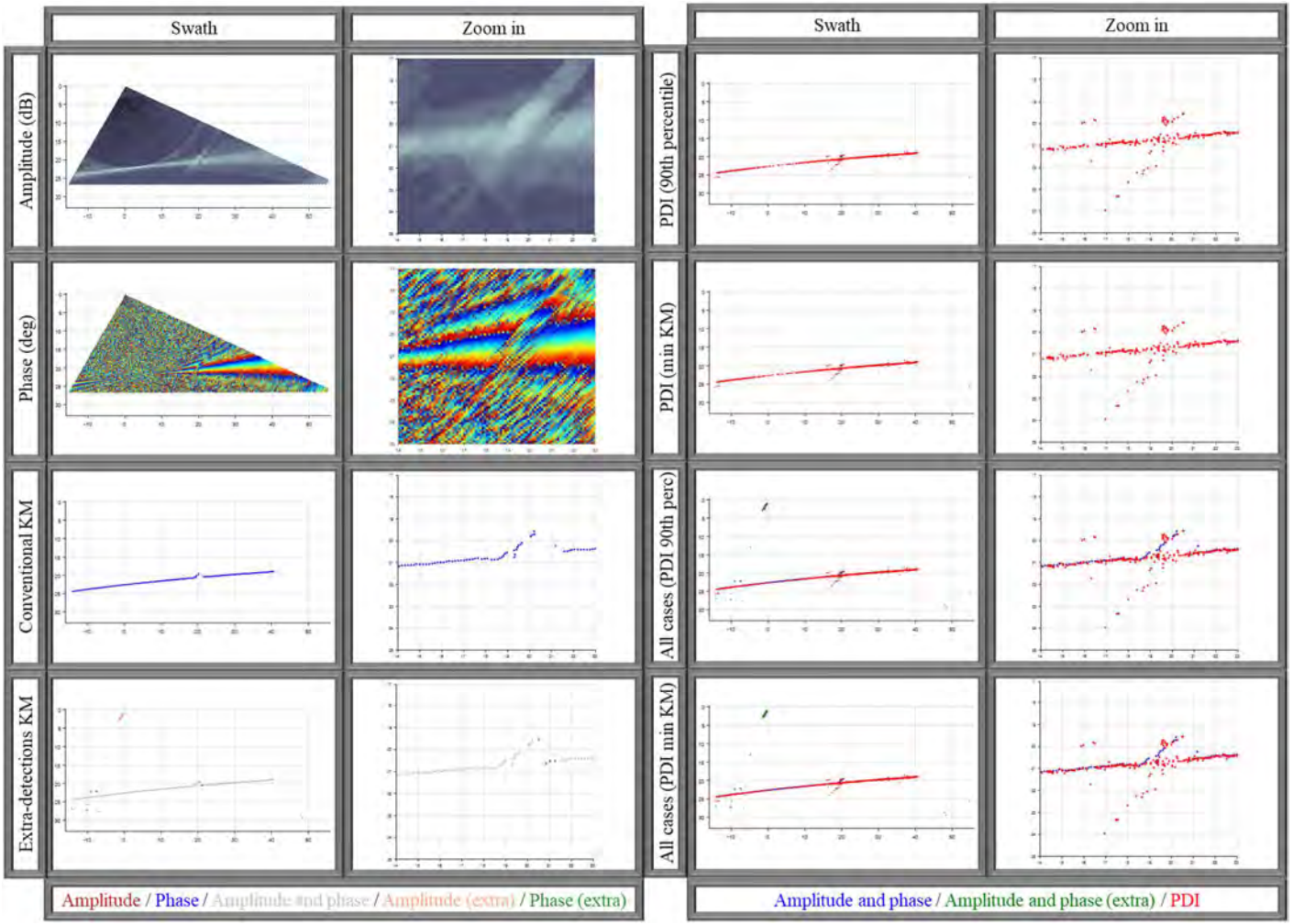

Case: 01-3d

Area: Cubes at 20 m depth. **Target:** Cube (1.0 meter side), no pole. **Line:** 0024_20191010_185857. **Ping number:** 1168.

Manual Threshold: 90th percentile: -16.5 dB. **Min KM:** -16.0 dB. **Incidence angle:** 56.48º.

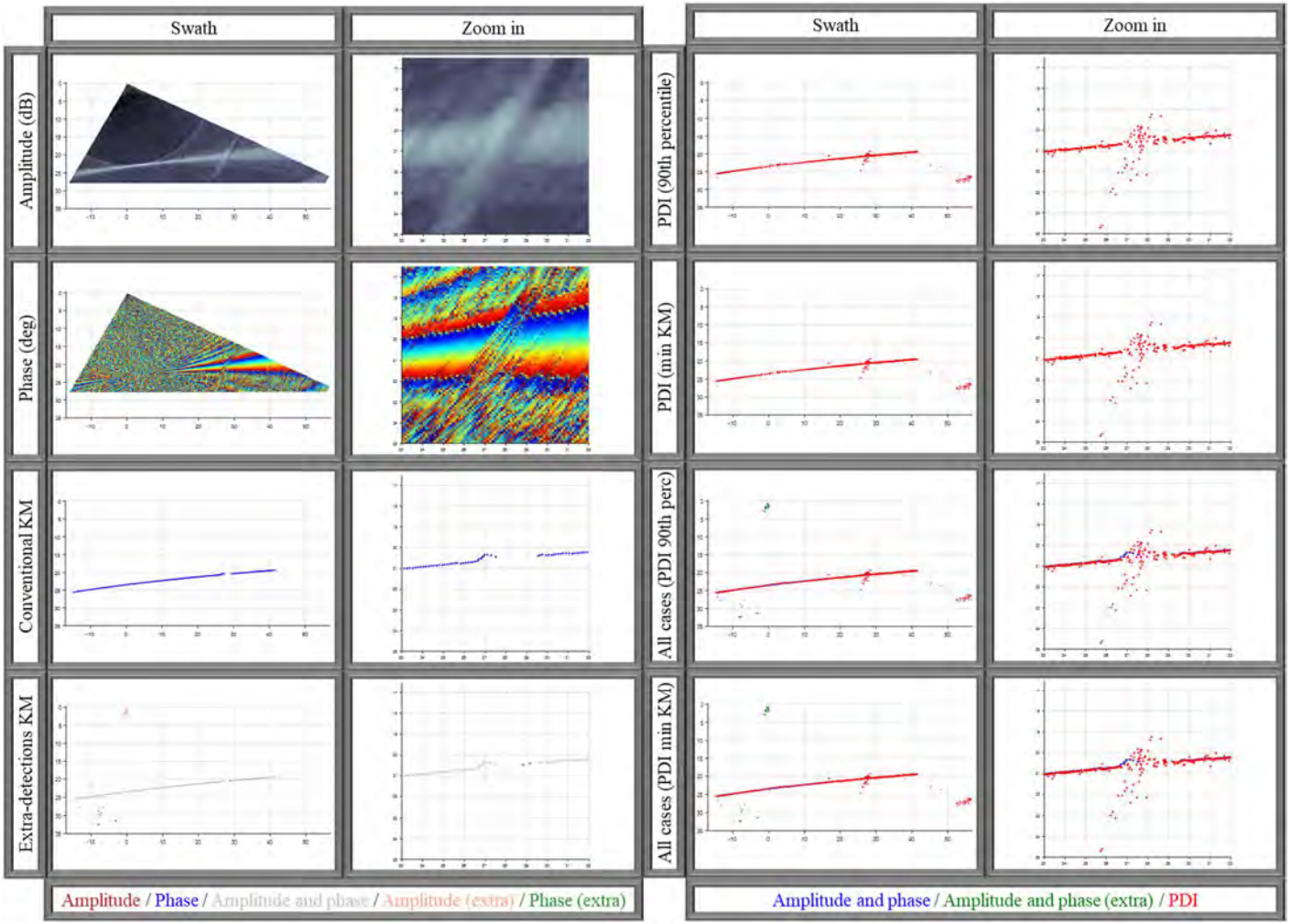

Case: 01-3e

Area: Cubes at 20 m depth. **Target:** Cube (1.0 meter side), no pole. **Line:** 0022_20191010_185001. **Ping number:** 1055.

Manual Threshold: 90th percentile: -10.0 dB. **Min KM:** -22.0 dB. **Incidence angle:** 62.94º.

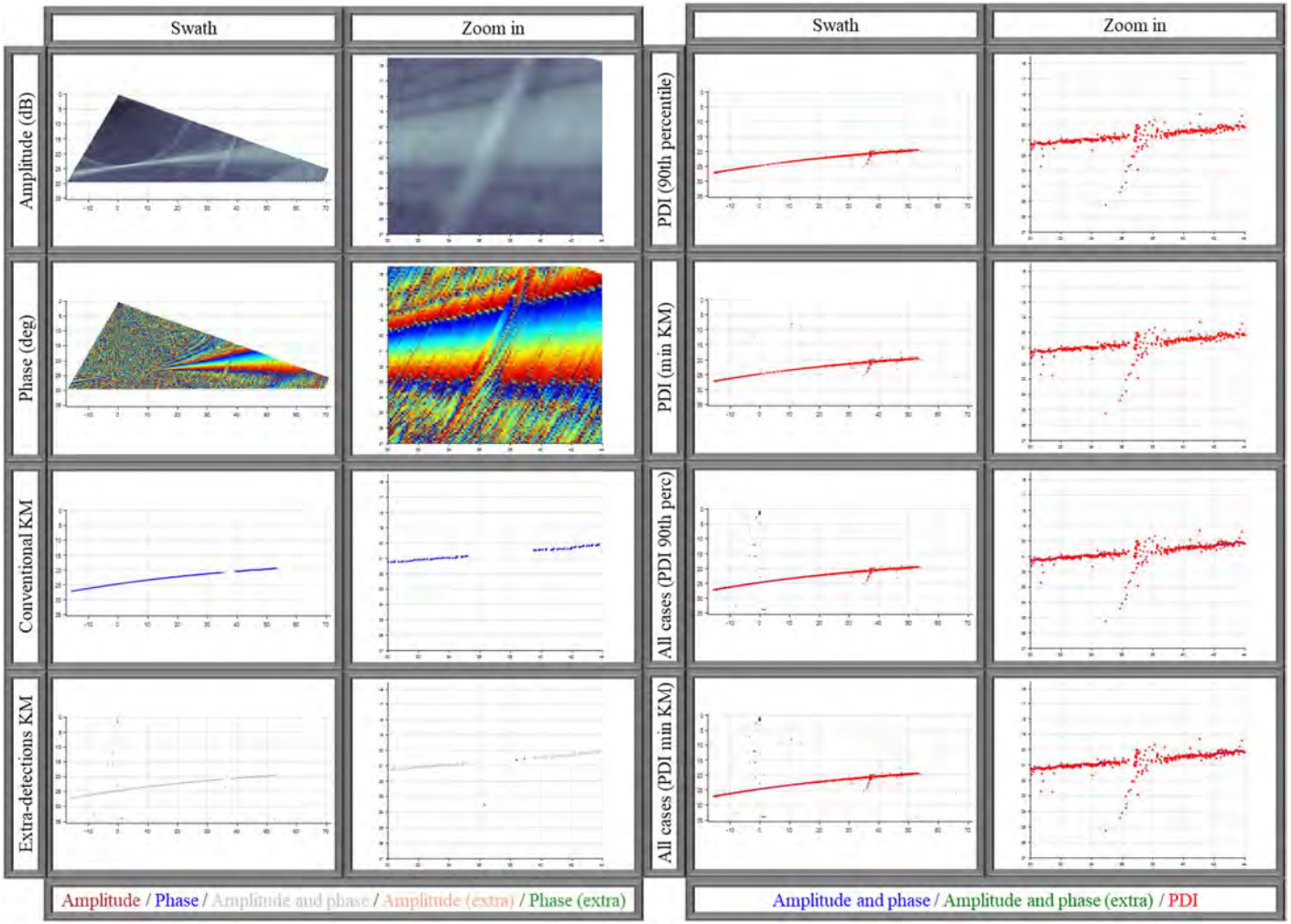

Case: 01-3f

Area: Cubes at 20 m depth. **Target:** Cube (1.0 meter side), no pole. **Line:** 0020_20191010_184042. **Ping number:** 1019.

Manual Threshold: 90th percentile: -7.5 dB. **Min KM:** -12.5 dB. **Incidence angle:** 66.81º.

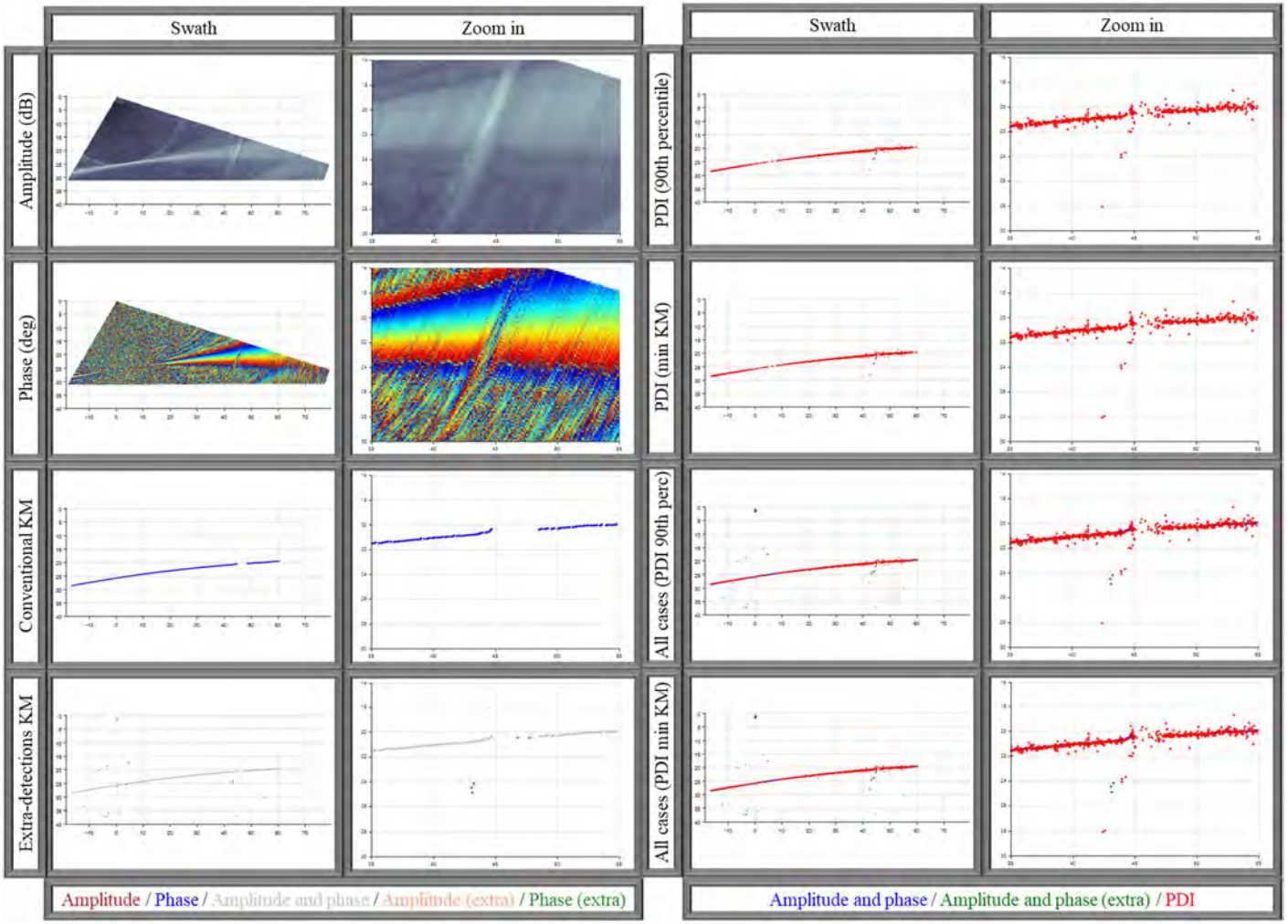

Case: 01-3g

Area: Cubes at 20 m depth. **Target:** Cube (1.0 meter side), no pole. **Line:** 0017_20191010_183108. **Ping number:** 894.

Manual Threshold: 90th percentile: -7.5 dB. **Min KM:** -20.5 dB. **Incidence angle:** 71.34º.

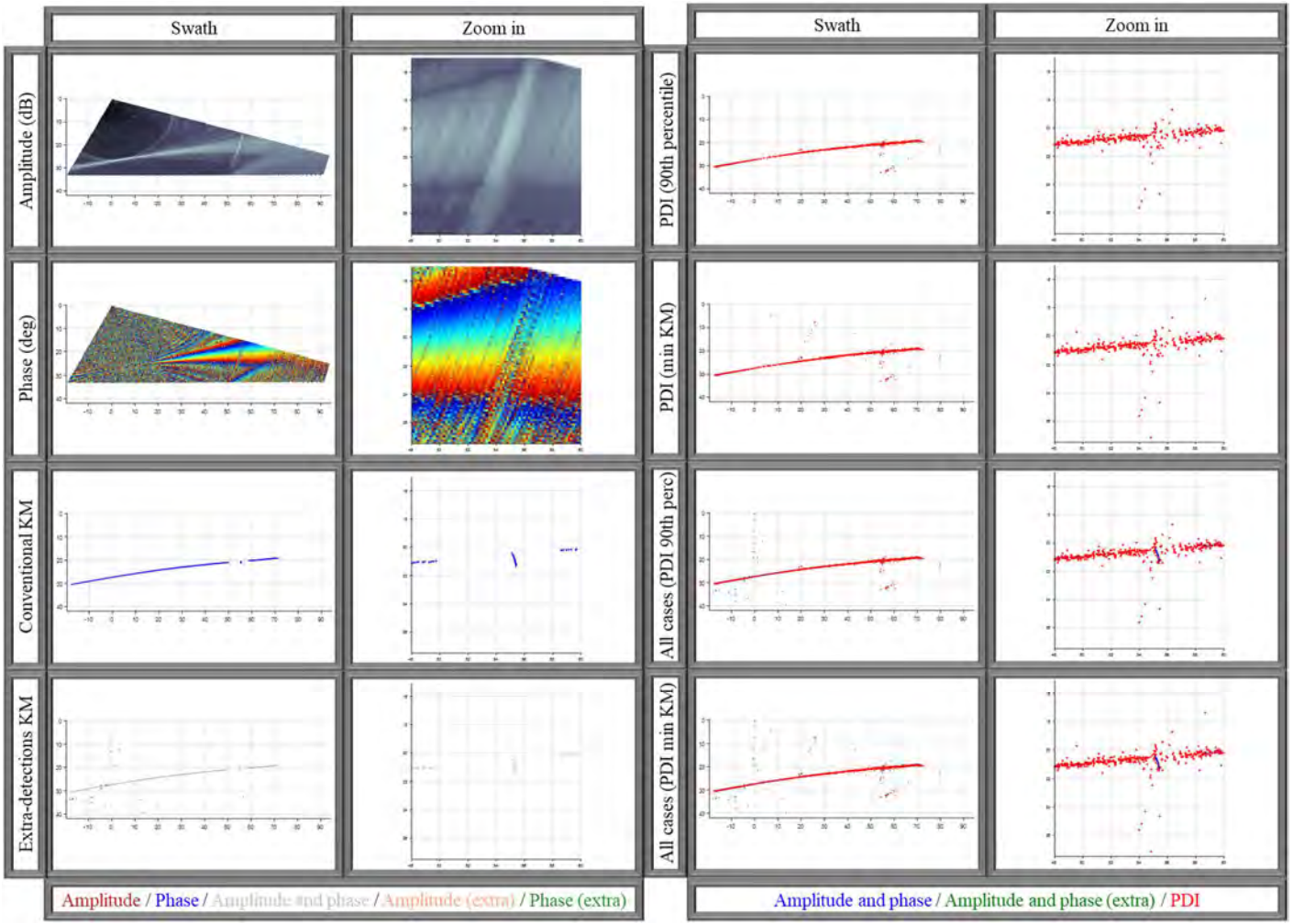

Case: 01-4a

Area: Cubes at 20 m depth. **Target:** Cube (0.5 meter side) with pole. **Line:** 0014_20191010_181817. **Ping number:** 1206.

Manual Threshold: 90th percentile: -19.5 dB. **Min KM:** -21.0 dB. **Incidence angle:** 6.89º.

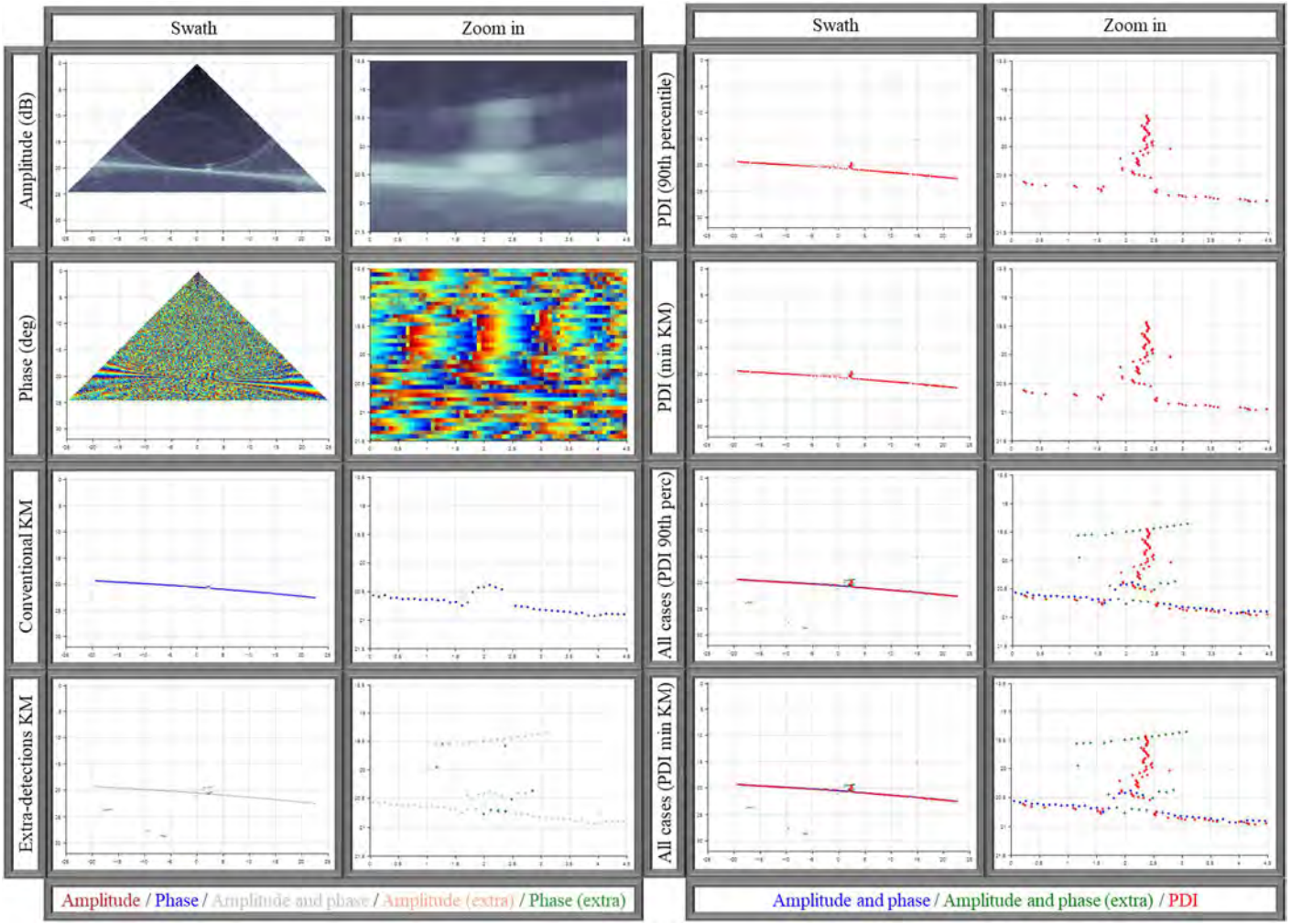

Case: 01-4b

Area: Cubes at 20 m depth. **Target:** Cube (0.5 meter side) with pole. **Line:** 0029_20191010_191602. **Ping number:** 954.

Manual Threshold: 90th percentile: -14.0 dB. **Min KM:** -13.5 dB. **Incidence angle:** 26.26º.

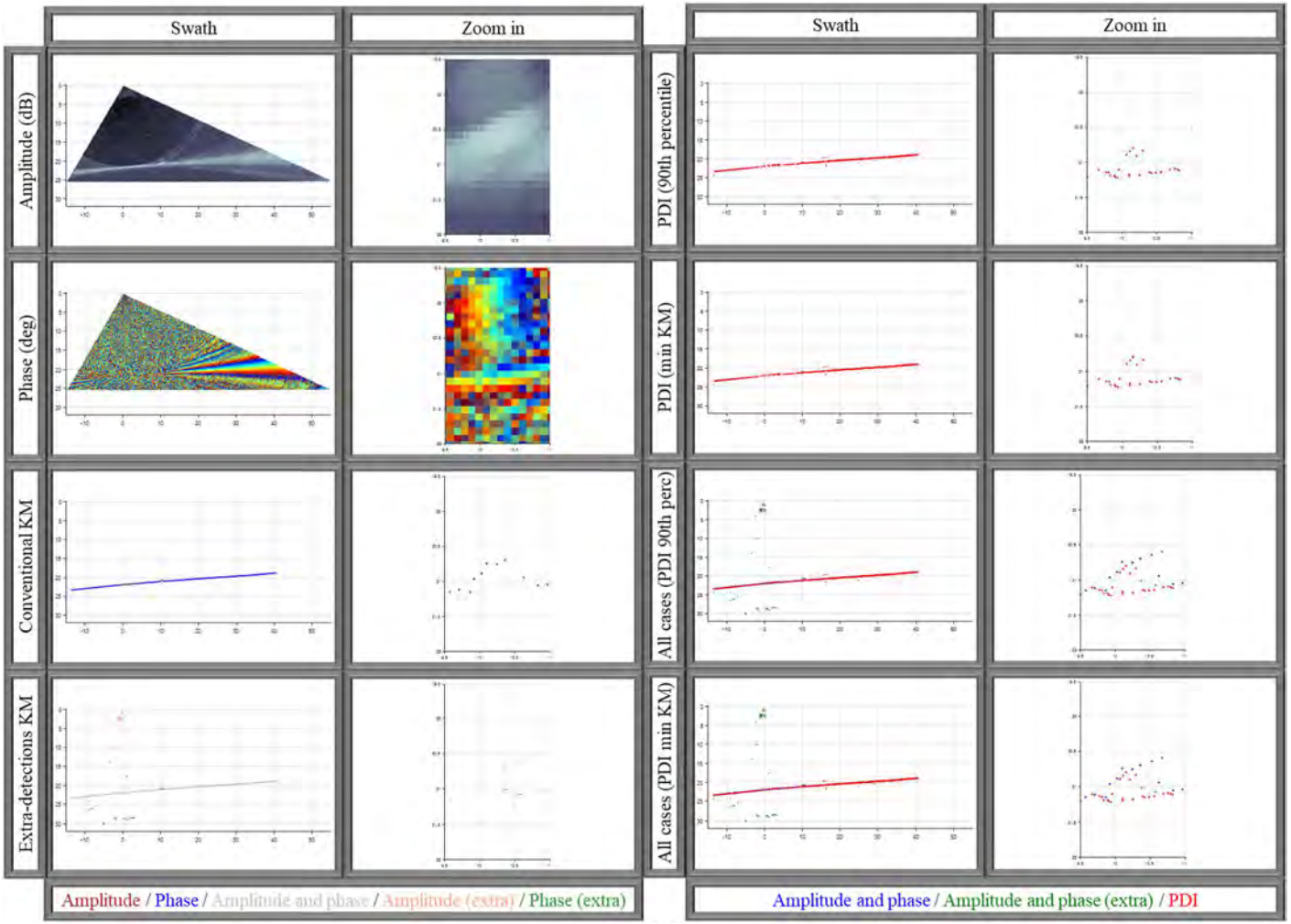

Case: 01-4c

Area: Cubes at 20 m depth. **Target:** Cube (0.5 meter side) with pole. **Line:** 0026_20191010_190729. **Ping number:** 916.

Manual Threshold: 90th percentile: -15.0 dB. **Min KM:** -14.5 dB. **Incidence angle:** 42.66º.

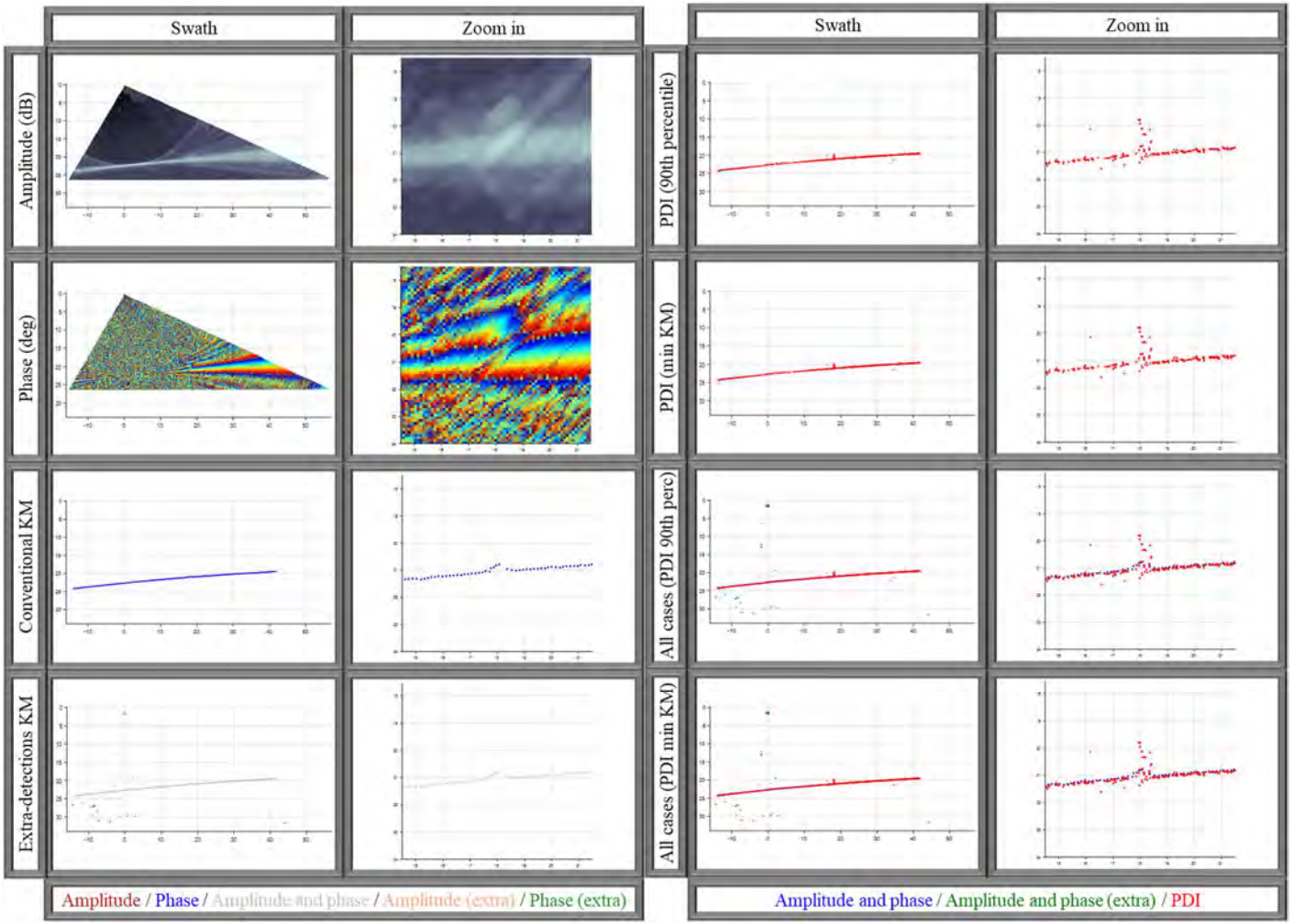

Case: 01-4d

Area: Cubes at 20 m depth. **Target:** Cube (0.5 meter side) with pole. **Line:** 0024_20191010_185857. **Ping number:** 971.

Manual Threshold: 90th percentile: -13.0 dB. **Min KM:** -17.5 dB. **Incidence angle:** 54.98º.

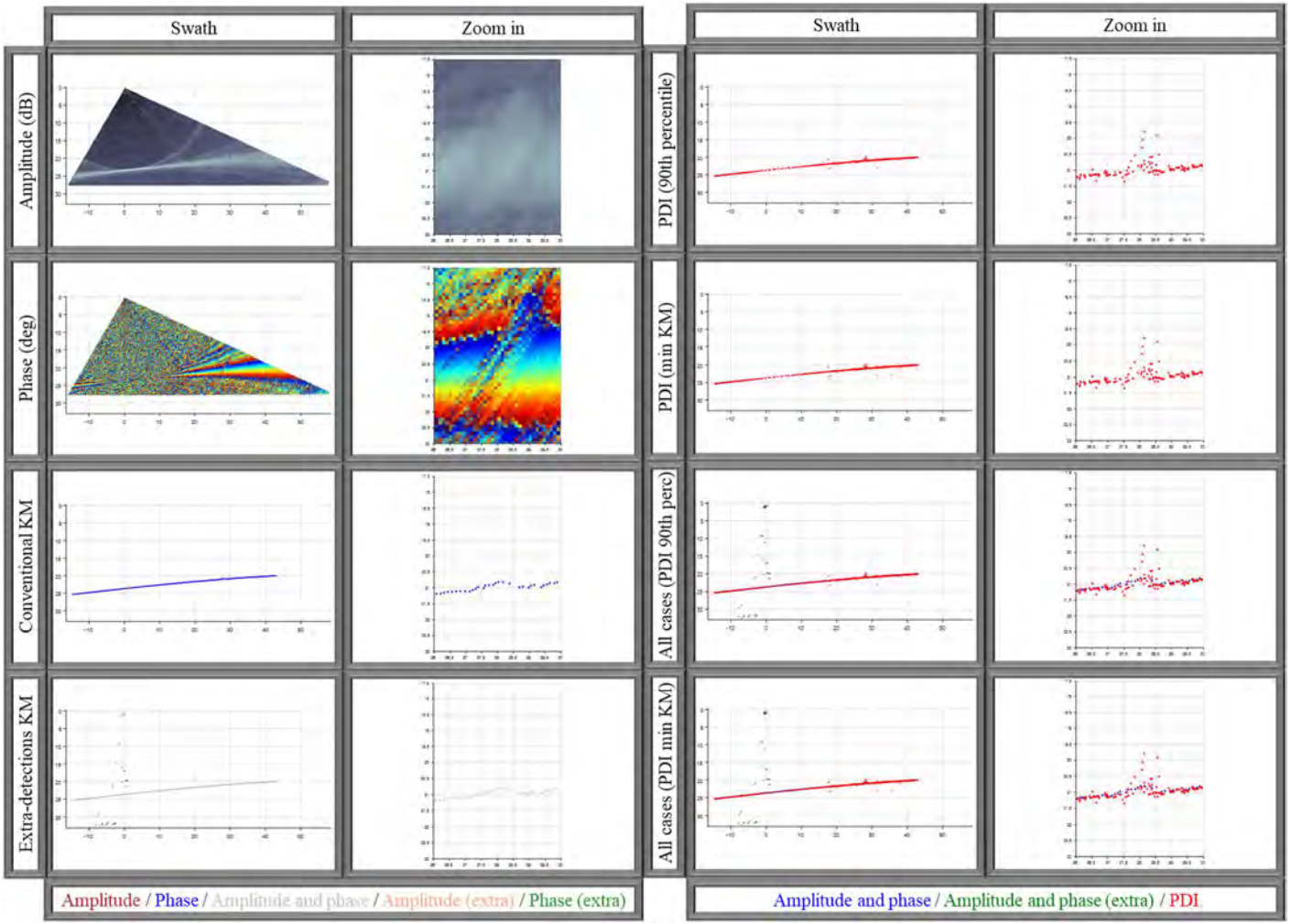

Case: 01-4e

Area: Cubes at 20 m depth. **Target:** Cube (0.5 meter side) with pole. **Line:** 0022_20191010_185001. **Ping number:** 878.

Manual Threshold: 90th percentile: -12.0 dB. **Min KM:** -15.5 dB. **Incidence angle:** 62.98º.

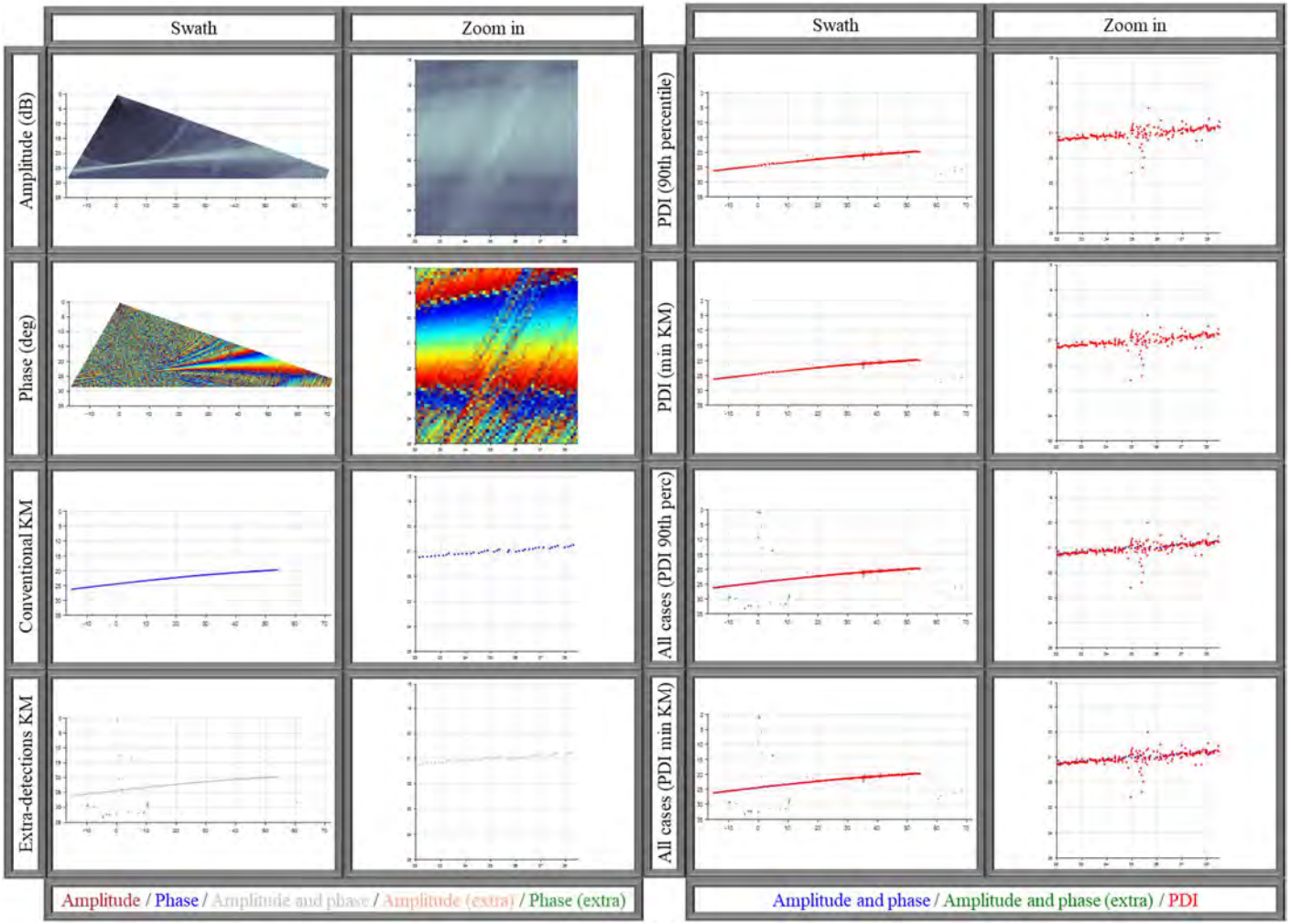

Case: 01-4f

Area: Cubes at 20 m depth. **Target:** Cube (0.5 meter side) with pole. **Line:** 0020_20191010_184042. **Ping number:** 847.

Manual Threshold: 90th percentile: -7.5 dB. **Min KM:** -17.0 dB. **Incidence angle:** 66.84º.

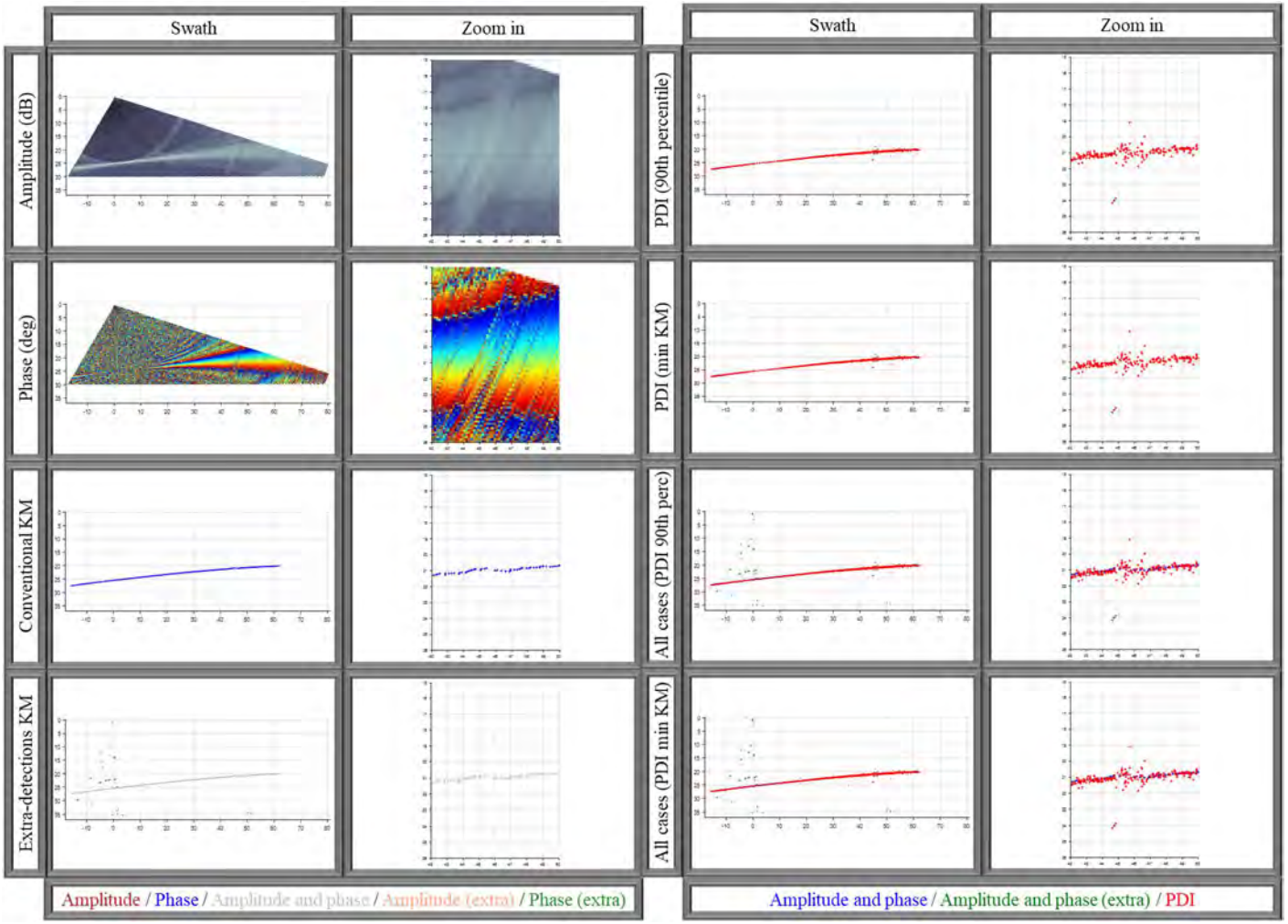

Case: 01-4g

Area: Cubes at 20 m depth. **Target:** Cube (0.5 meter side) with pole. **Line:** 0017_20191010_183108. **Ping number:** 735.

Manual Threshold: 90th percentile: -3.5 dB. **Min KM:** -23.0 dB. **Incidence angle:** 70.01º.

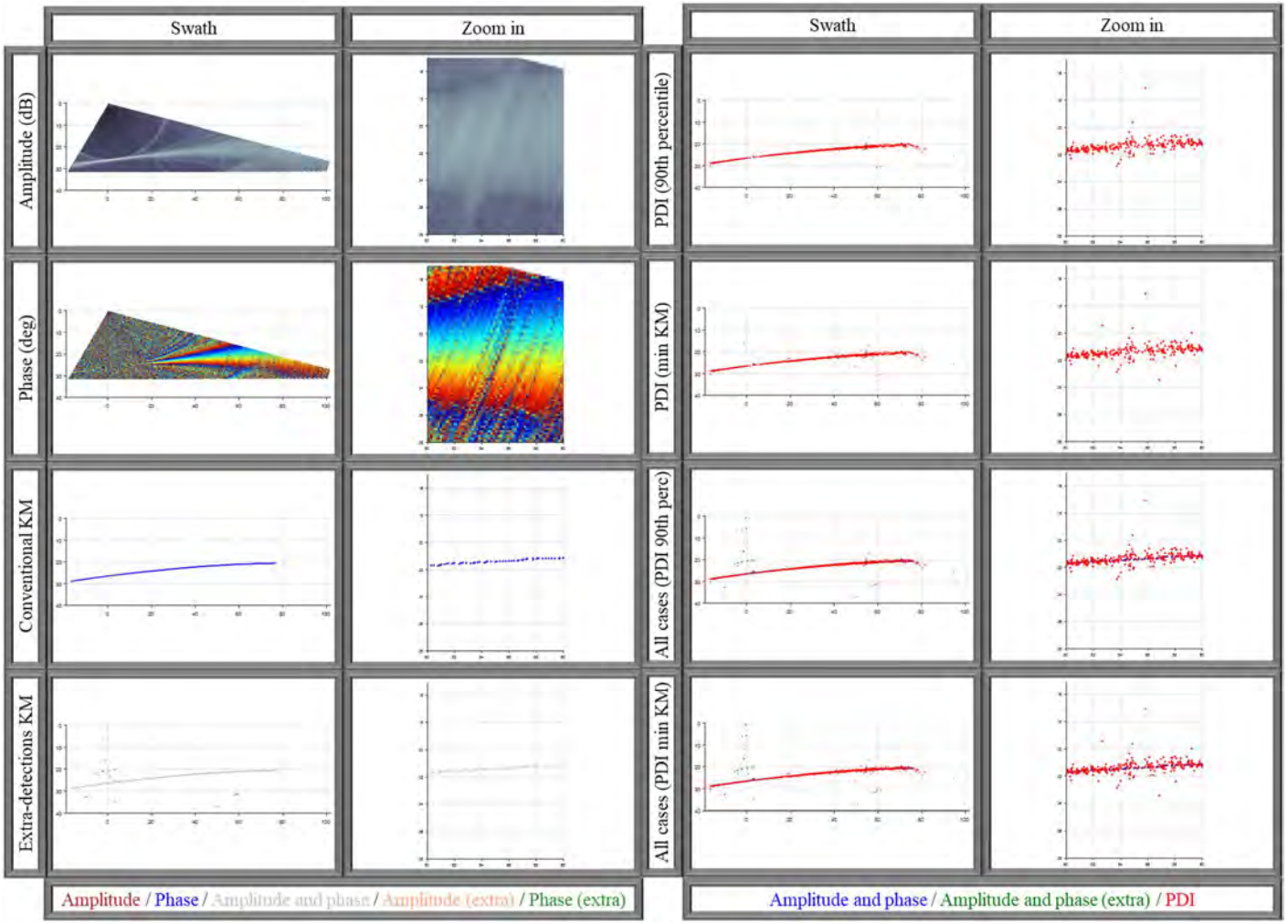

Case: 02-1a

Area: Cubes at 40 m depth. **Target:** Cube (1.0 meter side) with pole. **Line:** 0015_20191010_182233. **Ping number:** 617.

Manual Threshold: 90th percentile: -15.0 dB. **Min KM:** -12.0 dB. **Incidence angle:** 0.88º.

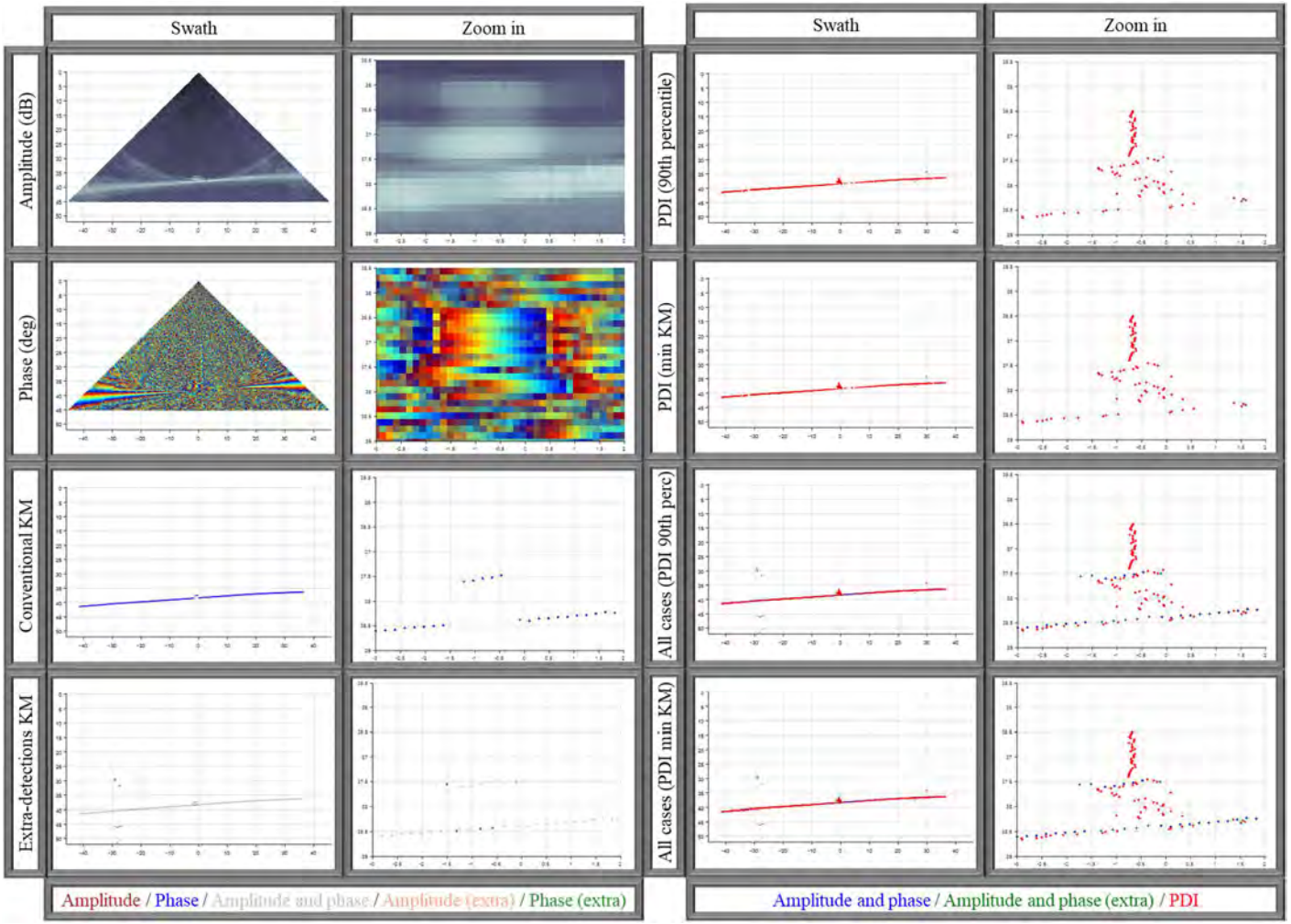

Case: 02-1b

Area: Cubes at 40 m depth. **Target:** Cube (1.0 meter side) with pole. **Line:** 0027_20191010_191150. **Ping number:** 789.

Manual Threshold: 90th percentile: -11.5 dB. **Min KM:** -20.5 dB. **Incidence angle:** 21.41º.

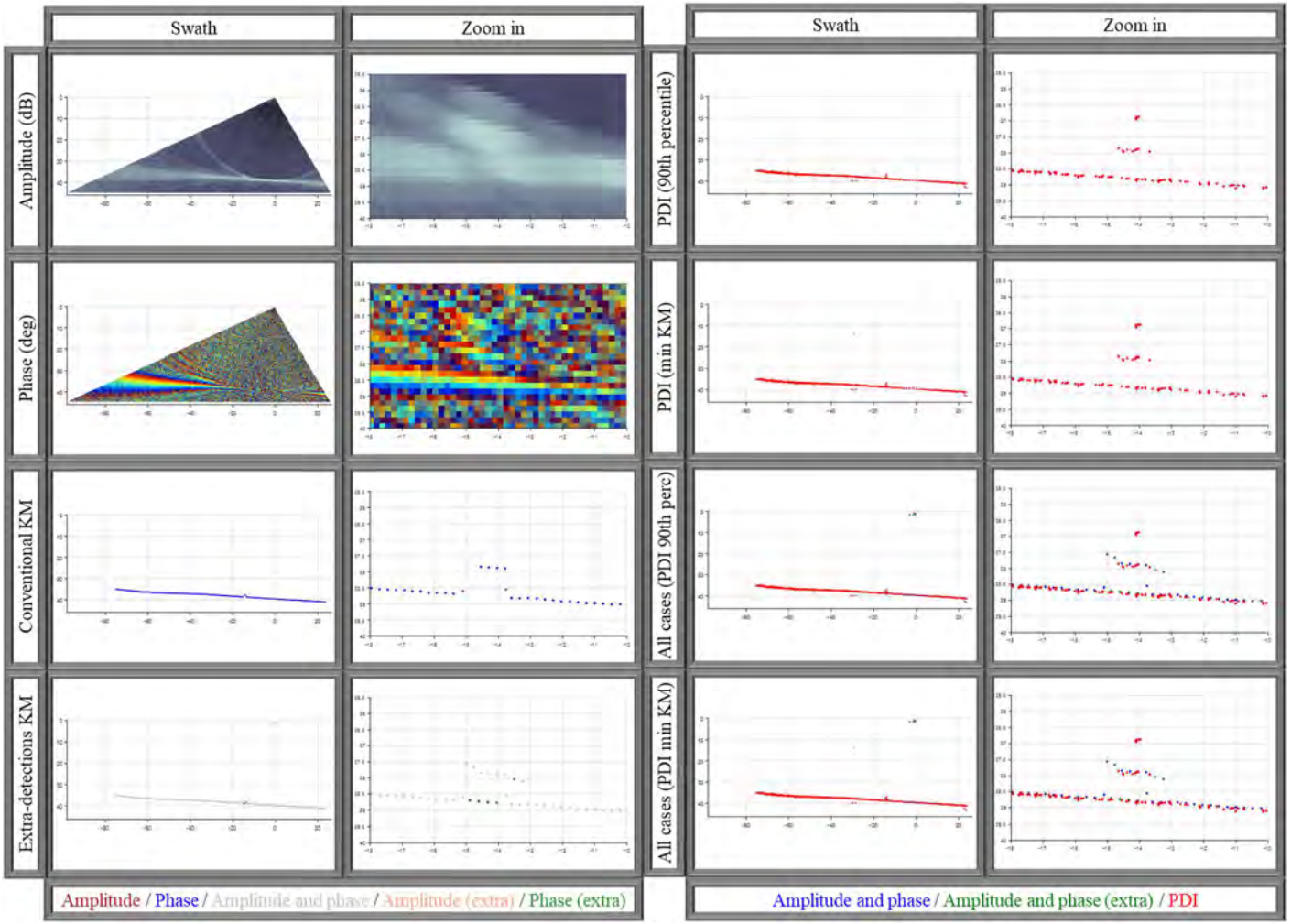

Case: 02-1c

Area: Cubes at 40 m depth. **Target:** Cube (1.0 meter side) with pole. **Line:** 0025_20191010_190323. **Ping number:** 774.

Manual Threshold: 90th percentile: -13.5 dB. **Min KM:** -18.0 dB. **Incidence angle:** 40.35º.

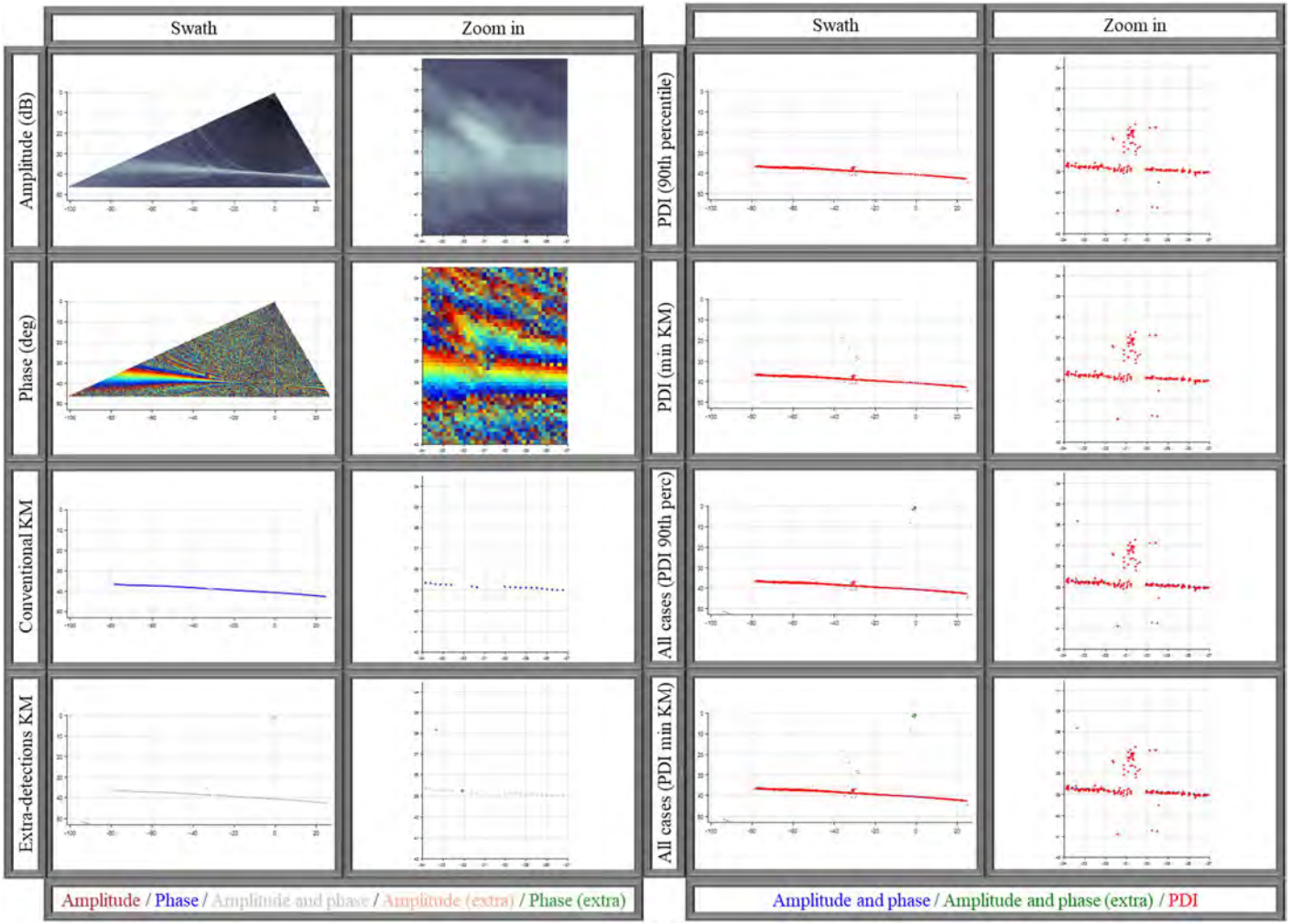

Case: 02-1d

Area: Cubes at 40 m depth. **Target:** Cube (1.0 meter side) with pole. **Line:** 0023_20191010_185445. **Ping number:** 755.

Manual Threshold: 90th percentile: -10.0 dB. **Min KM:** -15.0 dB. **Incidence angle:** 52.37º.

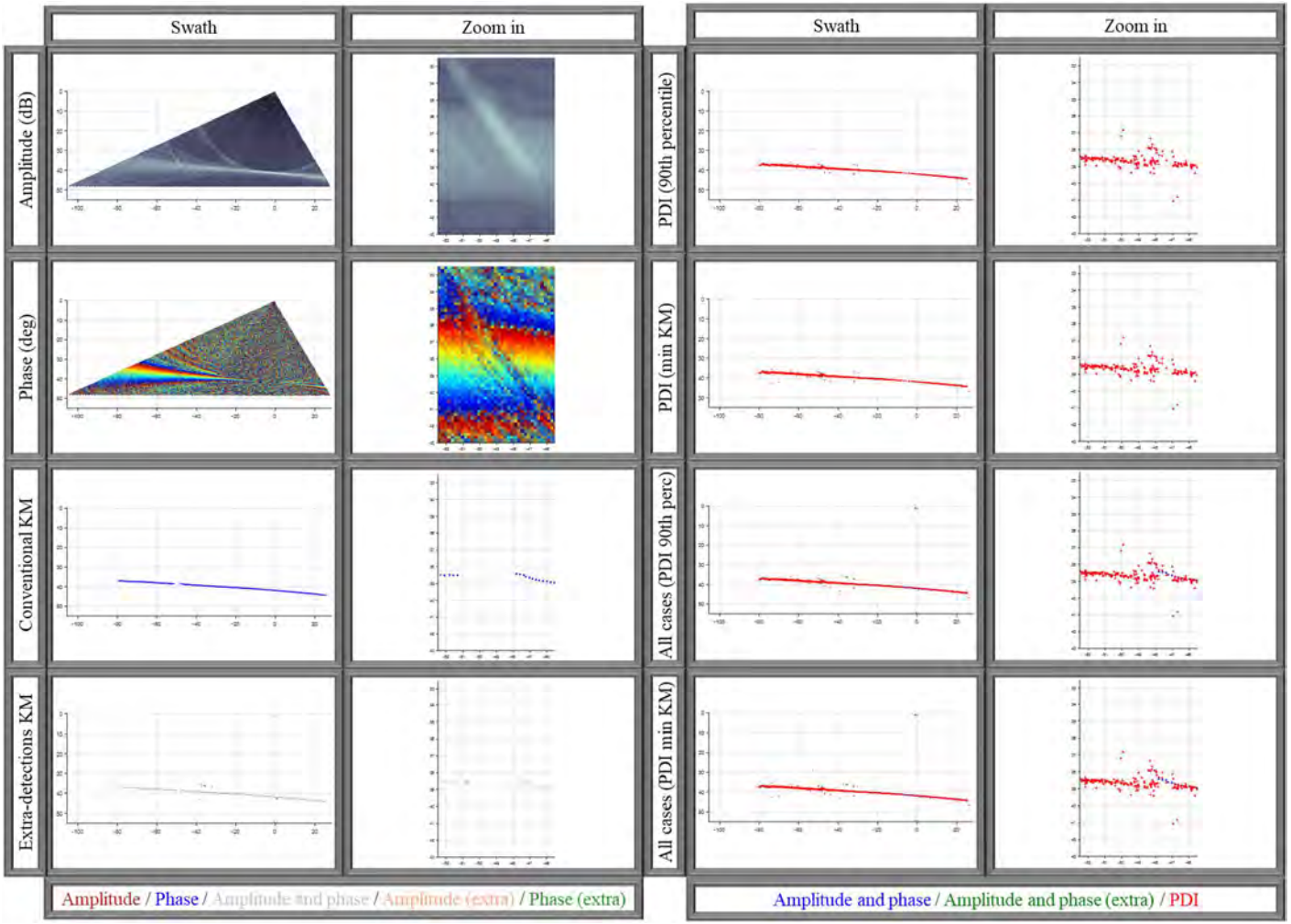

Case: 02-1e

Area: Cubes at 40 m depth. **Target:** Cube (1.0 meter side) with pole. **Line:** 0019_20191010_183610. **Ping number:** 634.

Manual Threshold: 90th percentile: -5.5 dB. **Min KM:** -9.0 dB. **Incidence angle:** 66.23º.

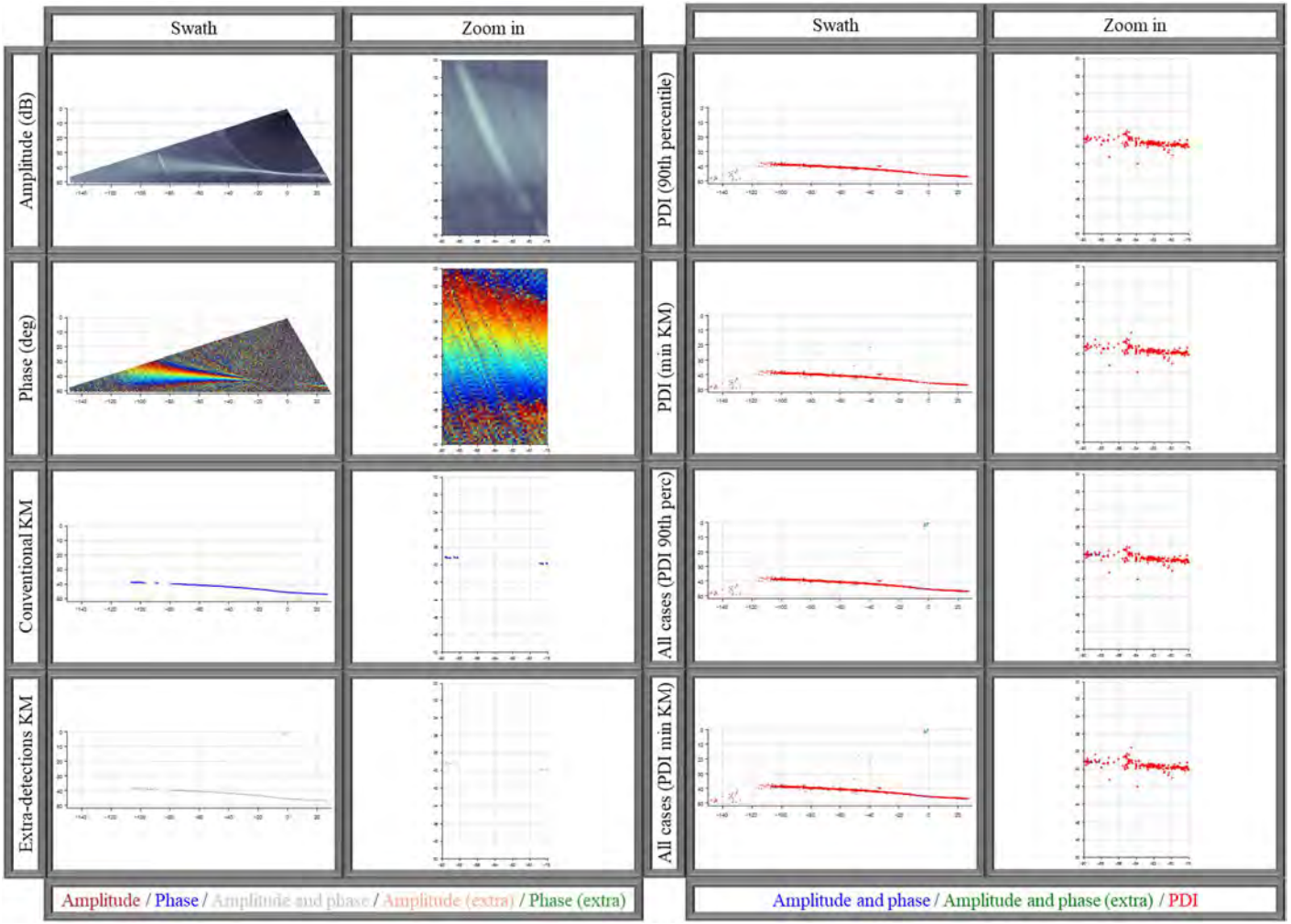

Case: 02-1f

Area: Cubes at 40 m depth. **Target:** Cube (1.0 meter side) with pole. **Line:** 0016_20191010_182619. **Ping number:** 658.

Manual Threshold: 90th percentile: +3.0 dB. **Min KM:** -13.5 dB. **Incidence angle:** 69.61º.

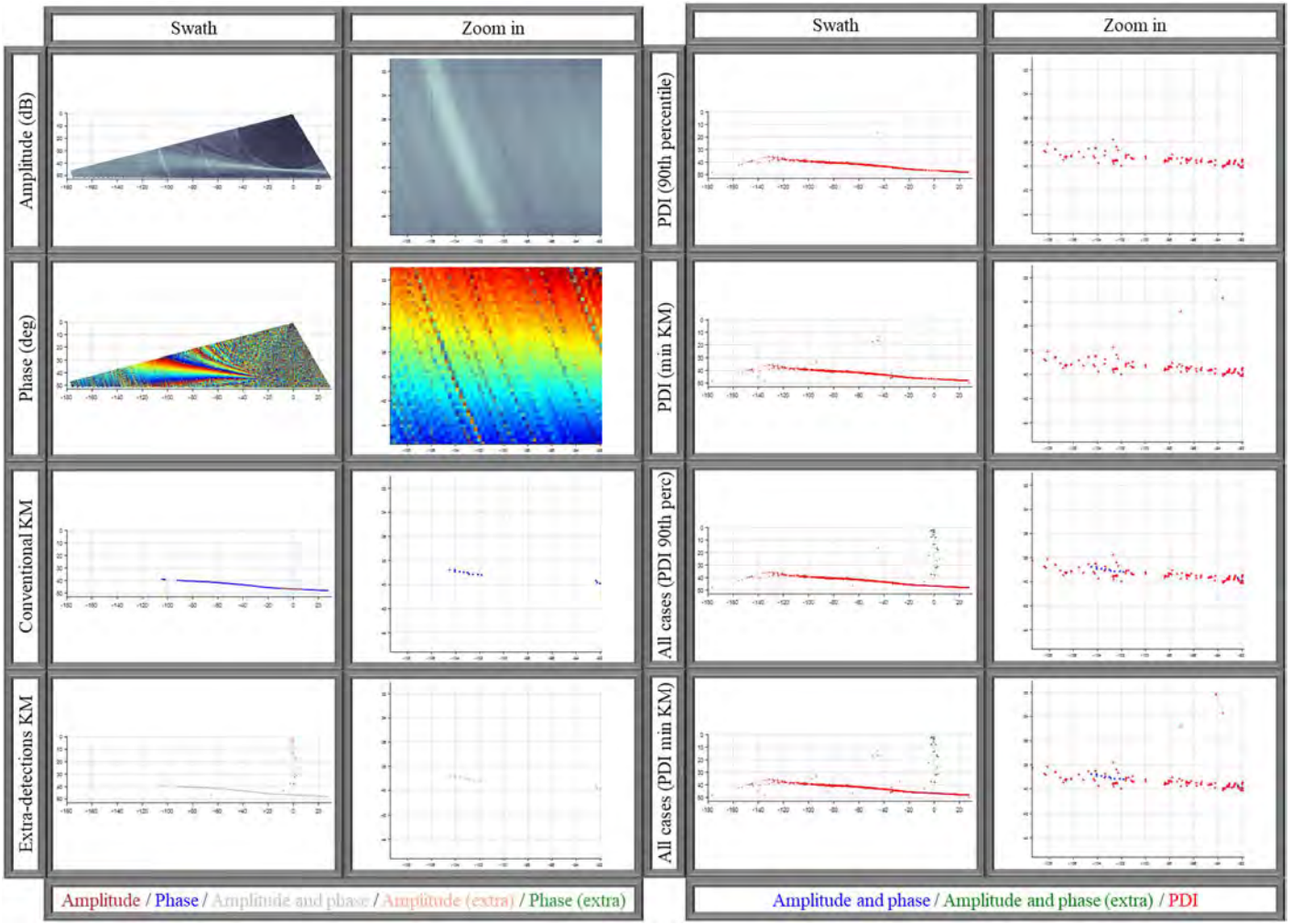

Case: 02-2a

Area: Cubes at 40 m depth. **Target:** Cube (1.0 meter side), no pole. **Line:** 0015_20191010_182233. **Ping number:** 279.

Manual Threshold: 90th percentile: -17.5 dB. **Min KM:** -20.5 dB. **Incidence angle:** 8.30º.

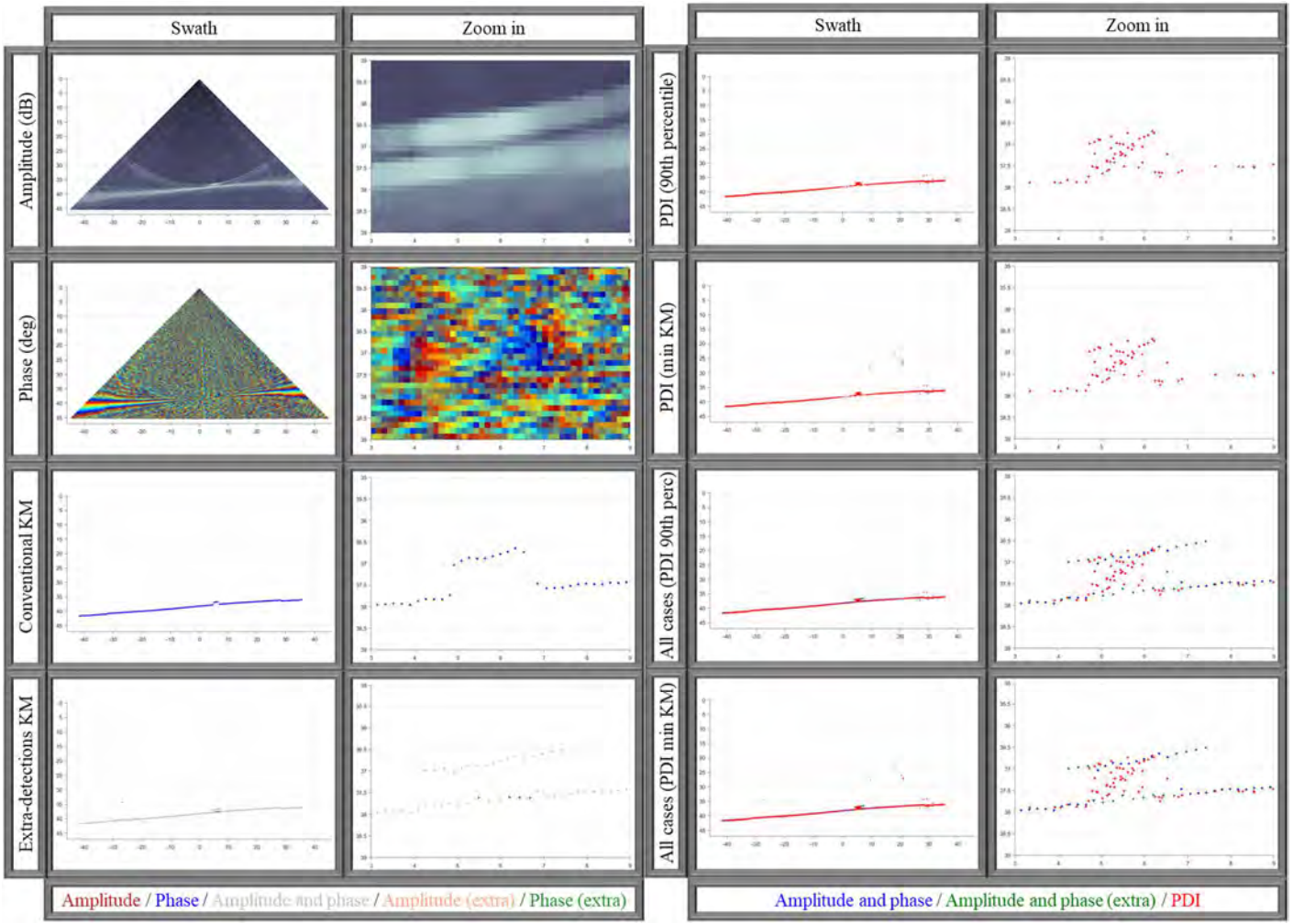

Case: 02-2b

Area: Cubes at 40 m depth. **Target:** Cube (1.0 meter side), no pole. **Line:** 0027_20191010_191150. **Ping number:** 1092.

Manual Threshold: 90th percentile: -15.0 dB. **Min KM:** -20.0 dB. **Incidence angle:** 29.24º.

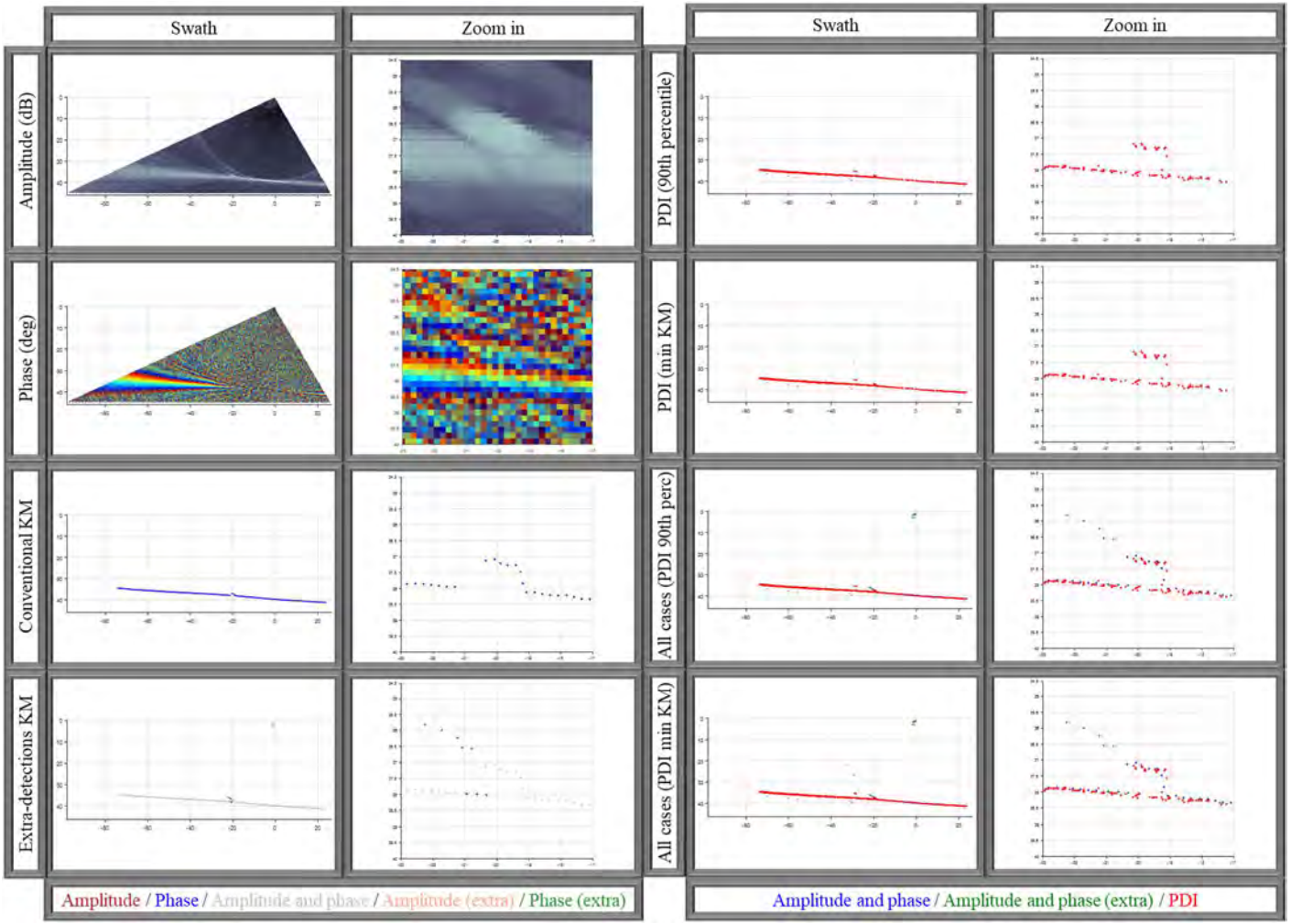

Case: 02-2c

Area: Cubes at 40 m depth. **Target:** Cube (1.0 meter side), no pole. **Line:** 0025_20191010_190323. **Ping number:** 1072.

Manual Threshold: 90th percentile: -14.5 dB. **Min KM:** -13.0 dB. **Incidence angle:** 45.26º.

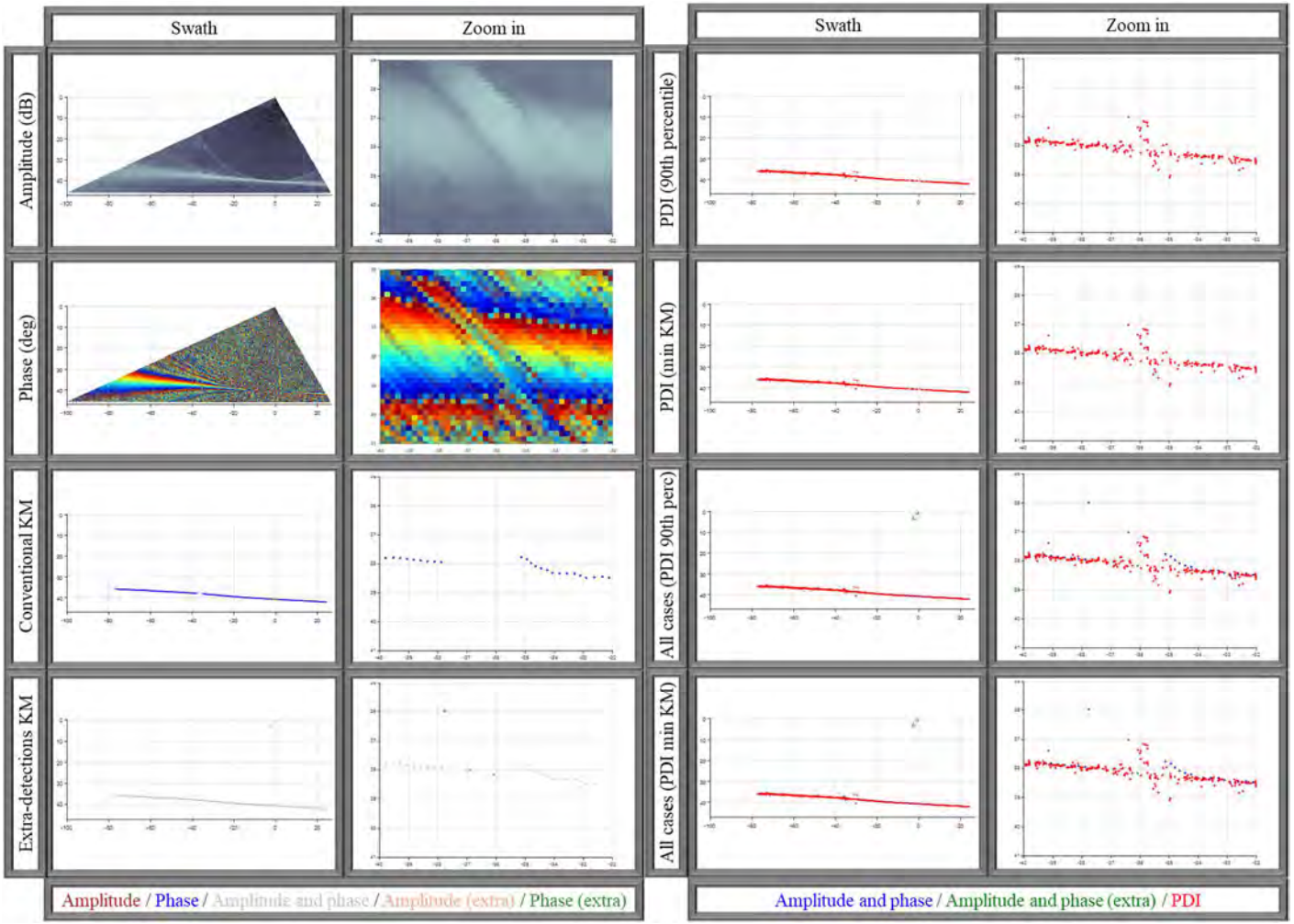

Case: 02-2d

Area: Cubes at 40 m depth. **Target:** Cube (1.0 meter side), no pole. **Line:** 0023_20191010_185445. **Ping number:** 1041.

Manual Threshold: 90th percentile: -13.0 dB. **Min KM:** -18.0 dB. **Incidence angle:** 56.76º.

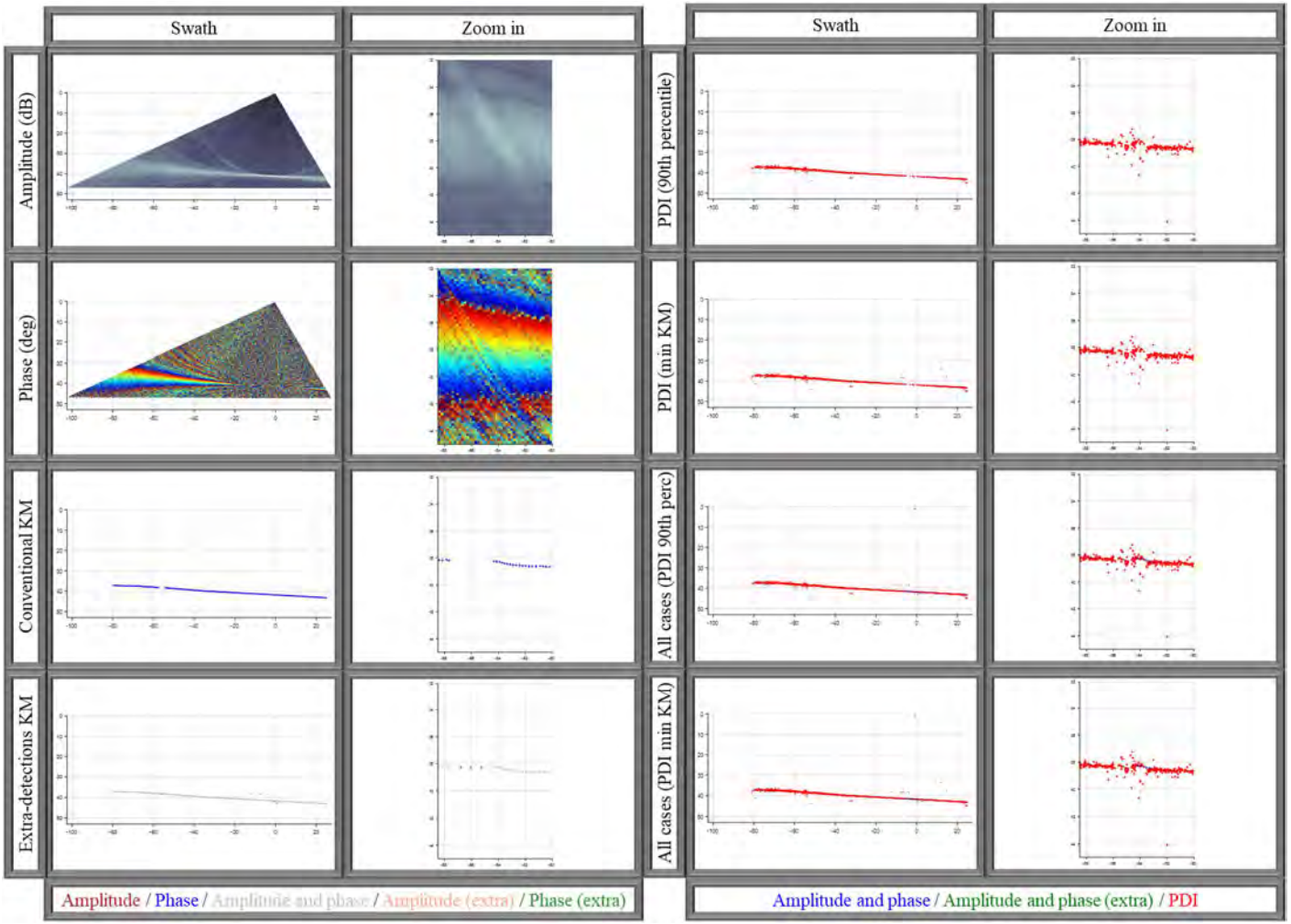

Case: 02-2e

Area: Cubes at 40 m depth. **Target:** Cube (1.0 meter side), no pole. **Line:** 0019_20191010_183610. **Ping number:** 885.

Manual Threshold: 90th percentile: -7.0 dB. **Min KM:** -26.5 dB. **Incidence angle:** 66.97º.

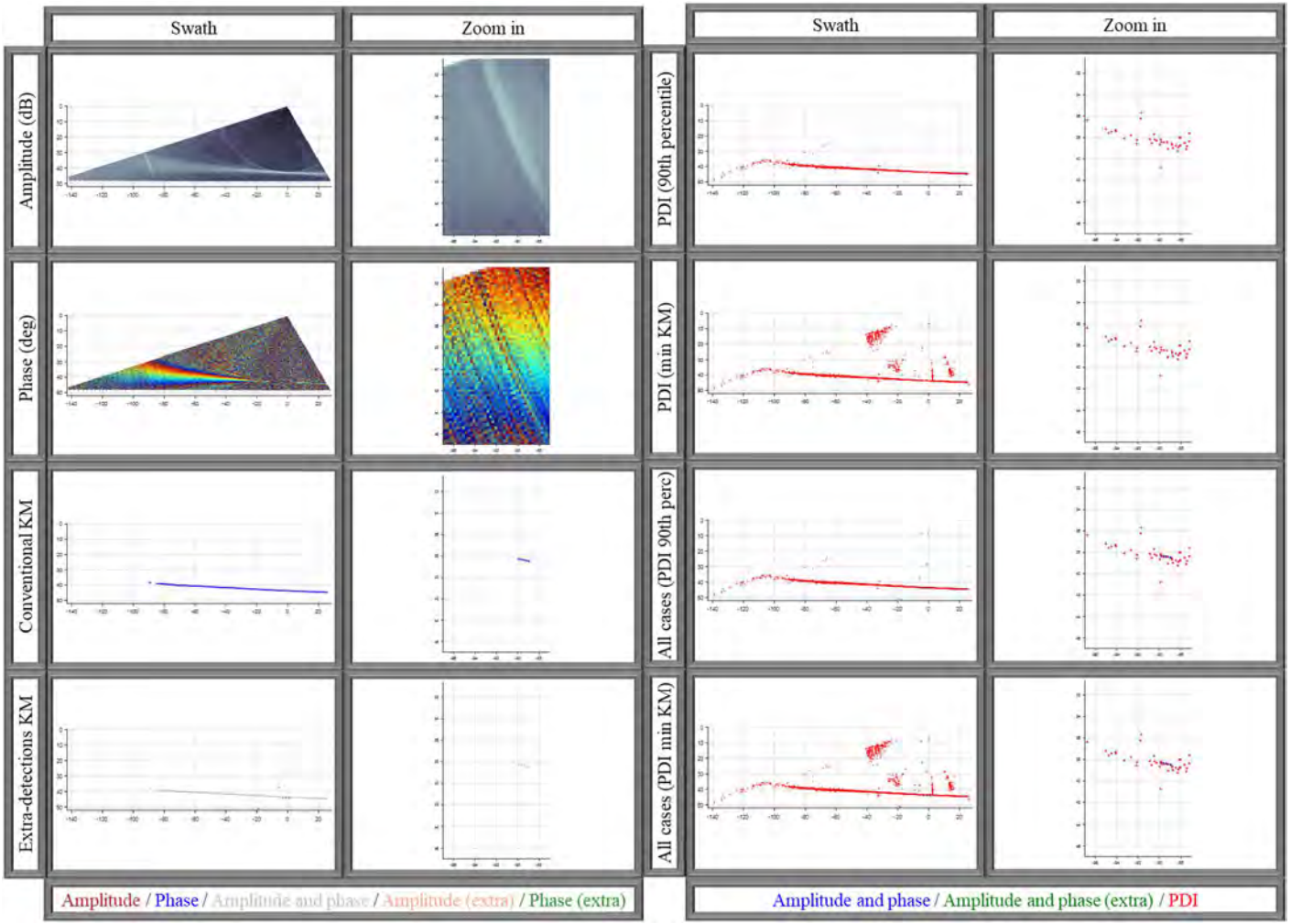

Case: 02-2f

Area: Cubes at 40 m depth. **Target:** Cube (1.0 meter side), no pole. **Line:** 0016_20191010_182619. **Ping number:** 903.

Manual Threshold: 90th percentile: -3.5 dB. **Min KM:** -41.5 dB. **Incidence angle:** 71.44º.

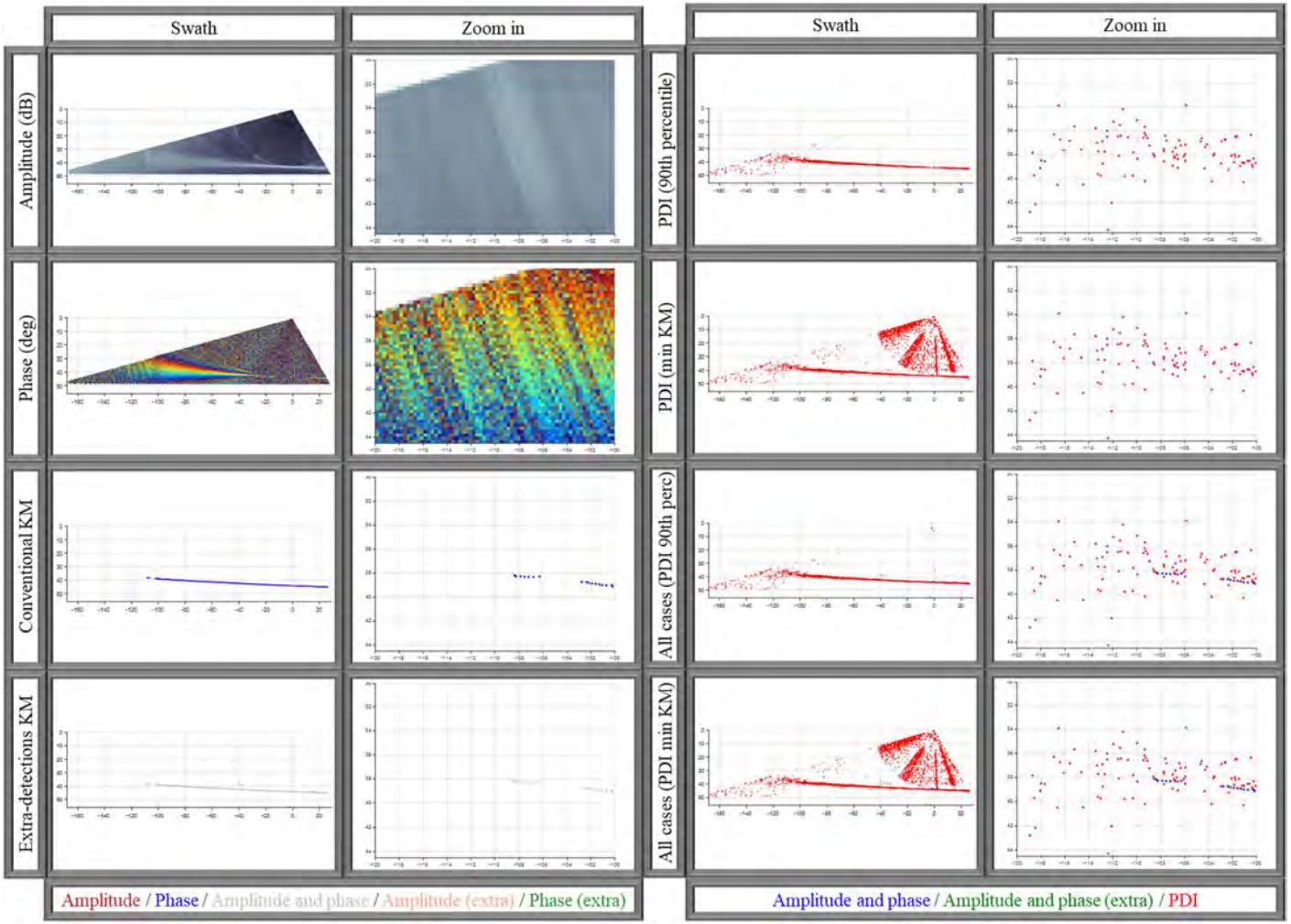

Case: 03-1

Area: HMCS Mackenzie shipwreck. **Target:** Low relief seafloor. **Line:** 0048_20191008_195040. **Ping number:** 322.

Manual Threshold: 90th percentile: -7.0 dB. **Min KM:** -20.5 dB.

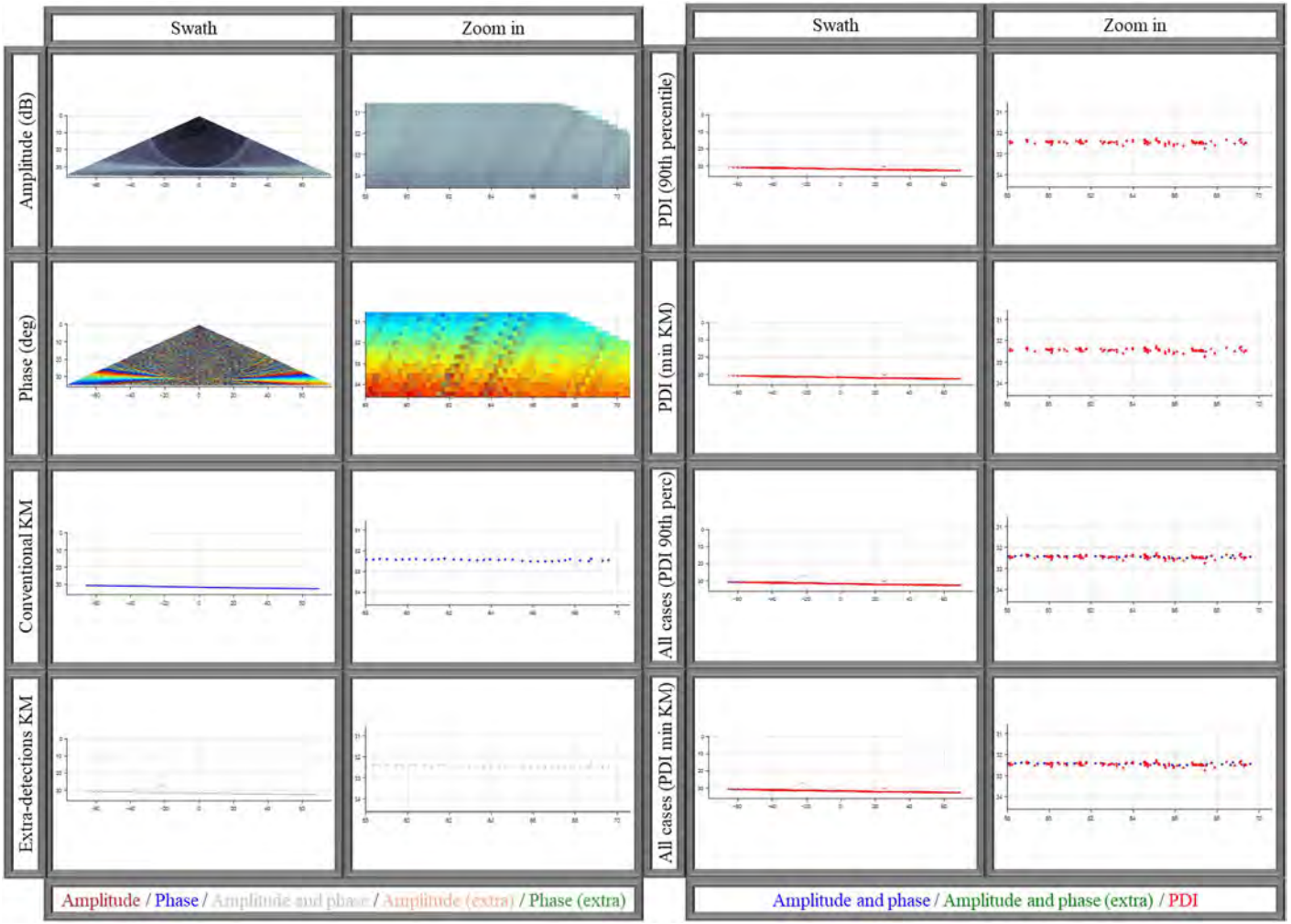

Case: 03-2

Area: MV GB Church shipwreck. **Target:** Low relief seafloor. **Line:** 0013_20191007_174133. **Ping number:** 327.

Manual Threshold: 90th percentile: -6.5 dB. **Min KM:** -17.0 dB.

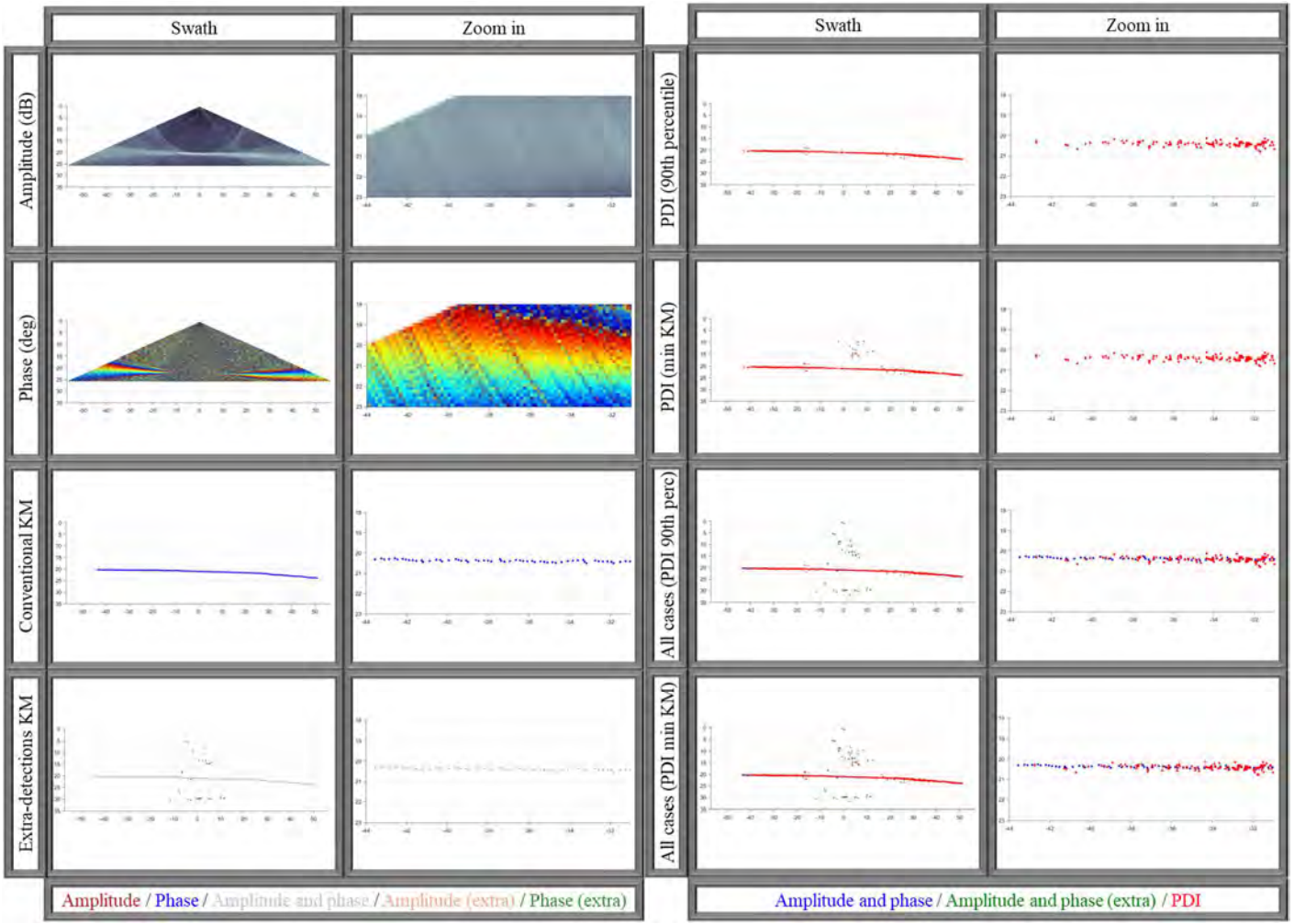

Case: 03-3

Area: Cubes at 20 m depth. **Target:** Low relief seafloor. **Line:** 0029_20191010_191602. **Ping number:** 2.

Manual Threshold: 90th percentile: -13.0 dB. **Min KM:** -16.5 dB.

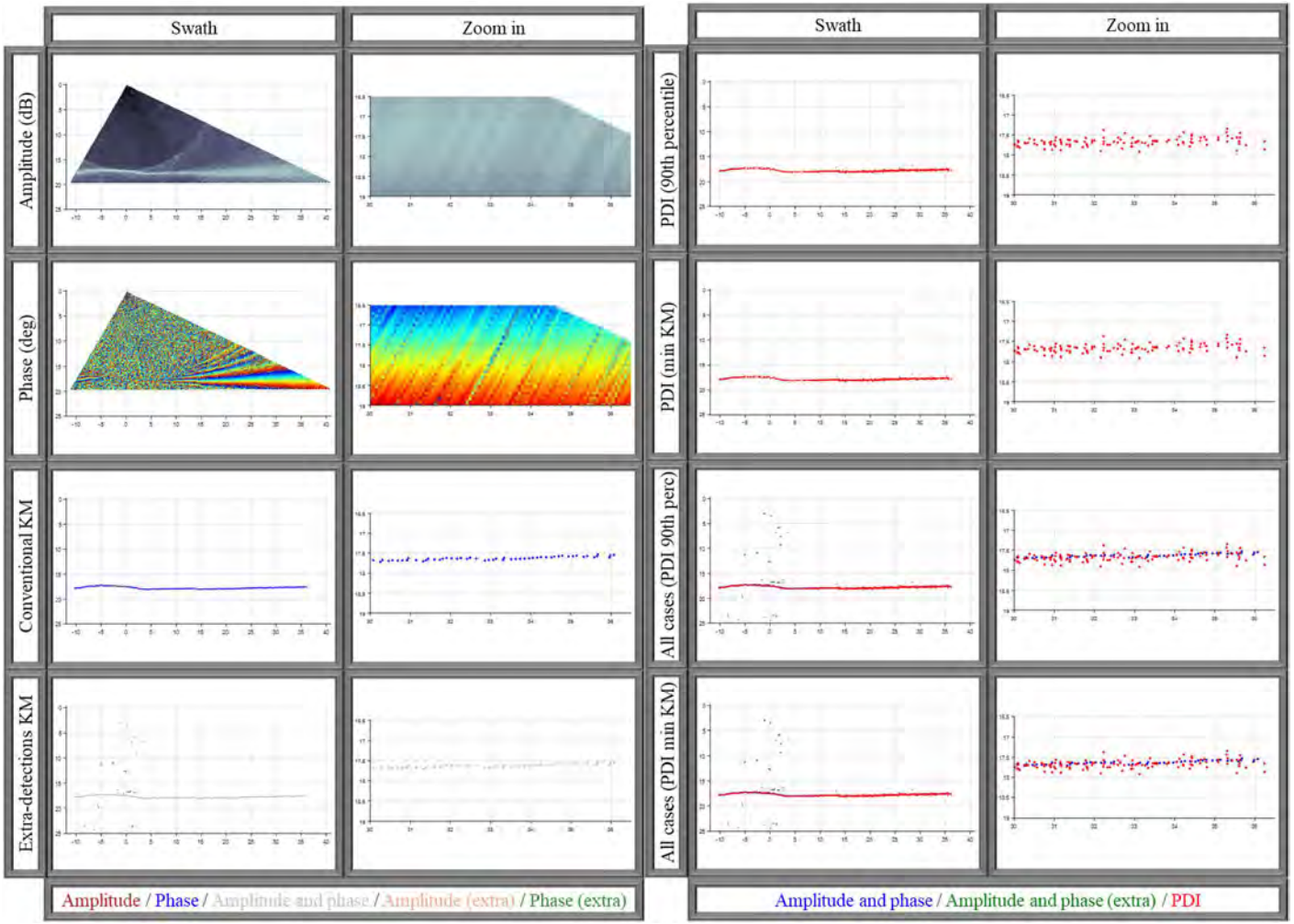

Case: 04-1

Area: Squamish Delta. **Target:** Extreme shallow water with shadows. **Line:** 0010_20190616_004957. **Ping number:** 5052.

Manual Threshold: 90th percentile: +1.0 dB. **Min KM:** -19.0 dB.

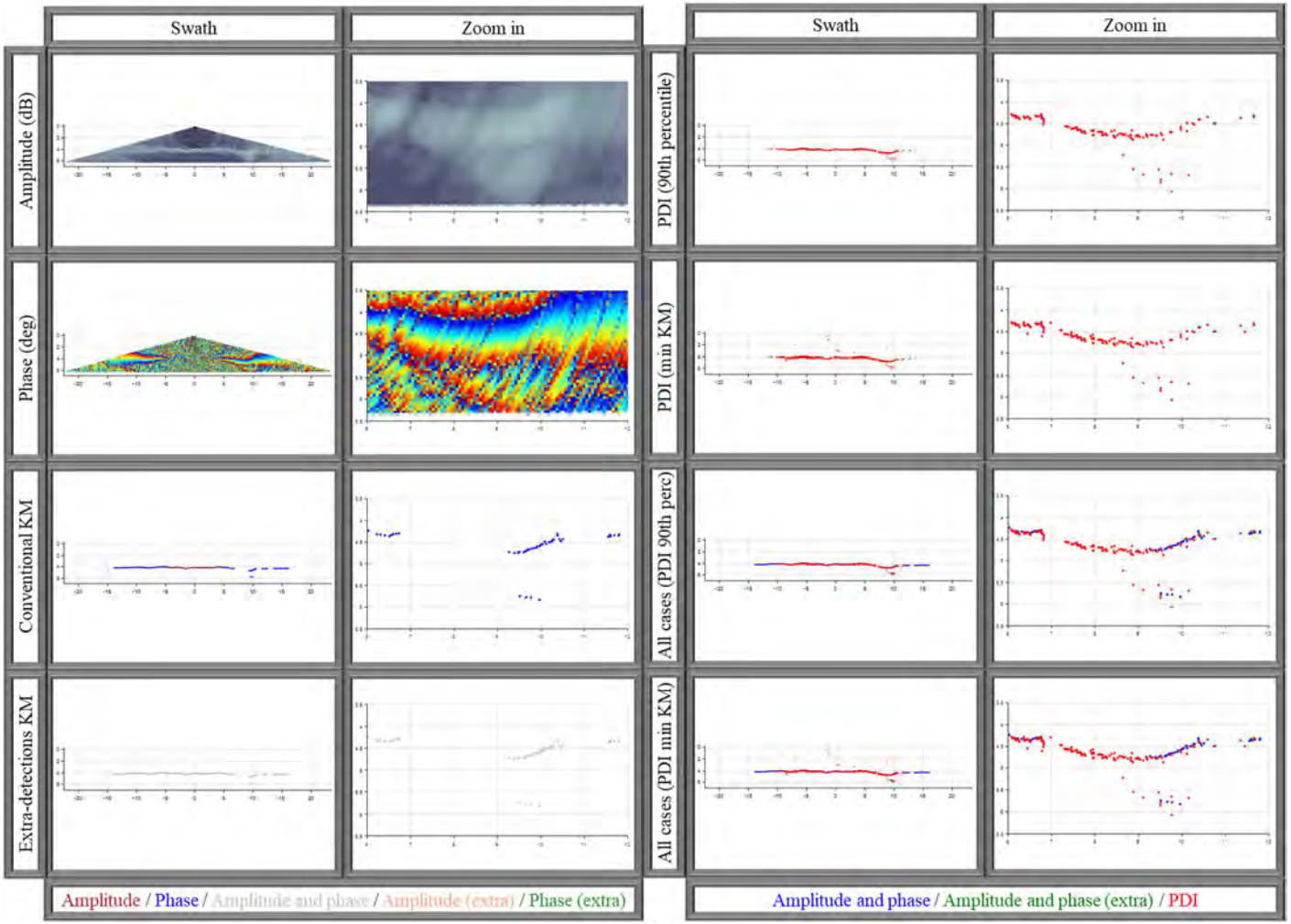

Case: 04-2

Area: Squamish Delta. **Target:** Extreme shallow water with shadows. **Line:** 0010_20190616_004957. **Ping number:** 5035.

Manual Threshold: 90th percentile: +0.0 dB. **Min KM:** -12.5 dB.

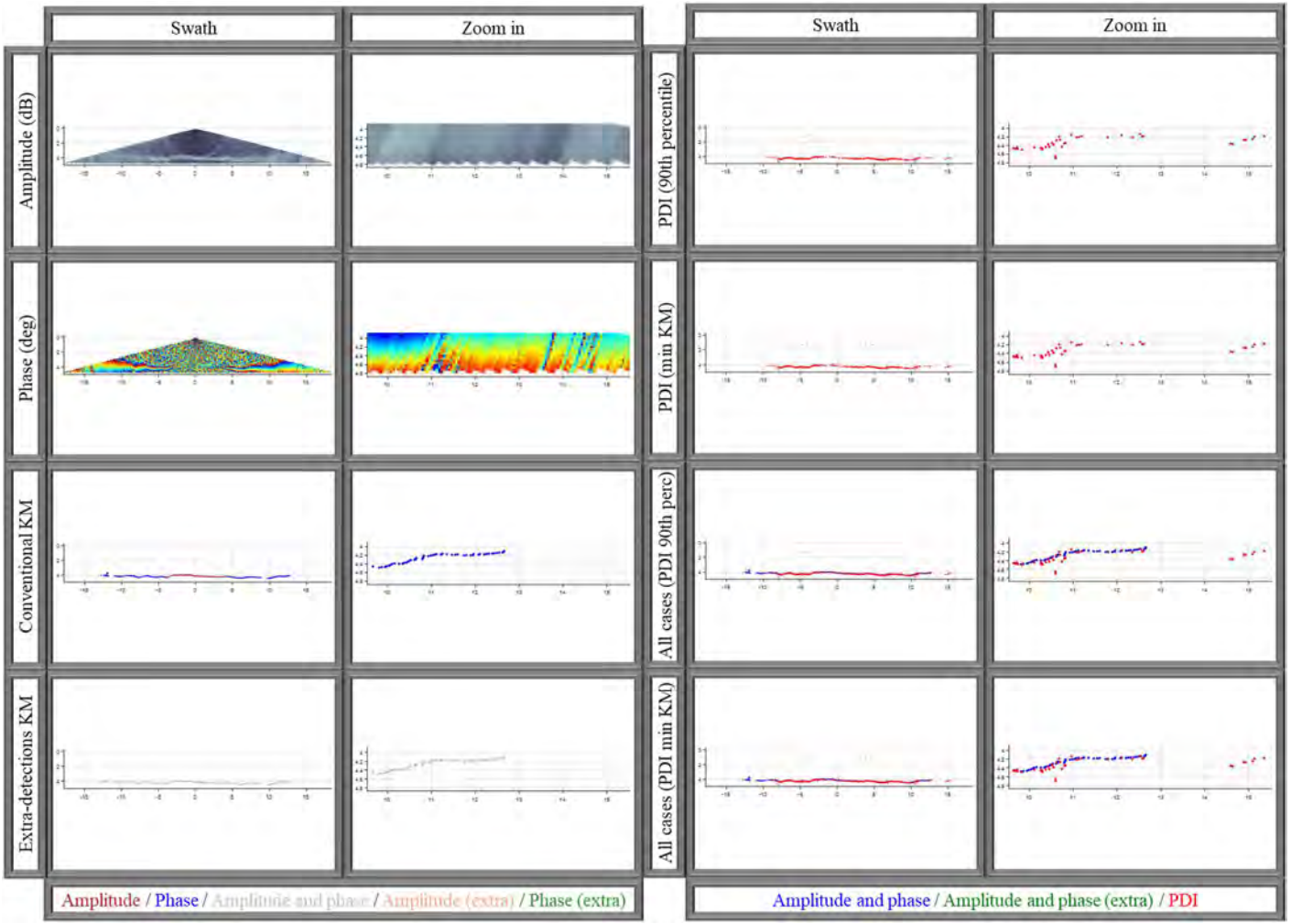

Case: 04-3

Area: Squamish Delta. **Target:** Extreme shallow water with shadows. **Line:** 0015_20190616_010445. **Ping number:** 1000.

Manual Threshold: 90th percentile: +2.0 dB. **Min KM:** -20.0 dB.

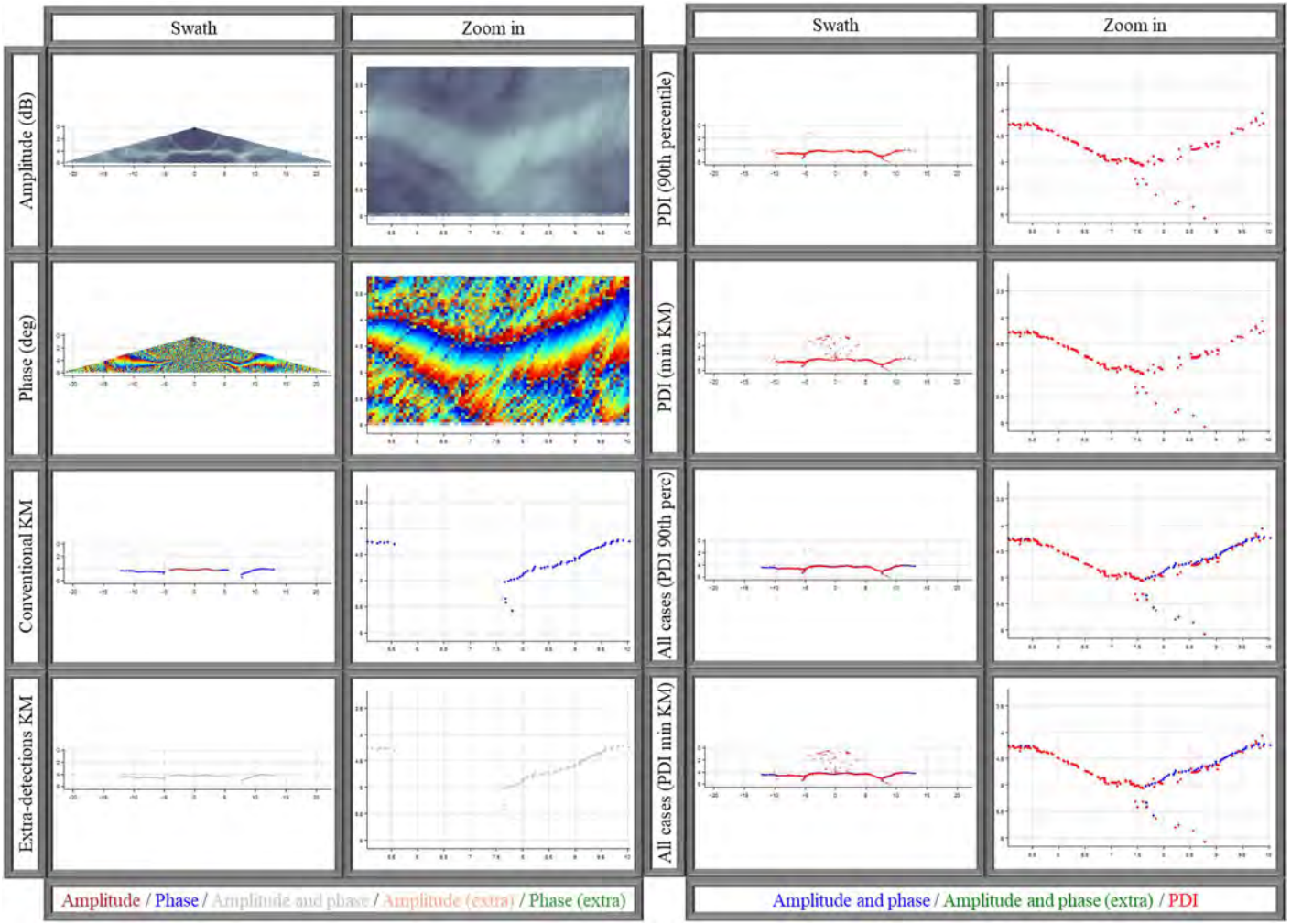

Case: 05-1

Area: HMCS Mackenzie shipwreck. **Target:** Mooring line to stern. **Line:** 0041_20191008_194038. **Ping number:** 439.

Manual Threshold: 90th percentile: -2.0 dB. **Min KM:** -9.0 dB.

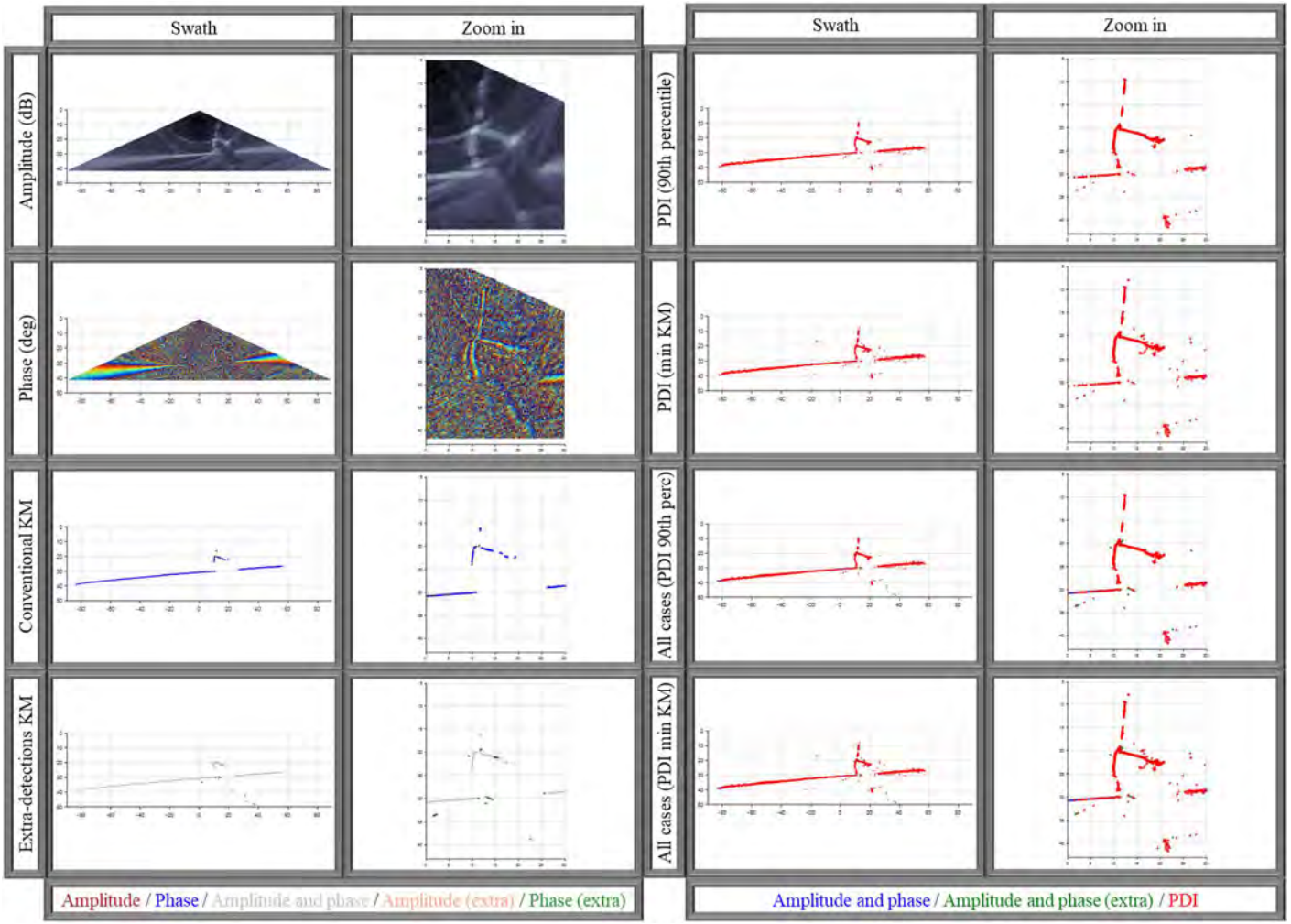

Case: 05-2

Area: HMCS Mackenzie shipwreck. **Target:** Longitudinal profile. **Line:** 0046_20191008_194820. **Ping number:** 186.

Manual Threshold: 90th percentile: -5.0 dB. **Min KM:** -29.5 dB.

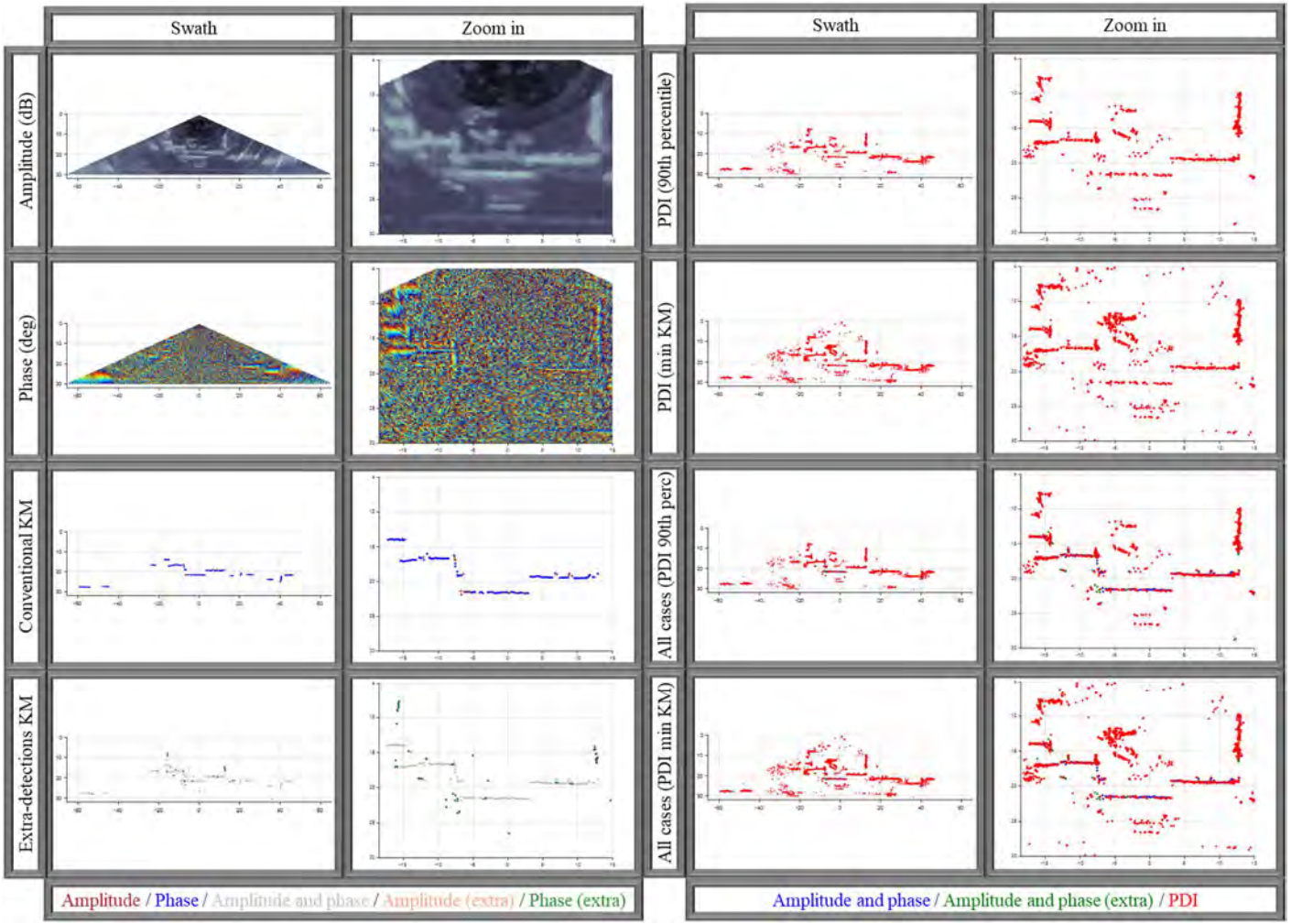

Case: 05-3

Area: HMCS Mackenzie shipwreck. **Target:** Rear Mast. **Line:** 0050_20191008_195405. **Ping number:** 403.

Manual Threshold: 90th percentile: -12.0 dB. **Min KM:** -23.0 dB.

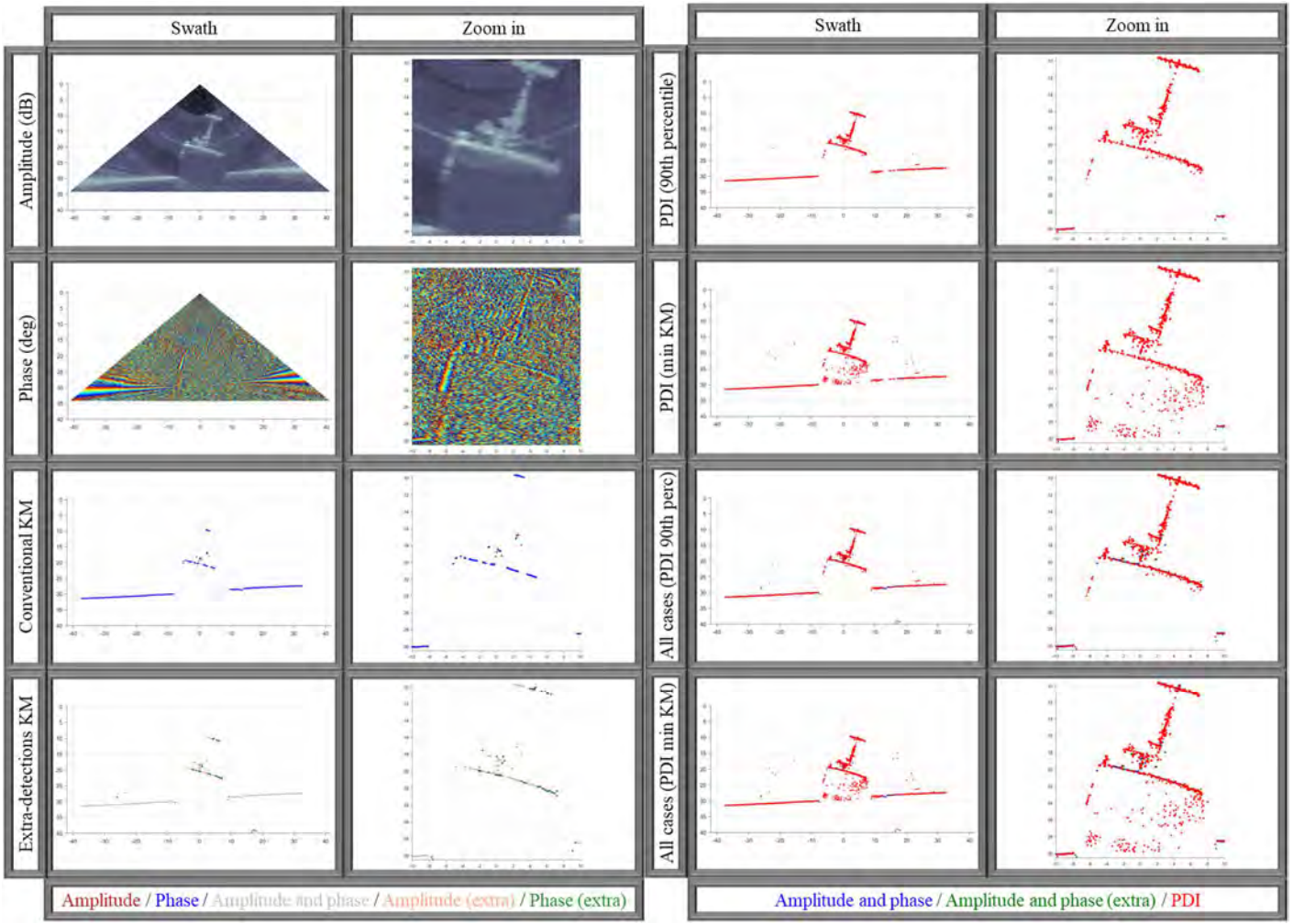

Case: 05-4

Area: HMCS Mackenzie shipwreck. **Target:** Rear Mast. **Line:** 0051_20191008_195549. **Ping number:** 274.

Manual Threshold: 90th percentile: -12.0 dB. **Min KM:** -46.0 dB.

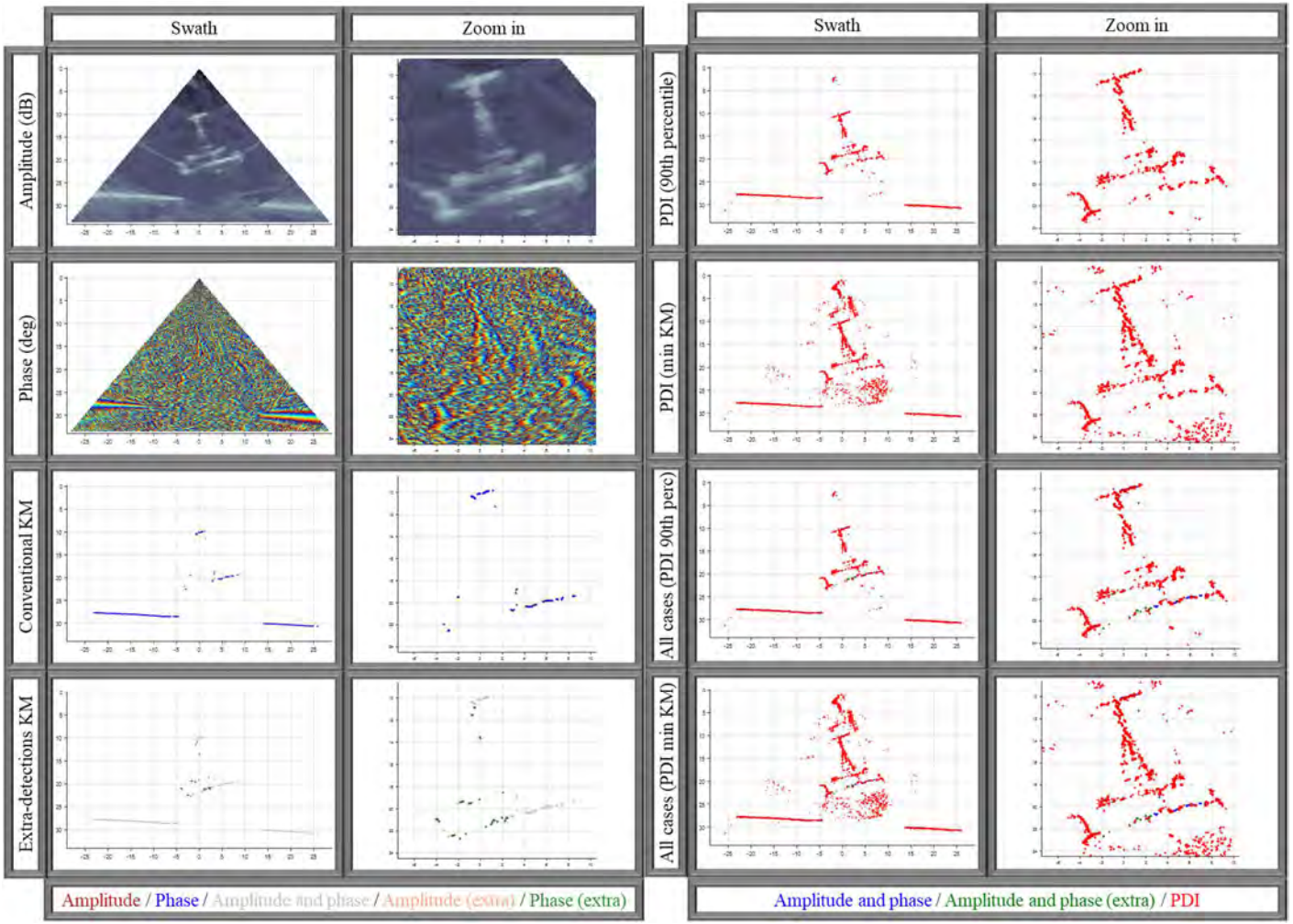

Case: 06-1

Area: MV GB Church shipwreck. **Target:** Longitudinal profile. **Line:** 0009_20191007_173625. **Ping number:** 153.

Manual Threshold: 90th percentile: -5.5 dB. **Min KM:** -21.5 dB.

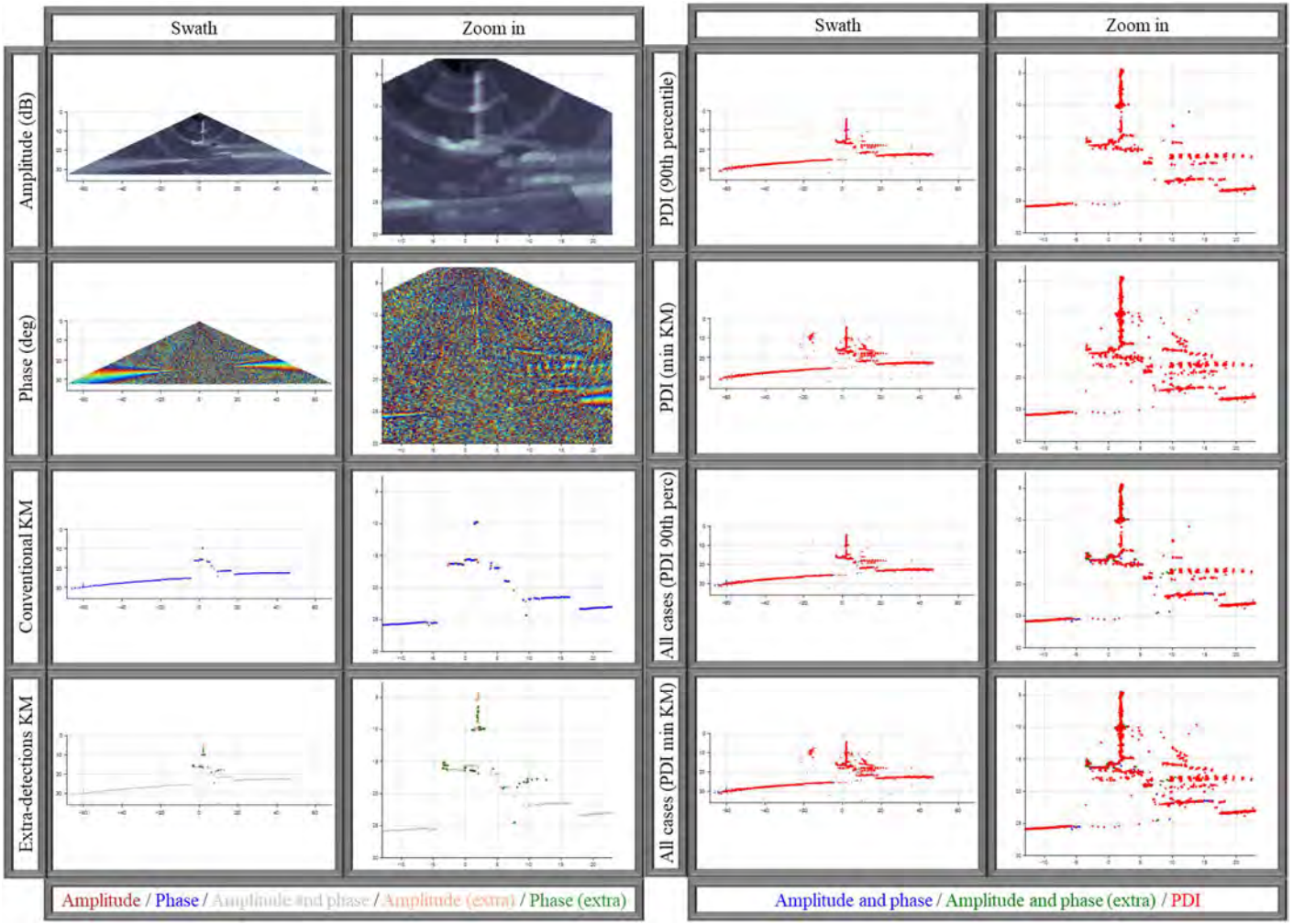

Case: 06-2

Area: MV GB Church shipwreck. **Target:** Longitudinal profile. **Line:** 0010_20191007_173733. **Ping number:** 257.

Manual Threshold: 90th percentile: -7.0 dB. **Min KM:** -25.0 dB.

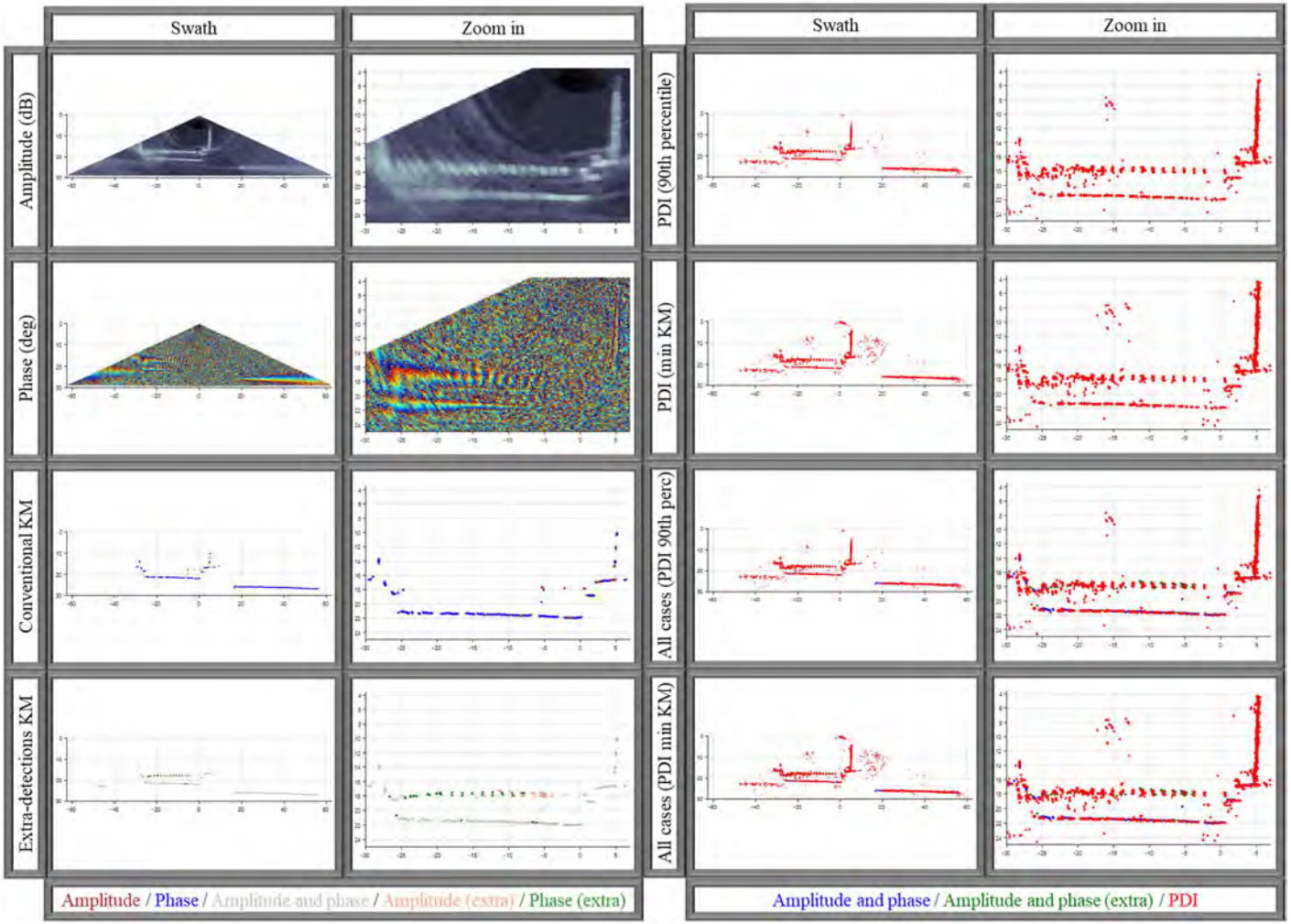

Case: 06-3

Area: MV GB Church shipwreck. **Target:** Foremast. **Line:** 0012_20191007_174024. **Ping number:** 440.

Manual Threshold: 90th percentile: -11.0 dB. **Min KM:** -20.0 dB.

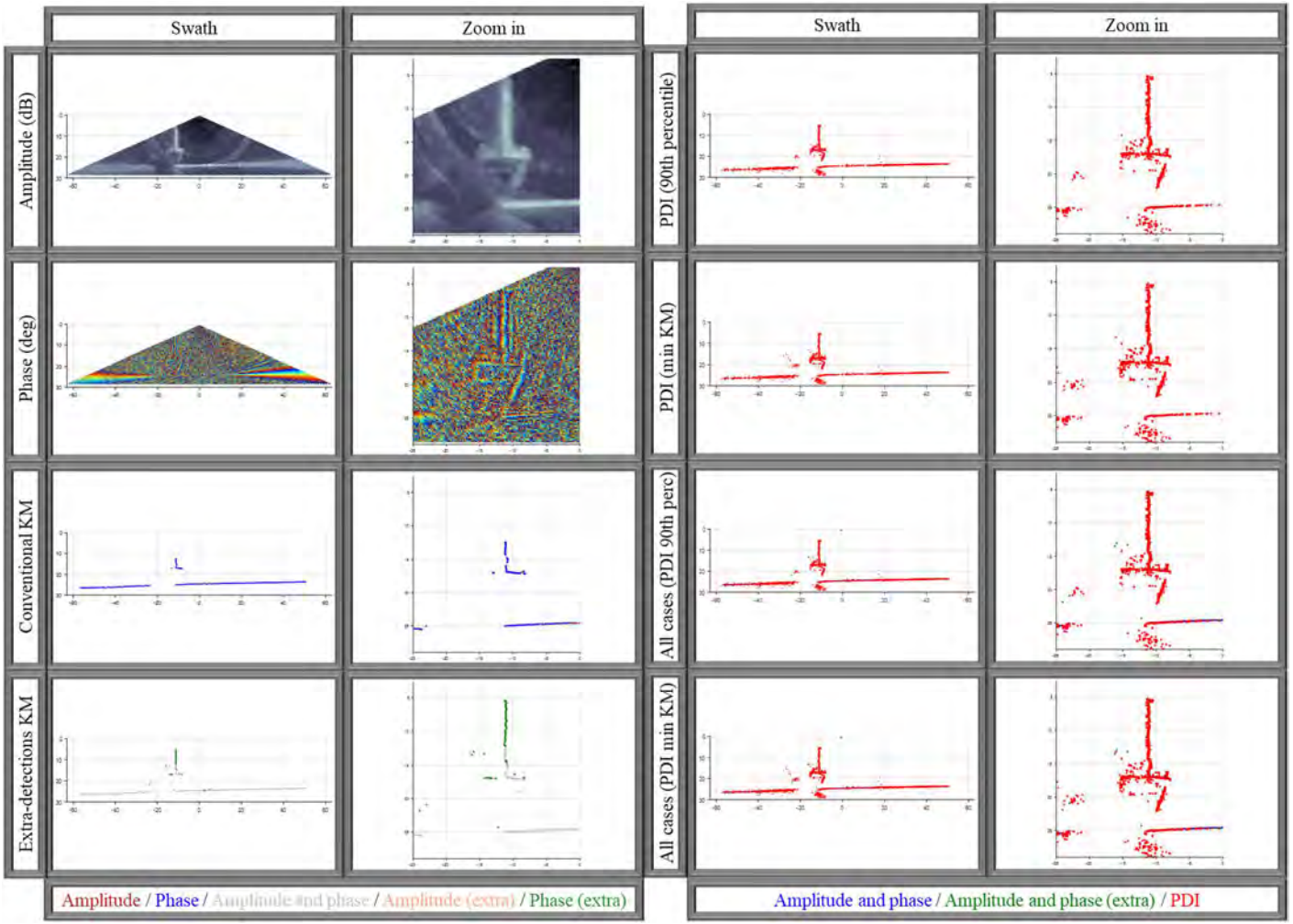

Case: 06-4

Area: MV GB Church shipwreck. **Target:** Lifeboat Davits. **Line:** 0014_20191007_174252. **Ping number:** 260.

Manual Threshold: 90th percentile: -11.5 dB. **Min KM:** -23.0 dB.

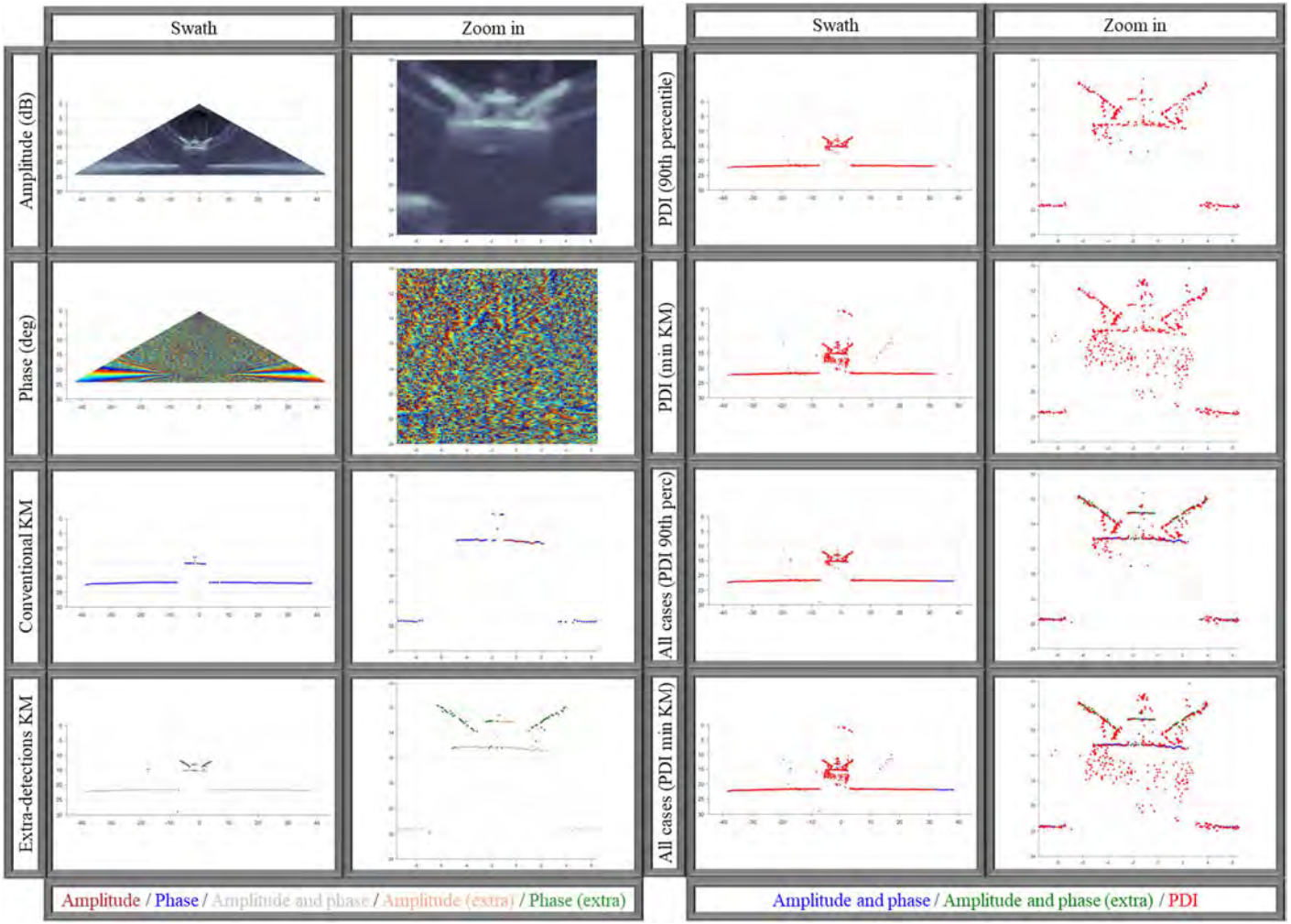

Case: 06-5

Area: MV GB Church shipwreck. **Target:** Mid section. **Line:** 0014_20191007_174252. **Ping number:** 346.

Manual Threshold: 90th percentile: -11.0 dB. **Min KM:** -27.5 dB.

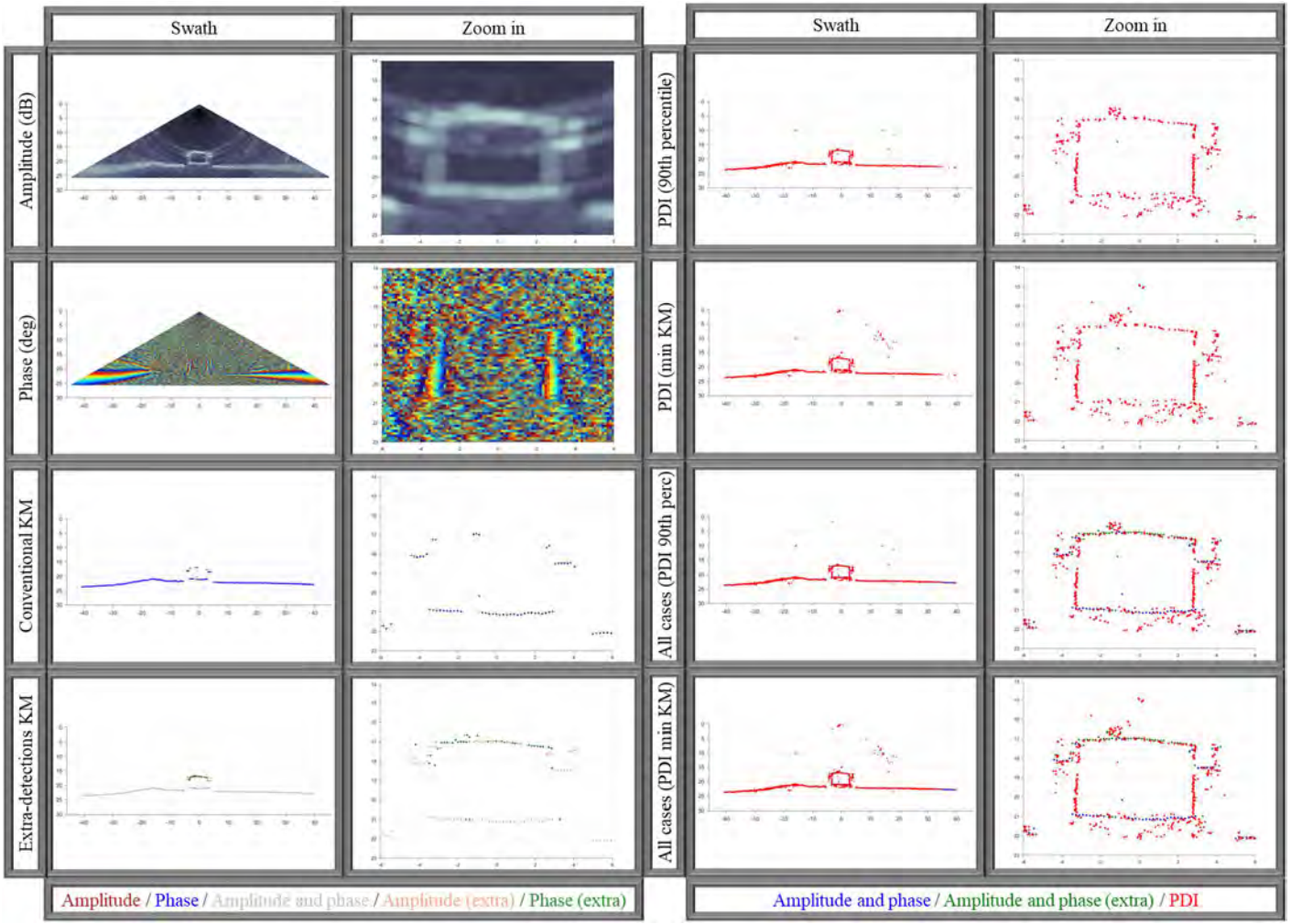

Case: 06-6

Area: MV GB Church shipwreck. **Target:** Mid section with loading spar. **Line:** 0014_20191007_174252. **Ping number:** 432.

Manual Threshold: 90th percentile: -13.0 dB. **Min KM:** -13.5 dB.

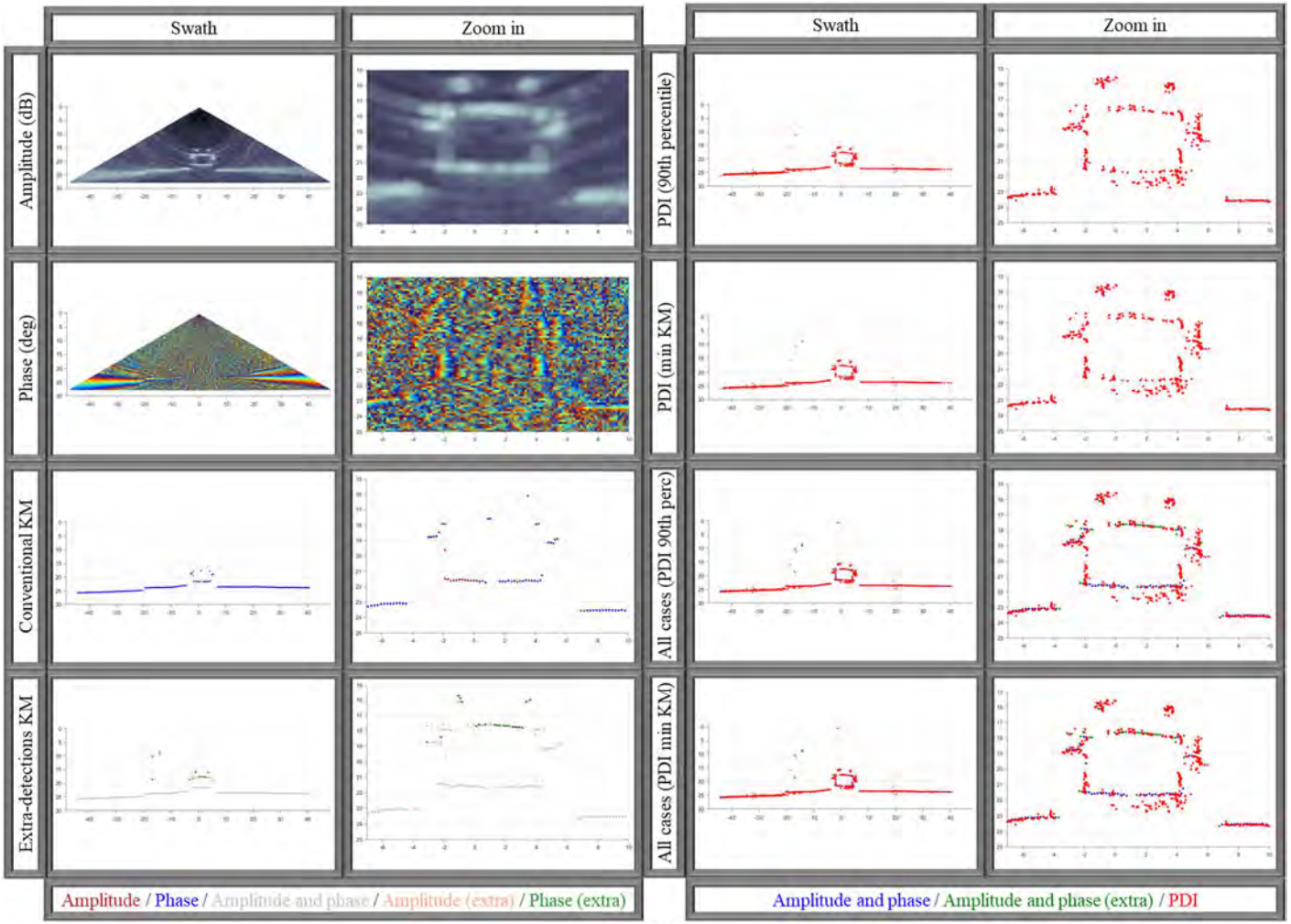

Case: 06-7

Area: MV GB Church shipwreck. **Target:** Longitudinal profile. **Line:** 0015_20191007_174438. **Ping number:** 217.

Manual Threshold: 90th percentile: -7.5 dB. **Min KM:** -19.5 dB.